ELECTROMAGNETIC MODELLING OF PLANAR CIRCUITS IN BOUNDED LAYERED MEDIA

THÈSE N^{O} 3746 (2007)

PRÉSENTÉE LE 16 MARS 2007
À LA FACULTÉ DES SCIENCES ET TECHNIQUES DE L'INGÉNIEUR
Laboratoire d'électromagnétisme et acoustique
SECTION DE GÉNIE ÉLECTRIQUE ET ÉLECTRONIQUE

ÉCOLE POLYTECHNIQUE FÉDÉRALE DE LAUSANNE

POUR L'OBTENTION DU GRADE DE DOCTEUR ÈS SCIENCES

PAR

Pedro CRESPO VALERO

Ing. de Telecomunicación, Universidad Politécnica de Madrid, Espagne
et de nationalité espagnole

acceptée sur proposition du jury:

Prof. M. Kayal, président du jury
Prof. J. R. Mosig, directeur de thèse
Dr C. Ernst, rapporteur
Prof. J. E. Page de la Vega, rapporteur
Dr F. Rachidi-Haeri, rapporteur

ÉCOLE POLYTECHNIQUE
FÉDÉRALE DE LAUSANNE

Lausanne, EPFL
2007

This thesis has been typeset using the MiKTEX2.4 distribution of LATEX 2_ε.
An electronic version is available at http://library.epfl.ch/theses/?nr=3746

A mis padres y hermanos.

En memoria de mi abuelo Bartolomé y mi tío Frasquito.

Abstract

Printed circuits in bounded media encompass a wide range of practical structures such as discontinuities in waveguides, planar circuits embedded in shielded multilayered media or even two-dimensional printed periodic structures.

The Electromagnetic (EM) modeling of printed circuits in layered bounded media is performed via an Integral Equation (IE) technique. Green's functions (GFs) are specially defined to satisfy both the Boundary Conditions (BCs) imposed by the layered media and by the transverse boundary enclosing the entire structure. Finally, a system of IEs on the equivalent sources can be solved numerically by means of the Method of Moments (MoM). Each of the problems enumerated above has already been solved by other authors using IE-MoM techniques. Nevertheless, our formulation introduces a *unified* approach applicable to all the aforementioned problems.

Due to the symmetry presented by a bounded layered media, the GF problem can be reduced into a two-dimensional transverse boundary problem and a one-dimensional transmission line problem in the normal direction. Both problems can be treated independently.

This thesis proposes and fully develops an efficient technique that encompasses different laterally bounded multilayered problems with a seamless transition between them. The method is based on a modal representation of the transverse boundary problem and on the expansion of the equivalent surface currents by zero-curl & constant-charge Basis Functions (BFs). It offers a unified and versatile approach that, on one hand eliminates redundancy in the formulation and on the other hand simplifies each particular problem to the evaluation of constant coefficients or basic line integrals. Analytical solutions can be found for the combination of linear subsectional basis functions in rectangular and circular Perfect Electric Conductor (PEC) boundaries as well as for periodic lattices.

This thesis then solves the problem of transmission line model in the longitudinal direction by proposing an efficient algorithm that guarantees numerical stability under a variety of known critical conditions where other already known formulations fail. In addition, it introduces alternate equivalent expressions of this formulation that allow new interpretations of the problem.

Due to its practical interest, the method is applied for the EM modeling of multilayered boxed printed circuits. This motivated the implementation of a *dedicated* software tool for the *efficient* analysis of these topologies including losses. Extensive numerical experiments have been carried out to assess the validity of the aforementioned theory and some properties of test-structures (losses, mesh, etc).

Keywords: *Computational electromagnetics, layered media, printed circuits, cavity.*

Résumé

Les circuits imprimés en milieux finis englobent un large éventail de structures pratiques telles que les discontinuités en guides d'ondes, les circuits planaires intégrés dans des milieux stratifiés voire des structures imprimées périodiques à deux dimensions.

La modélisation électromagnétique (EM) des circuits imprimés en milieux stratifiés finis est effectuée à l'aide d'une technique d'équation intégrale (IE). Les fonctions de Green (GF) sont définie spécifiquement pour respecter à la fois les conditions aux limites imposées par la structure multicouche et par le frontières transverses entourant la structure complète. Finalement, un système d'IE sur les sources équivalentes peut être résolu numériquement à l'aide de la méthode des moments (MoM). Les problèmes énumérés ci-dessus ont déjà été résolus par d'autres auteurs en utilisant des techniques d'IE-MoM. Néanmoins, la formulation introduite ici utilise une approche *unifiée* applicable à tous les problèmes mentionnés.

En raison de la symétrie présentée par les milieux stratifiés finis, la formulation de la GF peut être réduite à un problème de frontière transversale à deux dimensions et à une ligne de transmission unidimensionelle dans la direction perpendiculaire. Les deux problèmes peuvent être traités indépendemment.

Cette thèse propose et développe de manière approfondie une technique efficace qui couvre de façon simple différents problèmes multicouches ayant des dimensions latérales finies. La méthode est basée sur une représentation modale du problème à frontière transverse et sur une expansion des courants de surface équivalents à l'aide de fonctions de base à rotationnel nul et charge constante. Elle offre une approche unifiée et souple qui d'une part élimine la redondance dans la formulation, et de l'autre simplifie chaque problème particulier en une évaluation de coefficients constants et d'intégrales de ligne simples. Des solutions analytiques peuvent être trouvées pour la combinaisons de fonctions de base partielles dans les conducteurs électriques parfaits rectangulaire et circulaire, ainsi que dans les réseaux périodiques.

Cette thèse résout ainsi le problème du modéle de ligne de transmission dans la direction longitudinale en proposant un algorithme efficace qui garantit la stabilité numérique dans nombre de conditions critiques, où d'autres formulations connues échouent. De plus, elle introduit d'autres expressions équivalentes de cette formulation, qui permettent des interprétations nouvelles du problème.

De par son intérêt pratique, cette méthode est appliquée à la modélisation électromagnétique de circuits imprimés multicouches en boîtiers. Cela a conduit à l'implémentation d'un logiciel *spécialisé* pour l'analyse efficace de ces topologies, en incluant les pertes. De nombreux tests numériques ont été faits pour vérifier la validité de la théorie présentée ci-dessus et certaines propriétés des structures testées (pertes, maillage, etc.).

Mots-clés: *calculs électromagnétiques, milieux stratifiés, circuits imprimés, cavités.*

Resumen

Los circuitos impresos en medios cerrados comprenden a una amplia gama de estructuras prácticas tales como discontinuidades en guía de onda, circuitos impresos inmersos en un medio multi-estratificado y blindado o incluso estructuras periódicas en dos dimensiones.

El modelado electromagnético (EM) de circuitos impresos en medios estratificados y cerrados se lleva a cabo mediante la técnica de ecuación integral (IE). La función de Green (GF) está especialmente definida para satisfacer las condiciones de contorno impuestas por el medio estratificado y por la superficie transversal que engloba a toda la estructura. Finalmente, un sistema de IEs sobre las fuentes equivalentes son resueltas numéricamente por medio del método de los momentos (MoM). Cada uno de los problemas anteriormente mencionados han sido ya resueltos por otros autores mediante técnicas de IE-MoM. No obstante, esta formulación introduce una nueva solución *unificada* aplicable a todos ellos.

Debido a la simetría presente la estructura estratificada y cerrada, el problema de GF puede simplificarse a un problema de contorno transversal en dos dimensiones, y un problema de línea de transmisión en la dirección normal en una sola dimensión. Ambos problemas pueden ser tratados independientemente.

Esta tesis propone y desarrolla una técnica para resolver de forma general distintos problemas estratificados y encerrados lateralmente por ciertas condiciones de contorno. El método se basa en la representación modal del problema de contorno transversal y en la expansión de las corrientes de superficie equivalentes mediante funciones base con rotacional cero y carga constante. Esto permite un procedimiento unificado y versatil que, por un lado elimina la redundacia en la formulación y por otro simplifica cada problema específico a la evaluación de coeficientes constantes o simples integrales de línea. En concreto, la combinación de funciones lineales de soporte finito tanto con paredes de conductor perfecto (PEC) de formas rectangular o circular como con condiciones periódicas presentan solución analítica.

En esta tesis, el problema de línea de transmisión en la dirección longitudinal, se resuelve mediante un eficaz algoritmo que garantiza la estabilidad numérica incluso bajo condiciones críticas en las que otras formulaciones fallan. Además, se han desarrollado distintas variantes de la formulación que permiten nuevas interpretaciones del problema.

Debido a su interés práctico, este método ha sido aplicado para el modelado EM de circuitos impresos multi-estratificados en caja. Esto ha motivado la implementación de una herramienta software *especializada* en analizar eficazmente este tipo de topologías incluyendo efectos de pérdidas. Se han llevado a cabo un gran número de experimentos numéricos para garantizar la validez de esta teoría así como algunas de las propiedades de las estructuras de prueba (pérdidas, mallado, etc).

Palabras-clave: *Electromagnetismo computacional , medio estratificado, circuito impreso, cavidad.*

Acknowledgements

The work that you are about to read is not only the result of my own research but the continuous advise, collaboration and support of many other people. It is a pleasant aspect that I have now the opportunity to express my gratitude for all of them.

First and foremost, I would like to *deeply* thank my thesis advisor, Prof. Juan R. Mosig, who gave me the great opportunity of joining his laboratory and doing this work. I really appreciated his constant support, his effort to make a gap for me in his always busy agenda, his ideas, his honesty, and his trust on me. It has been an honor for me to work side by side with a great person and a worldwide renowned scientist.

My appreciation goes to the committee of experts who evaluated this thesis: Prof. Juan E. Page, from Universidad Politécnica de Madrid, Dr. Christoph Ernst from European Space Agency and Prof. Farhad Rachidi-Haeri from EPFL who kindly accepted to review my work and took the effort in reading and providing me with valuable comments. I also thank Prof. Maher Kayal from EPFL for charing this jury.

I have a great debt with my office mate and good friend Ivica Stevanović. It is difficult to explain in words the admiration and gratitude I feel for "my serbian brother". As a senior in the lab, he advised and discussed with me about technical matters and, as a good friend, he always encouraged me in the worst moments and enjoyed the good ones.

I also owe to my colleague and friend Daniel Llorens del Río a lot of the results in this thesis. He always shared with me, without any distrust, his deep knowledge in many fields. His overly enthusiasm and wish for providing "only high-quality work and not less", has made a deep impression on me and became a constant source of motivation.

My gratitude also goes to "l'enfant terrible", Michael Mattes. We were companions in all the ESA/EU projects where he was the best possible co-supervisor. I really appreciated and will not forget his kindness, encouragement and specially his patience.

Last but not least, I would like to thank the rest of the team, starting with my dear secretaries Eulalia Durussel and Alix Wend whose door was always open and helped me in all possible ways. I wish to thank also to Prof. Anja Skrivevik, among other things, for her persistence in making my French improve and for allowing me to work in the WIDE-RF project. As "Monsieur Bateau-Olive", I would also like to say thanks to Jean F. Zürcher. I really enjoyed and learned from his large expertise and from his "ça c'est impossible" while discussing about building one of my crazy prototypes. Finally, my greatest gratitude for all the former and current PhDs and collaborators from both, the Electromagnetics and Acoustics groups, of LEMA, with a special mention to Gregoire Walckiers who shared the office during the last days of this thesis and stoically stood my moody character.

I would be unfair if I do not mention to those who encouraged me to start and supported me during this adventure. My admiration and gratitude goes to the members of the the Electromagnetics group of Universidad Politécnica de Madrid, specially to Jorge Ruiz (he also provided valuable reference results for this thesis) and the Professors J. E. Page, J. M. Rebollar, J. R. Montejo and J. Esteban.

Outside the laboratory, I wish to deeply thank to Mari Cruz, Fran and Lara who always welcomed me as a member of their own family.

A big thanks also to all the members of the "cinema club" and my friend in Lausanne: Eugenia Cabot, Xavi, Katarina Blagović, Maurice & Karine, Jerome & Caroline, Pablo Dosil and Rodrigo García.

My fondest regards to my friends from Spain who did not forget me despite the distance: Bruno Fernández, Jose M. Duarte, Jose A. García, Fco. Rodriguez-Ameijeiras, Carlos Oliver, Oscar Cabral, Juanan & Leyre, Miguel Quetglas, Isa Ruiz, Pepa Soler and Luis Ridao.

Finally, I would like to thank to all my family. I dedicate this thesis to my parents and brothers, who always loved and supported me under any circumstances, and in the memory of my beloved grand father Bartolomé and my uncle Frasquito.

Table of Contents

1 Introduction **1**

1.1 Objectives . . . 3

1.2 Outline . . . 3

References . . . 5

2 Foundations **7**

2.1 Introduction . . . 7

2.2 Field Equations . . . 7

2.3 Surface Integral Equations . . . 8

2.4 Green's Function . . . 12

2.5 Method of Moments . . . 15

2.6 Network Characterization . . . 16

2.7 General Assessment . . . 20

References . . . 21

3 Transverse Boundary Problem **23**

3.1 Introduction . . . 23

3.2 Formulation . . . 23

3.3 Overlapping Integrals . . . 25

  3.3.1 Definition . . . 26

  3.3.2 Transformation Into Contour Integrals . . . 27

3.4 Basis Functions . . . 29

  3.4.1 Rooftops and RWG Functions . . . 30

  3.4.2 OIs for Linear Subsectional BFs . . . 31

3.5 Transverse Boundary Problems . . . 35

  3.5.1 Rectangular Waveguide . . . 36

  3.5.2 Circular Waveguide . . . 38

  3.5.3 Periodic Boundary . . . 40

3.6 Strategy Used for the Resolution of OIs. . . . 44

3.7 Numerical Results 46
3.8 Conclusion 50
References 53

4 Layered media **55**
4.1 Introduction 55
4.2 Transmission Line Model 56
  4.2.1 Formulation 56
  4.2.2 Intra-layer Interaction 60
  4.2.3 Inter-layer Interaction 60
4.3 Alternate Expressions for the TLMo 62
  4.3.1 Bilinear Form 62
  4.3.2 Decomposition in Multiple Reflections 64
4.4 Stability 66
  4.4.1 Review 66
  4.4.2 Cutoff Condition 69
4.5 Algorithm 74
4.6 Resonances 76
4.7 Application 80
4.8 Conclusion 84
References 91

5 Analysis of Multilayered Boxed Printed Circuits **93**
5.1 Review of Integral Equation Methods 94
5.2 Formulation 97
5.3 Modal Series 98
  5.3.1 Kummer's Transformation 98
  5.3.2 Asymptotic Sequences 99
  5.3.3 Quasi-static Series 103
  5.3.4 Dynamic Series 105
  5.3.5 Convergence 107
  5.3.6 Reaction Between Two Interfaces 111
  5.3.7 General Assessment Modal Series 114
5.4 Losses 116
  5.4.1 Metallic Enclosure 116
  5.4.2 Printed Circuits 119
  5.4.3 Losses in Dielectrics 121

5.5 Network Characterization. 122
5.5.1 Ports Loads and Interconnections 122
5.5.2 Connections to Ground. 124
5.6 Applications 126
5.6.1 Coupled-lines Filter 126
5.6.2 Multilayered Bandpass Filter 131
5.6.3 Ring Resonator 135
5.6.4 Tapped-combline Bandpass Filter 138
5.6.5 Notch Filter 143
5.7 Conclusion 147
References 148

6 Conclusions 151
6.1 General Assessment 151
6.2 Original Contributions 153
6.3 Perspectives 154

List of Abbreviations 156

List of Figures 162

List of Tables 163

CV 165

List of Publications 167
Refereed Journal Papers 167
Refereed Conference Papers 167
Workshop Presentations 168
Technical Reports 168

1 Introduction

Multilayered media with printed circuits embedded between dielectric layers are one of the most successful technologies for manufacturing planar structures with a good performance-to-price ratio. Planar structures include many different geometries, ranging from cavity-backed microstrip antennas, through Frequency Selective Surface (FSS) and photonic band-gap materials, to shielded printed circuits or waveguide filters with printed irises. The common denominator in all of them is a) the presence of planar metallic surfaces (printed lines, patches, and apertures in ground planes); b) a multilayered structure made of homogeneous and isotropic dielectric, and c) a certain BC imposed laterally.

We can classify all the above geometries into a generic structure denoted as *printed circuits* in a *bounded layered media* (Fig. 1.1). The concept of printed circuit must be understood in a general sense. In microstrip-type circuits, it means the metallic surface of the circuit but it refers to the metal-devoid surfaces in circuits like coplanar waveguide or slot-lines. On the other hand, bounded layered media are characterized by a constant cross section along transverse coordinates (u_1, u_2) and a filling medium whose properties vary stepwise along the normal direction z (the multilayered substrate).

We aim at analyzing the Electromagnetic (EM) behavior of these structures for two different scenarios. The first one corresponds to the excitation of the structure with EM waves $\mathbf{E}_1^{\mathrm{i}}, \mathbf{H}_1^{\mathrm{i}}$ impinging the medium with a certain angle and polarization. This situation is encountered, for example, when planar periodic structures are illuminated with plane waves or in the excitation of a waveguide with modes. The other scenario is more characteristic of planar shielded circuits using coaxial-type feeds and assumes a localized field $\mathbf{E}_2^{\mathrm{i}}, \mathbf{H}_2^{\mathrm{i}}$ at the edge of a printed circuit (Fig. 1.1).

The EM behavior of this problem can be modeled with a wide range of numerical techniques. The growth of computer technologies is pushing the utilization of generic methods like finite elements [1] , finite differences [2] or the transmission line method [3], where the volume of complex geometries is discretized and the EM problem can be solved systematically by performing a large amount of repetitive operations. As it is well known, these "generic" methods are essentially discrete formulations of the original differential Maxwell equations and can therefore be applied pointwise (or at least "pixelwise"). This means that complex geometries and arbitrary local variations of constitutive parameters can be easily accommodated. In turn, a high computational effort is needed and the achieved accuracy is insufficient for certain applications. The alternative, in order to gain in efficiency and accuracy, is to utilize methods specially suited to a specific topology. Some examples are the Mode Matching (MM) technique [4, 5], mainly applied to waveguide structures, or the IE approach in conjunction with the MoM, where the Green's function characterizes a specific environment. In general, aside from the geometry restrictions, one of the major drawbacks of the latter methods is the amount of quite sophisticated analytical pre-processing that they require. However if properly

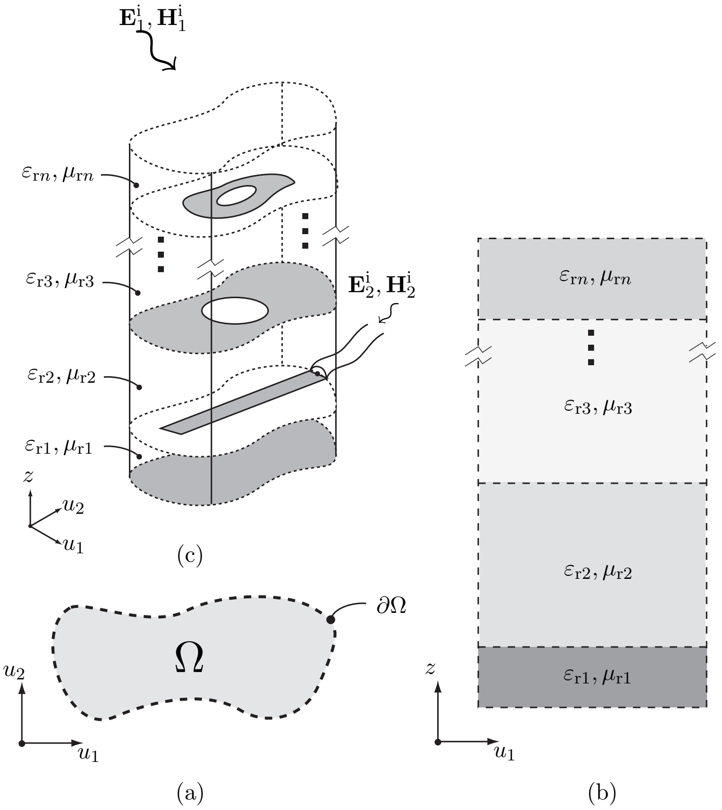

Figure 1.1: An example of printed circuits in a bounded layered media. (a) transverse boundary conditions, (b) layered media, (c) three-dimensional view.

treated, these methods can result in fast and efficient numerical algorithms. This is the main purpose of this thesis.

The IE technique has been successfully used in the analysis of multilayered printed circuits, and it has demonstrated accuracy and efficiency in the prediction of electrical responses of devices without lateral walls [6, 7], as well as shielded components [8]. Any systematic approach to these methods would contribute significantly towards the quality of the final algorithms, reducing the difficulty and implementation time.

Modern fabrication techniques introduce layers manufactured with new materials and dimensions, like the extremely thin high-resistive or semiconductor layers used in (Monolithic) Microwave Integrated Circuits (MMICs) and integrated antennas. Moreover, new functionalities calls for periodical arrangements (FSS, metamaterials, ...) and for partial or total shielding of devices (Electromagnetic Compatibility (EMC) problems, ...). This requires very different boundary conditions to be considered.

The existing numerical solvers and formulations are either specific for a given lateral BC or shown not to be numerically stable for every possible condition. A stable and efficient algorithm is thus needed that will give numerically accurate results for different critical conditions encountered in modern technology.

In this thesis we will demonstrate that an efficient technique that encompasses different laterally bounded multilayered problems with a seamless transition between them is still possible. The method will avoid having a specific formulation of printed circuits for each new boundary problem and it will offer a unified and versatile approach that eliminates redundancy in the formulation and eliminates error-prone numerical routines.

1.1 Objectives

The main research line in this thesis was strongly motivated by a project for the European Space and Technology Center of the European Space Agency (ESA-ESTEC).

The ESA-ESTEC project number 16332/02/NL/LvH, entitled “Integrated Planar and Waveguide Simulation Tools” and more specifically the activity associated with the “Analysis of Multilayered Boxed Printed Circuits” defined the main objectives of this thesis. The purpose of this research project was to bridge the gap between the printed circuit and the waveguide world developing a software tool (`MAMBO`) for the simulation of printed circuits embedded in multilayered media inside rectangular cavities. The model, based on an IE formulation, should take into account of the losses in the walls of the cavity, dielectrics and the metallic part of printed circuits. A dedicated formulation of the problem was required in order to produce an efficient EM solver showing definitive advantages with respect to available commercial softwares.

1.2 Outline

This section summarizes the contents of the chapters in the thesis. Every chapter contains a selective literature review substantial for the material presented in it.

Chapter 2 surveys the fundamental theorems and methods upon which the work in this thesis is built. The field equations and the surface BCs provides the starting point for the study of the EM problem. Based on the equivalence principle, we will demonstrate how the problem can be formulated in terms of two types of IE technique. We present a modal formulation of the GF for a general layered bounded media giving some insight into the physical meaning of the equations. We briefly describe the method of moment applied to the resolution of a system of integral equations emphasizing the role of the reaction concept within this method. Finally, we describe the model of port used for the network characterization of planar devices where the transfer function is deduced by exploring different visions of the system matrix.

Chapter 3 presents a unified approach to deal with transverse boundary problems. This Chapter first gives an overview of the formulation in connection with Chapter 2 and it outlines a canonic type of surface integrals relevant for the resolution of a generic transverse boundary problem. We describe how to reduce the dimension of these integrals, from surface to line integrals, by taking advantage of fundamental properties of the modal and BFs. Then, these expressions are specialized for the simulation of problems combining arbitrary transverse BCs and linear subsectional basis functions. The analytical solution for geometries with rectangular or circular perfect electric walls and two-dimensional periodic boundaries are also presented as example of application. Finally this approach is validated by investigating four free-standing structures with different transverse BCs. There, the response provided by this technique is compared with other methods.

Chapter 4 focuses on developing an efficient and stable algorithm for the EM modeling of layered media. It starts introducing the foundations of a transmission line model. The formulation is presented using various forms that will allow different interpretations of the problem. It follows a study of the stability in current algorithms to establish the bases for the definition of a new algorithm. Then, the new formulation is used to explore the resonances appearing in dielectric-filled cavities. Finally, the efficiency of this technique is verified by the simulation of a realistic multilayered filter.

Chapter 5 applies these techniques for the resolution of multilayered boxed printed circuits. After a review of existing numerical methods it presents an overview of the formulation for this problem in connections with the methods described in previous chapters. It examines the convergence of the modal series arising in the reaction terms filling the MoM matrix, and proposes an acceleration technique. The approach used to model all the losses in the structure is also addressed here. Then, it introduces a method to include lumped elements in the simulation of printed circuits. Finally, it validates the developed approach by means of extensive numerical experiments on several benchmark structures.

Chapter 6 summarizes the concluding remarks, enumerates the original contributions and outlines the possible future research directions inspired by the work presented here.

References

[1] J. Jin, *The Finite Element Method in Electromagnetics.* John Wiley & Sons Inc, 1993.

[2] A. Taflove, Ed., *Advances in Computational Electrodynamics: The Finite-difference Time-domain Method*, 3rd ed., ser. Antennas & Propagation Library: Electromagnetics. Boston: Artech House, 1998.

[3] C. Christopoulos, *The Transmission-Line Modeling Method: TLM.* Wiley-IEEE Press, May 1995.

[4] P. J. B. Clarricoats and K. R. Slinn, "Numerical method for the solution of waveguide discontinuity problems," *Electr. Lett.*, vol. 15, pp. 226–227, 1966.

[5] A. Wexler, "Solution of waveguides discontinuities by modal analysis," *IEEE Trans. Microwave Theory Tech.*, vol. Vol. 15, pp. 508–517, 1967.

[6] M.-J. Tsai, F. De Flaviis, O. Fordham, and N. Alexopoulos, "Modeling planar arbitrarily shaped microstrip elements in multilayered media," *IEEE Trans. Microwave Theory Tech.*, vol. 45, pp. 330–337, Mar. 1997.

[7] K. Michalski and J. Mosig, "Multilayered media green's functions in integral equation formulations," *IEEE Trans. Antennas Propagat.*, vol. 45, pp. 508–519, Mar. 1997.

[8] G.V.Eleftheriades, J.R.Mosig, and M.Guglielmi, "A fast integral equation technique for shielded planar circuits defined on nonuniform meshes," *IEEE Trans. Microwave Theory Tech.*, vol. 44, pp. 2293–2296, Dec. 1996.

2 Foundations

2.1 Introduction

In this chapter we give an overview of the fundamental theorems, methods and numerical techniques upon which the work presented in this thesis is built.

The Electromagnetic (EM) modeling of printed circuits in layered bounded media is performed via an *Integral Equation* (IE) technique [1]. A *Green's function* (GF) is specially defined to satisfy both the BCs imposed by the layered media and by the transverse boundary enclosing the entire structure. On the other hand, the printed circuits are considered as inhomogeneities that scatter any incident field inside the aforementioned medium. This scattering problem is conveniently converted into an equivalent problem for which a formal solution may be directly written. This is accomplished by application of the *equivalence principle* [2, §3.5] that replaces the inhomogeneities by equivalent induced currents (also denoted "sources" throughout this text). Finally, a system of IEs on the equivalent sources can be formulated by imposing boundary conditions on the printed circuit surfaces. The latter, is solved numerically by means of the *Method of Moments* (MoM) [3]. Further results can be derived from the MoM solution, like the multiport *network characterization* of the device under investigation.

2.2 Field Equations

The electric $\mathbf{E}$ [V/m] and magnetic $\mathbf{H}$ [A/m] fields in an EM problem are governed by the *Maxwell–Hertz–Heaviside* (MHH) equations*. A differential and symmetric form of these equations is used here:

$$\nabla \times \mathbf{E} = -\mathrm{j}\omega\mu\mathbf{H} - \mathbf{M} \tag{2.1a}$$

$$\nabla \times \mathbf{H} = +\mathrm{j}\omega\varepsilon\mathbf{E} + \mathbf{J}, \tag{2.1b}$$

where ω is the angular frequency [rad/s]; μ, ε are the permeability [H/m] and permittivity [F/m] and $\mathbf{J}, \mathbf{M}$ are electric [A/m^2] and magnetic current densities [V/m^2], respectively. All fields are assumed time harmonic with a time variation according to $\mathrm{e}^{\mathrm{j}\omega t}$.

The keystone in the application of the equivalence principle is that the equivalent surface currents are able to *artificially* introduce discontinuities in the EM fields across a surface. Therefore, a simplified scenario can reproduce the field solution in the original problem by introducing these currents conveniently. Formally, the effect of the currents is formulated as

---

[*] The work of James C. Maxwell (1831 – 1879) in electromagnetism was later reformulated by Heinrich R. Hertz (1857 – 1894) and Oliver Heaviside (1850 – 1925) into the field equations used nowadays.

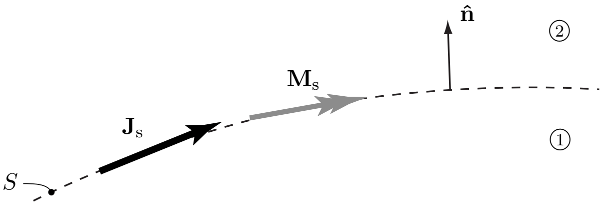

Figure 2.1: Discontinuity in fields produced by surface currents over S.

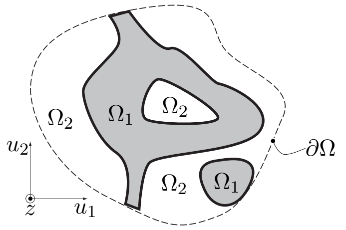

Figure 2.2: Transverse view of a general problem: a planar circuit (Ω_1) embedded in a medium bounded by $\partial\Omega$.

follows. Consider a surface distribution of currents $\mathbf{J}_\mathrm{s}$ [A/m] and $\mathbf{M}_\mathrm{s}$ [V/m] flowing over a surface S, as represented in Fig. 2.1. Under these conditions, the fields at each side of S satisfy the following relation [2, (1-86)]:

$$(\mathbf{E}_2 - \mathbf{E}_1) \times \hat{\mathbf{n}} = \mathbf{M}_\mathrm{s} \tag{2.2a}$$

$$\hat{\mathbf{n}} \times (\mathbf{H}_2 - \mathbf{H}_1) = \mathbf{J}_\mathrm{s} \tag{2.2b}$$

where $\hat{\mathbf{n}}$ is the unit vector normal to the surface and pointing into region ②. Obviously, the above equation above is applicable in the case $\mathbf{M}_\mathrm{s}$ or $\mathbf{J}_\mathrm{s}$ are zero resulting in continuous tangential field components along the surface interface.

2.3 Surface Integral Equations

The resolution of a scattering problem, within an IE context, starts by splitting the EM solution into two types of fields, those associated with a primary source, external to the problem, and another associated with the equivalent induced sources [4, §1.3]. The former, denoted *impressed* or incident fields $\mathbf{E}^\mathrm{i}$ and $\mathbf{H}^\mathrm{i}$, are obtained by illuminating the medium in the absence of the printed circuits. The secondary induced sources, which also radiate in the medium, produce the *scattered* fields $\mathbf{E}^\mathrm{s}$ and $\mathbf{H}^\mathrm{s}$. The superposition of the impressed and scattered fields yields the original fields in the presence of the printed circuits. In other words, the total field is expressed as

$$\mathbf{E} = \mathbf{E}^\mathrm{i} + \mathbf{E}^\mathrm{s} \tag{2.3a}$$

$$\mathbf{H} = \mathbf{H}^\mathrm{i} + \mathbf{H}^\mathrm{s}. \tag{2.3b}$$

The incident fields in the immediate vicinity of the printed circuit (away from the primary source) satisfy the homogeneous (source free) Maxwell–Hertz–Heaviside (MHH) equations (2.1) and the scattered fields are deduced from the equivalent induced currents as

$$\begin{bmatrix} \mathbf{E}^\mathrm{s} \\ \mathbf{H}^\mathrm{s} \end{bmatrix} = \begin{bmatrix} \overleftrightarrow{\mathbf{G}}_\mathrm{EE} & \overleftrightarrow{\mathbf{G}}_\mathrm{EH} \\ \overleftrightarrow{\mathbf{G}}_\mathrm{HE} & \overleftrightarrow{\mathbf{G}}_\mathrm{HH} \end{bmatrix} * \begin{bmatrix} \mathbf{J} \\ \mathbf{M} \end{bmatrix} \tag{2.4}$$

where $\overleftrightarrow{\mathbf{G}}_{\mathrm{PQ}}(\mathbf{r}|\mathbf{r}')$ is the dyadic GF relating *transverse* components of the P-type fields at $\mathbf{r}$ and Q-type sources at $\mathbf{r}'$ (where $\mathrm{P}, \mathrm{Q} = \{\mathrm{E}, \mathrm{H}\}$); and the operator $*$ denotes convolution integral over the pertinent source domain

$$\overleftrightarrow{\mathbf{G}}_{\mathrm{PQ}} * \mathbf{F} = \iint \overleftrightarrow{\mathbf{G}}_{\mathrm{PQ}}(\mathbf{r}|\mathbf{r}')\mathbf{F}(\mathbf{r}')\, \mathrm{d}S.$$

The sources on the surface, denoted from now on $\mathbf{J}, \mathbf{M}$ without subscript "s" for simplicity, are introduced by applying the equivalence theorem on the printed circuits. Starting from the representation of Fig. 2.2, two approaches are possible: either the conducting surfaces (Ω_1) are replaced by equivalent electric currents or the metal-devoid complementary surfaces (i.e. surfaces labeled with Ω_2) are represented by equivalent magnetic currents. Each case results in a different IE formulation as will be discussed next.

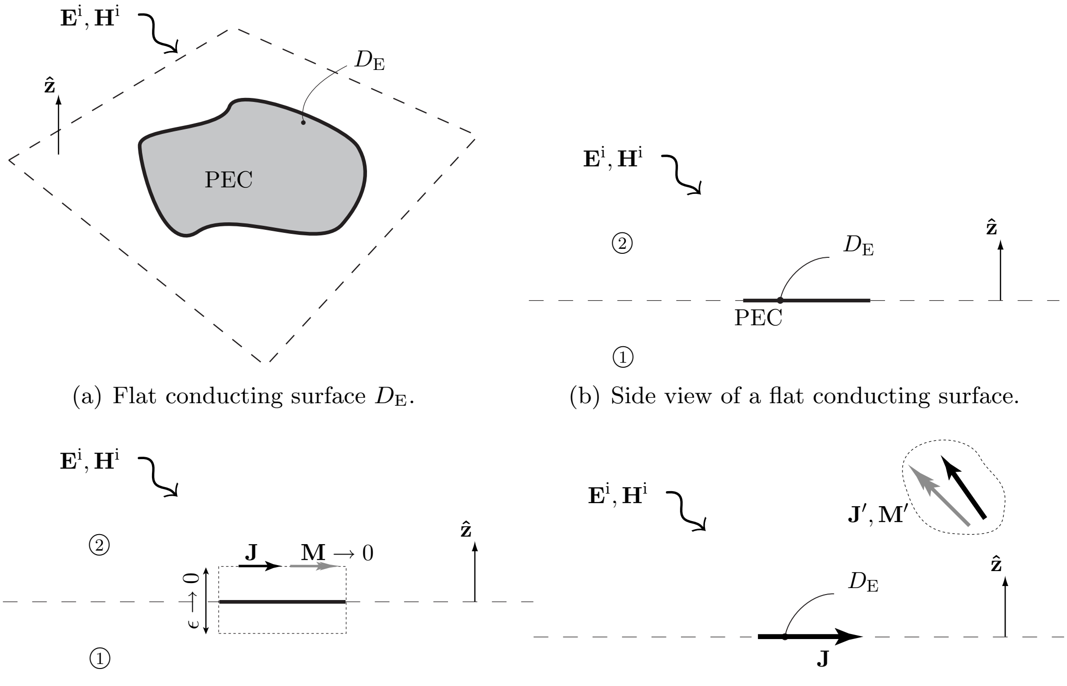

(a) Flat conducting surface D_{E}.

(b) Side view of a flat conducting surface.

(c) Mathematical surface S wrapping D_{E}.

(d) Equivalent scattering problem.

Figure 2.3: Equivalence principle for flat conducting screen.

Consider a flat conducting surface, infinitesimally thin and of finite size as represented in Fig. 2.3(a). Using the equivalence principle, a mathematical surface S [dotted line in Fig. 2.3(c)] with equivalent currents is defined around the conducting surface. If S is permitted to shrink until it coincides with the surface of the PEC (i.e. $\epsilon = 0$), (2.2) dictates that the tangential electric field must vanish on the surface [4, §1.7]. If follows that the equivalent sources replacing the conducting surface are

$$\mathbf{J} = \hat{\mathbf{z}} \times (\mathbf{H}_2 - \mathbf{H}_1) \tag{2.5a}$$

$$\mathbf{M} = 0, \tag{2.5b}$$

over the region covered by D_E. Here, $\mathbf{J}$ is a surface equivalent current that represents the sum of actual currents flowing above and below the conducting surface [5, §8.2].

Hence, the equivalent problem involves induced currents radiating in the medium, as depicted in Fig. 2.3(c). This representation shows a general scenario that considers the impressed fields originated in a primary source and the presence of additional currents $(\mathbf{J}', \mathbf{M}')$ from other secondary sources. Regarding the original problem, the tangential component of the total electric field must vanish on D_E:

$$\hat{\mathbf{z}} \times \mathbf{E} = 0 \text{ on } D_\mathrm{E}. \tag{2.6}$$

This BC in conjunction with (2.3) and (2.4) is used to formulate an *electric field IE* EFIE as

$$-\hat{\mathbf{z}} \times \mathbf{E}^\mathrm{i} = \overleftrightarrow{\mathbf{G}}_\mathrm{EE} * \mathbf{J} + \hat{\mathbf{z}} \times \mathbf{E}^\mathrm{s}(\mathbf{J}', \mathbf{M}'), \tag{2.7}$$

where $\mathbf{E}^\mathrm{s}(\mathbf{J}', \mathbf{M}')$ designates the electric field on the surface D_E by the sources $\mathbf{J}', \mathbf{M}'$.

Conversely, a *magnetic field* IE MFIE, based on the first identity in (2.5), cannot be formulated in this case being only possible on PEC surfaces enclosing a volume [4, p.18].

Let us now consider the scattering problem in an aperture over an infinite PEC plane, as represented in Fig. 2.4(a). This time, the formulation of the IE is obtained from two equivalent problems [4, §1.10], associated with the regions ① and ② in Fig. 2.4(b).

An equivalent representation of region ② can be constructed by placing a mathematical surface S [dotted lines in Fig. 2.4(c)] over the PEC ground plane and introducing equivalent currents there. Applying (2.2) with $\mathbf{E}_2 = 0, \mathbf{H}_2 = 0$ on the infinite PEC part of the plane S shows that the magnetic currents vanishe all along the plane except in the aperture, while the electric currents are nonzero everywhere. At this point, we can fill the aperture creating a uniform infinite PEC plane, provided that the aforementioned equivalent currents reproduce the fields in region ②, regardless of the problem below. With the infinite PEC ground plane under the complete surface S, the electric currents can not radiate† and they are not considered. Hence, only magnetic equivalent currents remain over S:

$$\mathbf{J} = 0 \tag{2.8a}$$

$$\mathbf{M} = \begin{cases} \mathbf{E} \times \hat{\mathbf{n}} & \text{in } D_\mathrm{H} \\ 0 & \text{otherwise} \end{cases}. \tag{2.8b}$$

The latter is also valid and derived analogously for the region ①.

The EM solution must satisfy continuity of the tangential components for the electric and

---

† This can be easily understood using image theory [2, §3.4] to replace the ground plane, since the superposition of a parallel electric source and its image cancel out.

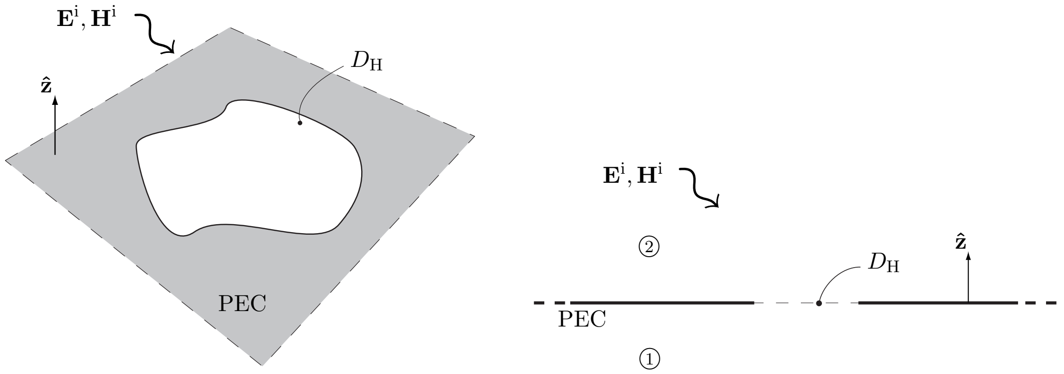

(a) Aperture D_{H} in an infinite PEC plane.

(b) Side view of an aperture in an infinite PEC plane.

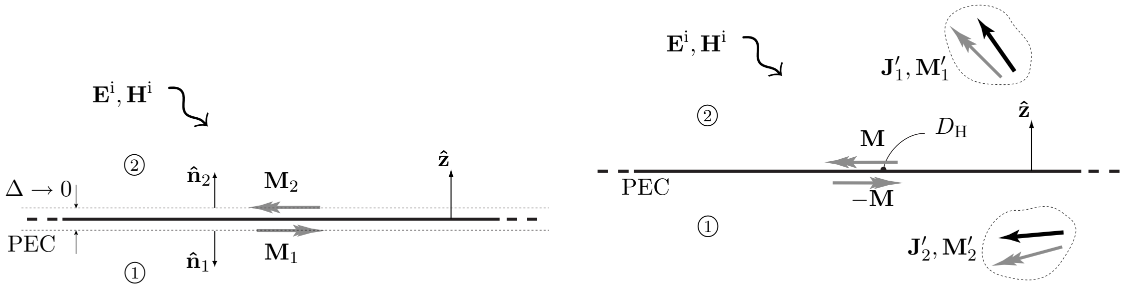

(c) Equivalent magnetic currents $\mathbf{M}$.

(d) Equivalent scattering problem.

Figure 2.4: Equivalence principle for an aperture in a conducting plane.

magnetic fields through the aperture. More specifically, using subscripts 1 and 2 to identify the region, it follows that

$$(\mathbf{E}_2 - \mathbf{E}_1) \times \hat{\mathbf{z}} = 0 \tag{2.9a}$$

$$\hat{\mathbf{z}} \times (\mathbf{H}_2 - \mathbf{H}_1) = 0 \tag{2.9b}$$

on D_{H}. The first equation establishes that the equivalent magnetic currents above and below the aperture are of the same magnitude but opposite signs. More specifically,

$$\left.\begin{aligned} \mathbf{M}_1 &= \mathbf{E}_1 \times (-\hat{\mathbf{z}}) \\ \mathbf{M}_2 &= \mathbf{E}_2 \times (+\hat{\mathbf{z}}) \end{aligned}\right\} \Rightarrow \mathbf{M}_1 = -\mathbf{M}_2 = \mathbf{M}, \tag{2.10}$$

provided that (2.2) is satisfied on each side. This leads to an equivalent problem as illustrated in Fig. 2.4(d) where, for the sake of generality, an impressed field and other secondary sources on both sides of the ground plane $(\mathbf{J}'_1, \mathbf{J}'_2, \mathbf{M}'_1, \mathbf{M}'_2)$ are also considered. Finally, considering an incident field $\mathbf{H}^{\mathrm{i}}$ in the upper semi-space, an IE can be formulated on $\mathbf{M}$ by imposing (2.9b) over the aperture surface D_{H}, as follows:

$$-\hat{\mathbf{z}} \times \mathbf{H}^{\mathrm{i}} = \left(\overleftrightarrow{\mathbf{G}}^{2}_{\mathrm{HH}} + \overleftrightarrow{\mathbf{G}}^{1}_{\mathrm{HH}}\right) * \mathbf{M} + \hat{\mathbf{z}} \times \left[\mathbf{H}^{\mathrm{s}}(\mathbf{J}'_2, \mathbf{M}'_2) - \mathbf{H}^{\mathrm{s}}(\mathbf{J}'_1, \mathbf{M}'_1)\right], \tag{2.11}$$

where $\mathbf{H}^{\mathrm{s}}$ denotes the scattered magnetic field on D_{H} originated by the secondary sources, $\overleftrightarrow{\mathbf{G}}^{1}_{\mathrm{HH}}, \overleftrightarrow{\mathbf{G}}^{2}_{\mathrm{HH}}$ are the GFs for the lower and upper region, respectively. Notice that the above IE couples the sources at both sides of the aperture.

A more general problem, involving different conducting surfaces or apertures (e.g. in [6]), can also be modeled using these two cases. The resulting formulation consists on a system of IEs composed of expressions like (2.7) and (2.11) that couple the equivalent sources over every circuit surface S_{P}, with $P = \{E, H\}$.

2.4 Green's Function

One analytical approach for developing more efficient IE models is the use of the specialized GFs which satisfy some boundary conditions of the problem. These GFs are available for layered bounded problems for which they provide a formal means to model the EM fields produced by an infinitesimal source embedded in this medium. The tradeoff in using such GFs is that of reducing the number of unknowns needed in the model at the expense of dealing with a more complex IE kernel [7].

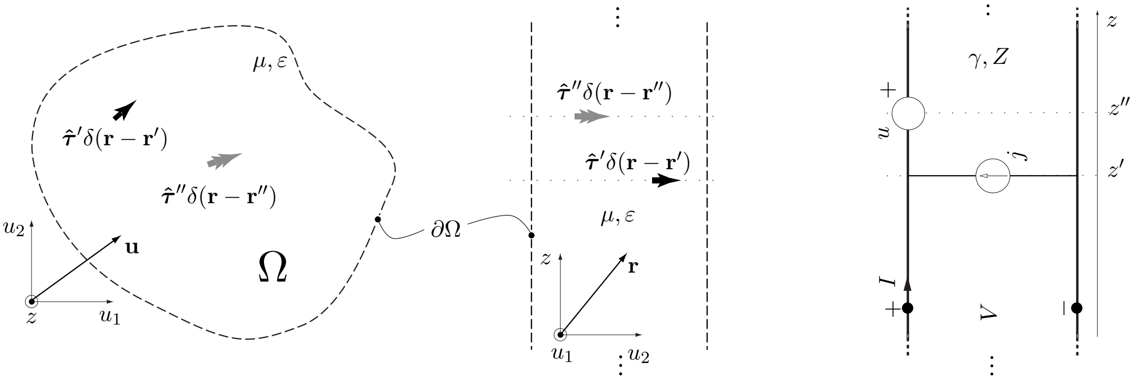

(a) Infinitesimal current sources in a homogeneous bounded medium. Transverse (left) and longitudinal views.

(b) Transmission line model.

Figure 2.5: General representation of the GF problem and an associated model.

The IEs (2.7) and (2.11), considered in the previous section, are defined over *planar* surfaces therefore requiring only the evaluation of the transverse components of the dyadic GF, i.e. G^{rs}_{PQ} where $r, s \in \{x, y\}$. A general representation for the GF problem of interest is shown in Fig. 2.5(a). It illustrates an electric (single arrow) and a magnetic (double-headed arrow) infinitesimal source oriented along $\hat{\boldsymbol{\tau}}'$ and $\hat{\boldsymbol{\tau}}''$ over transverse planes at two different levels in z. The medium is initially considered homogeneous to simplify the demonstration and later it can be easily extended to the layered case.

The method used to find the field radiated by an arbitrary infinitesimal source is to expand the radiated field in terms of a suitable set of modes. The latter are obtained as an orthonormal set of eigensolutions for the transverse boundary problem $\partial\Omega$. In a physical sense, an infinitesimal source in Fig. 2.5(a) will excite the complete modal spectrum in a transverse plane with a strength depending on its position and polarization. Then, the modes will propagate along the z direction in the medium. Hence, the radiated field can be reconstructed at any observer point $\mathbf{r}$ by superposition of its modal components [8, §5.6].

Let us now proceed formally with these ideas. Due to the invariance of the transverse BCs (over $\partial\Omega$) along the z direction, the MHH equations (2.1) can be reduced to a inhomogeneous vector field equation on the transverse components of the electric and magnetic fields:

$$\frac{\partial \mathbf{E}_\mathrm{t}}{\partial z} = -\mathrm{j}\omega\mu \left[1 + \frac{1}{k^2}\nabla_\mathrm{t}\nabla_\mathrm{t}\cdot\right](\mathbf{H}_\mathrm{t} \times \hat{\mathbf{z}}) - (\mathbf{M}_\mathrm{t} \times \hat{\mathbf{z}}) - \frac{\nabla_\mathrm{t} J_z}{\mathrm{j}\omega\varepsilon} \tag{2.12a}$$

$$\frac{\partial \mathbf{H}_\mathrm{t}}{\partial z} = -\mathrm{j}\omega\varepsilon \left[1 + \frac{1}{k^2}\nabla_\mathrm{t}\nabla_\mathrm{t}\cdot\right](\hat{\mathbf{z}} \times \mathbf{E}_\mathrm{t}) - (\hat{\mathbf{z}} \times \mathbf{J}_\mathrm{t}) - \frac{\nabla_\mathrm{t} M_z}{\mathrm{j}\omega\mu} \tag{2.12b}$$

where $k = \omega\sqrt{\mu\varepsilon}$ and, for the sake of completeness, all source components are considered. Notice that the transverse components of the modal field $\{\mathbf{e}, \mathbf{h}\}$ are solutions of the equivalent homogenous equations [9, §1.2], so we can express the fields in (2.12) as

$$\mathbf{E}_\mathrm{t} = \sum_i V_i(z)\mathbf{e}_i(u_1, u_2) \tag{2.13a}$$

$$\mathbf{H}_\mathrm{t} = \sum_i I_i(z)\mathbf{h}_i(u_1, u_2), \tag{2.13b}$$

where V_i, I_i are complex amplitudes that modulate the transverse field components of an ith mode along the propagation direction. Integrating over every mode and using the orthogonal property:

$$\iint_\Omega \mathbf{e}_i \cdot \mathbf{e}_j^* \,\mathrm{d}\Omega = \delta_{ij} \qquad\qquad \iint_\Omega \mathbf{h}_i \cdot \mathbf{h}_j^* \,\mathrm{d}\Omega = \delta_{ij}, \tag{2.14}$$

with δ_{ij} being the Kronecker delta function, eliminates from (2.12) the transverse component dependence. The resulting set of equations governs the behavior of the weighting functions along z for every mode as

$$\frac{\partial V}{\partial z} = -\gamma Z I + u \tag{2.15a}$$

$$\frac{\partial I}{\partial z} = -\gamma/Z V + j. \tag{2.15b}$$

Notice that these are the well-known Telegraphers equations and therefore γ, Z correspond to the propagation constant and the characteristic impedance in the equivalent transmission line and u, j correspond to voltage and current generators. The latter are calculated by

$$-u = \iint\limits_{\Omega} \big(\mathbf{M}_{\mathrm{t}} \times \hat{\mathbf{z}} + \frac{\nabla_{\mathrm{t}} J_z}{\mathrm{j}\omega\varepsilon}\big) \cdot \mathbf{e}^* \; \mathrm{d}\Omega = \iint\limits_{\Omega} \mathbf{M}_{\mathrm{t}} \cdot \mathbf{h}^* \; \mathrm{d}\Omega \tag{2.16a}$$

$$-j = \iint\limits_{\Omega} \big(\hat{\mathbf{z}} \times \mathbf{J}_{\mathrm{t}} + \frac{\nabla_{\mathrm{t}} M_z}{\mathrm{j}\omega\mu}\big) \cdot \mathbf{h}^* \; \mathrm{d}\Omega = \iint\limits_{\Omega} \mathbf{J}_{\mathrm{t}} \cdot \mathbf{e}^* \; \mathrm{d}\Omega, \tag{2.16b}$$

provided that $\mathbf{h} = \hat{\mathbf{z}} \times \mathbf{e}$ and only sources transverse to the Ω are considered here. These developments reveal that the propagation along z of the transverse components, governed by (2.15), can be interpreted in terms of a transmission line problem with external generators.

At this point, the formulation of the GF can be readily obtained by exciting the medium with the infinitesimal transverse sources, shown in Fig. 2.5(a). According to (2.16a), the sources are projected on the orthonormal modal basis to get the following values

$$-u = \mathbf{h}^*(\mathbf{u}') \cdot \hat{\boldsymbol{\tau}}''\delta(z - z'') \tag{2.17a}$$

$$-j = \mathbf{e}^*(\mathbf{u}') \cdot \hat{\boldsymbol{\tau}}'\delta(z - z') \tag{2.17b}$$

where $\mathbf{u}' = \mathbf{r}' - z'\hat{\mathbf{z}}$ is a two-dimensional vector that points to the source position in the plane Ω. The results obtained in (2.17) in conjunction with (2.15) show that the GF problem along the longitudinal dimension can be reduced to an equivalent transmission line with lumped generators as illustrated in Fig. 2.5(b). Hence, the radiated field in the medium of Fig. 2.5(a) can be obtained solving the equivalent transmission line model for every mode and adding up each contribution by means of (2.13). In addition, if the generators are set to $j = 1$ A and $u = 1$ V, the transverse components of the GF, denoted for simplicity with the symbol $\overleftrightarrow{\mathbf{G}}$, are given by

$$\overleftrightarrow{\mathbf{G}}_{\mathrm{EE}}(\mathbf{r}|\mathbf{r}') = \sum_i V_i^I(z, z')\, \mathbf{e}_i(u_1, u_2)\mathbf{e}_i^*(u_1', u_2') \tag{2.18a}$$

$$\overleftrightarrow{\mathbf{G}}_{\mathrm{EH}}(\mathbf{r}|\mathbf{r}'') = \sum_i V_i^V(z, z'')\, \mathbf{e}_i(u_1, u_2)\mathbf{h}_i^*(u_1'', u_2'') \tag{2.18b}$$

$$\overleftrightarrow{\mathbf{G}}_{\mathrm{HE}}(\mathbf{r}|\mathbf{r}') = \sum_i I_i^I(z, z')\, \mathbf{h}_i(u_1, u_2)\mathbf{e}_i^*(u_1', u_2') \tag{2.18c}$$

$$\overleftrightarrow{\mathbf{G}}_{\mathrm{HH}}(\mathbf{r}|\mathbf{r}'') = \sum_i I_i^V(z, z'')\, \mathbf{h}_i(u_1, u_2)\mathbf{h}_i^*(u_1'', u_2'') \tag{2.18d}$$

where V^I, I^I and V^V, I^V are the modal voltages and currents at the observer z in the equivalent transmission line of Fig. 2.5(b) produced by *normalized* excitations situated at z and z'', respectively. To refer to the ensemble of GFs represented above we will use the following notation

$$\overleftrightarrow{\mathbf{G}}_{\mathrm{PQ}}(\mathbf{r}|\mathbf{r}') = \sum_i P_i^Q(z, z')\, \mathbf{p}_i(\mathbf{u})\mathbf{q}_i^*(\mathbf{u}') \tag{2.19}$$

where $\mathbf{r} = \mathbf{u} + z\hat{\mathbf{z}}$, $\mathrm{P}, \mathrm{Q} = \{\mathrm{E}, \mathrm{H}\}$, $P, Q = \{V, I\}$ and $\mathbf{p}_i, \mathbf{q}_i = \{\mathbf{e}_i, \mathbf{h}_i\}$.

Finally, the GF formulation in a *layered* medium is a straightforward extension of the equivalent transmission line problem represented in Fig. 2.5(b). Each kth layer is replaced by an equivalent transmission line section $\{\gamma_k, Z_k\}$ for every mode considered. A detailed formulation of the transmission line model for layered media will be presented in Chapter 4.

In conclusion, the formulation of the GFs for bounded layered media (only transverse components), given in (2.19), involves two different problems. First, the modal field components $\{\mathbf{e}_i, \mathbf{h}_i\}$ must be calculated by solving the transverse boundary problem. And second, an equivalent transmission line model, derived from the layered media, is solved for each mode in order to calculate the series weight functions P_i^Q .

2.5 Method of Moments

The MoM [3] is applied for numerical resolution of system of surface IEs derived in §2.3. A general representation of a vector IE can be written as

$$-\mathbf{F}^{\mathrm{i}} = \mathcal{L}\left(\mathbf{K}\right) = \int\limits_S \overleftrightarrow{\mathbf{G}}\mathbf{K}\,\mathrm{d}S, \tag{2.20}$$

where S extends to all the *unknown* equivalent induced currents $\mathbf{K} = \{\mathbf{J}, \mathbf{M}\}$ in the medium. In the equation above, $\mathbf{F}^{\mathrm{i}}$ represents the *known* impressed field and $\mathcal{L}$ is a linear operator that returns the scattered field by convolution of the unknown equivalent induced sources with the pertinent dyadic GF $\overleftrightarrow{\mathbf{G}}$.

To proceed, let us define a set of *known* BFs $\{\mathbf{b}_1, \mathbf{b}_2, \ldots \mathbf{b}_N\}$ in the domain of $\mathcal{L}$, such that $\mathbf{K}$ is approximated as

$$\mathbf{K} \approx \sum_l \alpha_l \mathbf{b}_l \tag{2.21}$$

where α_l are in general complex coefficients. Introducing this form into (2.20) and using the linearity of the $\mathcal{L}$ operator we get

$$-\mathbf{F}^{\mathrm{i}} = \sum_l \alpha_l \mathcal{L}\left(\mathbf{b}_l\right). \tag{2.22}$$

Now, following the *Galerkin* procedure, the last equation is tested using weight functions $\mathbf{w}_k = \mathbf{b}_k$ and a suitable inner product $\langle \mathbf{a}, \mathbf{b} \rangle$ resulting in N linear equations with N unknowns α_l:

$$\langle \mathbf{w}_k, -\mathbf{F}^{\mathrm{i}} \rangle = \sum_l \alpha_l \langle \mathbf{w}_k, \mathcal{L}\left(\mathbf{b}_l\right) \rangle$$

for $k = 1, 2, \ldots, N$. Therefore, the original IE has been transformed into an algebraic linear system which can be written in matrix form as

$$\left[\, \langle \mathbf{b}_k, -\mathbf{F}^{\mathrm{i}} \rangle \,\right] = \Big[\langle \mathbf{b}_k, \mathcal{L}\left(\mathbf{b}_l\right) \rangle \Big] \cdot \left[\alpha_l\right]. \tag{2.23}$$

If the matrix is not singular then its inverse exists, the expansion coefficients are found and an approximation of the actual induced currents are obtained through (2.21).

From a physical point of view, testing using weight functions is a mathematical tool to "measure" the field on a surface D. Therefore, the MoM consists of adjusting, in magnitude and phase, auxiliary discrete sources (the BFs) such that by superposition they radiate a field on the circuit surface that compensates the "measured" incident field. Here, the inner product is defined as a *reaction* [10]. The reaction between two distribution of sources $\mathbf{K} \equiv \{\mathbf{J}, \mathbf{M}\}$ and $\mathbf{K}' \equiv \{\mathbf{J}', \mathbf{M}'\}$ is given by

$$\langle \mathbf{K}', \mathcal{L}(\mathbf{K}) \rangle = \iint\limits_{D'_{\mathrm{E}}} \mathbf{J}' \cdot \mathbf{E}(\mathbf{J}, \mathbf{M})\, \mathrm{d}S - \iint\limits_{D'_{\mathrm{H}}} \mathbf{M}' \cdot \mathbf{H}(\mathbf{J}, \mathbf{M})\, \mathrm{d}S \tag{2.24}$$

where $\mathbf{E}, \mathbf{H}$ can be interpreted as scattered or incident fields depending if they are produced by secondary or primary sources. This definition of inner product, due to the reciprocity principle [11, p.194], produces a symmetric matrix in the MoM [12, §1.6].

2.6 Network Characterization

Many engineering problems involve the measurement of the transfer of energy between different ports defined in a device. This process is commonly known as a *multiport network characterization* and in passive devices it is given by a linear transformation. In high frequency EMs the concept of port represents a value obtained by measure of a physical magnitude, normally by integration over a region (surface, line, point). First, we need to know what magnitudes of the problem (i.e. EM field, current density, etc) are available after the simulation and then a mathematical tool to measure them must be chosen. The latter should be defined such that it should only be correlated with the magnitude under investigation (i.e. a measure should only be affected when changes arises in this magnitude and not the others) and it should be reproducible in a laboratory. For example, in waveguide-based devices or FSS a port is normally associated to the fundamental waveguide or Floquet mode, respectively. Incident and reflection coefficients (values) are obtained by projection of the EM field over the correspondent mode (measurements tool). In addition, each measure is associated to each mode since they constitute an orthogonal set.

Here we are concerned with the multiport network characterization of planar circuits. The common mechanisms to access these circuits are normally small coaxial connectors or wafer probes. An approximate model consists in considering an incident field localized in an infinitesimal region at the device's input/output and using the reaction concept (2.24) as measurement tool. This is the idea behind commonly used excitation techniques like the delta-gap voltage and the impressed-current models [13]. In principle, only those BFs in the excitation region are susceptible of being excited, having $\langle \mathbf{b}_k, \mathbf{F}^{\mathrm{i}} \rangle \neq 0$. These BFs are denoted *terminals* and a set of terminals within an excitation region will reconstruct the currents at a *port*. The rest are denoted as *circuit* BFs [13]. Hence, without loss of generality, the MoM matrix (2.23), can be arranged according to circuit and terminal BFs as follows

$$\left[\begin{array}{c} x \\ \hline 0 \end{array}\right] = \left[\begin{array}{c|c} T & m \\ \hline m^{\mathrm{t}} & C \end{array}\right] \cdot \left[\begin{array}{c} t \\ \hline c \end{array}\right] \tag{2.25}$$

where the superscript "t" denotes transposed matrix and $T = T^{\mathrm{t}}, C = C^{\mathrm{t}}$ are symmetric submatrices. In the above equation, $x = [x_k]$ and $t = [t_k]$ are column vectors with complex values associated to the terminal BFs. The first contains non-zero excitation coefficients $x_k = \langle \mathbf{b}_k, -\mathbf{F}^{\mathrm{i}} \rangle \neq 0$ and the second are the expansion coefficients associated to each basis function. For the circuit BFs, these coefficients are stored in the column vector $c = [c_k]$. The network characterization will be derived from the relations between terminal BFs. To proceed, we can easily obtain from (2.25) the following identities

$$x = T \cdot t + m \cdot c \tag{2.26a}$$

$$c = \left(-C^{-1} \cdot m^{\mathrm{t}}\right) \cdot t. \tag{2.26b}$$

Recalling the discussion in §2.5, in the first equation the field radiated by the terminal and the circuit currents compensates the field impressed in the ports region. At the same time, the circuit and the terminal currents are related by the second equation. Now, by substituting the second into the first equation and inverting the result, we can directly obtain the terminal currents coefficients in terms of the excitation as

$$t = \left(T - m \cdot C^{-1} \cdot m^{\mathrm{t}}\right)^{-1} \cdot x = \mathcal{H} \cdot x. \tag{2.27}$$

Notice that from the expression above we can obtain the induced current at every port, reconstructed with the terminal currents t, for any given excitation x. In other words, $\mathcal{H}$ directly provides a transfer function between terminal currents, and therefore ports. Hence, a multiport network characterization of the circuit can be readily deduced from $\mathcal{H}$ (e.g. for multisegmented ports see [13, §7] or for entire domain BF see [14, §2]). Finally, if the currents in the rest of the circuit are required, the coefficients for the circuit BFs can be calculated using (2.26b).

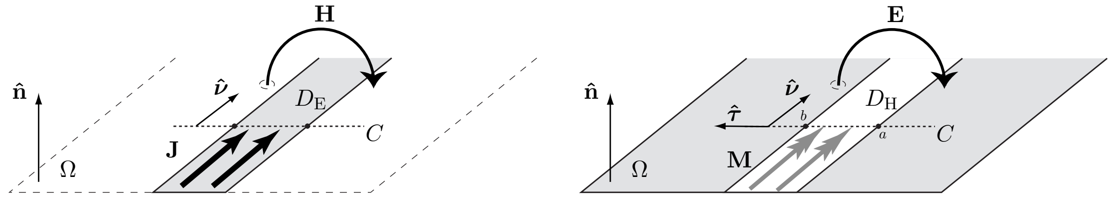

(a) Electric currents on a flat conducting strip.

(b) Magnetic currents on a slot over a infinite ground plane.

Figure 2.6: Dual electric and magnetic problems on a region D

Why do we claim that this is an approximated excitation model? The approximation arises because we are considering the reaction over an infinitesimal incident field in order to measure

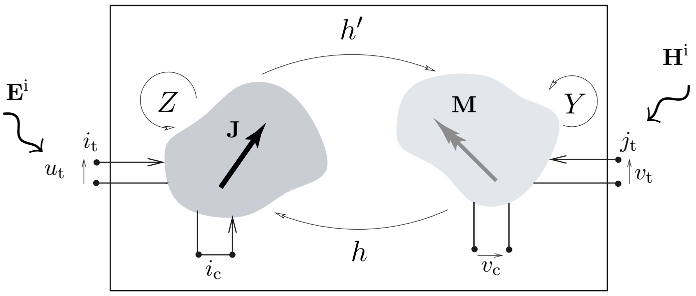

Figure 2.7: Representation of the reaction taking place when electric and magnetic sources are considered. The circuit terminals in the electric and magnetic case are short- and open-circuited respectively since the excitation coefficients are zero (in the lossless case). The electric terminals are represented as external accesses to the circuit

.

the ports. Let us clarify this idea by rearranging the MoM matrix in electric or magnetic BFs (i.e. according to the expansion of **J** and **M** currents):

$$\left[\begin{array}{c} u \\ \hline j \end{array}\right] = \left[\begin{array}{c|c} Z & h \\ \hline h^{\mathrm{t}} & Y \end{array}\right] \cdot \left[\begin{array}{c} i \\ \hline v \end{array}\right] \tag{2.28}$$

with $Z = Z'$ and $Y = Y'$ symmetric matrices due to reciprocity. The notation used for the vectors in (2.28) is deliberately chosen to indicate measures of voltage for $u = [u_k], v = [v_k]$ and current for $i = [i_k], j = [j_k]$. The unknowns i, v are naturally defined since, considering Fig. 2.6, we have

$$i_k = \int_C \mathbf{J} \cdot \hat{\boldsymbol{\nu}} \, \mathrm{d}l \qquad [\mathrm{A}] \tag{2.29a}$$

$$v_k = \int_C \mathbf{M} \cdot \hat{\boldsymbol{\nu}} \, \mathrm{d}l = \int_a^b \mathbf{E} \cdot \hat{\boldsymbol{\tau}} \, \mathrm{d}l \qquad [\mathrm{V}], \tag{2.29b}$$

while the excitation coefficients u, j are obtained through the reaction concept in (2.24), i.e.

$$u_k = \langle \mathbf{J}, -\mathbf{E}^{\mathrm{i}} \rangle \qquad [\mathrm{V}] \tag{2.30a}$$

$$j_k = \langle \mathbf{M}, -\mathbf{H}^{\mathrm{i}} \rangle \qquad [\mathrm{A}] \tag{2.30b}$$

The approximation arises in (2.30) since they do not represent exactly the voltages and currents at the device ports measured in the laboratory. The main reason is that the incident field is not only localized over an infinitesimal region but instead it actually illuminates the complete circuit. In order to see more formally this approximation, let us rearrange the MoM regarding (2.25) as

$$x = \left[\begin{array}{c} u_{\mathrm{t}} \\ \hline j_{\mathrm{t}} \end{array}\right] \qquad\qquad t = \left[\begin{array}{c} i_{\mathrm{t}} \\ \hline v_{\mathrm{t}} \end{array}\right] \qquad\qquad c = \left[\begin{array}{c} i_{\mathrm{c}} \\ \hline v_{\mathrm{c}} \end{array}\right] \tag{2.31}$$

where the subscript "t" denotes that it belongs to terminal basis functions, and analogously with "c" for circuit BFs. Hence, considering the real solution as $x^{\mathrm{r}} = \mathcal{H}^{\mathrm{r}} \cdot t^{\mathrm{r}}$ and the definition (2.30) being an approximation, i.e. $x \approx x^{\mathrm{r}}$, then we can conclude that $\mathcal{H} \approx \mathcal{H}^{\mathrm{r}}$ provided that $t = t^{\mathrm{r}}$ is very accurate.

An exact determination of the excitation field would require an effort comparable to the complete simulation since in that case the entire EM problem, including the port probes, should be solved in the absence of equivalent sources. Other non-exact methods aim to improve accuracy by better approximating the incident field, like the magnetic frill model [15, §7.3.2], or by carrying out a pre-calibration in x in order to infer x^{r} [16]. Nevertheless, it has been demonstrated that the aforementioned approximate models provide accurate results for excitations through small coaxial feeds or wafer probes in addition to a very low computational effort.

An interesting circuit interpretation of the MoM is found by substituting (2.31) into (2.25). An abstract representation is given in Fig. 2.7. The circuit is enclosed into a "black-box" accessed by terminals which are linked to the electric and magnetic currents. The interactions inside are given by the submatrices in (2.28) and the circuit currents in the MoM can be interpreted as open or close-circuited terminals.

Finally, the multiport network characterization of microwave circuits is commonly desired in terms of scattering parameters $\mathcal{S}$. In order to show the procedure from $\mathcal{H}$ to $\mathcal{S}$ let us first consider a MoM with only electric currents, such that (2.28) is reduced

$$u = Z \cdot i \tag{2.32}$$

where Z is sometimes called generalized impedance matrix [3, §5]. Arranging Z into terminals and circuits and following the procedure described above leads naturally to a transfer function between terminals that corresponds to the admittance matrix [3, §6]. Mathematically, this is written as

$$i_{\mathrm{t}} = \underbrace{\left(Z_{\mathrm{tt}} - Z_{\mathrm{tc}} \cdot Z_{\mathrm{cc}}^{-1} \cdot Z'_{\mathrm{tc}}\right)^{-1}}_{\mathcal{Z}^{-1}} \cdot u_{\mathrm{t}} = \mathcal{Y} \cdot u_{\mathrm{t}}. \tag{2.33}$$

The admittance matrix is now transformable into scattering parameters, using the definition of Kurokawa [17], as follows

$$\mathcal{S} = F \cdot (\mathbf{1} - G \cdot \mathcal{Y}) \cdot (\mathbf{1} + G \cdot \mathcal{Y})^{-1} \cdot F^{-1} \tag{2.34}$$

where $\mathbf{1}$ is the identity matrix, $F^{-1} = \mathrm{diag}(2\sqrt{R_{0p}})$, $G = \mathrm{diag}(R_{0p})$ and $R_{0p} \in \mathbb{R}$ is the reference impedance of the pth port. Analogously, in the general case, $\mathcal{H}^{-1} = \mathcal{G}$ is an hybrid matrix relating electric and magnetic ports. Analogously, the scattering parameters can be derived as

$$\mathcal{S} = TE \cdot (\mathbf{1} - D \cdot \mathcal{G}) \cdot (\mathbf{1} + D \cdot \mathcal{G})^{-1} \cdot E^{-1} \tag{2.35}$$

where, for pth electric and qth magnetic ports, we have defined $T = \mathrm{diag}[\mathbf{1}_p, -\mathbf{1}_q]$, $E = \mathrm{diag}[\mathrm{diag}(\sqrt{R_{0p}}), \mathrm{diag}(1/\sqrt{R_{0q}})]$ and $D = \mathrm{diag}[\mathrm{diag}(R_{0p}), \mathrm{diag}(1/R_{0q})]$.

2.7 General Assessment

Throughout this chapter we have shown the foundations of an IE-MoM technique for the EM modeling of printed circuits in bounded layered media.

The basis of this approach consists of the formulation of a canonical problem consisting of the radiation of an infinitesimal current inside bounded layered media. This defines the GF. On the other hand, using the equivalence principle, the printed circuits can be replaced by equivalent surface currents. In this way, the initial structure has been transformed into a problem of equivalent surface currents radiating in a bounded layered media. Using a IE technique in combination with the MoM these currents are obtained for the BCs imposed in the original problem. With this result any other field or derived magnitude can be then calculated, e.g. a multiport network characterization of the structure.

Due to the symmetry presented by a bounded layered media, the GF's problem has been reduced into a two-dimensional transverse boundary problem, in coordinates u_1, u_2 and a one-dimensional transmission line problem in z direction. The former consists in deriving the eigensolutions or modes satisfying Helmholtz equation in the transverse contour with certain BCs, while the latter describes how these modes propagate in the layered media.

The formulation of the overall problem is thus based on two main ingredients which can be treated independently. On one side the resolution of a transverse boundary problem, meaning the derivation of modes and the solution to operators associated with the IE for a giving transverse contour. On the other side, an efficient resolution of the equivalent transmission line problem along the normal coordinate for a generic mode. These two auxiliary problems will be the object of, respectively, the two next Chapter 3 and Chapter 4 in the thesis.

References

[1] J. R. Mosig, "Integral-equation technique," in *Numerical Techniques for Microwave and Millimeter-Wave Passive Structures*, T. Itoh, Ed. New York: Wiley, 1989, ch. 3, pp. 133–213.

[2] R. F. Harrington, *Time-Harmonic Electromagnetic Fields.* New York: McGraw-Hill, 1961.

[3] ——, *Field Computation by Moment Methods.* Florida: Krieger Publishing Company, 1968.

[4] A. F. Peterson, S. L. Ray, and R. Mittra, *Computational Methods for Electromagnetics.* New York: IEEE Press, 1998.

[5] J. R. Mosig, R. C. Hall, and F. E. Gardiol, "Numerical analysis of microstrip patch antennas," in *Handbook of microstrip antennas. I*, James and Hall, Eds. London: IEE electromagnetic waves series, 1989, ch. 8, pp. 393–453.

[6] I. Stevanović, P. Crespo-Valero, and J. R. Mosig, "An integral-equation technique for solving thick irises in rectangular waveguides," *IEEE Trans. Microwave Theory Tech.*, vol. 54, no. 1, pp. 189–197, Jan. 2006.

[7] E. Miller, "A selective survey of computational electromagnetics," *IEEE Trans. Antennas Propagat.*, vol. 36, no. 9, pp. 1281–1305, Sept. 1988.

[8] R. E. Collin, *Field Theory of Guided Waves*, 2nd ed. Wiley-IEEE Press, 1990.

[9] N. Marcuvitz, *Waveguide Handbook*, ser. Radiation Laboratory. New York: McGraw Hill, 1941, vol. 10.

[10] V. Rumsey, "Reaction concept in electromagnetic theory," *Phys. Rev.*, vol. 94, pp. 1483–1491, June 1954.

[11] L. B. Felsen and N. Marcuvitz, *Radiation and Scattering of Waves.* Englewood Cliffs, NJ: Prentice Hall, 1973.

[12] D. Llorens del Río, "Electromagnetic analysis of 2.5d structures in open layered media," Ph.D. dissertation, Ecole Polytecnique Fédéral de Lausanne, Lausanne, 2005, thèse No 3183 (2005). [Online]. Available: http://library.epfl.ch/theses/?nr=3183

[13] G. Eleftheriades and J. Mosig, "On the network characterization of planar passive circuits using the method of moments," *IEEE Trans. Microwave Theory Tech.*, vol. 44, no. 3, pp. 438–445, March 1996.

[14] M. Bozzi, L. Perregrini, A. Alvarez Melcon, M. Guglielmi, and G. Conciauro, "Mom/bi-rme analysis of boxed mmics with arbitrarily shaped metallizations," *IEEE Trans. Microwave Theory Tech.*, vol. 49, no. 12, pp. 2227–2234, Dec. 2001.

[15] B. M. Kolundzija and A. R. Djordjević, *Electromagnetic Modeling of Composite metallic and dielectric structures.* Boston: Artech House, 2002.

[16] L. Zhu and K. Wu, "Short-open calibration technique for field theory-based parameter extraction of lumped elements of planar integrated circuits," *IEEE Trans. Microwave Theory Tech.*, vol. 50, no. 8, pp. 1861–1869, Aug. 2002.

[17] K. Kurokawa, "Power waves and the scattering matrix," *IEEE Trans. Microwave Theory Tech.*, vol. 10, no. 5, pp. 314–320, Sept. 1965.

3 Transverse Boundary Problem

3.1 Introduction

In this chapter we present the details of the IE-MoM formulation for the EM modeling of printed circuits in laterally bounded media. This scheme encompasses a wide range of practical structures such as discontinuities in waveguides, planar circuits embedded in shielded multilayered media or even 2-D printed periodic structures. Each of the problems enumerated above has already been solved by other authors using IE-MoM techniques. Some examples can be found in the work of [1, 2] applied to waveguide iris filters, or the techniques for boxed printed circuits proposed in [3–5] or even the studies on infinite planar arrays or FSS in [6–8]. Nevertheless, our formulation introduces a *unified* approach applicable to all the aforementioned problems. Our method is based on a modal representation of the transverse boundary problem and on the expansion of the equivalent surface currents by divergence-conforming BFs. It starts with general and simplified forms of the integral operators. Then it establishes a systematic procedure that particularizes the solution to a specific combination of transverse BC and type of BFs.

This chapter is organized as follows. The first section commences with a review of the IE-MoM formulation in connection with the techniques presented in §§2.3–2.5. The purpose is to give a precise picture of the type of integral expressions to be solved and the role they play within the overall IE-MoM technique. The next section develops the approach followed to achieve a generic solution for these integrals. The formulation is then applied to rectangular and circular perfect electric conductors BCs (i.e. waveguides) and periodic BC in order to prove the generality, simplicity and elegance of this technique. Finally, the validity of the approach is demonstrated confronting the results obtained using the presented technique and other references from the literature.

3.2 Formulation

Consider a generic printed circuit structure transversally bounded by a surface $\partial\Omega$, as depicted in Fig. 3.1. By application of the equivalence principle the printed circuits are replaced by magnetic $\mathbf{M} \in \mathcal{D}_{\mathrm{H}}$ surface currents over ground planes or equivalent electric surface currents $\mathbf{J} \in \mathcal{D}_{\mathrm{E}}$. Within the equivalent problem, the formulation of the EM behavior arises from the enforcement of BCs over the currents surfaces $\mathcal{D}$, resulting in a coupled system of IEs on the unknown electric (on $\mathcal{D}_{\mathrm{E}}$) and magnetic (on $\mathcal{D}_{\mathrm{H}}$) equivalent currents [cf. §2.3].

We consider here a GF for laterally bounded media. As derived in §2.4, this GF can be expressed as a series expansion of “guided” modes. Rewriting (2.19) for the sake of clarity,

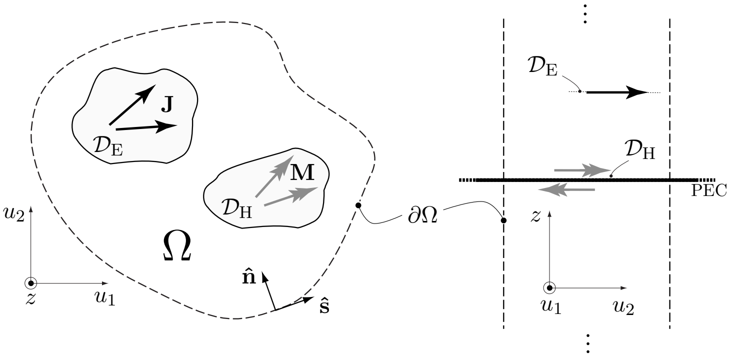

Figure 3.1: The cross-section (left) and longitudinal view (right) of planar electric (**J**) and magnetic (**M**) sources embedded in a medium with BCs imposed on an arbitrary cylindrical surface $\partial\Omega$

the GF is given by

$$\overleftrightarrow{\mathbf{G}}_{\mathrm{PQ}}(\mathbf{r}|\mathbf{r}') = \sum_i P_i^Q(z,z')\,\mathbf{p}_i(u_1,u_2)\,\mathbf{q}_i^*(u_1',u_2'), \tag{3.1}$$

where * denotes complex conjugate. Each modal term i in the series comprises the evaluation of the transverse field components $\mathbf{p}_i, \mathbf{q}_i = \{\mathbf{e}_i, \mathbf{h}_i\}$ in source and observer points and P_i^Q is the voltage/current calculated from the equivalent longitudinal transmission line model[*].

The equivalent electric and magnetic currents are expanded into a sum of BFs $\mathbf{b}_k \equiv \mathbf{b}(u_1', u_2')$, defined over domains $D_{\mathrm{Q}k} \subseteq \mathcal{D}_{\mathrm{Q}}$. Mathematically, this implies that

$$\mathbf{J} = \sum_k i_k \mathbf{b}_k \qquad\qquad \mathbf{M} = \sum_l v_l \mathbf{b}_l \tag{3.2}$$

where i_k, v_l are *unknown* complex coefficients. By application of the MoM in conjunction with the Galerkin procedure [cf. §2.5], the system of IEs is transformed into a linear system of equations that can be written in matrix form as follows

$$\left[\begin{array}{c|c} \mathbf{R}_{\mathrm{EE}} & \mathbf{R}_{\mathrm{EH}} \\ \hline \mathbf{R}_{\mathrm{HE}} & \mathbf{R}_{\mathrm{HH}} \end{array}\right] \cdot \left[\begin{array}{c} \mathbf{i} \\ \hline \mathbf{v} \end{array}\right] = \left[\begin{array}{c} \mathbf{u} \\ \hline \mathbf{j} \end{array}\right], \tag{3.3}$$

where $\mathbf{i}, \mathbf{v}$ and $\mathbf{u}, \mathbf{j}$ are column vectors. The first contains the surface currents coefficients defined in (3.2) and the second includes the results of the projection of the excitation fields over every BF

$$u_k = \int\limits_{D_{\mathrm{E}k}} \mathbf{b}_k \cdot \mathbf{E}^{\mathrm{e}}\,\mathrm{d}S \qquad j_l = \int\limits_{D_{\mathrm{H}l}} \mathbf{b}_l \cdot \mathbf{H}^{\mathrm{e}}\,\mathrm{d}S. \tag{3.4}$$

The four submatrices $\mathbf{R}_{\mathrm{PQ}}$ represent all the possible reactions between electric and magnetic sources and are calculated according to [9]. The reaction between the kth BF expanding a

---

[*] In the context of this chapter, this term is merely a weight factor in the series. The formulation and efficient evaluation of the transmission line model will be widely discuss in Chapter 4.

P-type current and the lth BF of Q-type is expressed as

$$R_{\mathrm{PQ}}(k,l) = \sum_i \mathcal{L}\big(P_i^Q\big)\, C_{\mathrm{P}}(k,i) C_{\mathrm{Q}}^*(l,i) \tag{3.5}$$

where i goes through all the modes (eigensolutions of the transverse boundary problem). The term $\mathcal{L}\big(P_i^Q\big)$ represents the sum of the P_i^Q values obtained from the transmission line models associated to every GF involved in the reaction. This will account for the superposition of GFs acting on both sides of ground planes when a reaction takes place over magnetic surfaces, as in (2.11), or for a single GF when it affects electric surfaces, as in (2.7). The remaining terms correspond to projections of kth BF over ith mode. More specifically, this is formulated as follows

$$C_{\mathrm{P}}(k,i) = \int_{D_{\mathrm{P}k}} \mathbf{b}_k(u_1,u_2) \cdot \mathbf{p}_i(u_1,u_2)\,\mathrm{d}S \tag{3.6}$$

and this expression is known as a coupling or Overlapping Integral (OI).

The cornerstone of this approach lies in the method used to solve these integrals since it will allow to deal, under a unified strategy, with different lateral BCs by selecting appropriate modal functions, and with random shaped printed circuits. Therefore, in the forthcoming sections, a special emphasis is made on the resolution of OIs.

In [10–12], the IE-MoM formulation uses entire domain BFs defined as resonant modes on the source domains. Consequently, the OIs are integrals coupling eigensolutions from two different boundary value problems, similar to those appearing in the MM technique, and are solved with a procedure as in [13]. Nevertheless, most of the IE-MoM implementations use sub-sectional BFs (e.g. rooftops [14] or Rao–Wilton–Glisson (RWG) functions [15]) since they can easily model currents on an arbitrary shaped surfaces. Contrary to the previous cases, to the author's knowledge, the OIs with this kind of BFs have been solved with a *different* method in each case, though a systematic and unified approach is still possible.

The method proposed here expresses the modal field components in terms of scalar potentials derived from the transverse boundary problem and takes advantage of the zero curl and constant divergence of the BFs to derive a general procedure. Notice that these properties apply to a wide variety of sub-sectional BFs, ranging from classical rooftops or RWG functions to more evolved definitions, like the generalized Poisson-Neumann polygonal basis [16].

All the combinations of OIs are reduced to common forms and transformed from surface to line integrals over the contour of the BF's domain. In particular, the OIs involving rooftops and RWG BFs are developed using the same formulation. The validity of the resulting expressions will also extend to any kind of transverse BCs if it is is definable in terms of modal functions.

3.3 Overlapping Integrals

This section presents a general formulation of OIs with BFs that exhibit constant divergence and zero curl within its domain. These BFs are classified as divergence conforming BFs which

Table 3.1: Transverse field components of a mode expressed in terms of scalar potentials.

[1/m]	$\mathbf{e}_i$	$\mathbf{h}_i$
TE_{mn}	$\hat{\mathbf{z}} \times \nabla_{\mathrm{t}}\chi_{mn}/\kappa_{mn}$	$-\nabla_{\mathrm{t}}\chi_{mn}/\kappa_{mn}$
TM_{mn}	$-\nabla_{\mathrm{t}}\chi_{mn}/\kappa_{mn}$	$-\hat{\mathbf{z}} \times \nabla_{\mathrm{t}}\chi_{mn}/\kappa_{mn}$
TEM_{m}	$-\nabla_{\mathrm{t}}\chi_{m}^{0}$	$-\hat{\mathbf{z}} \times \nabla_{\mathrm{t}}\chi_{m}^{0}$

subscript $i \equiv (m, n)$ or (m) identifies a modal term.

are specially suited for Electric Field Integral Equation (EFIE) formulations [17, §9.13]. The surface integrals resulting in these OIs can be expressed as line integrals along the boundary of the region over which the surface integration is performed. Such reduction in the dimensionality of the integration is specially convenient from a computational point of view when the integrals are numerically evaluated. This can arise at least in two cases: when an analytic solution is not available or the transverse boundary problem is computed numerically by some integral equation expressed on the boundary $\partial\Omega$ [18–20], since in that case the modal eigenfunctions are computed only in the contour $\partial\Omega$. The line integral formulation in that case is directly applicable without computing the eigenfunctions at internal points of the surface Ω. On the other hand, a systematic approach in the resolution of the OIs over polygonal subdomains is found with the contour integral representation as will be demonstrated in §3.4.2. Moreover, new properties about the OIs solutions, which help to avoid the evaluation of some specific cases, are also pointed out.

3.3.1 Definition

Recalling (3.6), an OI is a projection of every BF, denoted $\mathbf{b}$, onto the electric or magnetic transverse vector field components $\{\mathbf{e}, \mathbf{h}\}$ of each mode. Considering the electric and magnetic case and the classification of modes into Transverse Electric (TE),Transverse Magnetic (TM) and Transverse Electromagnetic (TEM) [21, §2.1], this gives six different possible expressions for the OIs, namely

$$C_{\mathrm{E}}^{\tau} = \int\limits_{D_{\mathrm{E}}} \mathbf{b} \cdot \mathbf{e}^{\tau} \, \mathrm{d}S \tag{3.7a}$$

$$C_{\mathrm{H}}^{\tau} = \int\limits_{D_{\mathrm{H}}} \mathbf{b} \cdot \mathbf{h}^{\tau} \, \mathrm{d}S, \tag{3.7b}$$

with $\tau = \{\mathrm{TE,TM,TEM}\}$.

A more convenient form for (3.7) is obtained by expressing the modal field components in terms of scalar potentials [21]. The relations needed are detailed in Table 3.1, where the scalar potentials χ (subscripts are omitted for simplicity) are eigensolutions, with associated eigenvalues $\kappa \neq 0$, of the Helmholtz equation

$$\left(\nabla_{\mathrm{t}}^{2} + \kappa^{2}\right) \chi = 0 \tag{3.8}$$

with Dirichlet or Neumann BC on the transverse boundary $\partial\Omega$. When $\kappa = 0$ (TEM case), the scalar potentials are denoted with χ^0 and are derived from the Laplace equation instead

$$\nabla_{\mathrm{t}}^2 \chi^0 = 0, \tag{3.9}$$

where $\nabla_{\mathrm{t}}^2 = \nabla^2 - \hat{\mathbf{z}}\partial^{\,2}/\partial z^2$.

Substitution of the expressions based on scalar potentials in Table 3.1 into (3.7) shows that all the aforementioned types of OIs can be written in terms of the following *two* surface integrals in χ (and analogously for χ^0)

$$\int_D \mathbf{b} \cdot (\hat{\mathbf{z}} \times \nabla_{\mathrm{t}}\chi)\, \mathrm{d}S = \int_D (\mathbf{b} \times \hat{\mathbf{z}}) \cdot \nabla_{\mathrm{t}}\chi \, \mathrm{d}S \tag{3.10a}$$

$$\int_D \mathbf{b} \cdot \nabla_{\mathrm{t}}\chi \, \mathrm{d}S. \tag{3.10b}$$

The relation between these integrals and (3.7) is detailed in the two first columns of Table 3.2. The expressions in (3.10) can be seen as the *same* surface integral over two different BFs, namely $\mathbf{b}$ and $\mathbf{b}^{\mathrm{c}} = \hat{\mathbf{z}} \times \mathbf{b}$. Notice that these functions have complementary divergence and curl, i.e. the curl of the first is the divergence of the second and viceversa:

$$(\nabla_{\mathrm{t}} \cdot \mathbf{b}^{\mathrm{c}}\,)\, \hat{\mathbf{z}} = \nabla_{\mathrm{t}} \times \mathbf{b} \tag{3.11a}$$

$$\nabla_{\mathrm{t}} \times \mathbf{b}^{\mathrm{c}} = (\nabla_{\mathrm{t}} \cdot \mathbf{b})\, \hat{\mathbf{z}} \tag{3.11b}$$

3.3.2 Transformation Into Contour Integrals

In EFIE formulations, it is necessary to employ expansion functions that ensure a finite divergence across domain boundaries, or equivalently BFs that maintain normal continuity between subdomains [17, 9.13]. BFs having finite divergence and possibly discontinuous tangential components are known as divergence-conforming BFs. A special subset exhibiting constant divergence and zero curl is considered here. These properties are satisfied at least by rooftops, RWG or generalized Poisson-Neumann polygonal basis [16] over retangular, triangular and polygonal subdomains, respectively.

Let us proceed formally. Assume BFs being locally curl-free and with locally constant charge density (constant divergence), i.e. any function $\mathbf{b} \in D$ satisfying

$$\nabla_{\mathrm{t}} \times \mathbf{b} = 0 \tag{3.12a}$$

$$\nabla_{\mathrm{t}} \cdot \mathbf{b} = d \tag{3.12b}$$

where d is a non-zero real constant and $\nabla_{\mathrm{t}} = \nabla - \hat{\mathbf{z}}\partial/\partial z$.

The transformation of (3.10) into equivalent contour integrals is based on Green's first identity

$$\int_D \mathbf{A} \cdot \nabla_{\mathrm{t}} B \, \mathrm{d}S = \oint_{\partial D} B \hat{\boldsymbol{\nu}} \cdot \mathbf{A} \, \mathrm{d}l - \int_D B \nabla_{\mathrm{t}} \cdot \mathbf{A} \, \mathrm{d}S \tag{3.13}$$

where $\{\mathbf{A}, \nabla_{\mathrm{t}} B\}$ denote two generic vector functions and $\hat{\boldsymbol{\nu}}, \hat{\boldsymbol{\tau}} = \hat{\mathbf{z}} \times \hat{\boldsymbol{\nu}}$ are the normal and tangential unitary vectors over the integration contour ∂D.

Let us proceed first with (3.10a). A convenient substitution in (3.13) is

$$\mathbf{A} = \mathbf{b} \times \hat{\mathbf{z}} = -\mathbf{b}^{\mathrm{c}}, \qquad B = \chi$$

since the resulting surface integral in the identity (3.13) will have the divergence operator applied to $\mathbf{b}^{\mathrm{c}}$. After substitution and considering that $\hat{\boldsymbol{\nu}} \cdot (\mathbf{b} \times \hat{\mathbf{z}}) = \mathbf{b} \cdot \hat{\boldsymbol{\tau}}$ and $\nabla_{\mathrm{t}} \cdot (\mathbf{b} \times \hat{\mathbf{z}}) = (\nabla_{\mathrm{t}} \times \mathbf{b}) \cdot \hat{\mathbf{z}}$, the integral can be rewritten as follows

$$\int\limits_D \mathbf{b} \cdot (\hat{\mathbf{z}} \times \nabla_{\mathrm{t}} \chi)\, \mathrm{d}S = \oint\limits_{\partial D} \chi\, \mathbf{b} \cdot \hat{\boldsymbol{\tau}}\, \mathrm{d}l - \int\limits_D \chi\, \nabla_{\mathrm{t}} \times \mathbf{b} \cdot \hat{\mathbf{z}}\, \mathrm{d}S.$$

Then, using (3.12a), the last integral term vanishes, leading (3.10a) to the following contour integral

$$\int\limits_D \mathbf{b} \cdot (\hat{\mathbf{z}} \times \nabla_{\mathrm{t}} \chi)\, \mathrm{d}S = \oint\limits_{\partial D} \chi\, \mathbf{b} \cdot \hat{\boldsymbol{\tau}}\, \mathrm{d}l. \tag{3.14}$$

The demonstration is analogous when (3.10a) is applied to the scalar potential χ^0.

The transformation of the integral (3.10b) is carried out differently depending on whether it involves χ or χ^0. In the first case, the identity (3.13) is used with

$$\mathbf{A} = \mathbf{b}, \qquad B = \chi,$$

and applying the property (3.12b), it reduces (3.10b) to

$$\int\limits_D \mathbf{b} \cdot \nabla_{\mathrm{t}} \chi\, \mathrm{d}S = \oint\limits_{\partial D} \chi\, \mathbf{b} \cdot \hat{\boldsymbol{\nu}}\, \mathrm{d}l - d \int\limits_D \chi\, \mathrm{d}S.$$

Now, the remaining surface integral does not vanish and further developments are needed in order to obtain a contour integral form. First, the scalar potential is expressed, using Helmholtz equation (3.8), as a divergent field

$$\chi = -\nabla_{\mathrm{t}}^2 \chi / \kappa^2 = -\nabla_{\mathrm{t}} \cdot (\nabla_{\mathrm{t}} \chi)/\kappa^2,$$

with $\kappa \neq 0$. Then applying the Gauss theorem, the resulting expression can be reduced to an integral over the surface contour as

$$-\kappa^2 \int\limits_D \chi\, \mathrm{d}S = \int\limits_D \nabla_{\mathrm{t}} \cdot (\nabla_{\mathrm{t}} \chi)\, \mathrm{d}S = \oint\limits_{\partial D} \nabla_{\mathrm{t}} \chi \cdot \hat{\boldsymbol{\nu}}\, \mathrm{d}l.$$

Gathering all these results leads to the following contour representation of (3.10b)

$$\int\limits_D \mathbf{b} \cdot \nabla_{\mathrm{t}} \chi\, \mathrm{d}S = \oint\limits_{\partial D} \chi\, \mathbf{b} \cdot \hat{\boldsymbol{\nu}}\, \mathrm{d}l + \frac{d}{\kappa^2} \oint\limits_{\partial D} \nabla_{\mathrm{t}} \chi \cdot \hat{\boldsymbol{\nu}}\, \mathrm{d}l, \tag{3.15}$$

for $\kappa \neq 0$.

Table 3.2: Different representation of OIs.

Overlapping	Surface	Contour (**b** satisfies (3.12))
$\kappa C_{\mathrm{E}}^{\mathrm{TE}}$, $-\kappa C_{\mathrm{H}}^{\mathrm{TM}}$, $-C_{\mathrm{H}}^{\mathrm{TEM}}$ (with $\chi = \chi^0$)	$\int_D \mathbf{b} \cdot (\hat{\mathbf{z}} \times \nabla_{\mathrm{t}}\chi)\,\mathrm{d}S$	$\oint_{\partial D} \chi b_\tau \,\mathrm{d}l$
$-\kappa C_{\mathrm{E}}^{\mathrm{TM}}$, $-\kappa C_{\mathrm{H}}^{\mathrm{TE}}$	$\kappa \neq 0$ $\int_D \mathbf{b} \cdot \nabla_{\mathrm{t}}\chi \,\mathrm{d}S$	$\oint_{\partial D} \chi b_\nu \,\mathrm{d}l + \frac{d}{\kappa^2} \oint_{\partial D} \frac{\partial \chi}{\partial \nu}\,\mathrm{d}l$
$-C_{\mathrm{E}}^{\mathrm{TEM}}$	$\kappa = 0$	$\oint_{\partial D} a \frac{\partial \chi^0}{\partial \nu}\,\mathrm{d}l$

Notation: $\frac{\partial \chi}{\partial s} \equiv \nabla_{\mathrm{t}}\chi \cdot \hat{\mathbf{s}}$ and $\mathbf{b} \cdot \hat{\mathbf{s}} \equiv b_s$ for $s = \nu, \tau$.

In order to deduce a contour form for (3.10b) applied to χ^0 ($\kappa = 0$), let us define an auxiliary function a such that

$$\mathbf{b} = \nabla_{\mathrm{t}} a, \tag{3.16a}$$

$$\nabla_{\mathrm{t}}^2 a = d, \tag{3.16b}$$

since $\mathbf{b}$ satisfies (3.12b). Then, we use the following substitution in (3.13)

$$\mathbf{A} = \nabla_{\mathrm{t}}\chi^0, \qquad\qquad B = a,$$

to rewrite the integral (3.10b) for χ^0 as

$$\int_D \mathbf{b} \cdot \nabla_{\mathrm{t}}\chi^0 \,\mathrm{d}S = \oint_{\partial D} a \nabla_{\mathrm{t}}\chi^0 \cdot \hat{\boldsymbol{\nu}} \,\mathrm{d}l - \int_D a \nabla_{\mathrm{t}}^2 \chi^0 \,\mathrm{d}S,$$

valid despite $\kappa = 0$. Finally, since χ^0 is a solution of the Laplace equation (3.9), the last surface integral is zero and therefore the following equivalence holds

$$\int_D \mathbf{b} \cdot \nabla_{\mathrm{t}}\chi^0 \,\mathrm{d}S = \oint_{\partial D} a \nabla_{\mathrm{t}}\chi^0 \cdot \hat{\boldsymbol{\nu}} \,\mathrm{d}l. \tag{3.17}$$

A summary of the OIs and their equivalent contour integral representations, when $\mathbf{b}$ satisfies (3.12), is given in Table 3.2. There, the notation is simplified with $\frac{\partial \chi}{\partial s} \equiv \nabla_{\mathrm{t}}\chi \cdot \hat{\mathbf{s}}$ and $\mathbf{b} \cdot \hat{\mathbf{s}} \equiv b_s$ for $s = \nu, \tau$.

3.4 Basis Functions

Up to now, the only restriction we used for the BFs is that they are curl-free and with a constant divergence. In this section we further specialize our OIs to linear subsectional BFs. Using the appropriate parametrization, the variation of these functions along any side of a subdomain, can be in general written as a polynomial function with constant coefficients. Then, the OIs maybe further simplified to the evaluation of two simple line integrals.

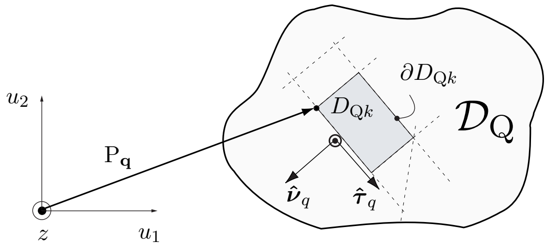

Figure 3.2: Discretization of planar surface with $\mathrm{Q} = \{\mathrm{E}, \mathrm{H}\}$-type sources into D domains.

3.4.1 Rooftops and RWG Functions

Rooftops [14] and RWG [15] functions are linear subsectional BFs and constitute a common choice for the expansion of currents in the IE-MoM formulation [see (3.2)]. The term "subsectional" means that the BF's support does not extend to the entire current's surface $\mathcal{D}_{\mathrm{Q}}$ [see Fig. 3.2] but to smaller domains D in which $\mathcal{D}_{\mathrm{Q}}$ is subdivided.

These BFs, denoted with $\mathbf{b}$, are defined piecewise by means of two "half-BFs" $\mathbf{g}^{\pm}$ on adjacent subdomains $D^{\pm}$ and joined by a common side denoted as ∂D^{C} as illustrated in Fig. 3.3. These subdomains can be triangles (half-RWG function) or rectangles (half-rooftop), as represented in Fig. 3.3. In the first case, $\mathbf{g}_p$ models the current flowing radially from the pth node $\mathbf{P}_p$ towards the cell's common side ∂D^{C} according to the following laws

$$\mathbf{g}_p = \frac{\boldsymbol{\rho}_p}{2D} = \frac{\mathbf{r} - \mathbf{P}_p}{2D} \tag{3.18a}$$

$$f_p = \frac{\rho_p^2}{4D}, \tag{3.18b}$$

where $f_p = \nabla_{\mathrm{t}} \cdot \mathbf{g}_p$, D is the area of the triangle and ± signs are suppressed for the sake of clarity. When the subdomain is rectangular, the vector function $\mathbf{g}_p$ is oriented parallel to the pth side and can be defined as

$$\mathbf{g}_p = \frac{\boldsymbol{\tau}_p}{D} = \frac{(\mathbf{r} - \mathbf{P}_p) \cdot \hat{\boldsymbol{\tau}}_p}{D} \, \hat{\boldsymbol{\tau}}_p \tag{3.19a}$$

$$f_p = \frac{\tau_p^2}{2D}, \tag{3.19b}$$

where D is the area of the rectangle. We can observe that in both cases the vectors have *linear* tangential component along the edges and a *constant* non-zero normal component over ∂D^{C}, as will be demonstrated later. Moreover, the properties (3.12) are satisfied with $d = 1/D$.

Finally, any vector BF $\mathbf{b}$ (resp. a) can be defined over $D = D^{+} \cup D^{-}$ as

$$\mathbf{b} = \mathbf{g}^{+} - \mathbf{g}^{-}, \qquad a = f^{+} - f^{-} \tag{3.20}$$

where $\mathbf{g}^{\pm}, f^{\pm}$ are oriented in $D^{\pm}$ with vectors flowing towards ∂D^{C} (by appropriate choice of index p in each case as in Fig. 3.3). The continuity of the current through ∂D^{C} is maintained by the constant normal component and the change of direction of one of the half-BFs [negative sign in (3.20)].

In the following sections, the nodes and sides of any subdomain are enumerated counterclockwise with subscripts $q = 0, 1, \cdots N$ while the subindex $p = 0, 1, \cdots N$ will designate the orientation of $\mathbf{g}$ (resp. f). Therefore, the common side for the pth half-BF can be readily obtained as

$$q = [p+1]_N, \tag{3.21}$$

where $[x]_y \equiv \mathrm{mod}(x, y) = x - ny$ such that $n = \lfloor x/y \rfloor$ if $y \neq 0$.

3.4.2 OIs for Linear Subsectional BFs

Let us define an affine transformation as parametrization function

$$\begin{array}{rccc} \boldsymbol{\sigma}_q : & [0,1] & \longrightarrow & \mathbb{R}^2 \\ & t & \rightsquigarrow & \begin{bmatrix} x(t) \\ y(t) \end{bmatrix} = \mathbf{P}_q + L_q t \hat{\boldsymbol{\tau}}_q = \mathbf{P}_q + \mathbf{L}_q t. \end{array} \tag{3.22}$$

that maps every side q of a polygonal subdomain D into a normalized segment $t \in [0, 1]$. The position vector $\mathbf{P}_q$ locates the qth node, corresponding to the origin of the side with the same index; $\mathbf{L}_q = L_q \hat{\boldsymbol{\tau}}_q$ denotes the vector along the qth side and $\hat{\boldsymbol{\tau}}_q$ its unitary vector. The integrals in Table 3.2 on D lead to a decomposition of the contour ∂D into segments ∂D_q defined over each side q of the polygon. Given

$$\mathrm{d}l = \|\boldsymbol{\sigma}_q'(t)\| \,\mathrm{d}t = L_q \,\mathrm{d}t,$$

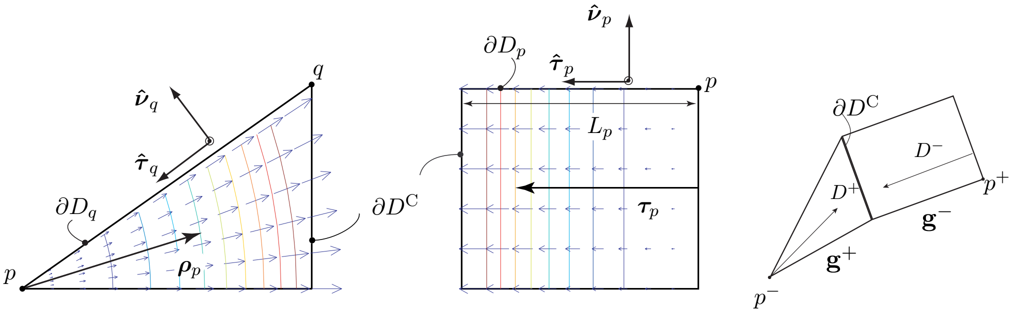

Figure 3.3: A half-BF $\mathbf{g}$ defined on a triangular (half-RWG function) and rectangular (half-rooftop) subdomain $D^{\pm}$. The arrows represent the vector function $\mathbf{g}_p$, the lines the contour plot of the auxiliary function f_p and the nodes and sides are enumerated counterclockwise.

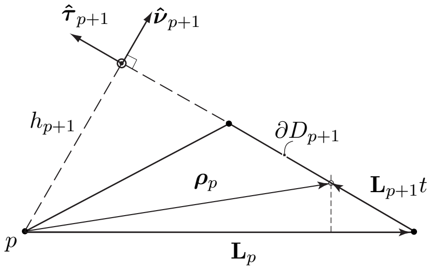

Figure 3.4: Triangular path.

the OIs are then expressed in the form

$$\oint_{\partial D} \cdots = \sum_{q=1}^{N} \Big(\int_{\partial D_q} \cdots \,\mathrm{d}l \Big) = \sum_{q=1}^{N} L_q \Big(\int_0^1 \cdots \,\mathrm{d}t \Big). \tag{3.23}$$

Consequently, the solution of (3.23) is subject to the variation of BFs along each path in function of the normalized variable t.

Variation of Half-BFs Along the Subdomain's Edge ∂D_q

As mentioned previously, the normal vector component on a triangle is constant along ∂D^{C}. This can be easily demonstrated if we note that normal component of the radial vector on the $(p+1)$th side, as depicted in Fig. 3.4, corresponds to the triangle's height $h_{p+1} = \boldsymbol{\rho}_p \cdot \hat{\boldsymbol{\nu}}_{p+1}$. Taking the definition from (3.18) and writing the area as $D = L_{p+1} h_{p+1}/2$ reveals that

$$\mathbf{g}_p \cdot \hat{\boldsymbol{\nu}}_{p+1} = \frac{1}{2D} \boldsymbol{\rho}_p \cdot \hat{\boldsymbol{\nu}}_{p+1} = \frac{1}{L_{p+1}}.$$

In a triangular subdomain, the parametrization of the sides radial to the pth node is trivial since they are parallel to $\boldsymbol{\rho}_p$. The opposite side is obtained by projecting the radial vector $\boldsymbol{\rho}_p = \mathbf{L}_p + t\mathbf{L}_{p+1}$ on the tangential unitary component directed along side $p+1$ [Fig. 3.4]. The linear deviation of the tangential components along every subdomain's edge is given as follows

$$\mathbf{g}_p(\boldsymbol{\sigma}_q) \cdot \hat{\boldsymbol{\tau}}_q = \frac{1}{2D} \begin{cases} L_q t, & q = p \\ L_{q-1} \hat{\boldsymbol{\tau}}_{q-1} \cdot \hat{\boldsymbol{\tau}}_q + L_q t, & q = [p+1]_3 \\ L_q (t-1), & q = [p-1]_3 \end{cases} \tag{3.24a}$$

The expression for the auxiliary function f_p on a triangle, given in (3.18), requires the parametrization of the radial distance $\rho_p(t)$. Simple geometric relations derived from Fig. 3.4 show that

$$\rho_p^2 = L_p^2 + L_{p+1}^2 t^2 + 2\mathbf{L}_p \cdot \mathbf{L}_{p+1} t.$$

Therefore, the evaluation of the auxiliary function along the edge can be expressed as

$$f_p(\boldsymbol{\sigma}_q) = \frac{1}{4D}\begin{cases} L_q^2 t^2, & q = p \\ L_{q-1}^2 + 2\mathbf{L}_{q-1}\cdot\mathbf{L}_q t + L_q^2 t^2, & q = [p+1]_3 \\ L_q^2\left(t-1\right)^2, & q = [p-1]_3 \end{cases} \tag{3.24b}$$

The normal vector component along ∂D^{C} in a rectangle is constant and equal to the inverse of the common side's length, as in the triangular case. A direct evaluation of (3.19) yields a constant and perpendicular vector at ∂D^{C}, i.e. $\hat{\boldsymbol{\tau}}_p \cdot \hat{\boldsymbol{\nu}}_{p+1} = 1$, that vanishes elsewhere. Expressing the area as $D = L_p L_{p+1}$ one obtains

$$\mathbf{g}_p \cdot \hat{\boldsymbol{\nu}}_{p+1} = \frac{L_p}{D}\hat{\boldsymbol{\tau}}_p \cdot \hat{\boldsymbol{\nu}}_{p+1} = \frac{1}{L_{p+1}}.$$

The law that rules the change of the transverse component and the auxiliary function along the sides of the rectangular domain can be easily deduced from the definitions of (3.19) and (3.22) as

$$\mathbf{g}_p(\boldsymbol{\sigma}_q)\cdot\hat{\boldsymbol{\tau}}_q = \frac{L_q}{D}\begin{cases} t, & q = p \\ 0, & q = [p\pm 1]_4 \\ t-1, & q = [p\pm 2]_4 \end{cases} \tag{3.25a}$$

and

$$f_p(\boldsymbol{\sigma}_q) = \frac{L_q^2}{2D}\begin{cases} t^2, & q = p \\ 1, & q = [p+1]_4 \\ 0, & q = [p-1]_4 \\ \left(t-1\right)^2, & q = [p\pm 2]_4 \end{cases}, \tag{3.25b}$$

respectively.

Finally, from (3.24) and (3.25) we can conclude that the variation of the pth half-BF along the qth side of any of the polygonal subdomains (rectangular or triangular) can be expressed in general in terms of t in the form

$$\mathbf{g}_p\left(\boldsymbol{\sigma}_q\right) = \left[A_1(p,q)t + A_0(p,q)\right]\hat{\boldsymbol{\tau}}_q + \frac{\delta_{[p+1]_N,q}}{L_q}\hat{\boldsymbol{\nu}}_q \tag{3.26a}$$

$$f_p\left(\boldsymbol{\sigma}_q\right) = B_2(p,q)t^2 + B_1(p,q)t + B_0(p,q), \tag{3.26b}$$

where $A_i, B_i \in \mathbb{R}$ are constant values, summarized in Table 3.3, for each combination of (p,q), N refers to the number of sides and $\delta_{[p+1]_N,q}$ is a Kronecker delta that equals one when q coincides with the common-side.

Table 3.3: Variation of $\mathbf{g}$-components on a triangular (2nd row) and rectangular (3rd row) subdomain.

$\mathbf{g}_p \cdot \hat{\boldsymbol{\nu}}_q$	$\mathbf{g}_p \cdot \hat{\boldsymbol{\tau}}_q = \sum_i A_i(p,q)t^i$	$f_p = \sum_i B_i(p,q)t^i$
$\begin{cases} \frac{1}{L_q}, & q = [p+1]_N; \\ 0, & \text{otherwise.} \end{cases}$	$\frac{1}{2D} \begin{cases} L_q t, & q = p \\ L_{q-1} \hat{\boldsymbol{\tau}}_{q-1} \cdot \hat{\boldsymbol{\tau}}_q + L_q t, & q = [p+1]_3 \\ L_q (t-1), & q = [p-1]_3 \end{cases}$	$\frac{1}{4D} \begin{cases} L_q^2 t^2, & q = p \\ L_{q-1}^2 + 2\mathbf{L}_{q-1} \cdot \mathbf{L}_q t + L_q^2 t^2, & q = [p+1]_3 \\ L_q^2 (t-1)^2, & q = [p-1]_3 \end{cases}$
	$\frac{L_q}{D} \begin{cases} t, & q = p \\ 0, & q = [p \pm 1]_4 \\ t-1, & q = [p \pm 2]_4 \end{cases}$	$\frac{L_q^2}{2D} \begin{cases} t^2, & q = p \\ 1, & q = [p+1]_4 \\ 0, & q = [p-1]_4 \\ (t-1)^2, & q = [p \pm 2]_4 \end{cases}$

$p, q = 0, 1, \ldots N (= 3, 4)$ are 0-*based* indices.

Integration Along the Subdomain's Edge ∂D_q

Now, we are at point to simplify the OIs of Table 3.2 using (3.23) and choosing (3.26) to designate the variation of a generic linear subsectional BF. The simplified representations for the integrals on a qth path are

$$\int_{\partial D_q} \chi\, \mathbf{g}_p \cdot \hat{\boldsymbol{\tau}}_q \,\mathrm{d}l = L_q \sum_{n=0}^{1} A_n(p,q) I_q^{(n)} \tag{3.27a}$$

$$\int_{\partial D_q} \chi\, \mathbf{g}_p \cdot \hat{\boldsymbol{\nu}}_q \,\mathrm{d}l = I_q^{(0)}\, \delta_{[p+1]_N,q} \tag{3.27b}$$

$$\int_{\partial D_q} \frac{\partial \chi}{\partial \nu_q} \,\mathrm{d}l = L_q\, I_q'^{(0)} \tag{3.27c}$$

$$\int_{\partial D_q} f_p \frac{\partial \chi^0}{\partial \nu_q} \,\mathrm{d}l = L_q \sum_{n=0}^{2} B_n(p,q) I_q'^{(n)} \tag{3.27d}$$

where

$$I_q^{(n)} \equiv \int_0^1 t^n\, \chi(\boldsymbol{\sigma}_q(t))\,\mathrm{d}t, \tag{3.28a}$$

$$I_q'^{(n)} \equiv \int_0^1 t^n\, \nabla_{\mathrm{t}}\chi(\boldsymbol{\sigma}_q(t)) \cdot \hat{\boldsymbol{\nu}}_q \,\mathrm{d}t \tag{3.28b}$$

for $n = 0, 1, 2$. Finally, the solution of the OI for the complete BF is straightforward by subtracting the partial solutions, i.e. following the notation of (3.6):

$$\int_D \mathbf{b} \cdot \mathbf{p}\,\mathrm{d}S = \int_{D^+} \mathbf{g}^+ \cdot \mathbf{p}\,\mathrm{d}S - \int_{D^-} \mathbf{g}^- \cdot \mathbf{p}\,\mathrm{d}S, \tag{3.29}$$

as can be deduced from (3.20).

Notice that the transition between the OI on the different BF considered here is seamless and it is reduced to the election of appropriate constant values $\{A_i, B_i\}$ in the formulation. In addition, the generality in the transverse BCs is still preserved at this point.

3.5 Transverse Boundary Problems

In this section we will specialize the results of the previous section to three useful BCs, namely perfect electric conductor (PEC) on a rectangular and circular contour (i.e. rectangular and circular waveguide) and periodic BCs on a skewed contour.

The eigensolutions of these three different transverse boundary problems have many common properties. An attempt to synthesize them has been done in Table 3.8. In general, the scalar

Table 3.4: Perfect electric conductor (PEC) boundary conditions on $\partial\Omega$.

Mode type	TE	TM	TEM
Equation $\forall(u_1, u_2) \in \Omega$	$(\nabla_t^2 + \kappa_i^2)\chi_i = 0$		$\nabla_t^2 \chi_i^0 = 0$
Boundary conditions $\in \partial\Omega$	$\frac{\partial \chi}{\partial n} = 0$	$\chi = 0$	$\frac{\partial \chi^0}{\partial s} = 0$

where $\frac{\partial f}{\partial u} = \hat{\mathbf{u}} \cdot \nabla_t f$ and $\hat{\mathbf{s}}, \hat{\mathbf{n}}$ are tangential and normal vectors to $\partial\Omega$.

potential for the ith mode will be denoted with χ_i. Each mode is also normalized with a scale factor ξ_i. Thus, assuming $f_i(u_1, u_2)$ is an eigensolution of the problem, then

$$\chi_i(u_1, u_2) = \xi_i f_i(u_1, u_2) = \left[\int_\Omega f_i f_i^* \, \mathrm{d}S \right]^{-\frac{1}{2}} f_i(u_1, u_2)$$

such that it satisfies an orthonormal relation between modes

$$\int_\Omega \chi_i \chi_j^* \, \mathrm{d}S = \delta_{ij}, \tag{3.30}$$

where δ_{ij} is the Kronecker delta. In occasions, this factor is constant for all modes so we will drop the subscript indices.

In what follows, the integrals (3.28), resulting from the OIs, will be solved for each particular BC.

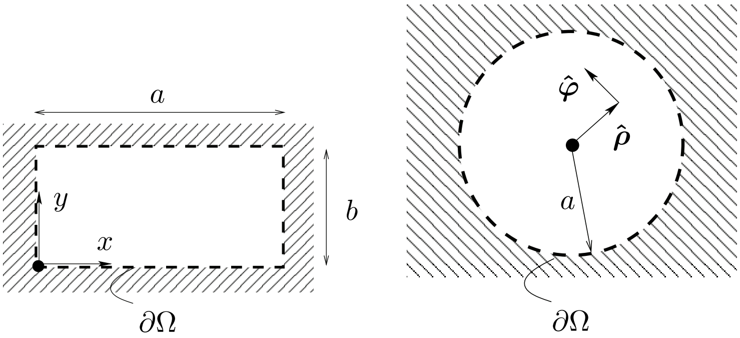

(a) Rectangular boundary. (b) Circular boundary.

Figure 3.5: Waveguide boundaries.

3.5.1 Rectangular Waveguide

Consider a uniform waveguide of rectangular cross section of width a and height b, as shown in Fig. 3.5(a). The eigensolutions of the Helmholtz equation (3.8) with rectangular PEC boundaries (Table 3.4) are given in Table 3.5.

These two expressions for the scalar potentials can be rewritten into a single formula

$$\chi_i = \xi_i \left\{ \begin{array}{c} \cos(k_m x)\cos(k_n y) \\ \sin(k_m x)\sin(k_n y) \end{array} \right. = \frac{\xi_i}{2}\left[\cos(\Delta_i) \pm \cos(\Sigma_i)\right] \tag{3.31}$$

where the positive or negative sign applies to the TE or the TM case, respectively. The arguments of the trigonometric functions are real values defined as

$$\Sigma_i = k_m x + k_n y = \boldsymbol{\kappa}_i \cdot \mathbf{r}, \tag{3.32a}$$

$$\Delta_i = k_m x - k_n y = \bar{\boldsymbol{\kappa}}_i \cdot \mathbf{r} \tag{3.32b}$$

with $\bar{\boldsymbol{\kappa}}_i = k_m\hat{\mathbf{x}} - k_n\hat{\mathbf{y}}$ and $\mathbf{r}$ being the position vector. The gradient is calculated as

$$\nabla_{\mathrm{t}}\chi_i = -\frac{\xi_i}{2}\left[\sin(\Delta_i)\ \nabla_{\mathrm{t}}\Delta_i \pm \sin(\Sigma_i)\ \nabla_{\mathrm{t}}\Sigma_i\right] = -\frac{\xi_i}{2}\left[\sin(\Delta_i)\ \bar{\boldsymbol{\kappa}}_i \pm \sin(\Sigma_i)\ \boldsymbol{\kappa}_i\right], \tag{3.33}$$

since $\boldsymbol{\kappa}_i$ is a constant vector and then $\nabla_{\mathrm{t}}(\boldsymbol{\kappa}\cdot\mathbf{r}) = (\boldsymbol{\kappa}\cdot\nabla_{\mathrm{t}})\mathbf{r} = \boldsymbol{\kappa}$ (analogously with $\bar{\boldsymbol{\kappa}}$).

OIs on Linear Subsectional BFs

An analytic solution to the integrals (3.28) with rectangular PEC boundaries can be found by expressing (3.31) and (3.33) in terms of the normalized space defined with (3.22). Thus, the arguments (3.32) on the qth side become linear functions of t

$$\Sigma_{i,q} = \boldsymbol{\kappa}_i \cdot \boldsymbol{\sigma}_q(t) = (\boldsymbol{\kappa}_i \cdot \mathbf{P}_q) + (\boldsymbol{\kappa}_i \cdot \mathbf{L}_q)t, \tag{3.34a}$$

$$\Delta_{i,q} = \bar{\boldsymbol{\kappa}}_i \cdot \boldsymbol{\sigma}_q(t) = (\bar{\boldsymbol{\kappa}}_i \cdot \mathbf{P}_q) + (\bar{\boldsymbol{\kappa}}_i \cdot \mathbf{L}_q)t. \tag{3.34b}$$

Table 3.5: Scalar potentials for rectangular PEC boundaries [21].

$\chi_i(x,y) = \{\phi_{mn}, \psi_{mn}\}$ and κ_{mn} [1/m]	
TE	$\psi_{mn} = \sqrt{\frac{\epsilon_m\epsilon_n}{\Omega}}\cos(k_m x)\cos(k_n y)$
TM	$\phi_{mn} = \frac{2}{\sqrt{\Omega}}\sin(k_m x)\sin(k_n y)$
with	$\Omega = ab$, $\boldsymbol{\kappa}_{mn} = k_m\hat{\mathbf{x}} + k_n\hat{\mathbf{y}} = \frac{m\pi}{a}\hat{\mathbf{x}} + \frac{n\pi}{b}\hat{\mathbf{y}}$

$\epsilon_n = 1$ (if $n = 0$), 2 (if $n \neq 0$)

Now, the direct substitution of these expressions into (3.31) and (3.33), transforms the integrals (3.28) for each ith mode on the qth side into the following expressions

$$I_{i,q}^{(n)} = \int_0^1 t^n\, \chi_i\,(x(t), y(t))\; \mathrm{d}t = \frac{\xi_i}{2}\Big[\int_0^1 t^n\, \cos\Delta_{i,q}\,\mathrm{d}t \pm \int_0^1 t^n\, \cos\Sigma_{i,q}\,\mathrm{d}t\Big] \tag{3.35a}$$

$$\begin{aligned} I_{i,q}^{\prime(n)} &= \int_0^1 t^n\, \nabla_{\mathrm{t}}\chi_i\,(x(t), y(t)) \cdot \hat{\boldsymbol{\nu}}_q\,\mathrm{d}t = \\ &- \frac{\xi_i}{2}\Big[(\bar{\boldsymbol{\kappa}}_i \cdot \hat{\boldsymbol{\nu}}_q)\int_0^1 t^n\, \sin\Delta_{i,q}\,\mathrm{d}t \pm (\boldsymbol{\kappa}_i \cdot \hat{\boldsymbol{\nu}}_q)\int_0^1 t^n\, \sin\Sigma_{i,q}\,\mathrm{d}t\Big], \end{aligned} \tag{3.35b}$$

for $n = 0, 1, 2$. The remaining integrals have trivial analytic solution [cf (A-3),(A-4)].

3.5.2 Circular Waveguide

The eigensolutions of the Helmholtz equation (3.8) for PEC BCs (Table 3.4) on a circle, as shown in Fig. 3.5(b), are given in Table 3.6. In general, we could write these functions as

$$\chi_i = \xi_i\, J_m(\kappa_i\rho)\exp(\mathrm{j}m\varphi), \tag{3.36}$$

where the real and imaginary parts are independent solutions representing orthogonal polarizations of the field. For each mode i, $\kappa_i a$ are calculated as non vanishing roots of the Bessel's function or its derivative, more specifically

$$\kappa'_{mn}a = q_{mn} \equiv n^{\mathrm{th}} \text{ zero of } J'_m(x), \tag{3.37a}$$

$$\kappa''_{mn}a = p_{mn} \equiv n^{\mathrm{th}} \text{ zero of } J_m(x) \tag{3.37b}$$

with indices $n = 1, 2, \ldots$, $m = 0, 1, \ldots$, for the TE and TM case respectively.

Table 3.6: Scalar potentials for PEC circular boundaries [21].

$\chi_i(\rho,\varphi) = \{\phi_{mn}, \psi_{mn}\}$ and $\kappa_i = \{\kappa'_{mn}, \kappa''_{mn}\}$ [1/m]	
TE	$\psi_{mn} = \sqrt{\frac{\epsilon_m}{\Omega}}\frac{q_{mn}}{\sqrt{q_{mn}^2 - m^2}J_m(q_{mn})}\,J_m(\kappa'_{mn}\rho)\begin{pmatrix}\cos\\ \sin\end{pmatrix} m\varphi$
TM	$\phi_{mn} = \sqrt{\frac{\epsilon_m}{\Omega}}\frac{1}{J_{m+1}(p_{mn})}\,J_m(\kappa''_{mn}\rho)\begin{pmatrix}\cos\\ \sin\end{pmatrix} m\varphi$
with	$\Omega = \pi a^2$, and $\kappa'_{mn} = \frac{q_{mn}}{a}$, $\kappa''_{mn} = \frac{p_{mn}}{a}$

$\epsilon_n = 1$ (if $n = 0$), 2 (if $n \neq 0$)

A more convenient representation of (3.36) uses a truncated series of exponentials in cartesian coordinates [22]

$$\chi_i = \xi_i J_m(\kappa_i \rho)\exp(\mathrm{j}m\varphi) \approx \frac{\mathrm{j}^m \xi_i}{N}\sum_{l=0}^{N-1}\exp\left(\mathrm{j}l\frac{2m\pi}{N}\right)\exp\left(-\mathrm{j}\kappa_i\,\mathbf{T}_l\cdot\boldsymbol{\rho}\right) \tag{3.38}$$

where

$$\mathbf{T}_l\cdot\boldsymbol{\rho} = x\cos\left(2\pi l/N\right) + y\sin\left(2\pi l/N\right)$$

and $N-1 > \kappa_i r + N_0$ with N_0 being a small integer. A few terms of the series are enough to reach a good estimation of the function [22].

The gradient of χ_i is also calculated following (3.38) and can be simplified to

$$\begin{aligned}\nabla_{\mathrm{t}}\chi_i &= \frac{\mathrm{j}^m \xi_i}{N}\sum_{l=0}^{N-1}\exp\left(\mathrm{j}l\frac{2m\pi}{N}\right)\nabla_{\mathrm{t}}\left[\exp\left(-\mathrm{j}\kappa_i\,\mathbf{T}_l\cdot\boldsymbol{\rho}\right)\right]\\ &= \frac{\mathrm{j}^m \xi_i}{N}\sum_{l=0}^{N-1}\exp\left(\mathrm{j}l\frac{2m\pi}{N}\right)\left[-\mathrm{j}\kappa_i\mathbf{T}_l\exp\left(-\mathrm{j}\kappa_i\,\mathbf{T}_l\cdot\boldsymbol{\rho}\right)\right].\end{aligned} \tag{3.39}$$

OIs on Linear Subsectional BFs

Simplified expressions for (3.28) with circular PEC boundaries are found straightforward by direct substitution of (3.38) and (3.39) into (3.28) as

$$\begin{aligned}I_{i,q}^{(n)} &= \int_0^1 t^n\,\chi_i\left(\rho(t),\varphi(t)\right)\,\mathrm{d}t =\\ &= \frac{\mathrm{j}^m \xi_i}{N}\sum_{l=0}^{N-1}\exp\left(\mathrm{j}l\frac{2m\pi}{N}\right)\int_0^1 t^n\,\exp\left[-\mathrm{j}\kappa_i\,\mathbf{T}_l\cdot\left(\mathbf{P}_q+\mathbf{L}_q t\right)\right]\,\mathrm{d}t\\ &= \frac{\mathrm{j}^m \xi_i}{N}\sum_{l=0}^{N-1}\exp\left[\mathrm{j}\left(l\frac{2m\pi}{N}-\kappa_i\mathbf{T}_l\cdot\mathbf{P}_q\right)\right]\int_0^1 t^n\,\exp\left(-\mathrm{j}\kappa_i\,\mathbf{T}_l\cdot\mathbf{L}_q t\right)\,\mathrm{d}t,\end{aligned} \tag{3.40a}$$

and

$$\begin{aligned}I_{i,q}^{\prime(n)} &= \int_0^1 t^n\,\nabla_{\mathrm{t}}\chi_i\left(\rho(t),\varphi(t)\right)\cdot\hat{\boldsymbol{\nu}}_q\,\mathrm{d}t =\\ &= \frac{-\mathrm{j}^{m+1}\xi_i\kappa_i}{N}\sum_{l=0}^{N-1}\exp\left[\mathrm{j}\left(l\frac{2m\pi}{N}-\kappa_i\mathbf{T}_l\cdot\mathbf{P}_q\right)\right]\left(\mathbf{T}_l\cdot\hat{\boldsymbol{\nu}}_q\right)\int_0^1 t^n\,\exp\left(-\mathrm{j}\kappa_i\,\mathbf{T}_l\cdot\mathbf{L}_q t\right)\,\mathrm{d}t,\end{aligned} \tag{3.40b}$$

where the path was defined by (3.22) as

$$\boldsymbol{\rho}(t) = \boldsymbol{\sigma}_q(t) = \mathbf{P}_q + \mathbf{L}_q t.$$

In summary, the solution to any of the integrals in (3.28) for the ith mode and qth side are given by

$$\left.\begin{matrix} I_{i,q}^{(n)} \\ I_{i,q}^{\prime(n)} \end{matrix}\right\} = \tag{3.41}$$
$$\frac{\mathrm{j}^m \xi_i}{N} \sum_{l=0}^{N-1} \exp\left[\mathrm{j}\left(l\frac{2m\pi}{N} - \kappa_i \mathbf{T}_l \cdot \mathbf{P}_q\right)\right] \begin{cases} \int\limits_0^1 t^n \exp\left(-j\kappa_i\,\mathbf{T}_l \cdot \mathbf{L}_q t\right)\,\mathrm{d}t \\ \left(-\mathrm{j}\kappa_i \mathbf{T}_l \cdot \hat{\boldsymbol{\nu}}_q\right) \int\limits_0^1 t^n \exp\left(-\mathrm{j}\kappa_i\,\mathbf{T}_l \cdot \mathbf{L}_q t\right)\,\mathrm{d}t \end{cases}$$

with $n = \{0, 1, 2\}$. The solutions are trivial for the remaining integrals [(A-1)].

3.5.3 Periodic Boundary

Suppose a periodic structure with a general skewed lattice of planar objects situated in the xy plane and illuminated with an arbitrary polarized plane wave propagating with

$$\mathbf{k} + k\cos\theta\hat{z} = k\sin\theta\cos\phi\,\hat{\mathbf{x}} + k\sin\theta\sin\phi\,\hat{\mathbf{y}} + k\cos\theta\hat{z}, \tag{3.42}$$

as represented in Fig. 3.6(a).

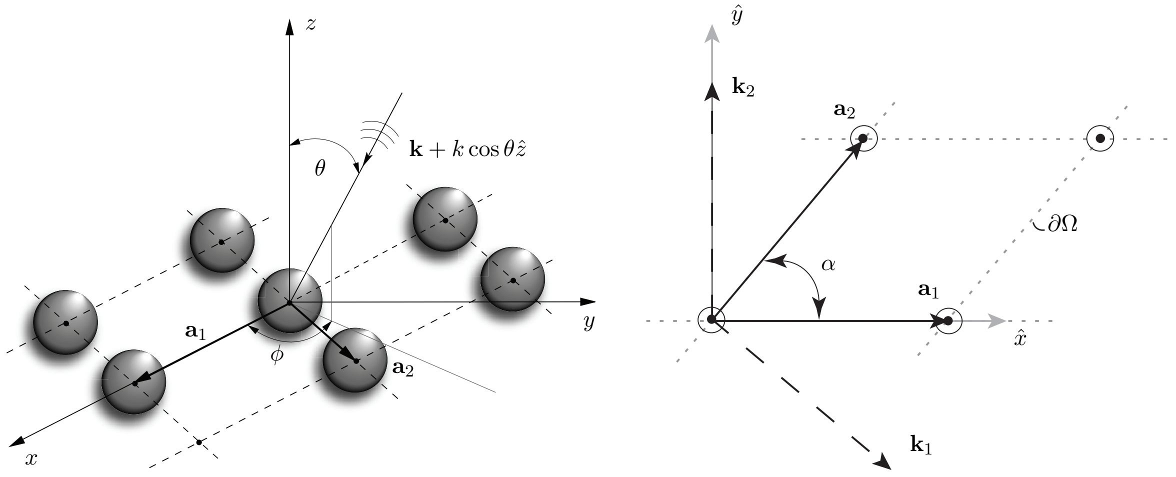

(a) A 2-D general skewed lattice illuminated by a plane wave [23].

(b) Representation of the direct $\{\mathbf{a}_i\}$ and reciprocal $\{\mathbf{k}_i\}$ lattice bases system.

Figure 3.6: General two-dimensional (2-D) skewed lattice of planar objects.

Floquet Modes for a General Skewed Lattice

The scalar potentials of the Floquet modes are eigensolutions of the 2-D Helmholtz equation

$$(\nabla_{\mathrm{t}}^2 + \kappa^2)\chi(\boldsymbol{\rho}) = 0 \tag{3.43}$$

with periodic BCs

$$\chi(\boldsymbol{\rho} + \boldsymbol{\rho}_{mn}) = \chi(\boldsymbol{\rho}) \exp(-\mathrm{j}\mathbf{k} \cdot \boldsymbol{\rho}_{mn}). \tag{3.44}$$

In the previous equation, $\rho = x\hat{\mathbf{x}} + y\hat{\mathbf{y}}$ sweeps any position on the unit cell's surface Ω and

$$\boldsymbol{\rho}_{mn} = m\mathbf{a}_1 + n\mathbf{a}_2 \tag{3.45}$$

is the translation vector in the skewed lattice.

Using separation of variables, the solution can be expressed as follows:

$$\chi_{mn} = \xi \ \exp(\mathrm{j}\boldsymbol{\kappa}_{mn} \cdot \boldsymbol{\rho}) \tag{3.46}$$

where $\xi = \frac{1}{\sqrt{\Omega}}$, $\boldsymbol{\kappa}_{mn} = \mathbf{k}_{mn} - \mathbf{k}$, and

$$\begin{aligned} \mathbf{k}_{mn} =& m\mathbf{k}_1 + n\mathbf{k}_2 = \\ =& \frac{2m\pi}{a_1}\hat{\mathbf{x}} + \left(\frac{2n\pi}{a_2 \sin\alpha} - \frac{2m\pi}{a_1 \tan\alpha}\right)\hat{\mathbf{y}}, \end{aligned} \tag{3.47}$$

is the translation vector of the reciprocal lattice. The vector bases expanding (3.45) and (3.47) are represented in Fig. 3.6(b). They satisfy the following relation of orthogonality [24]

$$\mathbf{k}_i \cdot \mathbf{a}_u = 2\pi\delta_{iu} \tag{3.48}$$

for $i, u \in \{1, 2\}$ and δ_{iu} being the Kronecker delta.

In the case of normal incidence ($\theta = 0$), the modes TEM$_x$ and TEM$_y$ replace the modes TM$_{0,0}$ and TE$_{0,0}$ in the GF, respectively. These are defined by the scalar potentials χ_s^0 that are now eigensolutions of the Laplace equation with periodic boundary conditions. Notice that, with normal incidence, the scalar potentials of the modes TE$_{0,0}$ and TM$_{0,0}$, according to Table 3.7, become constants. Hence, this would produce a zero field which means that the reflected wave, in normal direction, would not exist. Therefore, the actual formulation of this particular case is treated separately in Table 3.7 as TEM$_u$ modes.

OI on Linear Subsectional BFs

The TE/TM case is addressed first. The gradient of this scalar potential, omitting the indices m and n, can be expressed as

$$\nabla_{\mathrm{t}}\chi = \mathrm{j}\boldsymbol{\kappa}\chi. \tag{3.49}$$

[‡] Only for normal incidence ($\theta = 0$), the modes TM$_{00}$ and TE$_{00}$ become TEM$_x$ (x-polarized) and TEM$_y$ (y-polarized), respectively.

Table 3.7: Scalar potentials for skewed periodic boundaries.

$\chi_i(\boldsymbol{\rho})$ and κ_i [1/m]	
TE/TM	$\chi_{mn} = \frac{1}{\sqrt{\Omega}} \exp\left(\mathrm{j}\boldsymbol{\kappa}_{mn} \cdot \boldsymbol{\rho}\right)$
TEM$_u$ $(\theta = 0)^{\ddagger}$	$\chi_u^0 = \frac{u}{\sqrt{\Omega}} \qquad u = x, y$
with $\Omega = \lvert\mathbf{a_1} \times \mathbf{a_1}\rvert$, $\boldsymbol{\kappa}_{mn} = \mathbf{k}_{mn} - \mathbf{k}$ and $\mathbf{k}_{mn} = \frac{2m\pi}{a_1}\,\hat{\mathbf{x}} + \left(\frac{2n\pi}{a_2 \sin\alpha} - \frac{2m\pi}{a_1 \tan\alpha}\right)\hat{\mathbf{y}}$	

Then, using the variables substitution defined in (3.22)

$$\boldsymbol{\kappa}_i \cdot \boldsymbol{\sigma}_q(t) = (\boldsymbol{\kappa}_i \cdot \mathbf{P}_q) + (\boldsymbol{\kappa}_i \cdot \mathbf{L}_q)t, \tag{3.50}$$

the integrals in (3.28) are simplified into

$$I_{i,q}^{(n)} = \xi \exp\Big(\mathrm{j}\boldsymbol{\kappa}_i \cdot \mathbf{P}_q\Big) \int_0^1 t^n \exp\Big(\mathrm{j}\boldsymbol{\kappa}_i \cdot \mathbf{L}_q t\Big)\,\mathrm{d}t \tag{3.51a}$$

$$I_{i,q}^{\prime(n)} = \mathrm{j}(\boldsymbol{\kappa}_i \cdot \hat{\nu}_q) I_{i,q}^{(n)} \tag{3.51b}$$

where the remaining integrals have analytic and trivial solution [cf. (A-1)].

In the TEM case, only occurring for normal incidence, the evaluation of the OIs is simpler. It suffices to project the path into the u component (meaning x or y components). The derivative, in this case is constant. In summary,

$$\chi^0(t) = \xi(\mathbf{P}_q \cdot \hat{\mathbf{u}} + \mathbf{L}_q \cdot \hat{\mathbf{u}} t) \tag{3.52}$$

$$\nabla_{\mathrm{t}} \chi^0(t) = \xi \hat{\mathbf{u}} \tag{3.53}$$

where $\hat{\mathbf{u}} = \hat{\mathbf{x}}, \hat{\mathbf{y}}$. The solutions of (3.28) for (3.52) are straightforward:

$$I_{0,q}^{(n)} = \xi \left(\frac{\mathbf{P}_q \cdot \hat{\mathbf{u}}}{n+1} + \frac{\mathbf{L}_q \cdot \hat{\mathbf{u}}}{n+2}\right) \tag{3.54a}$$

$$I_{0,q}^{\prime(n)} = \xi \, \frac{\hat{\mathbf{u}} \cdot \hat{\boldsymbol{\nu}}_q}{n+1} \tag{3.54b}$$

for $n = 0, 1, 2$.

		general	TE	TM	TEM
Eigen -solution,-value		$\chi_i,\ \kappa_i$	$\psi_{mn},\ \kappa'_{mn}$	$\phi_{mn},\ \kappa''_{mn}$	ϕ^0_m
Propagation constant $[\mathrm{m}^{-1}]$		$\gamma_i = \alpha_i + \mathrm{j}\beta_i$	γ'_{mn}	γ''_{mn}	$k = \omega\sqrt{\mu\varepsilon}$
			$\sqrt{\kappa_i^2 - k^2} = \kappa_i\sqrt{1 - \left(\frac{\omega}{\omega_\mathrm{c}}\right)^2}$ [a]		
E,H-field $[\mathrm{m}^{-1}]$	transverse	$\mathbf{e}_i$ $\mathbf{h}_i = \hat{\mathbf{z}} \times \mathbf{e}_i$	$\mathbf{e}'_{mn} = \hat{\mathbf{z}} \times \nabla_\mathrm{t}\psi_{mn}/\kappa'_{mn}$ $\mathbf{h}'_{mn} = -\nabla_\mathrm{t}\psi_{mn}/\kappa'_{mn}$	$\mathbf{e}''_{mn} = -\nabla_\mathrm{t}\phi_{mn}/\kappa''_{mn}$ $\mathbf{h}''_{mn} = -\hat{\mathbf{z}} \times \nabla_\mathrm{t}\phi_{mn}/\kappa''_{mn}$	$\mathbf{e}^0_m = -\nabla_\mathrm{t}\phi^0_m$ $\mathbf{h}^0_m = -\hat{\mathbf{z}} \times \nabla_\mathrm{t}\phi^0_m$
	longitudinal	$\mathbf{e}_{zi},\ \mathbf{h}_{zi}$	$0,\ \frac{\kappa'_{mn}}{\gamma'_{mn}}\psi_{mn}$	$\frac{\kappa''_{mn}}{\gamma''_{mn}}\phi_{mn},\ 0$	$0,\ 0$
Modal impedance [Ω], admittance [S]		$Z_i,\ Y_i$	$Z'_{mn} = \frac{\mathrm{j}\omega\mu}{\gamma'_{mn}} = \mathrm{j}\zeta\frac{k}{\gamma'_{mn}}$	$Y''_{mn} = \frac{\mathrm{j}\omega\varepsilon}{\gamma''_{mn}} = \mathrm{j}\eta\frac{k}{\gamma''_{mn}}$	$\zeta = \eta^{-1} = \sqrt{\frac{\mu}{\varepsilon}}$

Table 3.8: Relations and expressions for modal functions.

---

[a] Cut-off condition $\kappa_i = k(\omega_\mathrm{c})$

3.6 Strategy Used for the Resolution of OIs.

In previous sections, a method for the systematic resolution of OIs has been demonstrated. This approach is applicable to a wide variety of problems built up from the combinations of a transverse boundary problem and a type of BFs. The diagram in the following page represents the backbone of the approach and intends to clarify the general strategy followed in each case.

Recall that an OI is essentially describing the projection of the pth BF with the ith mode associated to the transverse problem. Therefore we start with two parallel paths (lower part of the diagram) where proper identification and adequate operations are preformed in parallel on the pth BF and the ith mode. Then these paths converge into the common main branch of the diagram (upper part) where we can identify three common steps, in which the formulation is decomposed. The first, labeled with ①, consists of the evaluation of a set of line integrals, listed in (3.27), on every side of the integration surface ∂D_q. These integrals are calculated along the surface's contour $\partial D = \sum \partial D_q$ and the sum of each one, weighted with the side's length, provides the corresponding contour integral. This is done for every pair of subdomains $D^{\pm}$ constituting the integration surface $D = D^{+} \cup D^{-}$. The step ② is now achieved. Finally, the calculated contour integrals are used in the identities of Table 3.2 to obtain the required type of OI in step ③. Note that this three-step procedure is always performed independently of the imposed of BCs and linear subsectional BFs used. These details are actually introduced as parameters for the line integrals in ①. A BF is defined by means of a set of $k = 1, \cdots, N$ coefficients $\{A_{pq}(k), B_{pq}(k)\}$ for both types, rooftops or RWG BFs. On the other side, the formulation of *any* transverse boundary problem is reduced to the resolution of two basic line integrals (3.28), denoted as $\{I^{(n)}, I'^{(n)}\}$, on the pertinent scalar potential χ_i. In this work, as indicated in the diagram, we present analytical solutions for these integrals for three common transverse boundary problems: rectangular waveguide, circular waveguide and general periodic lattice. Nevertheless, the formulation is also applicable to any other case, whether the modes are calculated analytically (e.g. coaxial or eliptical waveguide) or numerically (e.g. waveguide with random-cross section [18]).

The organization of this approach allows a fast and easy implementation of various types of problems using the same backbone for the software. The specialization to a certain BC is thus only carried out at the bottom part of the diagram, with routines providing the corresponding basic line integrals. On the other hand, this approach allows a simple transition between RWG or rooftop BFs reducing it to the selection of appropriate constant coefficients. As a direct consequence, a simple and unified technique can be used in the treatment of problems using meshes that include rectangular and triangular cells. Finally, the rest of the process is the common branch, which is followed from bottom to top.

In addition, the reduced complexity and systematic of the final solution also allows an easy check of the numerical stability of the algorithm's formulation for all the different problem types. Moreover, the implementation errors are drastically reduced by suppressing the redundancy (i.e. common parts of the formulation) in the programming strategy.

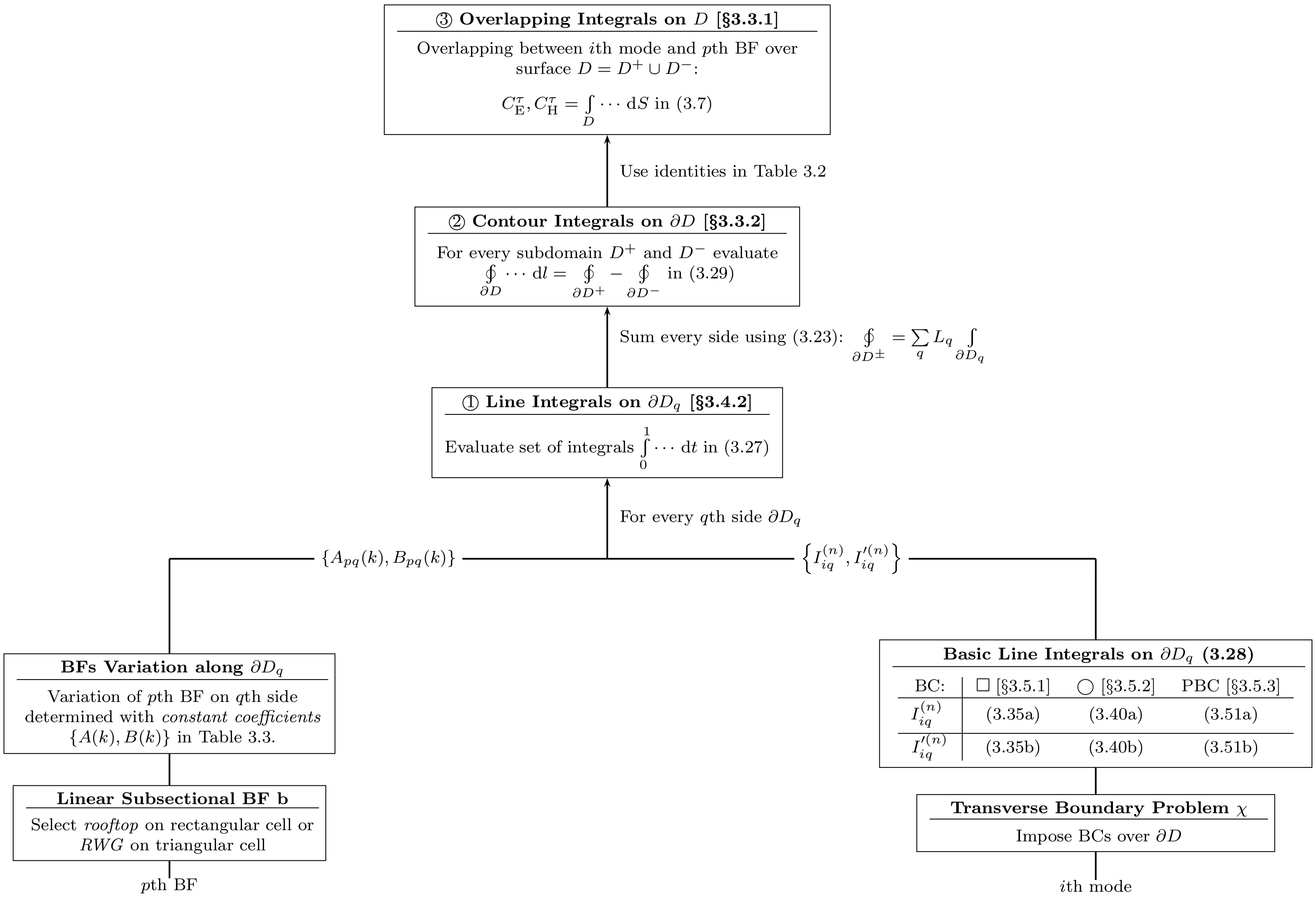
③ **Overlapping Integrals on D [§3.3.1]**
Overlapping between ith mode and pth BF over surface $D = D^+ \cup D^-$:
$C^\tau_{\mathrm{E}}, C^\tau_{\mathrm{H}} = \int_D \cdots \,\mathrm{d}S$ in (3.7)
Use identities in Table 3.2
② **Contour Integrals on ∂D [§3.3.2]**
For every subdomain D^+ and D^- evaluate
$\oint_{\partial D} \cdots \,\mathrm{d}l = \oint_{\partial D^+} - \oint_{\partial D^-}$ in (3.29)
Sum every side using (3.23): $\oint_{\partial D^\pm} = \sum_q L_q \int_{\partial D_q}$
① **Line Integrals on ∂D_q [§3.4.2]**
Evaluate set of integrals $\int_0^1 \cdots \,\mathrm{d}t$ in (3.27)
For every qth side ∂D_q
$\{A_{pq}(k), B_{pq}(k)\}$
$\left\{I^{(n)}_{iq}, I'^{(n)}_{iq}\right\}$
BFs Variation along ∂D_q
Variation of pth BF on qth side determined with *constant coefficients* $\{A(k), B(k)\}$ in Table 3.3.
Linear Subsectional BF b
Select *rooftop* on rectangular cell or *RWG* on triangular cell
pth BF
Basic Line Integrals on ∂D_q (3.28)
BC: | ☐ [§3.5.1] | ○ [§3.5.2] | PBC [§3.5.3]
$I^{(n)}_{iq}$ | (3.35a) | (3.40a) | (3.51a)
$I'^{(n)}_{iq}$ | (3.35b) | (3.40b) | (3.51b)
Transverse Boundary Problem χ
Impose BCs over ∂D
ith mode

3.7 Numerical Results

This section is devoted to the simulation of some simple structures to demonstrate the validity of the approach previously presented.

In Fig. 3.7 we show an example of a rectangular strip conductor inside three different transverse BCs, namely within a rectangular or circular PEC waveguides or as unit element of a 2D periodic lattice. The three geometries are simulated using the *same* software tool with only minor modifications in the treatment of each case. Hence, the strip surface is modeled keeping the same mesh throughout all the geometries. Two mesh schemes are considered. The equivalent electric currents are expanded with RWG or rooftops BFs [§3.4.1].

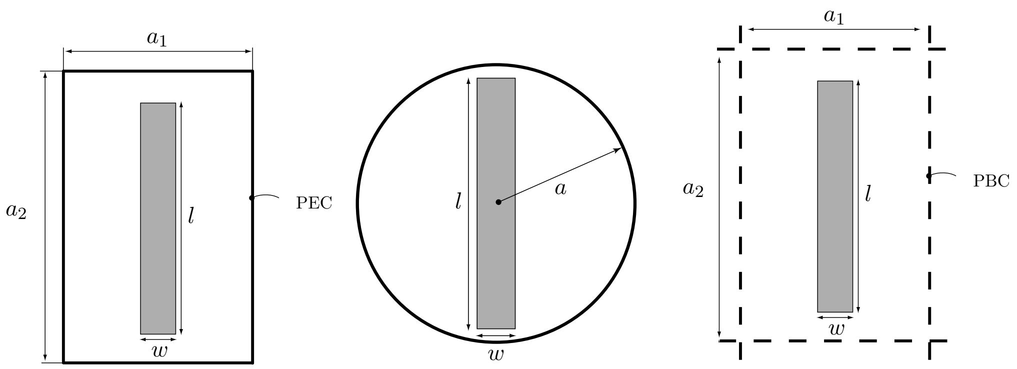

(a) Rectangular waveguide of $a_1 \times a_2 = 7.6 \times 15.2$ mm^2.

(b) Circular waveguide with radius $a = 7.0$ mm.

(c) Cell of $a_1 \times a_2 = 7.6 \times 15.2$ mm^2 in a 2-D periodic lattice with $\alpha = 90°$.

Figure 3.7: A rectangular strip conductor of $w \times l = 2.38 \times 13.3$ mm^2 of zero thickness with three different transverse boundary conditions.

The first structure, in Fig. 3.7(a), is excited with a mode TE$_{01}$ of the rectangular waveguide. The insertion and return losses, simulated with different methods, are compared in Fig. 3.8. The two first responses, shown with solid and dashed lines, correspond to this method using RWG and rooftop BFs, respectively. Another IE formulation, based on the method in [25], is also used as reference. Finally, the structure has been simulated with a MM/Generalized Transverse Resonance (GTR) by Ruiz-Cruz [26], which is specially suited for waveguide problems. The bandwidth simulated here is multimode, propagating up to 17 modes at 45 GHz. The cutoff frequency of the fundamental mode, TE$_{01}$, is 9.8 GHz and the next mode, TE$_{10}$ starts to propagate around 19.7 GHz. All four simulations show a good agreement despite the fact that the MM/GRT method is slightly shifted up in magnitude.

The scattering parameters simulated for the structure in Fig. 3.7(b), are plotted in Fig. 3.9. The response corresponds to TE$_{11}$ mode vertically polarized (y) and the monomode band spans from 12.56 to 16.41 GHz (TE$_{11}$-TM$_{01}$) as can be noticed from the abrupt change in the response.

Finally, the unit cell, delimited with dashed lines in Fig. 3.7(c), is repeated periodically (as $ma_1\hat{\mathbf{x}} + na_2\hat{\mathbf{y}}$, $m, n \in \mathbb{Z}$) in the xy-plane shaping a lattice of free standing strips. Fig. 3.10

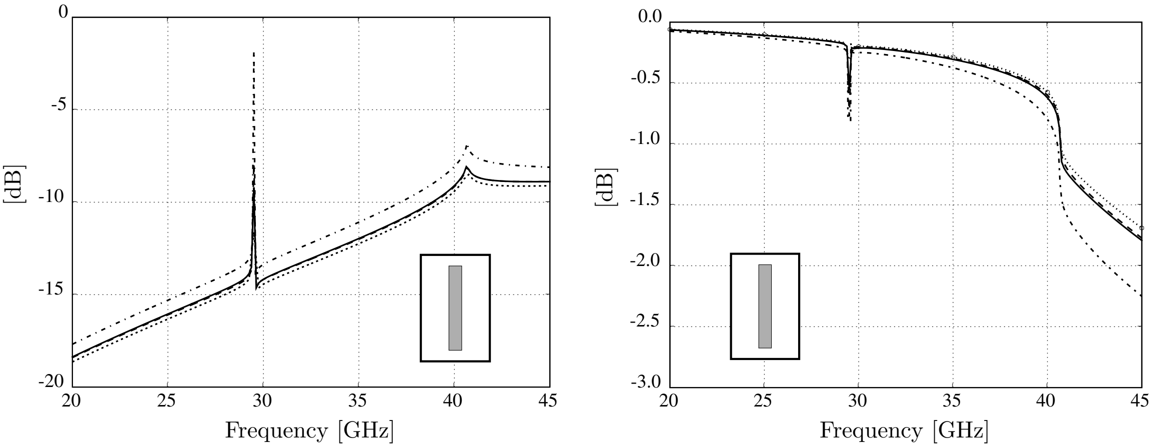

(a) Return Losses. (b) Insertion Losses.

Figure 3.8: Scattering of the TE_{01} mode from a strip inside a rectangular waveguide in Fig. 3.7(a). The presented method using only rooftops (solid line) or RWG BFs (dashed line), IE method of [25] (dotted line) and MM/GTR technique of [26] (dashed-dotted line).

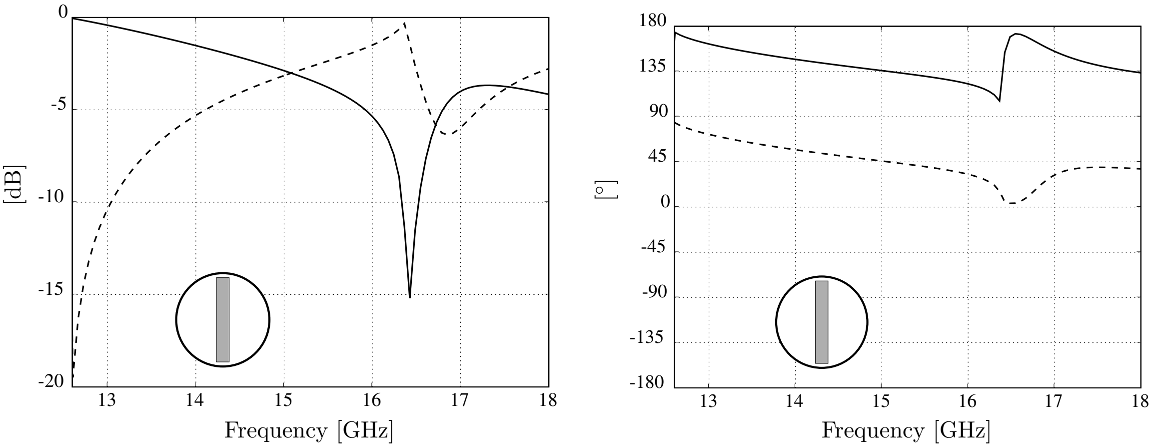

(a) Magnitude. (b) Phase.

Figure 3.9: Scattering of the TE_{11}^{y} mode (y-polarized) from a strip inside a circular waveguide as in Fig. 3.7(b). $\mathrm{S}_{11} = S_{22}$ (solid line) and $S_{21} = S_{12}$ (dashed line).

shows the reflection coefficient of a y-polarized plane wave (TE_{00}) impinging the periodic structure (strips) with angles $\theta = 1^\circ, \phi = 1^\circ$. These results are produced by simulations with two different types of BFs and compared with the results reported in [27]. Very good agreement can be observed.

Finally, Fig. 3.11 illustrates a FSS used inside a rectangular waveguide, as proposed by [28]. Here, the waveguide is analyzed entirely filled with dielectric of $\varepsilon_\mathrm{r} = 3.8$, showing good agreement with the reference results from [25].

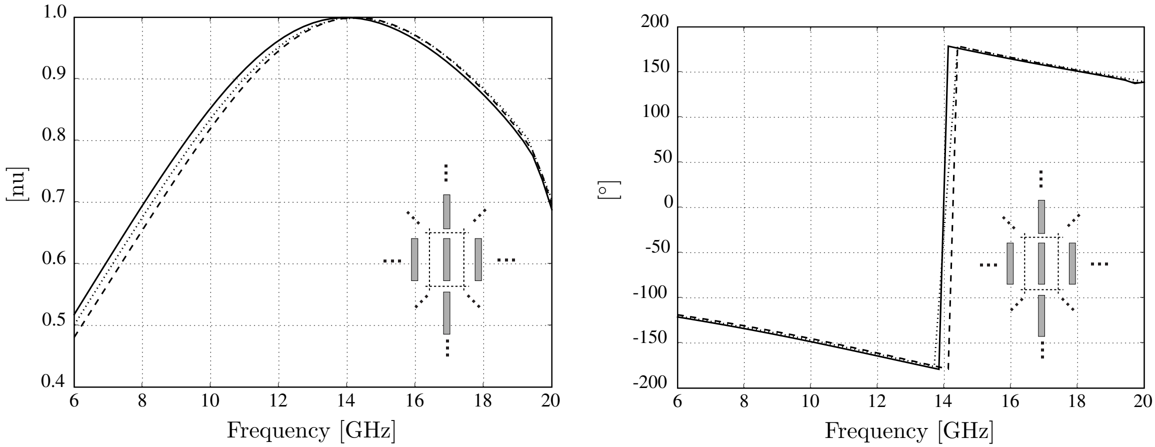

(a) Magnitude.

(b) Phase at the plane $z = 0^+$.

Figure 3.10: Reflection coefficient for a TE_{00} Floquet mode (y-polarized) impinging the periodic lattice Fig. 3.7(c) with angles $\theta = 1°, \phi = 1°$. This method using only rooftops (solid line) or RWG basis functions (dashed line) and simulations from [27] (dotted line).

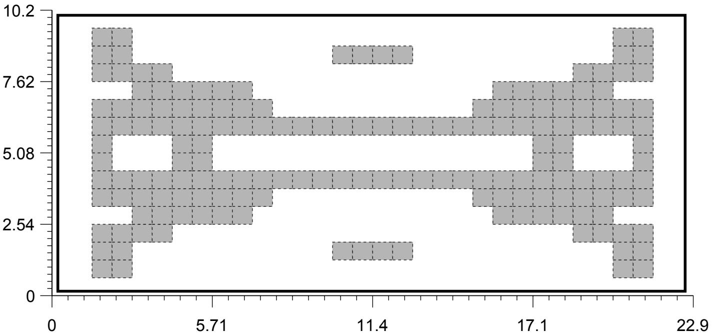

(a) FSS iris in a WR-90 waveguide [28] filled with dielectric $\varepsilon_{\mathrm{r}} = 3.8$.

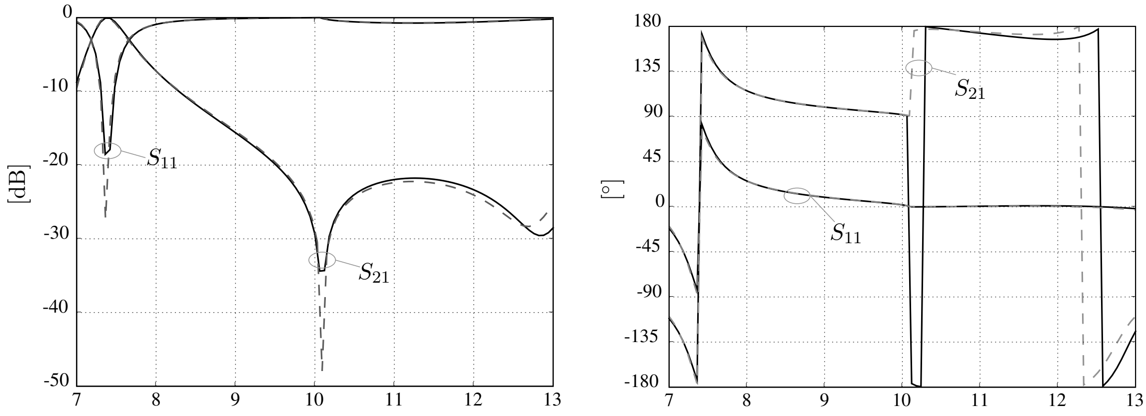

(b) Magnitude.

(c) Phase at the iris planes ($z = 0^{\pm}$).

Figure 3.11: Geometry and frequency response for the TE_{10} mode in the WR-90 waveguide (22.86×10.16 mm): this method (solid lines) and method of [25] (dashed lines).

3.8 Conclusion

This chapter presents an unified approach for the evaluation of a transverse boundary problem in the frame of an IE-MoM technique. Essential to this method is the strategy used for the resolution of OIs combining zero-curl and constant-change BFs and a modal function derived from the transverse boundary problem. The integrals are then specialized to linear subsectional BFs defined over rectangular or triangular domains with a seamless transition between the two. Finally, as an example of application, the OIs for rectangular and circular PEC boundaries as well as for periodic lattices have been derived, obtaining analytic solutions.

This technique avoids having a specific formulation for each type of problem. Moreover, it offers a unified and versatile approach that, on one hand eliminates redundancy in the formulation and on the other hand simplifies each particular problem to the evaluation of constant coefficients or basic line integrals.

The approach has been applied to the EM simulation of a variety of circuits ranging from rectangular or circular waveguides with PEC walls to periodic structures with general skewed lattices. The numerical results obtained using the presented technique have been compared to the results found in literature and obtained using different solvers. The full usefulness of the presented approach is evident since not only the agreement with the reference results is excellent, but our technique is equally valid for different boundary conditions. The reference results, however, are obtained using techniques specialized to a given BC at a time. Moreover, this approach is equally valid and easily extended to other lateral bounds whose modal vector functions are analytically (or numerically) known.

Appendices

Analytic Solution for Some Basic Integrals

Let us define the constants $a \in \mathbb{C}$, $m, c \in \mathbb{R}$ and $n \in \mathbb{N}$. The analytical solution of the basic integrals presented throughout this chapter are the following:

$$\mathcal{I}(a,n) = \int\limits_0^1 t^n \exp(at)\,\mathrm{d}t =$$

$$= \begin{cases} \frac{1}{a^{n+1}}\left[\exp(a)\left(a^n - na^{n-1} + n(n-1)a^{n-2} - \cdots + (-1)^n n!\right) - (-1)^n n!\right], & \text{for } a \neq 0; \\ \frac{1}{n+1} + a\frac{1}{n+2} + \frac{a^2}{2}\frac{1}{n+3} + \cdots, & \text{for } |a| \to 0; \\ \frac{1}{n+1}, & \text{for } a = 0. \end{cases} \tag{A-1}$$

$$\int\limits_0^1 t^n \exp\big(\mathrm{j}(c+mt)\big)\,\mathrm{d}t = \exp(\mathrm{j}c)\,\mathcal{I}(\mathrm{j}m, n), \tag{A-2a}$$

$$\int\limits_0^1 t^n \sin(c+mt)\,\mathrm{d}t = \mathrm{Im}\int\limits_0^1 t^n \exp\big(\mathrm{j}(c+mt)\big)\,\mathrm{d}t, \tag{A-2b}$$

$$\int\limits_0^1 t^n \cos(c+mt)\,\mathrm{d}t = \mathrm{Re}\int\limits_0^1 t^n \exp\big(\mathrm{j}(c+mt)\big)\,\mathrm{d}t. \tag{A-2c}$$

Explicit solutions are given for the integrals (A-2b) and (A-2c) for the case $n = 0$:

$$\int\limits_0^1 \sin(c+mt)\,\mathrm{d}t = \begin{cases} [\cos(c) - \cos(c+m)]/m, & \text{for } m \neq 0; \\ \sin(c), & \text{for } m = 0; \end{cases} \tag{A-3a}$$

$$= \begin{cases} \left[2\cos(c)\sin^2(m/2) + \sin(c)\sin(m)\right]/m, & \text{for } m \neq 0; \\ m\cos(c)/2 + \sin(c), & \text{for } m \to 0; \end{cases} \tag{A-3b}$$

$$\int\limits_0^1 \cos(c+mt)\,\mathrm{d}t = \int\limits_0^1 \sin(c + \frac{\pi}{2} + mt)\,\mathrm{d}t \tag{A-4}$$

and $n = 1$:

$$\int\limits_0^1 t\sin(c+mt)\,\mathrm{d}t = \int\limits_0^1 t\cos(c - \frac{\pi}{2} + mt)\,\mathrm{d}t \tag{A-5}$$

$$\int_0^1 t\cos(c+mt)\,\mathrm{d}t = \begin{cases} \left[\cos(c+m)-\cos(c)\right]/m^2 + \sin(c+m)/m, & \text{for } m \neq 0; \\ \cos(c)/2 & \text{for } m = 0; \end{cases} \tag{A-6a}$$

$$= \begin{cases} \sin(c+m)/m - \left[2\cos(c)\sin^2(m/2) + \sin(c)\sin(m)\right]/m^2, & \text{for } m \neq 0; \\ \cos(c)/2 - m\sin(c)/2, & \text{for } m \to 0; \end{cases} \tag{A-6b}$$

The case “b” in the solution of (A-3) and (A-6) offers a formulation with a stable behavior when m tends to zero. In the first case ($m \neq 0$), has been reformulated to avoid the difference operation and the solution for $m = 0$ has been replaced for an expression valid in the proximity of zero in order to provide a smooth transition.

The problem arising in the difference operation is made evident in the example represented in Fig. A.1. The roundoff error committed in the subtraction of the two functions is amplified with the division by a small number [29, §1.14]. In Fig. A.1 we represent the evaluation of the solution for (A-3) using (A-3a) and (A-3b) denoted with f and $\hat{f}$, respectively. For values of $m > 10^{-5}$, both formulations agree in more than ten significant digits but degenerates drastically as $m \to 0$.

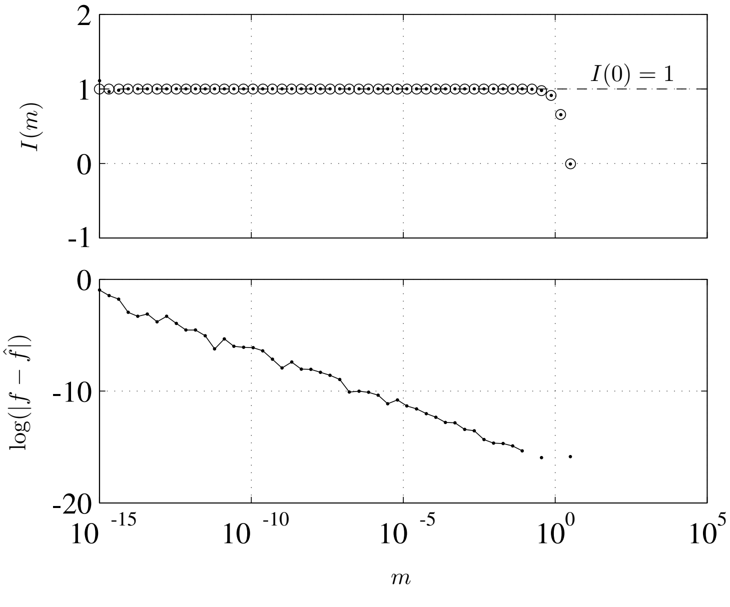

Figure A.1: Evaluation $I(m) = \int_0^1 \sin(\pi/2 + mt)\,\mathrm{d}t$ for small values of m, using the expression given in (A-3a) (denoted with f and plotted with • symbol) and the formula (A-3b) (denoted with $\hat{f}$ and represented with ∘). The difference between them is also plotted below.

References

[1] J. Schwinger and D. S. Saxon, *Discontinuities in Waveguides*, ser. Documents on Modern Physics. New York: Gordon and Breach Science Publishers, 1945.

[2] M. Mattes, "Contribution to the electromagnetic modelling and simulation of waveguide networks using integral equations and adaptive sampling," Ph.D. dissertation, Ecole Polytecnique Fédéral de Lausanne, Lausanne, 2003, thèse No 2693. [Online]. Available: http://library.epfl.ch/theses/?nr=2693

[3] J. C. Rautio and R. F. Harrington, "An electromagnetic time-harmonic analysis of shielded microstrip circuits," *IEEE Trans. Microwave Theory Tech.*, vol. 35, no. 8, pp. 726–730, Aug 1987.

[4] G. V. Eleftheriades, J. R. Mosig, and M. Guglielmi, "A fast integral equation technique for shielded planar circuits defined on nonuniform meshes," *IEEE Trans. Microwave Theory Tech.*, vol. 44, pp. 2293–2296, Dec. 1996.

[5] A. Álvarez-Melcón, "Applications of the Integral Equation Technique to the Analysis and Synthesis of Multilayered Printed Shielded Microwave Circuits and Cavity Backed Antennas," Ph.D. dissertation, Ecole Polytecnique Fédéral de Lausanne, 1998, thése No 1901 (1998).

[6] C.-C. Chen, "Transmission through a conducting screen perforated periodically with apertures," *IEEE Trans. Microwave Theory Tech.*, vol. MTT-18, no. 9, pp. 627–632, Sept. 1970.

[7] D. Pozar and D. Schaubert, "Analysis of an infinite array of rectangular microstrip patches with idealized probe feeds," *IEEE Trans. Antennas Propagat.*, vol. 32, no. 10, pp. 1101–1107, Oct 1984.

[8] I. Stevanović, P. Crespo-Valero, K. Blagović, F. Bongard, and J. R. Mosig, "Integral-equation analysis of 3-D metallic objects arranged in 2-D lattices using the Ewald transformation," *IEEE Trans. Microwave Theory Tech.*, vol. 54, no. 10, pp. 3688 – 3697, Oct. 2006.

[9] V. H. Rumsey, "Reaction concept in electromagnetic theory," *Phys. Rev.*, vol. 94, pp. 1483–1491, June 1954.

[10] A. Álvarez Melcón, J. R. Mosig, and M. Guglielmi, "Efficient CAD of boxed microwave circuits based on arbitrary rectangular elements," *IEEE Trans. Microwave Theory Tech.*, vol. 47, no. 7, pp. 1045–1058, July 1999.

[11] M. Bozzi and L. Perregrini, "Analysis of multilayered printed frequency selective surfaces by the MoM/BI-RME method," *IEEE Trans. Antennas Propagat.*, vol. 51, no. 10, pp. 2830–2836, Oct. 2003.

[12] M. Bozzi, L. Perregrini, A. Álvarez Melcón, M. Guglielmi, and G. Conciauro, "MoM/BI-RME analysis of boxed MMICs with arbitrarily shaped metallizations," *IEEE Trans. Microwave Theory Tech.*, vol. 49, no. 12, pp. 2227–2234, Dec. 2001.

[13] G. Figlia and G. Gentili, "On the line-integral formulation of mode-matching technique," *IEEE Trans. Microwave Theory Tech.*, vol. 50, no. 2, pp. 578–580, Feb. 2002.

[14] A. Glisson and D. Wilton, "Simple and efficient numerical methods for problems of electromagnetic radiation and scattering from surfaces," *IEEE Trans. Antennas Propagat.*, vol. 28, no. 5, pp. 593–603, Sep. 1980.

[15] S. Rao, D. Wilton, and A. Glisson, "Electromagnetic scattering by surfaces of arbitrary shape," *IEEE Trans. Antennas Propagat.*, vol. 30, pp. 409–418, May 1982.

[16] L. Knockaert, J. Sercu, and D. de Zutter, "Generalized Poisson-Neumann polygonal basis functions for the electromagnetic simulation of complex planar structures," *IEEE Trans. Microwave Theory Tech.*, vol. 52, pp. 954–961, Mar. 2004.

[17] A. F. Peterson, S. L. Ray, and R. Mittra, *Computational Methods for Electromagnetics.* New York: IEEE Press, 1998.

[18] C. Kim, S. Yu, R. Harrington, J. Ra, and S. Lee, "Computation of waveguide modes for waveguides of arbitrary cross-section," in *Microwaves, Antennas and Propagation, IEE Proceedings H*, vol. 137, no. 2, Apr 1990, pp. 145–149.

[19] G. Conciauro, M. Bressan, and C. Zuffada, "Waveguide modes via an integral equation leading to a linear matrix eigenvalue problem," *IEEE Trans. Microwave Theory Tech.*, vol. 32, no. 11, pp. 1495–1504, Nov 1984.

[20] ——, "Waveguide modes via an integral equation leading to a linear matrix eigenvalue problem (correction)," *IEEE Trans. Microwave Theory Tech.*, vol. 33, no. 9, pp. 839–839, Sep 1985.

[21] N. Marcuvitz, *Waveguide Handbook*, ser. Radiation Laboratory. New York: McGraw Hill, 1941.

[22] R. H. MacPhie and K.-L. Wu, "Scattering at the junction of a rectangular waveguide and a larger circular waveguide," *IEEE Trans. Microwave Theory Tech.*, vol. 9, pp. 2041–2045, Sept. 1995.

[23] I. Stevanović, P. Crespo-Valero, K. Blagović, F. Bongard, and J. R. Mosig, "Integral-equation analysis of 3-D metallic objects arranged in 2-D lattices using the Ewald transformation," *IEEE Trans. Microwave Theory Tech.*, vol. 54, no. 10, pp. 3688 – 3697, Oct. 2006.

[24] L. Brillouin, *Wave Progapation in Periodic Structures.* Dover Publications Inc., 1953, ch. VI, pp. 94–130.

[25] I. Stevanović, P. Crespo-Valero, and J. R. Mosig, "An integral-equation technique for solving thick irises in rectangular waveguides," *IEEE Trans. Microwave Theory Tech.*, vol. 54, no. 1, pp. 189–197, Jan. 2006.

[26] J. A. Ruiz-Cruz, "Contribution to the CAD of Microwave-Millimeter Wave Passive Devices by Mode-Matching Techniques," Ph.D. dissertation, Universidad Politécnica de Madrid, 2005.

[27] C. H. Chan and R. Mittra, "On the analysis of frequency-selective surfaces using subdomain basis functions," *IEEE Trans. Antennas Propagat.*, vol. 38, no. 1, pp. 40–50, Jan. 1990.

[28] M. Ohira, H. Deguchi, M. Tsuji, and H. Shigesawa, "Novel waveguide filters with multiple attenuation poles using dual-behavior resonance of frequency-selective surfaces," *IEEE Trans. Microwave Theory Tech.*, vol. 53, no. 11, pp. 3320–3326, Nov. 2005.

[29] N. J. Higham, *Accuracy and Stability of Numerical Algorithms*, 2nd ed. Society for Industrial and Applied Mathematics, 2002.

4 Layered Media

4.1 Introduction

The previous chapter developed a formulation for a general transverse boundary problem considering a homogeneous medium. In this chapter we extend and complete this formulation for printed circuits in bounded *layered* media.

As shown in Chapter 2, solving bounded layered media implies the resolution of an equivalent transmission line model (TLMo), where the source becomes a lumped generator and every layer corresponds to a transmission line (TL) section. Consider a general bounded layered medium consisting of N dielectric layers as shown in Fig. 4.1. For every mode arising in the transverse boundary problem, the equivalent TLMo is obtained by substituting each dielectric with a TL section of the same height. The propagation constant γ [1/m] and the characteristic impedance Z [Ω] of every TL section is determined according to the dielectric constants $\{\varepsilon, \mu\}$, the frequency $\omega/(2\pi)$ and the mode cutoff wavenumber κ [1/m] (also denoted as spectral variable). A procedure to find a solution to this circuit problem can be easily derived from the circuit theory.

Although this problem has been addressed by several authors in the past [1–3], we will show that none of these techniques happened to be stable for every mode and in every possible condition (propagating, evanescent, lossy, exactly at cutoff, etc.) Moreover, these classical formulations give rise to lengthy expressions that hide the physical insight and darken further analytical developments. The numerical routines based on these formulations become programmer-time intensive since they are error prone and difficult to implement [3].

In this chapter, we present a stable and efficient TLMo that obviates all the problems detected in approaches so far known by the author. The chapter starts by introducing the notation and foundations needed to derive the TLMo formulation. Then we present alternate equivalent expressions of the TLMo that allow new interpretations of the problem and give different physical insights. Through the stability study of the existing TLMo algorithms, we describe some critical conditions and propose techniques to avoid unstable results in these cases. This knowledge is used as basis to define a new stable and efficient TLMo algorithm. The new formulation allows exploring some interesting phenomena like the resonances appearing in dielectric-filled cavities. Finally, the efficiency of the proposed technique is verified by the simulation of a realistic multilayer filter.

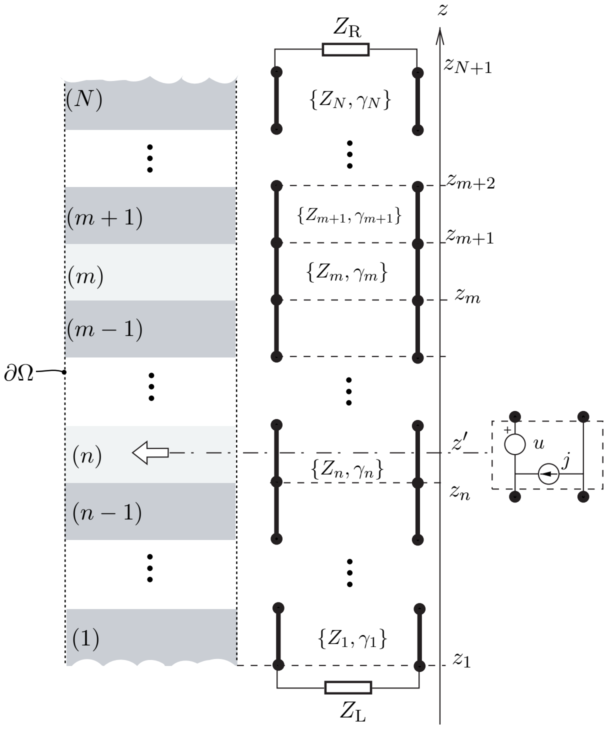

Figure 4.1: Source radiating in a bounded layered medium and the equivalent circuit for each mode.

4.2 Transmission Line Model

In the following section we will address the formulation of a TLMo as represented on the right hand side of Fig. 4.1. The foundations and the notation of the following developments are based in previous works from Michalski [2] and Llorens [4, §2.4].

4.2.1 Formulation

In order to solve the equivalent circuit in Fig. 4.1 we will first tackle the formulation of a *single* transmission line (TL). In Fig. 4.2 we have represented a TL described, from the electrical point of view, by its characteristic impedance Z and propagation constant γ. Recalling §2.4, the voltage V and current I of a wave at any point z of the TL follows the Telegraphers equations:

$$\frac{\mathrm{d}V}{\mathrm{d}z} = -Z\gamma I \tag{4.1a}$$

$$\frac{\mathrm{d}I}{\mathrm{d}z} = -\frac{\gamma}{Z}V. \tag{4.1b}$$

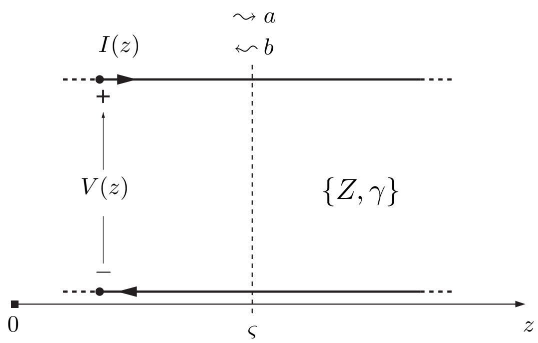

Figure 4.2: Voltage and current along a transmission line.

Any linear combination of exponential functions $\{e^{\pm\gamma z}\}$ is solution of the homogeneous equations (4.1). Thus, the voltage and the current in a TL can be written as a superposition of *traveling waves*:

$$V(z) = a\,e^{-\gamma(z-\varsigma)} + b\,e^{+\gamma(z-\varsigma)} \tag{4.2a}$$

$$ZI(z) = a\,e^{-\gamma(z-\varsigma)} - b\,e^{+\gamma(z-\varsigma)}, \tag{4.2b}$$

where a, b are constants (with respect to the variable z) representing the complex amplitudes, measured at $z = \varsigma$, of waves traveling along positive and negative z-axis, respectively. Analogously, the wave in the TL can also be expressed in terms of *standing waves* since hyperbolic functions can be found as linear combinations of exponentials. The equivalent standing wave representation is expressed as follows:

$$V(z) = A\cosh\gamma(z-\varsigma) - B\sinh\gamma(z-\varsigma) \tag{4.3a}$$

$$ZI(z) = A\cosh\gamma(z-\varsigma) + B\sinh\gamma(z-\varsigma) \tag{4.3b}$$

where $A = a + b$ and $B = a - b$.

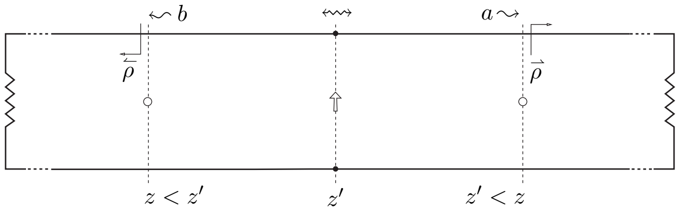

Figure 4.3: Interaction between source (vertical arrow) and observer (circle) points in a loaded TL.

These expressions are used as starting point for the resolution of the equivalent inhomogeneous problem [cf. (2.15)] that considers lumped generators (sources) at a given point on the TL. This situation is illustrated in Fig. 4.3. A vertical arrow at z' represents a source point where a given generator is connected. It excites the waves in the TL that propagate in both directions reaching two observers, situated above ($z' < z$) and below ($z < z'$) the source, with amplitude a and b, respectively. The voltage and current induced at the observer points must satisfy (4.1) and therefore can be expressed as in (4.2). In particular, when $z' < z$ they can be written as

$$\begin{aligned} V(z) &= a\,(1+\overrightarrow{\rho}\,) && (4.4a) \\ ZI(z) &= a\,(1-\overrightarrow{\rho}\,) && (4.4b) \end{aligned}$$

and if $z' < z$, as

$$\begin{aligned} V(z) &= b\,(1+\overleftarrow{\rho}\,) && (4.5a) \\ -ZI(z) &= b\,(1-\overleftarrow{\rho}\,)\,, && (4.5b) \end{aligned}$$

where $\overleftarrow{\rho}, \overrightarrow{\rho}$ are the reflection coefficients (ratio between reflected and incident waves) seen at the left and the right of the observers represented in Fig. 4.3, respectively. Notice that the exponential functions do not appear in (4.4) or (4.5) since the amplitudes are measured at the observer positions (i.e. $\varsigma = z$, such that $\gamma(z-\varsigma) = 0$). Moreover, the negative sign in the last equation was introduced in order to keep the orientation of the current along the z positive axis.

These equations, can be written in a compact fashion to deal simultaneously with the voltage and current as

$$\begin{aligned} P(z) &= s\,a\,(1+\sigma\overrightarrow{\rho}\,)\,, \quad z' < z && (4.6a) \\ P(z) &= s\,b\,(1+\sigma\overleftarrow{\rho}\,)\,, \quad z < z' && (4.6b) \end{aligned}$$

with $P = \{V, I\}$ and

$$\sigma = \begin{cases} +1, & P = V \\ -1, & P = I \end{cases} \qquad s = \begin{cases} 1, & P = V \\ \pm 1/Z, & P = I \text{ (if } z \gtrless z') \end{cases}\,, \tag{4.7}$$

where the positive (negative) sign applies if $z > z'$ ($z < z'$).

We can observe from (4.6) that any change in the position of the source point will only affect the wave amplitudes, since the reflection coefficients depend on the impedance seen by the observers. Therefore, the wave solution for the inhomogeneous problem $P(z, z')$ will be like (4.6) where $a \equiv a(z')$ and $b \equiv b(z')$.

Fig. 4.4 represents the waves in the vicinity of the source, showing the *discontinuity* produced between forward and backward waves at z'. Analogously to (4.7), introducing the following variables

$$\sigma' = \begin{cases} +1, & P' = V \\ -1, & P' = I \end{cases} \qquad s' = \frac{1}{2}\begin{cases} u, & P' = V \\ Z'j, & P' = I \end{cases} \tag{4.8}$$

for the source, generalizes the formulation for both the voltage and current generators as shown in Fig. 4.4(c). Finally, using the reflection coefficients $\overleftarrow{\rho}', \overrightarrow{\rho}'$ seen around the source, it

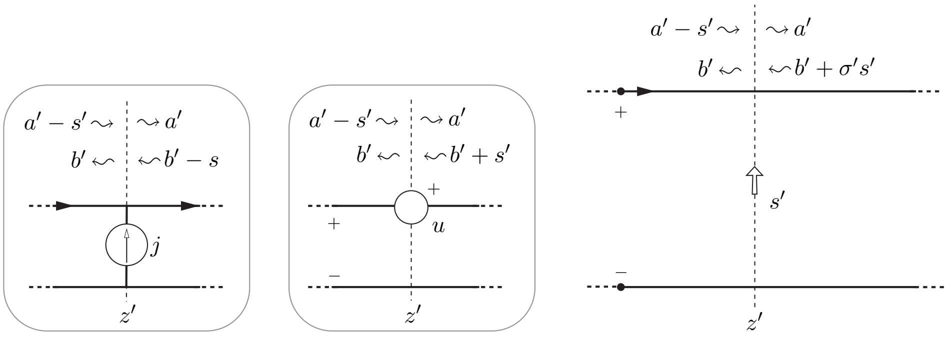

(a) (b) (c)

Figure 4.4: Representation of P'-type excitations: (a) parallel current ($P' = I$); (b) series voltage generator ($P' = V$) and (c) symbolic representation of a source in a TL. These relations are demonstrated in Appendix.

is proved in Appendix that the waves generated at z' give

$$a' = s' \frac{1 - \sigma' \overleftarrow{\rho}'}{1 - \overleftarrow{\rho}' \overrightarrow{\rho}'} \qquad\qquad b' = -s' \frac{\sigma' - \overrightarrow{\rho}'}{1 - \overleftarrow{\rho}' \overrightarrow{\rho}'}. \tag{4.9}$$

Now, the wave reaching any observer point within the TL can be obtained propagating a', b' as

$$a = a' \mathrm{e}^{-\gamma(z - z')} \qquad\qquad b = b' \mathrm{e}^{-\gamma(z' - z)} \tag{4.10}$$

provided that (4.2) applies.

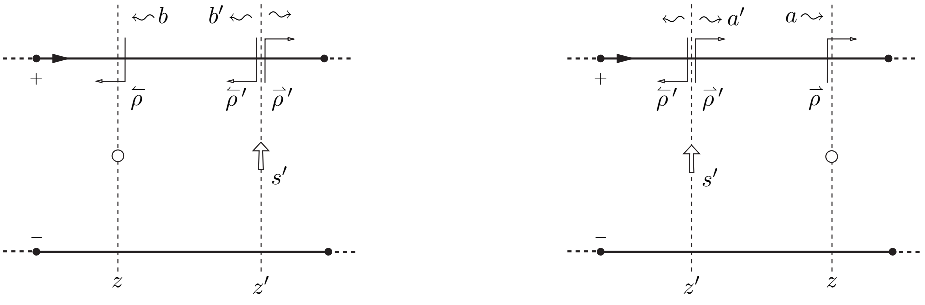

(a) $z < z'$. (b) $z' < z$.

Figure 4.5: Source and observer within the same layer.

Finally, substituting (4.9) into (4.10) and using the resulting expression into (4.6), a closed form for the solution of the inhomogeneous equation in a TL section is given as follows

$$P^{P'}(z,z') = +ss'\frac{1-\sigma'\overleftarrow{\rho}'}{1-\overleftarrow{\rho}'\overrightarrow{\rho}'}\,\mathrm{e}^{-\gamma(z-z')}\left(1+\sigma\overrightarrow{\rho}\right), \qquad z'<z \tag{4.11a}$$

$$P^{P'}(z,z') = -ss'\frac{\sigma'-\overrightarrow{\rho}'}{1-\overleftarrow{\rho}'\overrightarrow{\rho}'}\,\mathrm{e}^{-\gamma(z'-z)}\left(1+\sigma\overleftarrow{\rho}\right), \qquad z<z'. \tag{4.11b}$$

The cases considered in the above equation are depicted in Fig. 4.5.

4.2.2 Intra-layer Interaction

The last section provided us with a solution when a source and an observer are inside a loaded TL [cf. Fig. 4.3]. Consider now a TL *section* corresponding to one layer of a multilayered medium situated between ς_0 and ς_1. Let both source position z' and observer position z, be within this layer $z, z' \in [\varsigma_0\, \varsigma_1]$, as represented in Fig. 4.6. The TL, of characteristic parameters $\{\gamma, Z\}$, is now loaded at both ends with the rest of the structure. This is measured in terms of a reflection coefficient $\{\overleftarrow{\Gamma}, \overrightarrow{\Gamma}\}$ for the upper and lower interfaces, respectively. It is easily demonstrated that these coefficients can also be obtained at any point z of the TL as

$$\overleftarrow{\rho} = \overleftarrow{\Gamma}\mathrm{e}^{-2\gamma(z-\varsigma_0)} \qquad\qquad \overrightarrow{\rho} = \overrightarrow{\Gamma}\mathrm{e}^{-2\gamma(\varsigma_1-z)} \tag{4.12}$$

and that its product remains constant all along the TL:

$$\overleftarrow{\rho}'\overrightarrow{\rho}' = \overleftarrow{\Gamma}\,\overrightarrow{\Gamma}t = 1-D, \tag{4.13}$$

where $t = \mathrm{e}^{-2\gamma h}$ and D a complex constant.

Equation (4.11) can now be written in terms of the parameters of Fig. 4.6 using the relations in (4.12) and (4.13) to provide a solution for the intra-layer interaction. This solution can be written as follows

$$P^{P'}(z,z') = \frac{ss'}{D}\mathrm{e}^{-\gamma|z-z'|}\begin{cases} +\left(1-\sigma'\overleftarrow{\Gamma}\mathrm{e}^{-2\gamma(z'-\varsigma_0)}\right)\left(1+\sigma\overrightarrow{\Gamma}\mathrm{e}^{-2\gamma(\varsigma_1-z)}\right), & z'<z \\ -\left(1+\sigma\overleftarrow{\Gamma}\mathrm{e}^{-2\gamma(z-\varsigma_0)}\right)\left(\sigma'-\overrightarrow{\Gamma}\mathrm{e}^{-2\gamma(\varsigma_1-z')}\right), & z<z' \end{cases} \tag{4.14}$$

where $P, P' = \{V, I\}$ denote all the observer and source combinations that interact within a TL-section defined by the characteristic parameters $\{\gamma, Z\}$ and with the BCs $\{\overleftarrow{\Gamma}, \overrightarrow{\Gamma}\}$.

4.2.3 Inter-layer Interaction

The formulation will be now extended to a situation in which the source and observer are placed in different layers. The difference with respect to the previous case lies in the transmission of the wave between the two points. Here, the wave must be propagated through different layers taking into account the interfaces between adjacent TL sections.

Consider the source and observer placed in two separate layers, say $\{i'\}$ and $\{i\}$, within a multilayered media (see Fig. 4.7). Let a' denote the wave amplitude generated at the

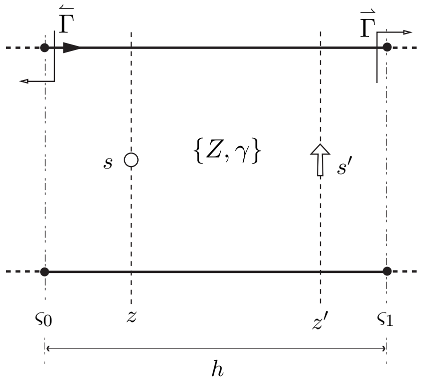

Figure 4.6: TL section with source and observer interaction in the same layer $z, z' \in [\varsigma_0\, \varsigma_1]$.

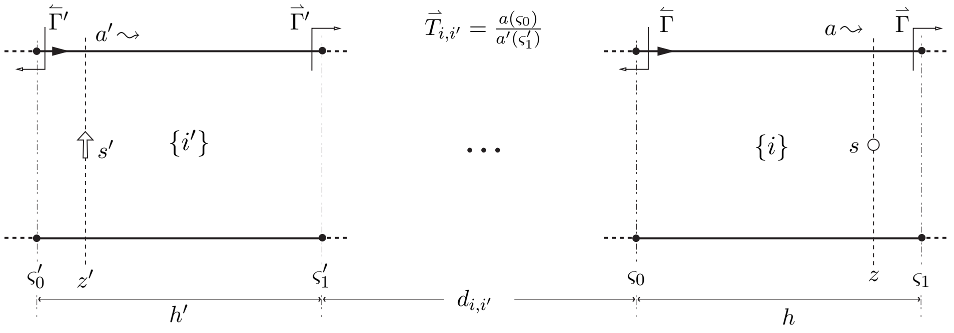

Figure 4.7: Source and observer in different sections of a layered media.

source point and a the amplitude after reaching the observer. Therefore, the transmission is formulated as

$$a' \mathrm{e}^{-\gamma'(\varsigma_1' - z')}\, \overrightarrow{T}_{i',i}\, \mathrm{e}^{-\gamma(z-\varsigma_0)} = a, \qquad i' < i \tag{4.15a}$$

and analogously in the complementary case (i.e. if $z < z'$)

$$b = \mathrm{e}^{-\gamma(\varsigma_1 - z)}\, \overleftarrow{T}_{i,i'}\, \mathrm{e}^{-\gamma'(z'-\varsigma_0')}\, b', \qquad i < i', \tag{4.15b}$$

where (4.10) is used in the transmission through the lines and $\overrightarrow{T}_{i',i}$, $\overleftarrow{T}_{i,i'}$ specify the transfer functions between the interfaces of the sections $\{i'\}$ and $\{i\}$ and viceversa, respectively. Expressions for $\overrightarrow{T}_{i',i}$, $\overleftarrow{T}_{i,i'}$ are derived in Appendix by imposing continuity of the voltage and current through the interface. These are given by

$$\overrightarrow{T}_{i',i} = \overrightarrow{\tau}_i \prod_{k=i'+1}^{i-1} \overrightarrow{\tau}_k \theta_k \qquad\qquad \overleftarrow{T}_{i,i'} = \overleftarrow{\tau}_{i'} \prod_{k=i+1}^{i'-1} \overleftarrow{\tau}_k \theta_k, \tag{4.16}$$

where $\overrightarrow{\tau}_j$ ($\overleftarrow{\tau}_j$), as defined in (A-7a), account for the discontinuity in the upper (lower) interface of the jth section and $\theta = \exp(-\gamma h)$. Hence, the inter-layer interaction can be readily formulated by analogy with (4.14), giving

$$P^{P'}(z,z') = \frac{ss'}{D'} \times \begin{cases} +\left(1-\sigma'\overleftarrow{\Gamma}'\mathrm{e}^{-2\gamma'(z'-\varsigma_0')}\right)\,\mathrm{e}^{-\gamma(\varsigma_1'-z')}\,\overrightarrow{T}_{i',i}\,\mathrm{e}^{-\gamma(z-\varsigma_0)}\left(1+\sigma\overrightarrow{\Gamma}\mathrm{e}^{-2\gamma(\varsigma_1-z)}\right), & i'<i \\ -\left(1+\sigma\overleftarrow{\Gamma}\mathrm{e}^{-2\gamma(z-\varsigma_0)}\right)\,\mathrm{e}^{-\gamma(\varsigma_1-z)}\,\overleftarrow{T}_{i,i'}\,\mathrm{e}^{-\gamma(z'-\varsigma_0')}\left(\sigma'-\overrightarrow{\Gamma}'\mathrm{e}^{-2\gamma'(\varsigma_1'-z')}\right), & i<i'. \end{cases} \tag{4.17}$$

Prior to the application of these equations, the reflection $\{\overleftarrow{\Gamma},\overrightarrow{\Gamma}\}$ and the transition $\overleftarrow{\tau},\overrightarrow{\tau}$ coefficients at the interfaces can be calculated using an iterative algorithm detailed in the Appendix.

4.3 Alternate Expressions for the TLMo

In the previous section, we have derived the inhomogeneous solution using a traveling wave formulation. This, however is not the only possibility. For example, in the homogeneous solution we have shown two different approaches: one in terms of traveling waves (4.2), and other with standing waves (4.3). In occasions, hybrid expressions are preferred but it is not always easy to explore all the possibilities.

Hence, we have investigated two different formulations for (4.14) and (4.17). The first leads us to a bilinear form that separates the dependence in z and z'. This can be useful, for example, in the integration of z-dependent sources as introduced by Llorens del Río in [4, §2.5]. It also puts in evidence how to combine different expressions by means of linear transformations of the bilinear bases. The second formulation explores a decomposition into a multiple reflection series, which is essentially more useful in acceleration techniques.

4.3.1 Bilinear Form

We have previously shown that the inhomogeneous solution can be written as

$$P^{P'}(z,z') = a(z')\,\mathrm{e}^{-\gamma z} + b(z')\,\mathrm{e}^{+\gamma z}. \tag{4.18}$$

It can be demonstrated, by virtue of the reciprocity principle, that the z-constants a, b have the same dependency with respect to z', meaning that [5, §6.4]

$$a(z') = \xi_1\mathrm{e}^{-\gamma z'} + \xi_2\mathrm{e}^{+\gamma z'} \qquad b(z') = \xi_3\mathrm{e}^{-\gamma z'} + \xi_4\mathrm{e}^{+\gamma z'}. \tag{4.19}$$

Substituting these expressions into (4.18), $P^{P'}(z,z')$ can be represented in the following bilinear form

$$P^{P'}(z,z') = \begin{bmatrix} \mathrm{e}^{-\gamma z} & \mathrm{e}^{+\gamma z} \end{bmatrix} \cdot \begin{bmatrix} \xi_1 & \xi_2 \\ \xi_3 & \xi_4 \end{bmatrix} \cdot \begin{bmatrix} \mathrm{e}^{-\gamma' z'} \\ \mathrm{e}^{+\gamma' z'} \end{bmatrix} = \mathbf{x}^{\mathrm{t}} \cdot \boldsymbol{\xi} \cdot \mathbf{x}' \tag{4.20}$$

where the superscript "t" denotes the transpose operator. We can distinguish two different basis*, depending on z and z', and four constant coefficients ξ_i which are determined from the BCs. It is readily verified that simple manipulations of (4.14) or (4.17) provide the same type of expression. For instance, (4.14) can be rewritten as

$$P^{P'}(z,z') = \frac{ss'}{D'}\,T(i,i') \times \begin{cases} \left[\begin{array}{cc} \mathrm{e}^{-\gamma(z-\varsigma_0)} & \mathrm{e}^{-\gamma(h+\varsigma_1-z)} \end{array}\right] \cdot \left[\begin{array}{cc} 1 & -\sigma'\overleftharpoonup{\Gamma}' \\ \sigma\overrightharpoonup{\Gamma} & -\sigma\overrightharpoonup{\Gamma}\sigma'\overleftharpoonup{\Gamma}' \end{array}\right] \cdot \left[\begin{array}{c} \mathrm{e}^{-\gamma'(\varsigma_1'-z')} \\ \mathrm{e}^{-\gamma'(h'+z'-\varsigma_0')} \end{array}\right], & i' < i \\ \left[\begin{array}{cc} \mathrm{e}^{-\gamma(\varsigma_1-z)} & \mathrm{e}^{-\gamma(h+z-\varsigma_0)} \end{array}\right] \cdot \left[\begin{array}{cc} -\sigma' & \overrightharpoonup{\Gamma}' \\ -\sigma\sigma'\overleftharpoonup{\Gamma} & \sigma\overrightharpoonup{\Gamma}'\overleftharpoonup{\Gamma} \end{array}\right] \cdot \left[\begin{array}{c} \mathrm{e}^{-\gamma'(z'-\varsigma_0')} \\ \mathrm{e}^{-\gamma'(h'+\varsigma_1'-z')} \end{array}\right], & i < i' \end{cases} \tag{4.21a}$$

or using a short notation as

$$P^{P'} = \frac{ss'}{D'}T(i,i') \begin{cases} \mathbf{x}_0^{\mathrm{t}} \cdot \left[\begin{array}{cc} 1 & -\overleftharpoonup{u}' \\ \overrightharpoonup{u} & -\overrightharpoonup{u}\overleftharpoonup{u}' \end{array}\right] \cdot \mathbf{x}_1', & i' < i \\ \mathbf{x}_1^{\mathrm{t}} \cdot \left[\begin{array}{cc} 1 & -\overrightharpoonup{u}' \\ \overleftharpoonup{u} & -\overleftharpoonup{u}\overrightharpoonup{u}' \end{array}\right] \cdot \mathbf{x}_0', & i < i' \end{cases} \tag{4.21b}$$

where $\mathbf{x}_i$ is a column vector of exponential functions

$$\mathbf{x}_0 = \left[\begin{array}{c} \mathrm{e}^{-\gamma(z-\varsigma_0)} \\ \mathrm{e}^{+\gamma(z-\varsigma_0)} \end{array}\right] \qquad \mathbf{x}_1 = \left[\begin{array}{c} \mathrm{e}^{-\gamma(\varsigma_1-z)} \\ \mathrm{e}^{+\gamma(\varsigma_1-z)} \end{array}\right], \tag{4.22}$$

the transmission through intermediate layers is given by

$$T(i,i') = \begin{cases} \overrightharpoonup{T}_{i',i}, & i' < i \\ -\sigma'\overleftharpoonup{T}_{i,i'}, & i < i' \end{cases}, \tag{4.23}$$

and

$$\overleftharpoonup{u} = \sigma\overleftharpoonup{\Gamma}t, \qquad \overrightharpoonup{u} = \sigma\overrightharpoonup{\Gamma}t. \tag{4.24}$$

The matrices in (4.21) can be transformed by means of a change of basis

$$\mathbf{x}^{\mathrm{t}} \cdot \boldsymbol{\xi} \cdot \mathbf{x}' = \mathbf{y}^{\mathrm{t}} \cdot (\mathbf{M}^{\mathrm{t}} \cdot \boldsymbol{\xi} \cdot \mathbf{M}) \cdot \mathbf{y}'$$

provided that $\mathbf{x} = \mathbf{M} \cdot \mathbf{y}$. For example, a useful transformation changes the exponential into hyperbolic basis:

$$\mathbf{x}_k = \left[\begin{array}{cc} +1 & +1 \\ +1 & -1 \end{array}\right] \cdot \mathbf{y}_k \qquad k = 0, 1 \tag{4.25}$$

---

[*] Eigensolutions of the homogeneous equation of (4.1) for z and z'.

where we have denoted

$$\mathbf{y}_0 = \begin{bmatrix} +\cosh(\gamma(z-\varsigma_0)) \\ -\sinh(\gamma(z-\varsigma_0)) \end{bmatrix} \qquad \mathbf{y}_1 = \begin{bmatrix} +\cosh(\gamma(\varsigma_1-z)) \\ -\sinh(\gamma(\varsigma_1-z)) \end{bmatrix}. \tag{4.26}$$

With this procedure a seamless combination of exponential (4.22) and hyperbolic (4.26) bases on the source and/or observer coordinates is possible. This is specially useful in the design of stable algorithms, as will be discussed later. In order to show this concept, the right hand side of (4.21a) has been transformed into four equivalent formulations, leading to the following expressions:

$$\mathbf{x}_i^{\mathrm{t}} \cdot \begin{bmatrix} 1 & -u' \\ u & -uu' \end{bmatrix} \cdot \mathbf{x}'_j \tag{4.27a}$$

$$\mathbf{y}_i^{\mathrm{t}} \cdot \begin{bmatrix} 1+u & -u'(1+u) \\ 1-u & -u'(1-u) \end{bmatrix} \cdot \mathbf{x}'_j \tag{4.27b}$$

$$\mathbf{x}_i^{\mathrm{t}} \cdot \begin{bmatrix} 1-u' & 1+u' \\ u(1-u') & u(1+u') \end{bmatrix} \cdot \mathbf{y}'_j \tag{4.27c}$$

$$\mathbf{y}_i^{\mathrm{t}} \cdot \begin{bmatrix} (1+u)(1-u') & (1+u)(1+u') \\ (1-u)(1-u') & (1-u)(1+u') \end{bmatrix} \cdot \mathbf{y}'_j \tag{4.27d}$$

where u represents $\overleftarrow{u}$ when $i' < i$ and $\overrightarrow{u}$ if $i < i'$.

Obviously, further choices are possible. An interesting one obtains a matrix $\boldsymbol{\xi}$ with measures of voltages and currents V, I at the interfaces of the TL sections. This expression, for $z > z'$, is given by

$$\begin{aligned} P^{P'}(z,z') &= \frac{s}{\sinh(\gamma h)\sinh(\gamma' h')} \\ &\times \begin{bmatrix} \sinh(\gamma(\varsigma_1 - z)) & \sinh(\gamma(z-\varsigma_0)) \end{bmatrix} \cdot \begin{bmatrix} V^I_{0,0'} & V^I_{1,0'} \\ I^V_{0,1'} & I^V_{1,1'} \end{bmatrix} \cdot \begin{bmatrix} \sinh(\gamma(\varsigma'_1 - z')) \\ \sinh(\gamma(z' - \varsigma'_0)) \end{bmatrix} \end{aligned} \tag{4.28}$$

where the elements in the matrix, in general $P^{P'}_{i,i'} \equiv P^{P'}(\varsigma_i, \varsigma'_i)$, corresponds to the magnitude P at the interface ς_i when a P'-type source excites at ς'_i. This result can be understood by using an analogy with the ABCD matrix formalism [6, §4.9] where the constants weighs of the hyperbolic functions are actually measures of V, I at the TL interfaces.

4.3.2 Decomposition in Multiple Reflections

Another more revealing form of the TL solution is found by decomposition into multiple reflections [2]. This concept can been used, for example, in the acceleration of the GF [7]. It provides a knowledge about the asymptotic behavior of the spectral domain GF that can be exploited in the method of averages, or to extract quasi-static parts from the spectral kernels. In the context of this work, the purpose of this section is twofold: first, to deduce this decomposition from our formulation and second, as a backbone for discussions about resonances and modal series accelerations that will take place in later chapters.

The decomposition of (4.14) can be readily achieved by adding and subtracting the exponential function as:

$$P^{P'}(z,z') = ss' \begin{cases} \mathrm{e}^{-\gamma|z-z'|} + \frac{1}{D}\sum\limits_{k=1}^{4} A_k \mathrm{e}^{-\gamma d_k}, & z' < z \\ -\,\sigma'\left(\mathrm{e}^{-\gamma|z-z'|} + \frac{1}{D}\sum\limits_{k=1}^{4} B_k \mathrm{e}^{-\gamma d_k}\right), & z < z' \end{cases} \tag{4.29}$$

where we denoted

$$A_1 = \sigma\overrightarrow{\Gamma} \qquad B_1 = -\sigma'\overrightarrow{\Gamma} \qquad d_1 = 2\varsigma_1 - |z+z'| \tag{4.30a}$$

$$A_2 = -\sigma'\overleftarrow{\Gamma} \qquad B_2 = \sigma\overleftarrow{\Gamma} \qquad d_2 = |z+z'| - 2\varsigma_0 \tag{4.30b}$$

$$A_3 = \overleftarrow{\Gamma}\,\overrightarrow{\Gamma} \qquad B_3 = A_3 \qquad d_3 = 2h - |z-z'| \tag{4.30c}$$

$$A_4 = A_1 A_2 \qquad B_4 = B_1 B_2 \qquad d_4 = 2h + |z-z'| \tag{4.30d}$$

and $d_i > 0$ are distances. The first term in (4.29) represents the direct ray between the source and the observer point, while the other terms embrace the rays that undergo partial reflections at the upper and lower interfaces before reaching the observation point as illustrated in Fig. 4.8. Actually the infinite number of rays reflected in the interfaces [6, §3.2] can be recovered in the formulation by considering the sum of a geometric series as

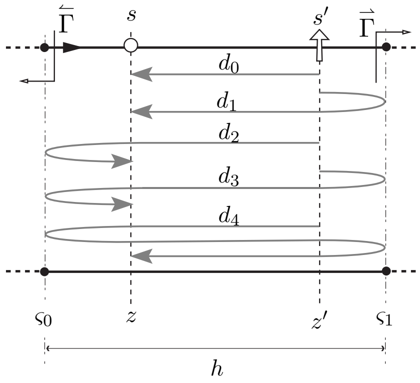

Figure 4.8: Paths followed by each ray component in the multiple rays decomposition.

$$\frac{1}{D} = \frac{1}{1-\overleftarrow{\Gamma}\,\overrightarrow{\Gamma}t} = \sum_{i=0}^{\infty}\left(\overleftarrow{\Gamma}\,\overrightarrow{\Gamma}t\right)^i =$$

$$= 1 + \overleftarrow{\Gamma}\,\overrightarrow{\Gamma}\mathrm{e}^{-2\gamma h} + \overleftarrow{\Gamma}^2\overrightarrow{\Gamma}^2\mathrm{e}^{-4\gamma h} + \cdots \tag{4.31}$$

provided that $|\overleftarrow{\Gamma}\,\overrightarrow{\Gamma}t| = |\overleftarrow{\Gamma}\,\overrightarrow{\Gamma}| < 1^\dagger$.

[†] This condition is always satisfied by propagating modes not being at resonance condition [cf. §4.6].

4.4 Stability

The stability, together with the efficiency, plays a major role in the design of a numerical algorithm, and the TLMo is not an exception. It is difficult, if not impossible, to define a *systematic* procedure to design/analyze the stability of a method. However some guidelines are given following [8, §1.18]. In our case, the review of different TLMo algorithms, found in the literature, revealed some unstable formulations that would cause erroneous results.

4.4.1 Review

In TLMos, the danger of overflows and underflows is found in two types of formulations:

- *Methods based on impedance/admitance.* Some authors, e.g. [9], use a formulation based on impedance functions. The latter is an unbounded function since it tends to infinity as the current vanishes (open circuit BC). An analogous situation arises with an admittance formulation in a short circuit. Hence, it is more advisable to use *reflection coefficients* which, in most conditions[‡], are bounded functions.

- *Highly attenuated waves.* This problem arises with the exponential functions inherited from the reflected wave part in the traveling wave solutions (4.1). Formulations using the so called wave amplitude transmission line matrix [6, §4.9] or simply transmission line matrix, in [3, (3)] and [10, (37)], can suffer from over/underflows due to fast growing positive exponential functions. This occurs when the wave is highly attenuated or in other words, for large values of the exponential argument αz, provided that $\gamma = \alpha + \mathrm{j}\beta$ with $\alpha \in \mathbb{R}^+$ and $\beta \in \mathbb{R}$. This type of functions can be avoided by selecting a new reference point "ς" [cf. (4.1)] for the reflected wave component, as can be observed in the expressions (4.14) and (4.17) that include only decreasing exponential functions.

The highly attenuation condition *also* affects a standing wave formulation, based on hyperbolic functions (4.26). The latter are asymptotically exponential functions that tend to infinity as αz increases. Nevertheless, an early instability arises before this formulation reaches overflow. To understand this phenomena, let us consider an evanescent wave in a TL with $\{\gamma, Z\} = \{\alpha, \mathrm{j}X(\alpha)\}$ where $X \in \mathbb{R}$. Without loss of generality, the voltage and current in the TL can be obtained by means of a standing wave formulation[§] for $z \in [0, h]$ as:

$$V(z) = +v\cosh(\gamma z) - Zi\sinh(\gamma z) \tag{4.32a}$$

$$ZI(z) = -v\sinh(\gamma z) + Zi\cosh(\gamma z), \tag{4.32b}$$

where $v = V(0), i = I(0)$ are constants. Considering the high attenuation condition in the line, $\alpha h \gg 1$, the impedance Z_{in} seen at the TL's input equates the characteristic impedance Z. Consequently, the constants v and Zi become the same. More specifically, calculating the

---

[‡] It can happen that $|\rho| > 1$ if the reference impedance is complex (see Appendix).

[§] We have chosen an equivalent to the so called voltage-current transmission matrix or ABCD matrix [6, §4.9].

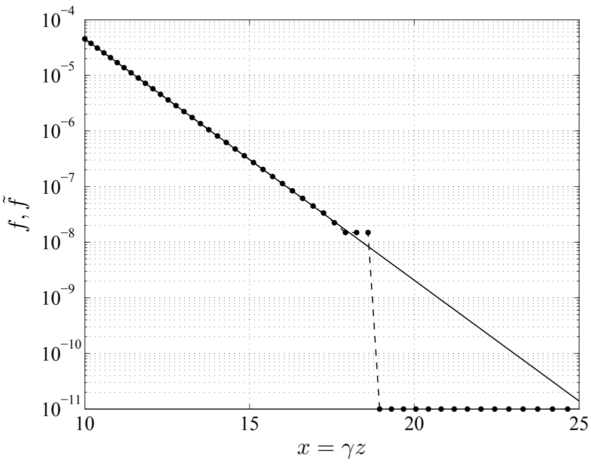

Figure 4.9: Computation of a decreasing exponential using hyperbolic functions $\tilde{f} = \cosh(x) - \sinh(x)$ (dashed line with dot markers) and the exact formula $f = \mathrm{e}^{-x}$ (solid line). Note: Results equal to zero are plotted as 10^{-11}.

impedance using [6, (3.52)]

$$Z_{\text{in}} \approx Z = \mathrm{j}X(\alpha) \qquad \Rightarrow \qquad v = Z_{\text{in}} i = Zi,$$

provided that $\tanh(\alpha h) \approx 1$. Finally, as expected for an evanescent wave, (4.32) decreases exponentially as

$$V(z), ZI(z) \propto [\cosh(\gamma z) - \sinh(\gamma z)] = \mathrm{e}^{-\gamma z}. \tag{4.33}$$

The left and right hand side of the equality in (4.33) are mathematically identical but not numerically when $\alpha z \gg 1$, as it follows from the plots in Fig. 4.9. The origin of this instability is found in the loss of precision in the subtraction operation combined with the accuracy in the evaluation of hyperbolic functions with big arguments. Notice that from $\gamma z \approx 18$ both formulas diverge and $\gamma z > 19$, the difference is directly giving zero. Moreover, the evaluation of still larger values for x will produce overflow in the hyperbolic functions, which will result in `Inf-Inf=NaN`.

The bi-layer problem analyzed in Fig. 4.10 emphasizes the importance of considering this instability in the formulation of the TLMo. The structure, represented in Fig. 4.10(a), consists of two TL sections in between two ground planes. The attenuation and the electric length for every layer are plotted Fig. 4.10(b) at the operating frequency. The wave propagates approximately 0.7 wavelengths in medium ① and in the medium ② it becomes evanescent and attenuates. The variations of the current and voltage with respect to z are given in Fig. 4.10(c)-(d). Two formulations are considered, namely, a standing wave approach using (4.32) and our traveling wave-based formulation. The results plotted show how the former breaks down while the latter tends smoothly to the short circuit condition ($V = 0$ and $\frac{\partial I}{\partial z} = 0$).

Zeros in the current and voltage functions can be also source of inaccuracies. We have already dealt with one case while discussing about the impedance/admitance formulation. Another

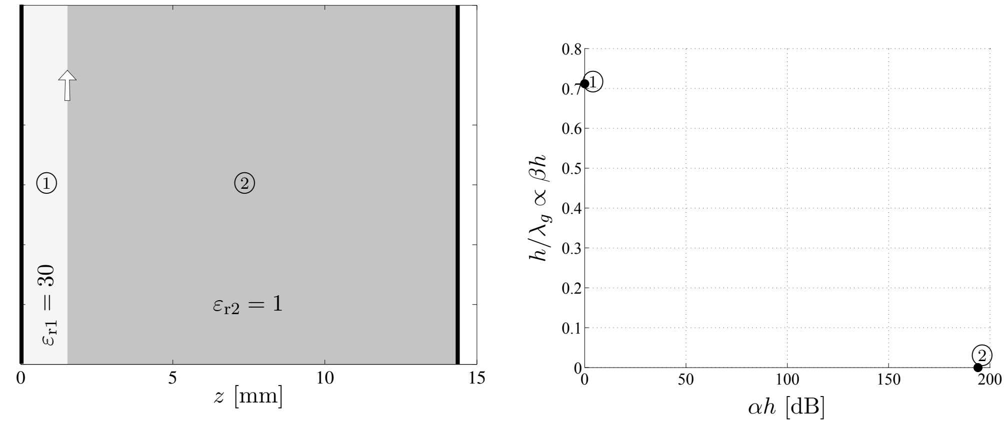

(a) Layered media. (b) Propagation constant in each layer γ_i.

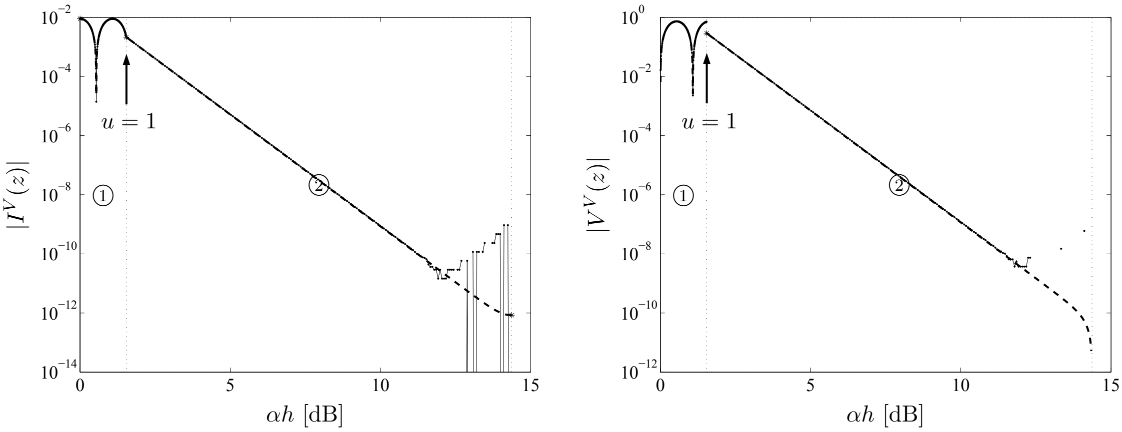

(c) Measured *current* for a *voltage* source. (d) Measured *voltage* for a *voltage* source.

Figure 4.10: Comparison between a method based on a standing-wave formulation (solid • line) and this method (dashed line) when the wave is highly attenuated. Voltage/Current distribution for $\kappa \approx 0.59\pi$ and $k_0 \approx \frac{\pi}{5}$ mm^{-1} (TE$_{50,21}$-mode in a 92×92 mm^2 waveguide at 30 GHz) generated by a current source injected at the interface between ① and ②. The multilayered configuration is: $\varepsilon_{r1} = 30$, $h_1 = 1.54$ mm (high permittivity dielectric); $\varepsilon_{r2} = 1$, $h_2 = 12.83$ mm (TL section *under cutoff*). This structure is short-circuited at both ends and $\mu_r = 1$ in all dielectric layers.

situation emerges in the formulation proposed by [2, (67)], where the incident wave, at the interface, is actually obtained from the knowledge of the *voltage*, $a = v/(1+\rho)$, with the reflection coefficient ρ and the voltage v measured at the same reference plane. As a matter of fact, the above formula is perfectly stable except when $\rho \to -1$ or equivalently, when the reference plane sees a short-circuit. In that case, the numerator and denominator tend both to zero. Analogously, a current-based formulation of the incident wave [1], i.e. $a = Zi/(1-\rho)$, has the same behavior with an open-circuit condition at the reference plane ($i = 0$ and $\rho = +1$). Is this numerically accurate and/or stable? This will depend on many factors like the machine precision or the roundoff errors committed during the evaluation of i, v and ρ

[8, §2.3]. Nonetheless, it is an unnecessary risk that can be easily avoided by using instead $a = v + Zi/2$.

4.4.2 Cutoff Condition

Another condition that produces uncertain results in the TLMo algorithms happens when the propagation constant γ equals zero. In waveguide terminology, this is commonly known as the "cutoff condition" and it is achieved when $\kappa = k$. If this is the case in a TL, its characteristic impedance Z gets limiting values

$$\lim_{\gamma\to 0} Z = \lim_{\gamma\to 0} \begin{cases} \frac{\mathrm{j}\omega\mu}{\gamma} = \infty & \text{for TE mode} \\ \frac{\gamma}{\mathrm{j}\omega\varepsilon} = 0 & \text{for TM mode} \end{cases}, \tag{4.34}$$

that forces the reflection coefficient to a constant

$$\lim_{\gamma\to 0} \rho(z) = \lim_{\gamma\to 0} \frac{V(z) - ZI(z)}{V(z) + ZI(z)} = \mp 1 \tag{4.35}$$

regardless of the actual impedance seen at z. In other words, with this definition of reflection coefficient[¶], the information about the impedance (boundary conditions) is missing and therefore it is not possible to evaluate the current and the voltage. Is this a problem derived from the mathematical formulation or is it the consequence of a particular physical effect?

In order to find some answers, we will come back to the Telegraphers equations (4.1):

$$\frac{\partial V}{\partial z} = -\gamma Z I \tag{4.36a}$$

$$\frac{\partial I}{\partial z} = -\frac{\gamma}{Z} V \tag{4.36b}$$

where the constants, that determine the distributed elements $\{Z_\mathrm{s}, Y_\mathrm{p}\}$ of the TL, are expressed in terms of γ as

$$Z\gamma = Z_\mathrm{s} = \begin{cases} \mathrm{j}\omega\mu & \text{if TE} \\ \frac{\gamma^2}{\mathrm{j}\omega\varepsilon} & \text{if TM} \end{cases} \quad [\Omega/\mathrm{m}] \qquad \frac{\gamma}{Z} = Y_\mathrm{p} = \begin{cases} \frac{\gamma^2}{\mathrm{j}\omega\mu} & \text{if TE} \\ \mathrm{j}\omega\varepsilon & \text{if TM} \end{cases} \quad [\mathrm{S/m}], \tag{4.37}$$

according to the identities in Table 3.8. Let us now derive the formulation from (4.36) for both cases simultaneously[‖], that is:

$$\gamma \neq 0 \qquad \text{and} \qquad \gamma = 0. \tag{4.38}$$

[¶] i.e. Defined as in (A-14) and taking the TL's characteristic impedance Z as reference.

[‖] Subsequent equations keep the same order, i.e. the equation on the left(right) hand side assumes $\gamma \neq 0 (= 0)$.

Then, equations (4.36) specialized to TE waves can be expressed as follows

$$\begin{cases} \frac{\partial V}{\partial z} &= -\mathrm{j}\omega\mu I \\ \frac{\partial I}{\partial z} &= -\frac{\gamma^2}{\mathrm{j}\omega\mu} V \end{cases} \qquad \begin{cases} \frac{\partial V}{\partial z} &= -\mathrm{j}\omega\mu I \\ \frac{\partial I}{\partial z} &= 0 \end{cases}. \tag{4.39a}$$

We can already observe how the variation of I is decoupled from V in the cutoff case, which leads to a linear variation of the voltage and a constant current through the TL. We can compare both sets of equations next:

$$\begin{cases} V &= a\mathrm{e}^{-\gamma z} + b\mathrm{e}^{+\gamma z} \\ I &= \frac{\gamma}{\mathrm{j}\omega\mu}\left(a\mathrm{e}^{-\gamma z} - b\mathrm{e}^{+\gamma z}\right) \end{cases} \qquad \begin{cases} V &= Az + B \\ I &= \frac{-A}{\mathrm{j}\omega\mu} \end{cases} \tag{4.39b}$$

provided that $a \equiv a(\gamma), b \equiv b(\gamma), A, B \in \mathbb{C}$ are constants with respect to z and that they satisfy

$$\left(\frac{\partial^2}{\partial z^2} - \gamma^2\right) P = 0 \qquad \frac{\partial^2}{\partial z^2} P = 0, \tag{4.40}$$

for $P = \{V, I\}$. Results in (4.39b) show that the TL becomes a *distributed* series inductance of μ [H/m] at cutoff or a lumped series inductance $L = \mu h$ [H] if considered interface-to-interface, as represented in Fig. 4.11. This demonstrates that we can still evaluate the voltage and current at any point of the TL even at cutoff condition. Therefore, the answer to the previous question is that the problem detected in (4.35) is actually derived from the definition of the reflection coefficient.

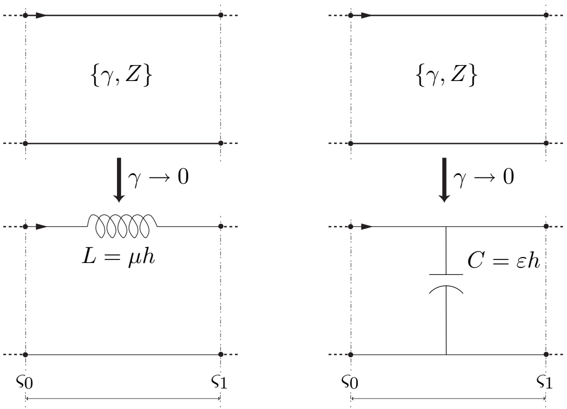

(a) TE (b) TM

Figure 4.11: TL at cutoff condition.

Let us study the convergence taking place between the TL solutions in (4.39b) as $\gamma \to 0$. For values of $\gamma \ll 1$ we can approximate the exponentials with two terms of a Taylor expansion $\mathrm{e}^{\gamma z} \approx 1 + \gamma z$. This will reduce the expressions on the left side into linear functions of z. Then, identifying terms in both equations shows how the function converges to the constants

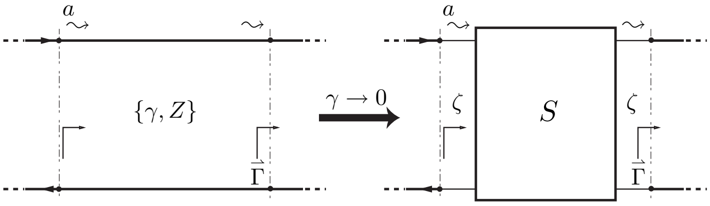

Figure 4.12: Adapting TL section to a new reference impedance ζ.

A and B:

$$\left.\begin{array}{l}\gamma[b-a] \\ \gamma[a+b]\end{array}\right\} \xrightarrow{\gamma\to 0} \left\{\begin{array}{l} A \\ B\end{array}\right.$$

Now, dividing the equations above and recalling the definition of reflection coefficient $\rho = \frac{b}{a}$ shows that

$$\frac{\rho(\gamma)-1}{\rho(\gamma)+1} \xrightarrow{\gamma\to 0} \frac{A}{B} \in \mathbb{C} \tag{4.41}$$

which indicates that this ratio tends to a constant as $\gamma \to 0$, *regardless* of the actual value of the impedance. This is *another* proof to justify that the definition of reflection coefficient can not be used under the cutoff condition.

The same conclusions can be deduced analogously from the TM case, where (4.36) is given by

$$\begin{cases} \frac{\partial V}{\partial z} &= -\frac{\gamma^2}{\mathrm{j}\omega\varepsilon} I \\ \frac{\partial I}{\partial z} &= -\mathrm{j}\omega\varepsilon V \end{cases} \qquad \begin{cases} \frac{\partial V}{\partial z} &= 0 \\ \frac{\partial I}{\partial z} &= -\mathrm{j}\omega\varepsilon V \end{cases} \tag{4.42a}$$

and the TL solutions are

$$\begin{cases} V &= a\mathrm{e}^{-\gamma z} + b\mathrm{e}^{+\gamma z} \\ I &= \frac{\mathrm{j}\omega\varepsilon}{\gamma}\left(a\mathrm{e}^{-\gamma z} - b\mathrm{e}^{+\gamma z}\right) \end{cases} \qquad \begin{cases} V &= \frac{-A}{\mathrm{j}\omega\varepsilon} \\ I &= Az + B \end{cases}. \tag{4.42b}$$

All the methods presented so far are based on reflection coefficients and consequently they become unstable in the proximity of a cutoff condition. It would be desirable to find a technique that avoids this problem without implying a drastic modification of our algorithm.

The basic idea consists of re-normalizing the formulation of the reflection coefficient to a suitable reference impedance within the TL sections under cutoff condition. This is equivalent to considering these sections as "black boxes" with scattering parameters referred to a new non-zero and finite impedance ζ, selected arbitrarily. In fact, this method will only affect the "shift" operation (A-8) within the TL because the new reference impedance does not coincide with the characteristic impedance of the TL. Instead, this is now calculated as follows:

$$a \longrightarrow \frac{S_{21}}{1 - S_{11}\overrightarrow{\Gamma}}a \tag{4.43}$$

$$S_{11} + \frac{S_{21}^2\overrightarrow{\Gamma}}{1 - S_{11}\overrightarrow{\Gamma}} \longleftarrow \overrightarrow{\Gamma}, \tag{4.44}$$

where S are the new scattering parameters of the TL referred to ζ. Hence, the reflection $\{\overleftarrow{\Gamma}, \overrightarrow{\Gamma}\}$ and the transition $\{\overleftarrow{\tau}, \overrightarrow{\tau}\}$[**] coefficients at the interfaces can still be calculated using the same iterative procedure as before [see Appendix]. Once these interface coefficients are available, the solution can be again found using the formulas (4.14) or (4.21a) by using the appropriate combination of (4.27) such that a hyperbolic formulation is used when either the source or the observer layers are close to cutoff condition. This is advisable in order to guarantee a stable transition in the vicinity of the cutoff. Recalling the traveling wave formulation from (4.2) in terms of the standing wave coefficients a, b, the following expressions

$$\begin{cases} V &= (a+b)\cosh\gamma z + (b-a)\sinh\gamma z \\ ZI &= \frac{\gamma}{\mathrm{j}\omega\mu}\big[(a-b)\cosh\gamma z + (a+b)\sinh\gamma z\big] \end{cases}$$

show a smoother transition when $\gamma \to 0$ since $\cosh(\gamma z) \approx 1$ and $\sinh(\gamma z) \approx \gamma z$ and therefore, the relation (4.41) is directly obtained without combination of the standing wave coefficients, unlike in the exponential formulation.

Let us apply this technique for the resolution of a three-layer medium in between two infinite conducting plates, as presented in Fig. 4.13. The chart in Fig. 4.13(b) shows that layer ② satisfies the cutoff condition. On the other hand, sections ① and ③ incorporate some losses and the waves propagate suffering a small attenuation. The voltage and current induced in the medium are represented in Fig. 4.13(c) and Fig. 4.13(d) for the two types of generators considered. The plots show how the wave solution goes through the layer ② with constant or linear variation. It should be noted that, without any special treatment, the calculation of this response would not be possible. The wave in the rest of the structure shows the expected behavior taking into account the electric length of each section and the short-circuit terminations.

[**] Here, the factor θ is substituted by $\frac{S_{21}}{1-S_{11}\overrightarrow{\Gamma}}$ as indicated in (4.43).

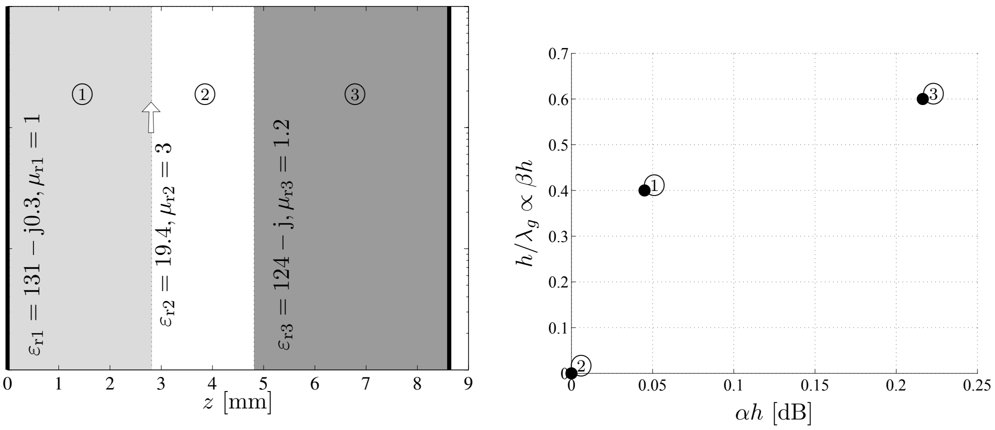

(a) Layered medium. (b) Propagation constant in each layer γ_i.

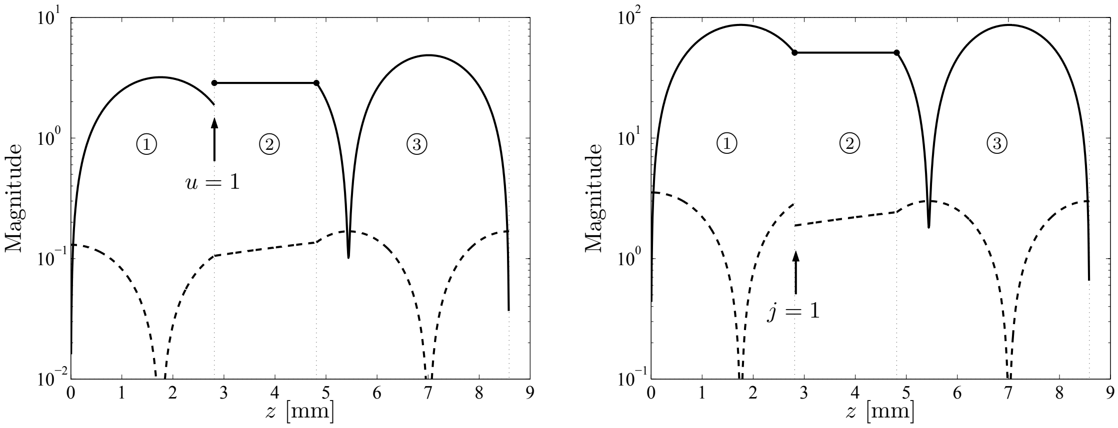

(c) Series *voltage* source. (d) Parallel *current* source.

Figure 4.13: Voltage/Current amplitude (solid/dashed lines) for $\kappa \approx 0.25\pi$ and $k_0 \approx \frac{\pi}{30}$ mm^{-1} (TM$_{1,2}$-mode in a 21×8 mm^2 waveguide at 5 GHz) generated by a voltage source injected at the interface between ① and ②. The multilayered medium is: $\varepsilon_{\mathrm{r}1} = 131 - \mathrm{j}0.3, \mu_{\mathrm{r}1} = 1, h_1 = 2.81$ mm (lossy $0.4\lambda_g$ section); $\varepsilon_{\mathrm{r}2} = 19.4, \mu_{\mathrm{r}2} = 3, h_2 = 2$ mm (*line at cutoff*); $\varepsilon_{\mathrm{r}3} = 124 - \mathrm{j}, \mu_{\mathrm{r}3} = 1.2, h_3 = 3.77$ mm (lossy $0.6\lambda_g$ TL). The structure is short-circuited at both ends.

4.5 Algorithm

Based on the discussion presented in the previous sections we summarize here an algorithm for the systematic evaluation of the TLMo in a multilayered medium problem. This procedure has to be repeated for every frequency $\omega/(2\pi)$ and κ_ρ values[††]:

1. Initialization.
    - Define a TL from each layer section: $\{\varepsilon, \mu\} \rightarrow \{Z, \gamma\}$
        - if $\gamma \ll 1$ then evaluate $\{S_{11}, S_{21}\}$ of the TL with reference ζ.
    - Iterative computation of $\{\overleftarrow{\Gamma}, \overrightarrow{\Gamma}\}$ and $\{\overleftarrow{\tau}, \overrightarrow{\tau}\}$ from the outermost interfaces according to §4.8.
        - if $\gamma \ll 1$ then use (4.43) instead of (A-8).

    At this point, the values $\{\overleftarrow{\Gamma}, \overrightarrow{\Gamma}\}$ and $\{\overleftarrow{\tau}, \overrightarrow{\tau}\}$ are pre-calculated for every TL section.

2. The voltage/current for a voltage/current generator can be now calculated.
    - Search the TL sections including z and z' and retrive: i, i'.
    - Evaluation of $P^{P'}(z, z')$:
        - If intra-layer interaction use (4.14).
        - If inter-layer interaction use (4.21a).
        - In any of the above cases, if $\gamma \ll 1$ then modify the formulation according to the choices in (4.27): if i (resp. i') satisfies $\gamma \ll 1$ use $\mathbf{y}$ (resp. $\mathbf{y}'$).

The reciprocity relations (Appendix) can also be used to reduce the number of evaluations when only discrete evaluations (e.g. only in the dielectric interfaces) are required [11].

This algorithm is used in the resolution of the multilayered problem illustrated in Fig. 4.14. The voltage and current induced along the TLs by any type of excitation is calculated. The chart in Fig. 4.14(b) shows the propagation characteristics throughout the 10 layers of the structure. The problem combines a selection of critical cases, namely a section at cut-off (⑥), two very-thin conductive layers (④ and ⑧), a TL with high losses (②), an evanescent wave (⑩) and a number of sections with stationary waves. The wave, in all cases, is excited[‡‡] in the interface between ⑤ and ⑥. It goes through the section at cut-off with constant value or linear variation. In the thin conductive layers V and $\partial I/\partial z$ tend to zero but are able to cross the layer before they lose all the energy. Finally, the voltage and current also satisfy the short circuit conditions at both ends of the structure.

[††] In general, κ_ρ is a continuous and complex value, but here it is discretized into the real the cutoff wavenumber κ_i of every mode, such that $\gamma^2 = \kappa_i^2 - \omega^2\mu\varepsilon$.

[‡‡] The finite discontinuity for I^I and V^V is not clearly seen in Fig. 4.14(d) and Fig. 4.14(d) because the modulus hides the change in sign in the function.

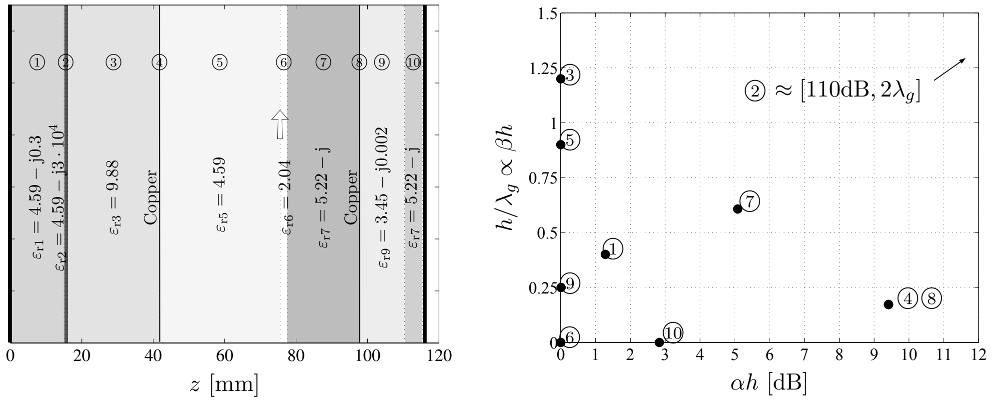

(a) Layered medium. (b) Propagation constant in each layer γ_i.

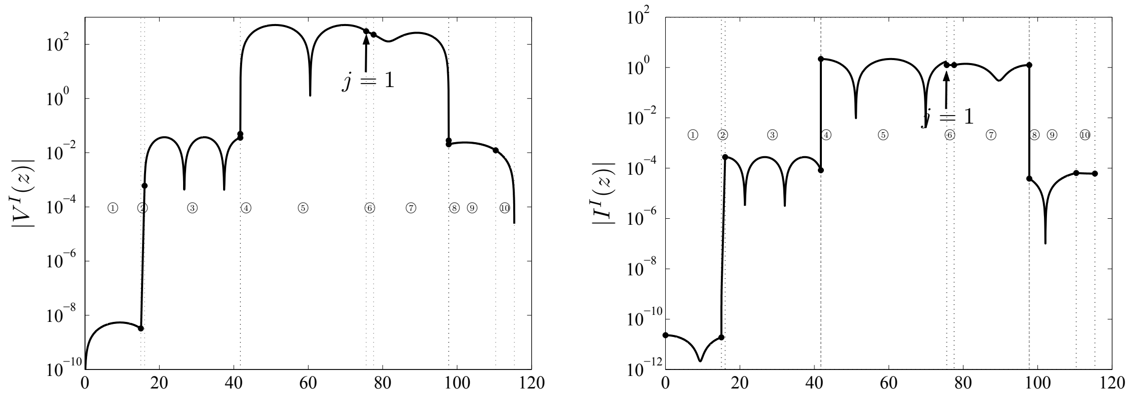

(c) Measured *voltage* for *current* excitation. (d) Measured *current* for *current* excitation.

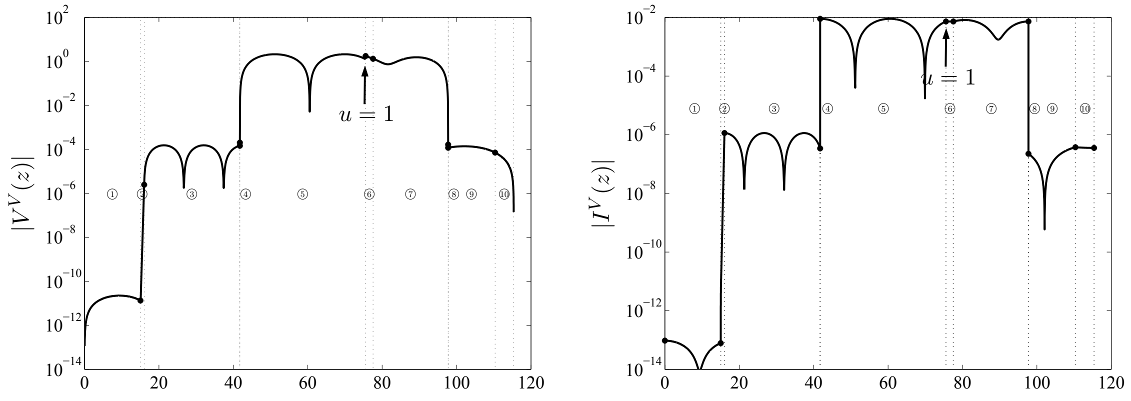

(e) Measured *current* for *voltage* excitation. (f) Measured *current* for *voltage* excitation.

Figure 4.14: Voltage/Current distribution for for $\kappa \approx \frac{\pi}{21}$ and $k_0 \approx \frac{\pi}{30}$ mm^{-1} (TE$_{10}$-mode in a 21×8 mm^2 waveguide at 5 GHz) generated by a current source injected at the interface between media ⑤ and ⑥. The multilayered configuration is: $\varepsilon_{r1} = 4.59 - j0.3$, $h_1 = 15.026$ mm; $\varepsilon_{r2} = 4.59 - j3 \cdot 10^4$, $h_2 = 1$ mm (0.012Ωcm low resistivity silicon); $\varepsilon_{r3} = 9.88$, $h_3 = 25.72$ mm; $\varepsilon_{r4} = 1 - j2.14 \cdot 10^8$, $h_8 = 1$ mm (copper sheet); $\varepsilon_{r5} = 4.59$, $h_5 = 33.809$ mm; $\varepsilon_{r6} = 2.04$, $h_6 = 2$ mm; $\varepsilon_{r7} = 5.22 - j$, $h_7 = 20.176$ mm; in ⑧ copper sheet again; $\varepsilon_{r9} = 3.45 - j0.002$, $h_9 = 12.641$ mm and $\varepsilon_{r10} = 1.65$, $h_{10} = 5$ mm. The structure is short-circuited at both ends and $\mu_r = 1$ in all cases.

4.6 Resonances

Consider the structure described in Fig. 4.15. It consists of a quarter-wavelength stub in shielded microstrip technology. The response of the circuit has a transmission zero at 2.75 GHz, as shown in Fig. 4.16, and two additional resonances at 2.3 and 3.5 GHz, respectively. The former is produced by the microstrip circuit where the $\lambda_g/4$ open-ended stub short-circuits the main line and avoids the transmission of power between the two ports. The phase difference in the reflection waves at each port [see S_{11}, S_{22} in Fig. 4.16(b)] is due to the position of the stub (notice that $l + w/2 \neq a/2$) within the line. The additional resonances, are not caused by the printed circuit but by the resonant modes of the cavity.

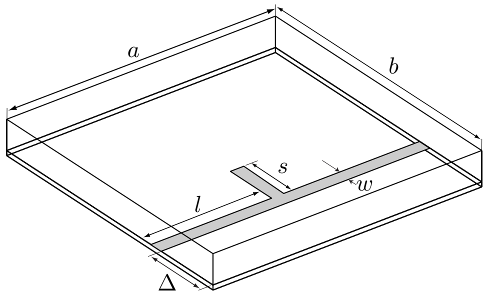

Δ	w	s	l	
23	4.6	18.4	41.4	mm

Dielectric	Height [mm]	R. Permitt.	Losses
i	h_i	ε_{ri}	$\tan\delta_{e_i}$
2. Air	9.83	1.0006	0
1. Duroid 5870	1.57	2.33	0.0012

- Cavity: $a = 92$, $b = 92$ mm; PEC
- Microstrip: 50 Ω ($\varepsilon_{\text{eff}} = 1.94$) in PEC

Figure 4.15: Description of Parallel Stub [12].

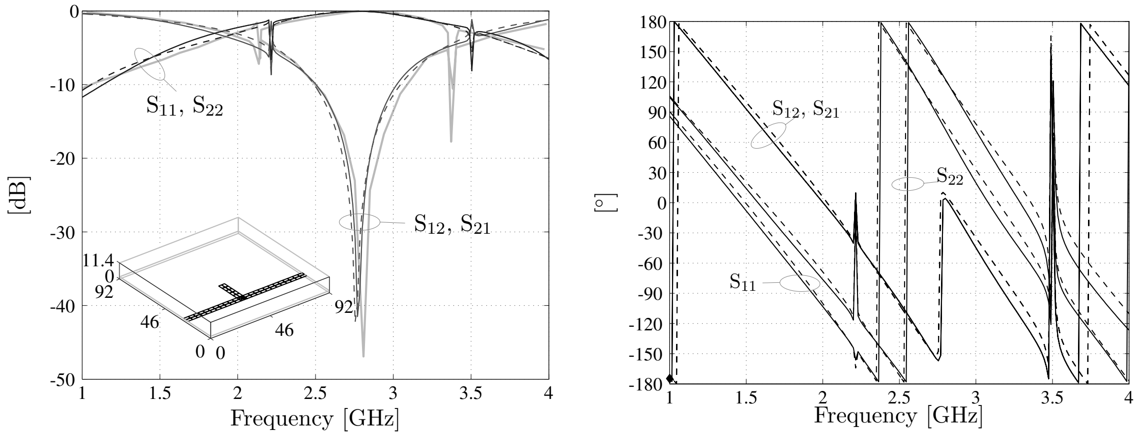

(a) Magnitude. (b) Phase.

Figure 4.16: Frequency response simulated with this method (solid line), with commercial software (dashed line) and measurements from [12] (in gray and only available in magnitude).

The complete EM behavior of the dielectric filled cavity is defined by its GF. As discussed in §2.4, the GF computation is reduced to the calculation of a two-line equivalent TLMo for every mode of the rectangular waveguide. Hence, the resonances are found when a pole arises in the equivalent TLMo at the same time that a mode is excited, i.e. the resonances must be produced simultaneously transversally and longitudinally. A glance to the expressions developed in §4.2 reveals that these poles are produced in (4.14) [equivalently (4.17)] when (4.13) equals zero, provided a non-vanishing numerator. Rewriting the reflection coefficient in terms of impedance (A-14) shows that the loads in the interface must satisfy the following relations:

$$D' = 1 - \overleftarrow{\rho}'\overrightarrow{\rho}' = 0 \qquad \Leftrightarrow \qquad \overleftarrow{\mathcal{Z}} = -\overrightarrow{\mathcal{Z}} \xrightarrow{\mathcal{R} \geq 0} \mathrm{j}\overleftarrow{\mathcal{X}} = -\mathrm{j}\overrightarrow{\mathcal{X}}. \tag{4.45}$$

The last identity coincides with the classical definition of circuit resonance. It can be interpreted as parallel LC resonator at the layers interface.

Let us now proceed with the analysis of our two-layered structure in Fig. 4.15. The spectral components here are discretized to the modes of the transverse rectangular waveguide, meaning that the continuous spectrum κ_ρ is sampled with the modal cutoff wavenumbers κ_{mn}. IN this structure, a mode is resonant when it satisfies the following characteristic equation, derived from (4.45):

$$\mathcal{F}(\kappa_\rho) \equiv Z_1 \tanh(\gamma_1 h_1) + Z_2 \tanh(\gamma_2 h_2) = 0, \tag{4.46}$$

derived from the resonance condition (4.45) and where $Z_i \equiv Z_i(\kappa_\rho)$ and $\gamma_i \equiv \gamma_i(\kappa_\rho)$. The function $\mathcal{F}$ has been evaluated in the complex spectrum plane κ_ρ/k_0 at 3.5 GHz and represented in Fig. 4.17. The zeros of the function can be identified by concentric contour plot showing the magnitude and the equi-phase lines that join poles with zeros in $\mathcal{F}$. Along the real axis, we have also represented the samples corresponding to the rectangular modes. Hence we can visually identify a resonant mode when a zero of $\mathcal{F}$ coincides with a modal sample κ_{mn}. At 3.5 GHz, this is actually happening in Fig. 4.17(a) where two degenerate modes, TM_{12} and TM_{21}, are resonant in the cavity and therefore are responsible for the upper resonance identified in the circuit response of Fig. 4.16. Analogously, it can be demonstrated that the lower resonance at 2.3 GHz is produced by the TM_{11} mode.

The impedance $\mathcal{Z}$ loading both sides of the interface plays a major role in the resonance condition. A general representation of $\mathcal{Z} = \mathrm{j}\mathcal{X}$ is given in Fig. 4.18 for the TE (dashed line) and TM (solid line) cases. The plots show the variation of the normalized reactance $\mathcal{X}/\eta_0$ against the *real* part of the normalized continuous spectrum κ_ρ/k_0. The point $\mathrm{Re}\,\kappa_\rho/k_0 = \sqrt{\varepsilon_\mathrm{r}}$ determines the cutoff condition that separates propagating ($\mathrm{Re}\,\kappa_\rho/k < 1$) from evanescent ($\mathrm{Re}\,\kappa_\rho/k > 1$) waves. We have specialized the formulation for each of these intervals in Table 4.1. In the propagating region, the function alternates between inductive and capacitive values, as highlighted in Fig. 4.18 . The impedance zeros and poles are given by the electric length of the short-circuited TL that reaches $n\lambda_\mathrm{g}/2$ and $(2n-1)\lambda_\mathrm{g}/4$, respectively. Both the TE and TM functions follow the same pattern and they converge to each other as $\mathrm{Re}\,\kappa_\rho/k_0$ tends to zero. In the evanescent region, the impedance is permanently inductive (capacitive) for TE (TM) waves.

Specializing the function in Fig. 4.18 for two TLs with different dielectrics ε_r, the characteristic

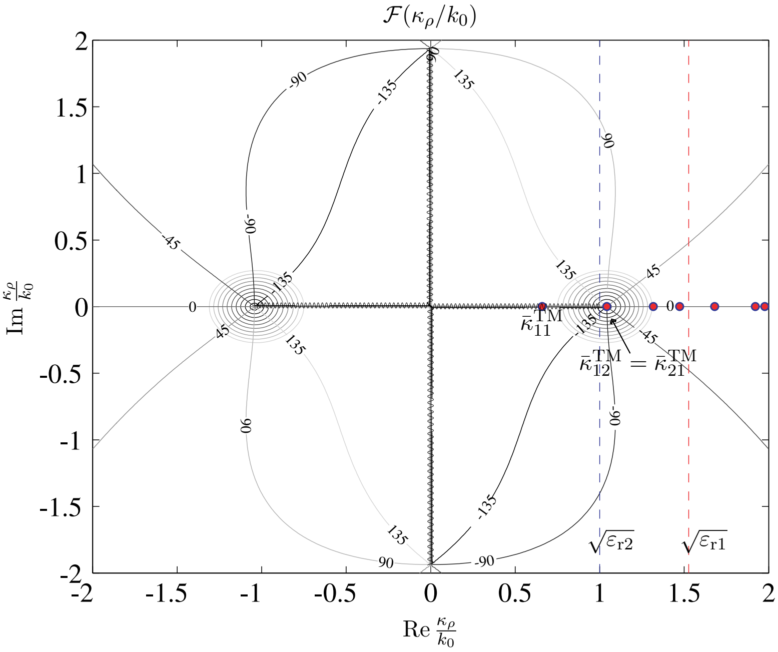

(a) TM case.

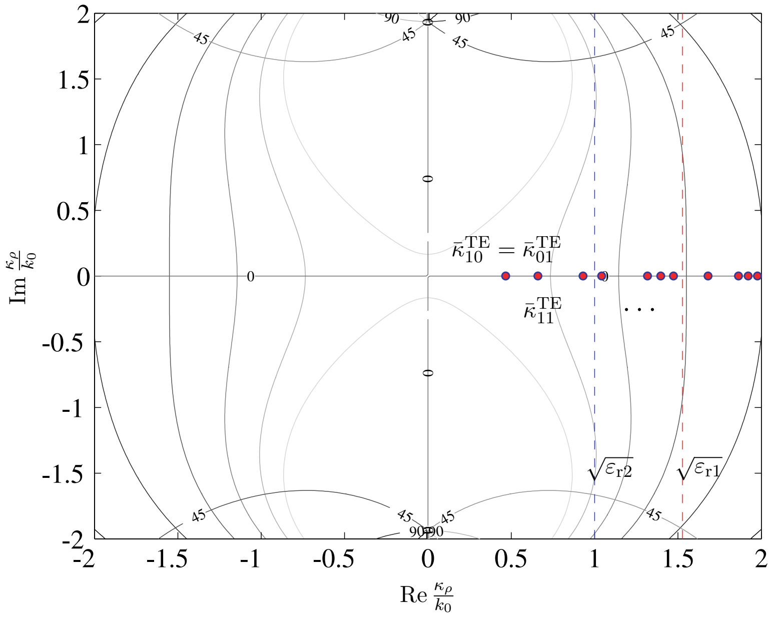

(b) TE case.

Figure 4.17: Magnitude and phase of the characteristic function at 3.5 GHz in the $\mathbb{C}$-plane (contour plot) and mode wavenumbers (positive real eigenvalues $\bar{\kappa}_{mn}^2 k_0^2 = (m\pi/a)^2 + (n\pi/b)^2$) of the rectangular waveguide (dots).

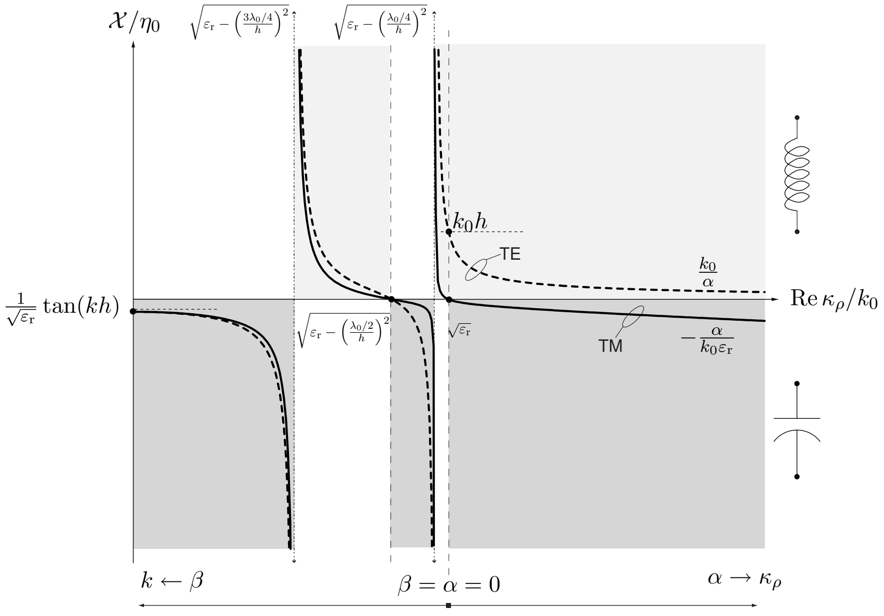

Figure 4.18: Variation of the normalized reactance in function of real values of κ_ρ/k_0.

Re $\frac{\kappa_\rho}{k} = \frac{\omega_c}{\omega}$	< 1	$= 1$	> 1
γ	$j\beta = jk_0\sqrt{\varepsilon_r - (\kappa_\rho/k_0)^2}$	0	$\alpha = k_0\sqrt{(\kappa_\rho/k_0)^2 - \varepsilon_r}$
Z	$R = \eta\begin{cases} k/\beta \\ \beta/k \end{cases}$	$\infty/0$	$\pm jX = \pm j\eta\begin{cases} k/\alpha & \text{TE} \\ \alpha/k & \text{TM} \end{cases}$
$\mathcal{Z} = Z\tanh(\gamma h)$	$jR\tan(\beta h)$	$k_0 h \ / \ 0$	$\pm jX\tanh(\alpha h)$

Notation: $\eta = \eta_0/\sqrt{\varepsilon_r} = \sqrt{\mu/\varepsilon}$ and $k = k_0\sqrt{\varepsilon_r} = \omega\sqrt{\mu\varepsilon}$

Table 4.1: Expressions for the propagation constant, characteristic impedance and general impedance for different intervals of κ_ρ/k, assuming $\kappa_\rho \in \mathbb{R}$ (see Fig. 4.18).

equation (4.46) will reach a solution within two overlapping inductive-capacitive regions. In principle, simultaneous overlapping may occur all along the Re κ_ρ/k_0 axis, therefore producing multiple resonances at a given frequency. Recalling our discussion about Fig. 4.17(a), we can observe that the zero falls inside the interval $\sqrt{\varepsilon_{r2}} < \mathrm{Re}\,\kappa_\rho/k_0 < \sqrt{\varepsilon_{r1}}$. According to Fig. 4.18, this means that the resonant field is confined in the Duroid dielectric (subscript 1) since the wave is attenuating in the air (subscript 2). This behavior is identified with surface waves in unbounded problems [13, §6.1][14]. On the contrary, if the zero is located in $\mathrm{Re}\,\kappa_\rho/k_0 < \min(\sqrt{\varepsilon_{ri}})$ it would produce the resonance of guided modes propagating all along the cavity. The remaining case, namely $\mathrm{Re}\,\kappa_\rho/k_0 > \max(\sqrt{\varepsilon_{ri}})$, will not contain zeros since the impedance remains, as shown in Fig. 4.18, purely inductive or capacitive.

Finally, we will track the position of the zero in the complex plane [Fig. 4.17(a)] with respect to the frequency in order to predict the resonances in the circuit response. Let us consider for this experiment the structure in Fig. 4.15 substituting the square by a rectangular cavity of dimensions $a = 92$ mm, $b = 1.1a$. In the upper plot of Fig. 4.19 we have represented the variation of the aforementioned TM zero along the real part of the spectral component. Thus, each intersection with a rectangular mode will locate the resonant frequency. The lower plot shows the simulated frequency response of the circuit having resonances produced by the microstrip and cavity simultaneously. As in the previous example, the lower resonance is produced by the TM_{11} mode but the upper ones are split in two since the modes TM_{12} and TM_{21} are not degenerated now.

After the analysis of resonances in multilayered boxed printed circuits we believe that the combination of resonant modes in printed circuits and cavities may have a potential use in filter design.

4.7 Application

In order to validate the method developed throughout this chapter we have selected a Broadside Coupled Filter proposed in [9, §5.2.3]. It consists of a multilayered filter composed of strip resonators printed on suspended dielectrics inside the cavity. This design provides a compact realization of a bandpass filter using vertical coupling and quarter wavelength resonators. An illustration and the details of the structure are given in Fig. 4.20. There are three types of resonators, denoted with C_1, C_2 and C_3, and printed on the dielectric. One end-edge of the resonators C_2 and C_3 is grounded to the cavity wall. The filter is excited by means of coaxial-type ports connected to the strips of type C_1. This is illustrated by means of arrows and the labels P_1 and P_2 at the top and bottom of the structure.

The frequency response, in magnitude and phase, for this filter is represented in Fig. 4.21. The simulations have been carried out with our method and a commercial software [16] finding a good agreement between both responses. We have used a symmetric rectangular mesh for the strip resonators in order to avoid the inaccuracies ($S_{11} \neq S_{22}$) introduced in the response simulated with the commercial software, despite the fact that the device is symmetric.

The efficiency of our algorithm can be demonstrated after examination of the time required per simulation. The comparison has been performed setting two benchmarks that use different mesh schemes, and therefore different number of unknowns. The simulations were carried out using a `MAMBO` software, based on this method, and the commercial tool Ansoft Designer® [16]. The simulation times for the aforementioned setups and using the same computer are presented in Fig. 4.22. The time marks for our method are given in two parts corresponding to the initialization time and the time per frequency. The former is due to the operations required to apply the acceleration technique [cf. §5.3.1]. The results obtained demonstrates the efficiency of the TLMo even in structures with a large number of layers. Notice, that the simulations carried out with our method, for a comparable precision, are already faster than the commercial software from the first frequency point despite the fact that the schemes included a higher number of unknowns.

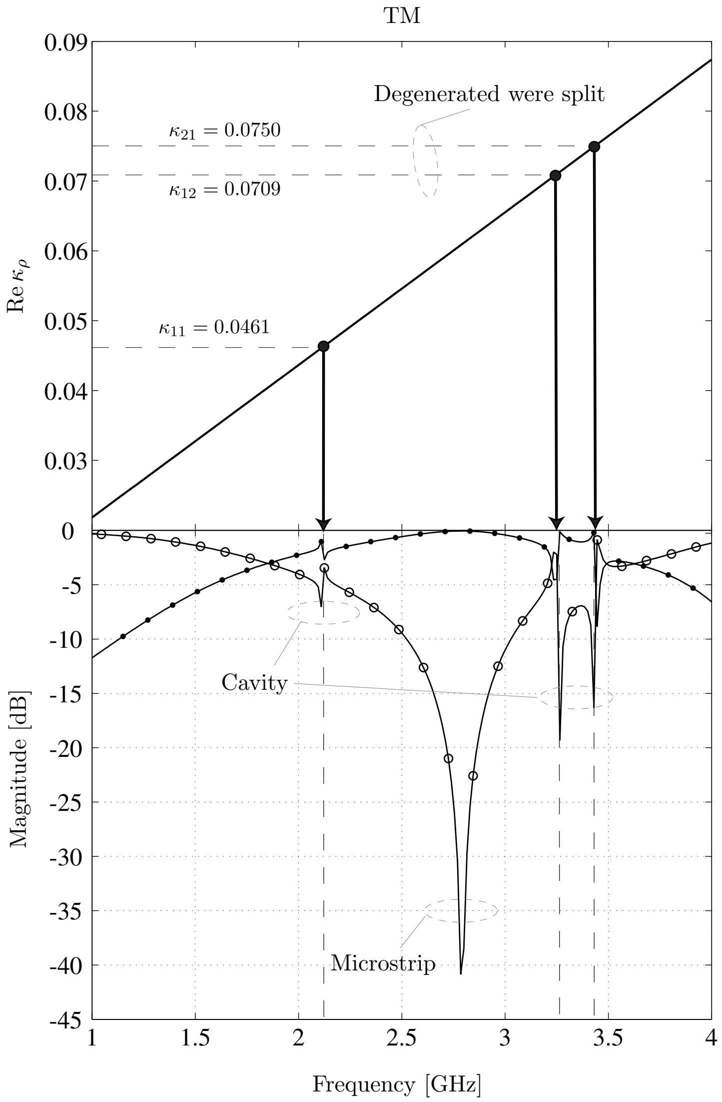

Figure 4.19: Prediction of resonances in the frequency response [below: insertion (○) and return (●) losses] from the TM-resonance chart (above). The cavity dimensions are $a = 92$ mm, $b = 1.1a$.

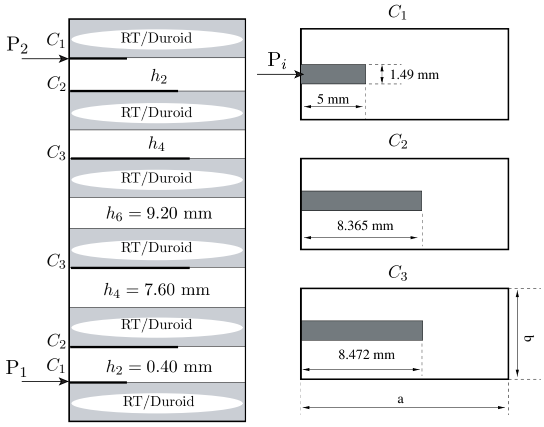

Dielectric i	Height [mm] h_i	R. Permitt. ε_{ri}	Losses $\tan\delta_{e_i}$
1. RT/Duroid 5870	0.51	2.33	0.0012
Air gaps 2, 10	0.4	1.0	0
Air gaps 4, 8	7.6	1.0	0
Air gaps 6	9.2	1.0	0

- Cavity: $a = 10.5$ mm, $b = 8$ mm; PEC.
- Microstrip: PEC

(*)Figure not scaled.

Figure 4.20: Layout of Broadside Filter [15]. From left to right: Vertical distribution of dielectric layers, printed circuits and ports; Top view of three types of resonators; Dielectrics and metallizations.

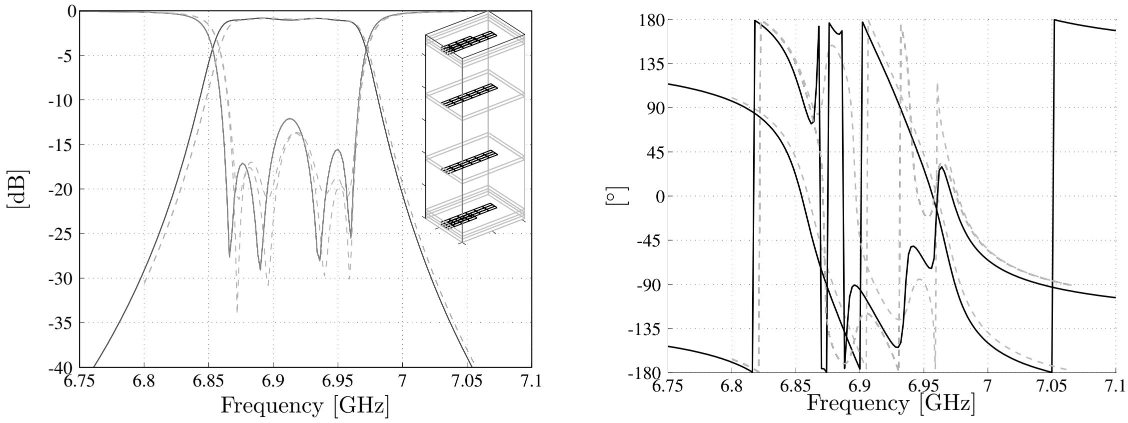

(a) Magnitude.

(b) Phase.

Figure 4.21: Broadside bandpass filter simulated with this method (solid line) and a commercial software (dashed line).

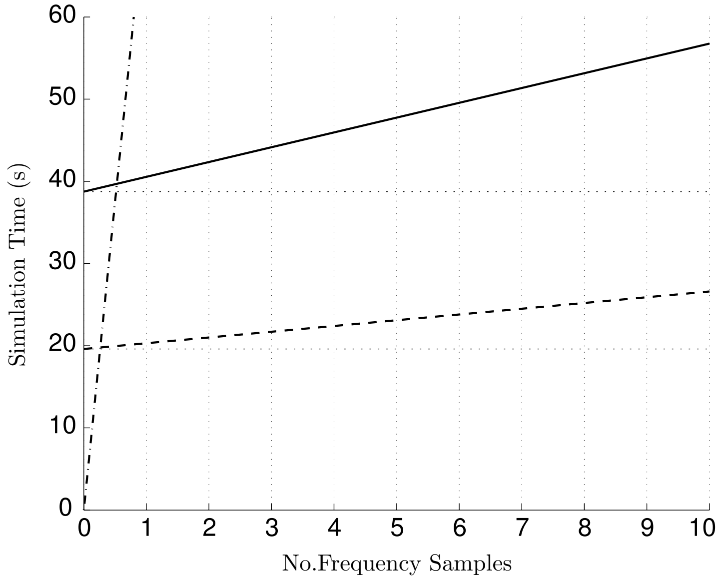

Simulations	No.unknowns	Simulation time
This method: #1 (dashed line)	160	19.6 secs + (0.7 secs/freq)
#2 (solid line)	256	38.75 secs + (1.8 secs/freq)
Ansoft Designer® #1,2 (dashed dotted line)	52, 79	≈ 1.25 mins/freq

Simulations performed on a PC-win Intel Pentium 4, 2.8GHz and 1GHz RAM.

Figure 4.22: Time profile for simulations with this method and a commercial software. Legend in table.

4.8 Conclusion

In this chapter, an stable and efficient algorithm to solve the TLMo, which has an essential role in the formulation of a layered media has been derived. The algorithm is based on a traveling wave approach and provides solution for all the combination of voltage/current, source/observer positions and inter/intra layer interactions in the multilayered structure using a general notation.

Two alternate formulations were also presented to tackle with other analytical approaches. A bilinear form, that reduces the formulation to four constants, derived from the BCs, and two bases, separable in source z' and observer coordinates. The whole set provides a very flexible tool allowing to transform independently the formulation of the source and observer bases. We have also decomposed our TLMo equations into multiple reflections in order to provide physical insight to the formulation.

We have paid special attention to the stability of the algorithm. A review of current TLMo approaches reveals critical cases where a special treatment is required. This chapter introduces criteria to deal with these critical situations and uses the acquired knowledge to build our final algorithm.

The resonances in the scattering parameters appearing in dielectric-filled cavities attracted our attention: instability or a physical phenomenon? The first choice can be discarded as this effect was associated to the resonance of modes inside the layered media and identified in the formulation of the equivalent TLMo. Based on a particular circuit structure, we have explored which conditions produce these resonances, and how the field behaves at every resonance. The knowledge of these mechanisms could be applied to filter synthesis by exploiting the printed-circuits and the multilayered-cavity resonances simultaneously.

Finally, a realistic multilayered filter composed of eleven layers was simulated using our algorithm and a commercial solver. The simulations a) confirmed that a layered media involves an important computational burden in currently available methods and b) demonstrated that we have overcome this problem with the presented algorithm, which showed, for a comparable accuracy, a high efficiency with respect to widely used commercial solvers.

Appendix

Reciprocity

The solutions to (4.1) satisfy reciprocity relations [17, p.194]

$$V^I(z', z) = V^I(z, z') \tag{A-1a}$$

$$I^V(z', z) = I^V(z, z') \tag{A-1b}$$

$$I^I(z', z) = -\frac{j}{u} V^V(z, z') \tag{A-1c}$$

$$V^V(z', z) = -\frac{u}{j} I^I(z, z') \tag{A-1d}$$

that can be used advantageously to reduce the number of evaluations in the TL problem.

Voltage/Current and Incident/Reflected Waves

The relation between voltage/current and incident/reflected waves can be derived from (4.2). The direct and reciprocal transformations are the following:

$$\begin{aligned} v &= a + b \qquad & 2a &= v + Zi \\ Zi &= a - b \qquad & 2b &= v - Zi \end{aligned} \tag{A-2}$$

where $v = V(\varsigma), i = I(\varsigma)$.

Excitation

Consider lumped current and voltage generators placed at the source point z', as illustrated in Fig. 4.4.

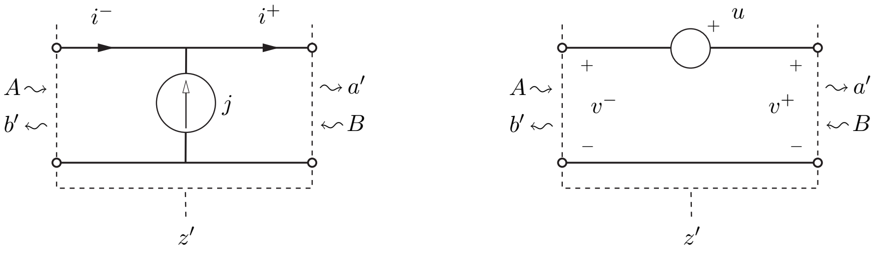

(a) $s' = Z'j/2$. (b) $s' = u/2$.

Figure A.1: Lumped current and voltage generators.

It is well known that the current and voltage waves are risen by j [A] (a) and u [V] (b), respectively. But, what is the effect in terms of wave amplitudes? The answer can be found by using the previous assertion and the identities (A-2). Therefore, a current generator as depicted in Fig. 4.1(a) satisfies

$$\left\{\begin{array}{c} i^{+} = i^{-} + j \\ v^{+} = v^{-} \end{array}\right. \Rightarrow \left\{\begin{array}{c} a' - B = A - b' + jZ \\ a + B = A + b' \end{array}\right.$$

or considering a voltage generator [Fig. 4.1(b)] we can formulate:

$$\left\{\begin{array}{c} i^{+} = i^{-} \\ v^{+} = v^{-} + u \end{array}\right. \Rightarrow \left\{\begin{array}{c} a' - B = A - b' \\ a + B = A + b' + u \end{array}\right. .$$

Then, by summation and subtraction of the above equations, we can find the scattered waves A, B:

$$A = a' - s' \qquad\qquad B = b' + \sigma' s' \tag{A-3}$$

where

$$s' = \frac{1}{2}\left\{\begin{array}{ll} u, & P' = V \\ Z'j, & P' = I \end{array}\right. \qquad\qquad \sigma' = \left\{\begin{array}{ll} +1, & P' = V \\ -1, & P' = I \end{array}\right. . \tag{A-4}$$

Hence, the reflection coefficients at both ends of the source, can be expressed in terms of the scattered waves leaving the source as

$$\overleftarrow{\rho}' = \frac{a - s'}{b'} \qquad\qquad \overrightarrow{\rho}' = \frac{b' + \sigma' s'}{a}. \tag{A-5}$$

Finally, combining the expressions in (A-5), the waves scattered in the sources are given by

$$a' = s' \frac{1 - \sigma' \overleftarrow{\rho}'}{1 - \overleftarrow{\rho}' \overrightarrow{\rho}'} \qquad\qquad b' = -s' \frac{\sigma' - \overrightarrow{\rho}'}{1 - \overleftarrow{\rho}' \overrightarrow{\rho}'}. \tag{A-6}$$

The expressions above only depend of the generator (s') and the source's load at z' (i.e. $\{\overleftarrow{\rho}', \overrightarrow{\rho}'\}$).

Discontinuity in the Interface

The variation of the wave amplitude a and the reflection coefficient Γ along z are piecewise continuous functions in a multilayered medium due to finite discontinuities produced at the interfaces between adjacent TLs.

To determine this discontinuty, we base our demonstration on the continuity of voltage and current function at every point of a source-free TL. Hence, considering the interface

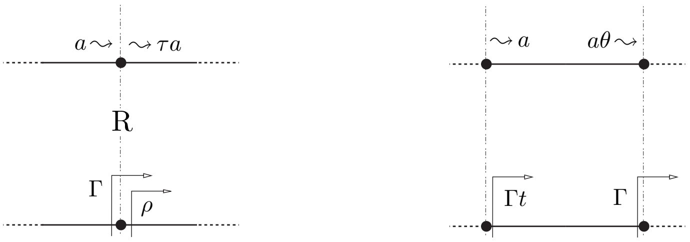

(a) “Jump”. (b) “Shift”.

Figure A.2: Wave and reflection coefficient propagation (a) through an interface between adjacent TLs and (b) along a TL.

in Fig. 4.2(a), the continuity equations can be written using the identities of (A-2) as

$$\begin{aligned} a(1+\Gamma) &= \tau a(1+\rho) \\ \frac{1-R}{1+R}a(1-\Gamma) &= \tau a(1-\rho) \end{aligned}$$

where R is the Fresnel reflection coefficient [18, §2.1.2] calculated from the characteristic impedance of the adjacent TLs*. After some simple manipulations in the above equations, τ can be found in terms of Γ and the latter in terms of ρ:

$$\tau = \frac{1-R\Gamma}{1-R} \tag{A-7a}$$

$$\frac{\Gamma}{R} = \frac{1+\rho/R}{1+\rho R} \tag{A-7b}$$

where it is easily verified that $\Gamma \to R$ and $\tau \to (1+R)$ as $|\rho| \to 0$. As a matter of fact, the function ρ is calculated by shifting the reflection coefficient from the next interface in the way shown in Fig. 4.2(b):

$$a \longrightarrow a\theta \tag{A-8a}$$

$$\Gamma t \longleftarrow \Gamma \tag{A-8b}$$

with

$$\theta = \mathrm{e}^{-\gamma h} \qquad\qquad t = \theta^2 = \mathrm{e}^{-2\gamma h}.$$

Iterative Evaluation of Characteristic Coefficients at the Interfaces

Regarding the results of the previous subsection, the evaluation of the $\{\Gamma, \tau\}$ directed towards positive $\{\overrightarrow{\Gamma}, \overrightarrow{\tau}\}$ and negative $\{\overleftarrow{\Gamma}, \overleftarrow{\tau}\}$ z-axis can be performed *iteratively* starting from the BCs

---

[*] Represents the reflection coefficient in the interface when the second TL is infinite or matched.

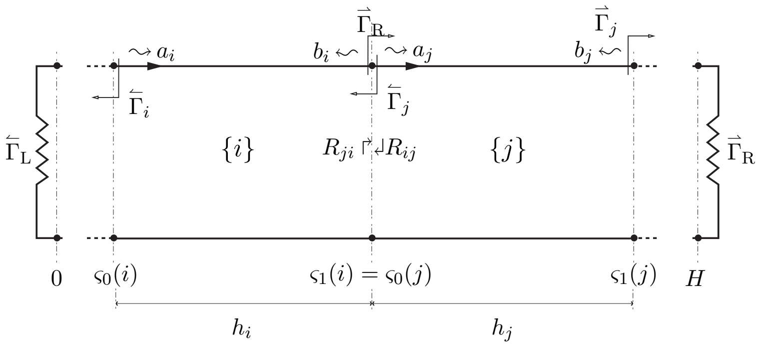

Figure A.3: Transition between adjacent TLs.

(defined in terms of reflection coefficients $\overleftarrow{\Gamma}_{\mathrm{L}}$ and $\overrightarrow{\Gamma}_{\mathrm{R}}$) imposed on the outermost interfaces. Let us consider two TLs, denoted with i and j from Fig. A.3, representing in general two *adjacent* TLs of a multilayered structure. The values for Γ and τ at each interface can be obtained in the following order:

$$a_i \to a_j \qquad \cdots \leftarrow \overrightarrow{\Gamma}_i \leftarrow \overrightarrow{\Gamma}_j \leftarrow \cdots \leftarrow \overrightarrow{\Gamma}_{\mathrm{R}} \tag{A-9}$$

$$b_i \leftarrow b_j \qquad \overleftarrow{\Gamma}_{\mathrm{L}} \to \cdots \to \overleftarrow{\Gamma}_i \to \overleftarrow{\Gamma}_j \to \cdots \tag{A-10}$$

where the transition from one element to the next is performed using (A-7) and (A-8). More specifically:

$$\overrightarrow{\tau}_j = \frac{a_j}{a_i} = \frac{1 - R_{ji}\overrightarrow{\Gamma}_i}{1 - R_{ji}}\theta_i \qquad \overrightarrow{\tau}_i = \frac{b_i}{b_j} = \frac{1 - R_{ij}\overleftarrow{\Gamma}_j}{1 - R_{ij}}\theta_j \tag{A-11}$$

and

$$\overrightarrow{\Gamma}_i = \frac{\overrightarrow{\Gamma}_j t_j + R_{ji}}{1 + \overrightarrow{\Gamma}_j t_j \, R_{ji}} \qquad \overleftarrow{\Gamma}_j = \frac{\overleftarrow{\Gamma}_i t_i + R_{ij}}{1 + \overleftarrow{\Gamma}_i t_i \, R_{ij}} \tag{A-12}$$

where

$$R_{ji} = \frac{Z_j - Z_i}{Z_j + Z_i} = -R_{ij} \qquad \frac{Z_j}{Z_i} = \frac{1 - R_{ji}}{1 + R_{ji}} \tag{A-13}$$

denote the Fresnel reflection coefficient.

About the Reflection Coefficient

According to the definition of incident and reflected waves, given in (A-2), the reflection coefficient Γ is calculated with respect to the characteristic impedance Z of the current TL. The value of Z is in general complex (e.g. lossy TL or evanescent waves in TL under cutoff) which makes Γ an unbounded function. Hence, given a reference impedance Z, let us derive what impedances $\mathcal{Z}$ will keep the reflection below/over unity.

Suppose an impedance $\mathcal{Z} = \mathcal{R} + \mathrm{j}\mathcal{X} = \rho \mathrm{e}^{\mathrm{j}\varphi}$. The reflection coefficient with respect to a complex impedance $Z = R + \mathrm{j}X = r\mathrm{e}^{\mathrm{j}\phi}$ is calculated as

$$\Gamma = \frac{\mathcal{Z} - Z}{\mathcal{Z} + Z} = \frac{p-1}{p+1} \tag{A-14}$$

where $p = \frac{\mathcal{Z}}{Z} = \frac{\rho}{r}\mathrm{e}^{\mathrm{j}(\varphi-\phi)}$ is the normalized impedance. In this general definition we can not guarantee that the reflection coefficient will remain bounded to one. The region in the normalized p-plane that satisfies $|\Gamma| \leq 1$ is defined by

$$|p-1| \leq |p+1|.$$

Considering the complex plane in Fig. 4.4(a), the latter condition is satisfied by all p values in within the real positive semiplane $\mathrm{Re}\, p > 0$ (shaded region). A glance to Fig. 4.4(a) suffices to verify that the ray $|p-1|$ will always be shorter than the ray $|p+1|$ in this region. Analogously, the p-regions for $|\Gamma| \geq 1$ can be deduced from the illustration.

Taking into account the phase of p in the positive semiplane changes within $|\varphi - \phi| < \frac{\pi}{2}$, we can deduce the following equivalent limits on the impedance phase:

$$\left(-\frac{\pi}{2} + \phi\right) < \varphi < \left(\frac{\pi}{2} + \phi\right). \tag{A-15}$$

The previous condition determines the region of impedances in the $\mathcal{Z}$-plane mapping to $|\Gamma| < 1$, provided that $\mathcal{R} \geq 0$. This has been illustrated in Fig. 4.4(b) with a shadowed surface. Given a reference impedance, its phase ϕ will define the line (dashed line) that delimits the different impedance regions and where $|\Gamma| = 1$. Over one semi-infinite perpendicular line (with angle ϕ, here in the first quadrant), the phases of the actual and reference impedance are the same and therefore

$$|\Gamma| = \left|\frac{\rho - r}{\rho + r}\right|$$

or eventually $|\Gamma| = 0$ if the magnitude coincide too. In other the semi-infinite perpendicular line (with angle $\pi + \phi$, here in the forth quadrant), the phase difference reaches π, thus

$$|\Gamma| = \left|\frac{\rho + r}{\rho - r}\right|$$

which tends to infinity with identical modules $\rho = r$. In order to get this point within the plane of realizable impedances ($\mathcal{R} \geq 0$) the reference impedance must have a phase $\frac{\pi}{2} \leq \phi \leq \pi$.

Finally, in Fig. 4.4(b), we have evaluated $|\Gamma|$ for an impedance with constant magnitude.

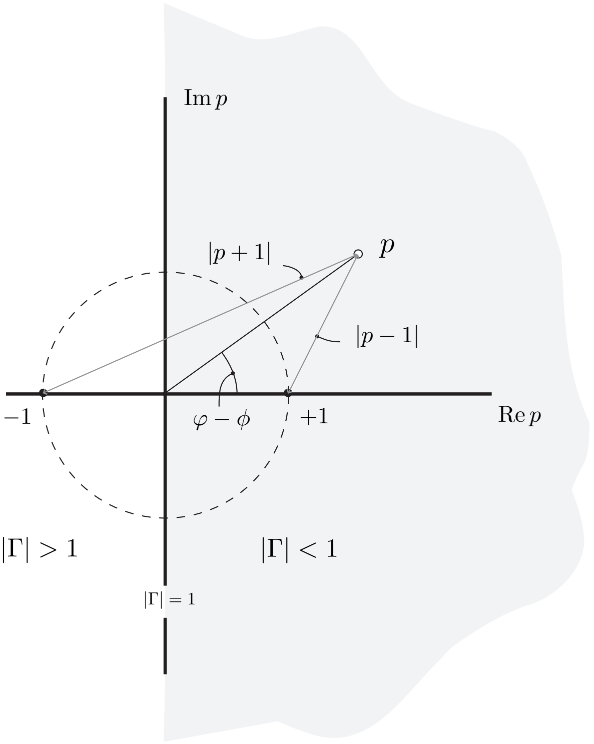

(a) p-plane.

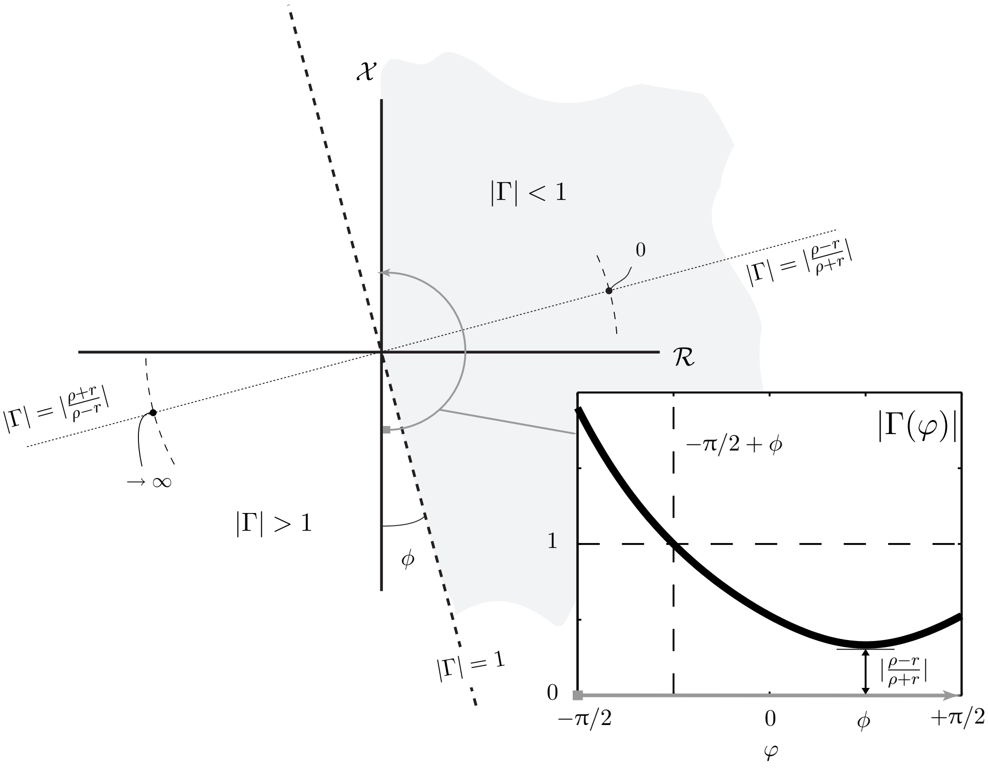

(b) $\mathcal{Z}$-plane.

Figure A.4: Determination of impedance regions giving $|\Gamma| \lesseqgtr 1$ in function of the reference impedance.

References

[1] N. K. Das and D. Pozar, “A generalized spectral-domain Green’s function for multilayer dielectric substrates with application to multilayer transmission lines,” *IEEE Trans. Microwave Theory Tech.*, vol. 35, pp. 326–335, Mar. 1987.

[2] K. A. Michalski and J. R. Mosig, “Multilayered media Green’s functions in integral equation formulations,” *IEEE Trans. Antennas Propagat.*, vol. 45, pp. 508–519, Mar. 1997.

[3] Y. L. Chow, N. Hojjat, S. Safavi-Naeini, and R. Faraji-Dana, “Spectral green’s functions for multilayer media in a convenient computational form,” *IEE Proc. Microwaves, Antennas and Propagation*, vol. 145, pp. 85–91, Feb. 1998.

[4] D. Llorens del Río, “Electromagnetic analysis of 2.5D structures in open layered media,” Ph.D. dissertation, École Polytechnique Fédérale de Lausanne, Lausanne, 2005. [Online]. Available: http://library.epfl.ch/theses/?nr=3183

[5] T. M. Grzegorczyk, “Integrated 3D antennas for millimeter-wave applications: Theoretical study and technological realization,” Ph.D. dissertation, Ecole Polytecnique Fédéral de Lausanne, 2000, thése No. 2299.

[6] R. E. Collin, *Foundations for Microwave Engineering*, 2nd ed. McGraw-Hill, 1992.

[7] E. Simsek, Q. H. Liu, and B. Wei, “Singularity subtraction for evaluation of Green’s functions for multilayer media,” *IEEE Trans. Microwave Theory Tech.*, vol. 54, no. 1, pp. 216–225, Jan. 2006.

[8] N. J. Higham, *Accuracy and Stability of Numerical Algorithms*, 2nd ed. Society for Industrial and Applied Mathematics, 2002.

[9] A. Álvarez-Melcón, “Application of the integral equation technique to the analysis and synthesis of multilayered printed shielded microwave circuits and cavity backed antennas,” Ph.D. dissertation, École Polytechnique Fédérale de Lausanne, Switzerland, 1998, thèse No. 1901.

[10] S.-G. Pan and I. Wolff, “Scalarization of dyadic spectral green’s functions and network formalism for three-dimensional full-wave analysis of planar lines and antennas,” *IEEE Trans. Microwave Theory Tech.*, vol. 42, no. 11, pp. 2118–2127, Nov. 1994.

[11] P. Crespo-Valero, M. Mattes, I. Stevanović, and J. R. Mosig, “A numerically stable transmission line model for multilayered Green’s functions,” in *Proc. IEEE Antennas and Propagation Society Symposium (AP-S)*, vol. 3A, Washington DC, July 3–8, 2005, pp. 200–203.

[12] G. V. Eleftheriades and J. R. Mosig, “On the network characterization of planar passive circuits using the method of moments,” *IEEE Trans. Microwave Theory Tech.*, vol. 44, pp. 438–445, Mar. 1996.

[13] J. R. Mosig, “Integral-equation technique,” in *Numerical Techniques for Microwave and Millimeter-Wave Passive Structures*, T. Itoh, Ed. New York: Wiley, 1989, ch. 3, pp. 133–213.

[14] F. Ling, J. Liu, and J.-M. Jin, “Efficient electromagnetic modeling of three-dimensional multilayer microstrip antennas and circuits,” *IEEE Trans. Microwave Theory Tech.*, vol. 50, no. 6, pp. 1628–1635, June 2002.

[15] A. Álvarez-Melcón, J. R. Mosig, and M. Guglielmi, “Efficient CAD of boxed microwave circuits based on arbitrary rectangular elements,” *IEEE Trans. Microwave Theory Tech.*, vol. 47, pp. 1045–1058, July 1999.

[16] “Ansoft corporation.” [Online]. Available: http://www.ansoft.com/

[17] L. B. Felsen and N. Marcuvitz, *Radiation and Scattering of Waves.* Englewood Cliffs, NJ: Prentice Hall, 1973.

[18] W. C. Chew, *Waves and Fields in Inhomogeneous Media.* New York: Van Nostrand Reinhold, 1990.

5 Analysis of Multilayered Boxed Printed Circuits

> He who loves practice without theory is like the sailor who boards ship without a rudder and compass and never knows where he may cast.
>
> *(Leonardo da Vinci)*

The current trends in Radio Frequency (RF) and microwave circuits and high speed electronics search for high-performance, adequate EMC behavior, low cost and miniaturized chip-type passive devices. These specifications can be matched by multilayered printed circuits integrated inside metallic enclosures for mechanical and environmental protection [1].

We will denote in general these structures, illustrated in Fig. 5.1, as multilayered boxed printed circuits*. It contemplates a good part of *passive* components found in the omnipresent MMICs, frequently encountered in industry, such as filters, phase shifters, power dividers, etc.

This EM problem motivated the implementation of a *dedicated* software tool for the *efficient* analysis of these topologies. The simulation tool we developed was called `MAMBO`, which stands for siMulation of Arbitrary Multilayer BOxed printed circuits [2].

The structure in Fig. 5.1 is a particular case of printed circuit in bounded layered media. Hence, the EM simulation of these devices can be performed using a specialization of our generic method, described in previous chapters, for perfect electric boundary conditions on a rectangular contour. The formulation for this type of boundaries was already developed in §3.5.1, providing an analytical solution. Moreover, the linear subsectional basis functions are very well suited for the modeling of currents on arbitrarily shaped printed circuits. In addition, a realistic simulation must also incorporate the effect of losses in the structure. A multiport network characterization of the device can use the strategy described in §2.6, provided that the ports access are small coaxial-type feeding lines attached to the cavity walls.

The first part of this chapter presents a *review* of the most relevant published works concerning numerical techniques based on IE for the time-harmonic EM analysis of planar circuits including shielding effects. Based on this review, we present an outline a *mathematical formulation* in connection with the methods developed in previous chapters. A key concept in the method are the *modal series* which correspond to the reaction terms filling the MoM matrix. Questions about the acceleration of these series and its convergence will cover a big part of

---

*Although some terms as *shield*, *cavity*, *packaging* of *metallic enclosure* can be used as synonymous of box.

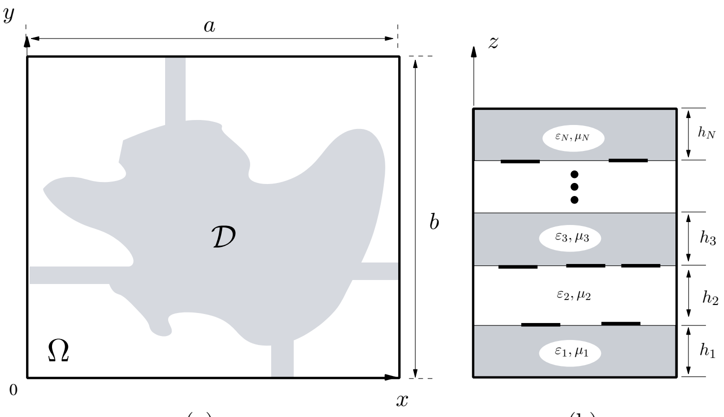

(a) (b)

Figure 5.1: Transverse (a) and longitudinal (b) cross section views of a multilayer boxed printed circuit.

the discussions. Then the modeling of *losses* will be addressed. It follows with details about the network characterization and the connection of lumped elements to the printed circuits. Finally, the chapter is closed with an extensive set of simulations of test-structures. This will serve to validate the method and to demonstrate the degree of accuracy and achieved performance by comparison with prototype measurements or simulations carried out with other EM solvers.

5.1 Review of Integral Equation Methods

The efficient evaluation of the GF is the key for the success of an IE technique. In our case, the multilayered cavity GF can be formulated mainly by means of two equivalent methods, namely, a modal expansion [3] or a set of images [4]. Other methods are usually refinements or clever combinations of these two techniques.

In the first case, the GF is expressed as a series expansion of rectangular waveguide modes. Assuming G is a generic (field or potential) GF component, this expansion comprises a double infinite trigonometric Fourier series

$$G = \sum_{m,n} \widetilde{G}(k_m, k_n) f(k_m, x, x') g(k_n, y, y'), \tag{5.1}$$

where f, g are products of trigonometric functions and k_m, k_n are discrete spectral components.

By virtue of Poisson's formula [5], an equivalent formulation for the Fourier series above can be found. Here, the effect of the side walls is represented by an infinite set of periodically spaced image sources radiating in a laterally unbounded medium [4, 6].

Both formulations, the Modal Expansion (ME) and the set of Images (IM), as presented in Table 5.1, have more advantages under certain conditions. The singular behavior in the

Formulation	Singular Behavior for $R \rightarrow 0$	BCs on the cavity walls
Modal Sum	By augmenting the number of modal terms	Naturally satisfied by each mode
Set of Images	Preserved on each image source	By increasing the number of images

Table 5.1: Quantitative comparison between modal and image-based formulations.

vicinity of the source is inherited from the equivalent quasi-static problem (low frequency) in the IM. The spectra of this singular response is represented by the tail of the ME providing a low convergent series. On the other hand, the BCs are achieved by each term of the ME while it is necessary to sum up a high number of images in the IM to fulfill them on the box walls.

The ME approaches are typically accelerated by extracting and evaluating separately the quasi-static (QS) part in the sense of Kummer's transformation [7]. In [8] the evaluation of the QS part is accelerated by obtaining an analytic sum of one of the double infinite series into exponentially decaying Bessel functions.

This strategy is also followed by hybrid approaches which take advantage of the dual representation of Table 5.1 and evaluate the QS part using image theory [9, 10]. The so-called Ewald technique can be also framed in this kind of hybrid methods. It has been traditionally used to accelerate the convergence of periodic problems [11] although it has also being applied, for instance, in an empty cavity problem [12]. The GF is transformed into two series with gaussian convergence, one involving images and the other one modal functions. The Ewald technique can be applied to the multilayer shielded structure [13], being computationally more expensive as it involves the approximation of spectral domain by the Generalized Pencil-of-Function method [14].

The ME series is also summed up efficiently using the Fast Fourier Transform (FFT) algorithm [15, 16] but it is only applicable to uniform meshes. Other numerical techniques are available for series accelerations as referred in Table 5.2.

The IM formulation allows the lateral wall effects on the circuit response to appear as a correcting term which can be added or removed from the unbounded case [17]. Some refinements of this method are made with the Truncated Set of Images technique [18] which sums up the images using weighting functions to satisfy the BCs on the walls with a truncated set of images.

A summary and references to all the methods involving ME and IM is presented in Table 5.2. Further improvements on this algorithm can also be achieved by adding other features like a wideband estimation of the EM response by means of a reduced order model of the multilayered media response [19] or reducing the number of unknowns of the MoM matrix by using higher order or entire domain BFs like in [20, 21] and [22–25].

Classification	Method	Comments	References
Modal Expansion	Direct Sum	Direct sum of modal expansion.	[3]
	QS Extraction + Kummer	Kummer's Transformation and acceleration of QS part using a special mathematical formulation.	[8, 26, 27]
	FFT	Limited to uniform meshes.	[15, 16]
	Other Numerical Techniques	Summation by parts, residue theorems and contour-integration, Shanks' transformation, Wynn's ϵ-algorithm, etc.	[28–30]
Set of Images	Side Walls Images	Direct sum.	[4, 6, 17, 31]
	Truncated Set of Images	Truncation and weighting of the image sum.	[18]
Hybrid	Hybrid approach	QS represented with IM.	[10]
	Ewald Transformation	Reduce to two rapidly convergent series. More efficient in empty cavities.	[12, 13]

Table 5.2: List of methods and some relevant publications for the formulation of multilayered rectangular cavity GF.

5.2 Formulation

The EM problem of Fig. 5.1 is formulated in terms of an EFIE where, unlike to §2.3, here an impedance (Leontovich) BC [32, p. 137] is imposed on the printed circuit surfaces. Hence, the new IE is given by

$$\hat{\mathbf{z}} \times \mathbf{E}^{\mathrm{i}} + \overleftrightarrow{\mathbf{G}}_{\mathrm{EE}} * \mathbf{J} = Z_{\mathrm{s}} \mathbf{J} \tag{5.2}$$

where the incident field $\mathbf{E}^{\mathrm{i}}$ is localized at the edge ports of the microstrip lines (§2.6), Z_{s} is the surface impedance of the printed circuit and $\overleftrightarrow{\mathbf{G}}_{\mathrm{EE}}$ represents the transverse components of the dyadic GF accounting for the metallic box and the multilayered media (§2.4 and §3.5.1). This modification of the EFIE will account for the ohmic losses in the metallizations of the planar circuit, as will be discussed in §5.4.

The resolution of the (5.2) is carried out by application of the MoM and the Galerkin procedure, as explained in §2.5. Some remarks follow.

The surface currents $\mathbf{J}$ on the printed circuits are approximated by a superposition of linear subsectional basis functions $\{\mathbf{b}_k\} \in D_k$ (§3.4.1) as

$$\mathbf{J} = \sum_k i_k \mathbf{b}_k, \tag{5.3}$$

where $\{i_k\}$ [A] are unknown current coefficients. This technique discretizes the surface of any arbitrary shaped circuit into rectangular and/or triangular cells forming a mesh $\bigcup_k D_k = \mathcal{D}$. The final MoM matrix is obtained by the difference of densely populated matrix $\mathbf{Z}$ and a sparse matrix $\mathbf{\Lambda}$. The algebraic system of equation is the following

$$\mathbf{u} = [\mathbf{Z} - \mathbf{\Lambda}] \cdot \mathbf{i}, \tag{5.4}$$

where $\mathbf{u}$ and $\mathbf{i}$ are column vectors that contain the excitation (§2.6) and the unknown current coefficients, respectively. The first matrix corresponds to a generalized impedance matrix containing the reactions [(2.24) in §2.5] taking place in basis functions expanding currents on a PEC surface. Each term of this matrix is evaluated as follows

$$R_{\mathrm{EE}}(k,l) = Z_{kl} = \int_{D_k} \mathbf{b}_k(\mathbf{r}) \int_{D_l} \overleftrightarrow{\mathbf{G}}_{\mathrm{EJ}}(\mathbf{r}|\mathbf{r}') \mathbf{b}_l(\mathbf{r}') \, \mathrm{d}S \, \mathrm{d}S' = \langle \mathbf{b}_k, \overleftrightarrow{\mathbf{G}}_{\mathrm{EJ}} * \mathbf{b}'_l \rangle. \tag{5.5}$$

The effect of losses in the metallizations is included in the second matrix $\mathbf{\Lambda}$. Every entry of this matrix integrates every pair of BFs as

$$\Lambda_{kl} = Z_{\mathrm{s}} \int_{D_k \cap D_l} \mathbf{b}_k(\mathbf{r}) \mathbf{b}_l(\mathbf{r}') \, \mathrm{d}S. \tag{5.6}$$

This matrix is sparse because all non-overlapping subsectional basis function will vanish.

Finally, solving the linear system (5.4) provides the solution to the unknown currents (5.3). This result is used to determine (see §2.6): a) the induced surface currents for a given excitation scheme (2.26b) and b) a multiport network characterization of the circuits in terms of scattering parameters $\mathcal{S}$ (2.34).

5.3 Modal Series

In a transverse boundary problem, as demonstrated in Chapter 3, the explicit calculation of GF is not needed since the reaction terms (5.5) can be directly formulated [33]. In general, the reaction between two BFs k, l belonging to any type of sources was anticipated in (3.5) of §3.2 as

$$R_{\mathrm{PQ}}(k,l) = \langle\, \mathbf{b}_k, \overleftrightarrow{\mathbf{G}}_{\mathrm{PQ}} * \mathbf{b}'_l \,\rangle = \sum_i \mathcal{L}\big(P_i^Q(\omega, z_k, z_l)\big)\, C_{\mathrm{P}}(k,i) C^*_{\mathrm{Q}}(l,i). \tag{5.7}$$

The reaction is therefore formulated as series extended to all the eigenmodes of the transverse boundary problem (here, a rectangular waveguide) and we will refer to it as *modal series*. The index i enumerates each mode in the spectrum sorted following an order of increasing cutoff frequencies. Each term of the series can be separated in two parts according to the dependency on the longitudinal (z) or transverse ($x, y; x', y'$) coordinates. The first part, P_i^Q, determines the propagation of the ith mode along the z-axis (§2.4). It is computed using a transmission line model (TLMo) *for each mode and frequency*, as discussed in Chapter 4. The second part consists of the product of the OIs defined over the ith mode and the source and observer BFs, respectively. It should be underlined that the source and observer contributions are *separated* and *frequency independent*. The analytic solution to these integrals were also derived in Chapter 3.

The major disadvantage is that the modal series are slowly convergent [5, 29], specially when the reaction takes place between two nearby BFs ($|\mathbf{r} - \mathbf{r}'| \to 0$). Some arguments that explain this behavior can be found in the discussion presented in Table 5.1. The sum of slowly converging series is performed using special acceleration techniques based on Kummer's transformation and will be treated in the following sections.

5.3.1 Kummer's Transformation

Ernst Kummer's method [7, 34] is a classical series acceleration technique that may be used to accelerate the convergence of modal series. The idea is to subtract from a given convergent series $\sum a_i$ another equivalent series $\sum b_i$, whose sum $B = \sum_{i\geq 0} b_i$ is well known, provided that both series' *terms* are *asymptotically* proportional

$$\lim_{i\to\infty}\left(\frac{a_i}{b_i}\right) = c \neq 0, \tag{5.8}$$

with a non-zero constant c. Applying the Kummer's transformation on $\sum a_i$ as

$$\sum_{i=0}^{\infty} a_i = c\sum_{i=0}^{\infty} b_i + c\sum_{i=0}^{\infty}(a_i - b_i) = cB + \sum_{i=0}^{\infty}\left(1 - c\frac{b_i}{a_i}\right) a_i, \tag{5.9}$$

expresses the series sum in terms of a new series, on the right hand side, which converges faster since $1 - cb_i/a_i$ tends to 0 as i tends to infinity [35].

Before transforming the series sum, let us first rewrite (5.7) using a reduced notation:

$$R = \sum_{i=0}^{\infty} g_i \, C_i C_i'^{*}, \tag{5.10}$$

where $g_i \equiv \widetilde{G}_{\mathrm{PQ}i}(\omega, z_k, z_l')$ corresponds to the spectral domain GF and $C_i \equiv C_{\mathrm{P}}(k,i)$, $C_i' \equiv C_{\mathrm{Q}}(l,i)$ complex values representing the solutions to the OIs over observer and source BFs, respectively. Suppose an equivalent series

$$\widehat{R} = \sum b_i = \sum_{i=0}^{\infty} \hat{g}_i \, C_i C_i'^{*}. \tag{5.11}$$

Using an asymptotic function of the spectral domain GF satisfying (5.8) as

$$\lim_{i\to\infty} \left(\frac{g_i C_i C_i'^{*}}{b_i} \right) = \lim_{i\to\infty} \frac{g_i}{\hat{g}_i} = 1 \tag{5.12}$$

allows us to apply the Kummer's transformation (5.9) on (5.10) and evaluate the reaction as

$$R = \widehat{R} + \sum_{i=0}^{\infty} (g_i - \hat{g}_i) \; C_i C_i'^{*} = \widehat{R} + \widetilde{R}, \tag{5.13}$$

where $\widetilde{R}$ converges faster. The equivalent series $\widehat{R}$ is called *quasi-static* and $\widetilde{R}$ is denoted as the *dynamic* series. These names will be justified later. Usually, this transformation is done separately for series comprising groups of TE and TM modes resulting in four different series, namely, two quasi-static and two dynamic.

5.3.2 Asymptotic Sequences

Actually, there is an infinite number of sequences $\{\hat{g}_i\}$ approaching asymptotically $\{g_i\}$ but not all of them can build an equivalent series whose sum is known or presents an advantage with respect to the original series. Here, we will rather discuss the approach followed in [8, 33, 36, 37] aiming to give a wider perspective about the series acceleration: its advantages and limitations.

In order to define a suitable $\{\hat{g}_i\}$, we must first recall from Chapter 4 that the ith mode component of the spectral domain GF $\{g_i\}$ is calculated by solving an equivalent transmission line problem. Depending on the source, it corresponds to the voltage (resp. current) $V(\omega)$ (resp. $I(\omega)$) frequency response of the equivalent circuit problem between the interfaces z and z' to a current (resp. voltage) excitation.

Suppose that an electric source excites the structure of Fig. 5.2(a) at z'. The equivalent circuit problem, as represented in Fig. 5.2(b), is therefore excited with a current generator ($u = 0$ V,

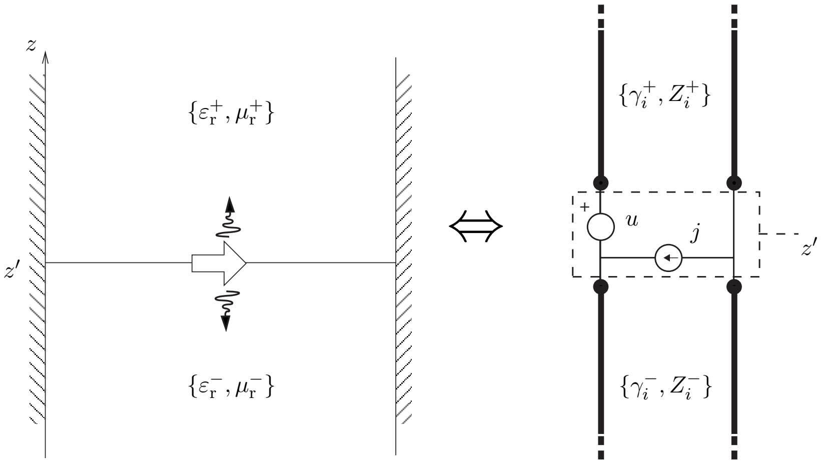

(a) (b)

Figure 5.2: Simplified scheme for the resolution of a quasi-static problem. (a) Evanescent field at the interface between two layers; (b) Equivalent circuit consisting of two semi-infinite TLs.

$j = 1$ A). For each mode, the spectral GF component is calculated as the voltage induced at the same point $z = z'$ (i.e. $\hat{g}_i \equiv \widehat{V}_i$). In addition, this calculation will assume that the propagation constant for each mode is equal to its cutoff wavenumber:

$$\gamma_i = \kappa_i. \tag{5.14}$$

The circuit is easily reduced to the parallel connection of the transmission line impedances loading the generator. Substituting the values of $Z^{\pm}$ for the TE or TM waves (Table 3.8), the voltage response at $z = z'$ can be expressed as

$$\widehat{V}_i^{\mathrm{TE}}(\omega) = \frac{\mathrm{j}\omega\mu_{\mathrm{e}}}{\kappa_i} \tag{5.15a}$$

$$\widehat{V}_i^{\mathrm{TM}}(\omega) = \frac{\kappa_i}{\mathrm{j}\omega\varepsilon_{\mathrm{e}}} \tag{5.15b}$$

where

$$\varepsilon_{\mathrm{e}} = \varepsilon_0 \left(\varepsilon_{\mathrm{r}}^{+} + \varepsilon_{\mathrm{r}}^{-}\right)$$

$$\mu_{\mathrm{e}} = \mu_0 \frac{\mu_{\mathrm{r}}^{+}\mu_{\mathrm{r}}^{-}}{\mu_{\mathrm{r}}^{+} + \mu_{\mathrm{r}}^{-}}$$

are dielectric constants of an *equivalent* homogeneous dielectric medium. The resulting sequence

$$\{\hat{g}_i\} = \{\widehat{V}_i^{\mathrm{TE}}(\omega), \widehat{V}_i^{\mathrm{TM}}(\omega)\}$$

is actually asymptotic to $\{g_i\}$. To demonstrate this, let us tend both sequences with $i \to \infty$[†]

[†] Modes sorted by increasing cutoff frequency.

until

$$\kappa_i \gg k = \omega\sqrt{\mu\varepsilon}, \qquad (\omega_\mathrm{n} \ll 1)$$

ensures that the modes achieved are *evanescent.* These modes represent a *quasi-static* EM behavior since they do not propagate. The wave is instead attenuated exponentially in the proximity of the source at the rate of

$$\gamma_i = \alpha_i = \kappa_i\sqrt{1-\omega_\mathrm{n}^2} \approx \kappa_i\left(1 - \frac{\omega_\mathrm{n}^2}{2} - \frac{\omega_\mathrm{n}^4}{8}\cdots\right) \tag{5.17}$$

nepers per unit length, as deduced from Table 3.8. The evanescent modes are reactive and have a localized effect that is influenced only by the media near the source, as depicted in Fig. 5.2(a). Under these circumstances the sequence $\{\hat{g}_i\}$ converges to $\{g_i\}$, provided that (5.14) corresponds to the first term of the Taylor expansion of (5.17).

Let us consider the TM waves generated by an electric source on a two-dielectric filled cavity of square cross-section as shown in Fig. 5.3. Fig. 5.3(a) shows how the asymptotic $\widehat{V}_i$ (dashed lines) tend to the voltage V_i sequences (in solid lines) as κ_i increases. When the dielectric thickness is doubled ($2h$), the difference between V_i and $\widehat{V}_i$ drops faster. The reason is that by separating the lower ground plane avoids reflections of the "less attenuated" evanescent modes and the *quasi-static conditions* simulated in Fig. 5.2(a) are matched earlier.

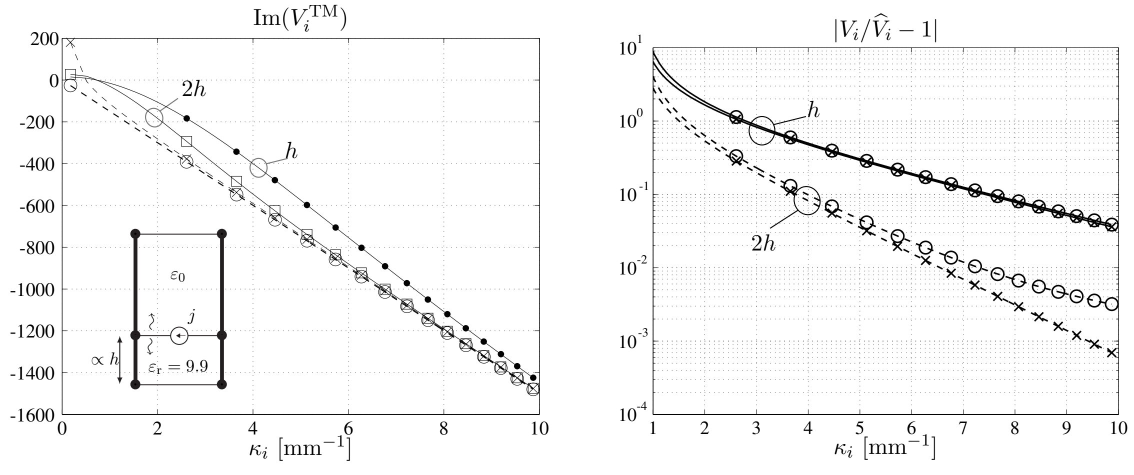

(a) Voltage induced in $z = z'$ @11GHz: V_i are solid lines; $\widehat{V}_i$ (○) and $\widehat{V}_i^{(1)}$ (×) in dashed lines.

(b) Relative error by the limit (5.12) definition, with respect to $\widehat{V}_i$ (○) and $\widehat{V}_i^{(1)}$ (×) sequences.

Figure 5.3: TM-voltage response generated by a current excitation with two different substrate thickness: h and $2h$. Dielectric filled cavity ($h = 0.4$ mm, $\varepsilon_\mathrm{r} = 9.9$) with a 25.4×25.4 mm^2 cross-section and height 4 mm.

Another factor that shall influence the attenuation of the evanescent modes is the dielectric constant of the substrates. For a given frequency, a *decrease* of ε_r will rise the cutoff-frequency in the dielectric and therefore increase the wave attenuation. Under these circumstances, the quasi-static conditions are also achieved faster as can be verified in the plots of Fig. 5.4.

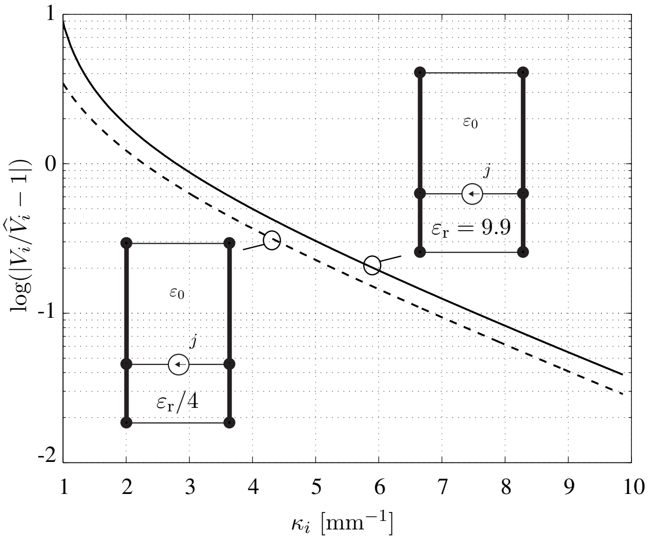

Figure 5.4: Relative error by the limit (5.12) definition, with respect to $\widehat{V}_i$ when the substrate permittivity is $\varepsilon_r = 9.9$ (solid line) or $\varepsilon_1/4$ (dashed line).

It is reasonable that the asymptotic sequence may be improved by augmenting the order of the approximation (5.14) and taking instead two terms of (5.17) as

$$\gamma_i = k_i \left[1 - \frac{1}{2} \left(\frac{\omega\sqrt{\mu\varepsilon}}{\kappa_i} \right)^2 \right]. \tag{5.18}$$

The new asymptotic sequences are plotted with × markers in Fig. 5.3 and are expressed by [33]

$$\widehat{V}_i^{(1),\mathrm{TM}} = \widehat{V}_i^{\mathrm{TM}} - \frac{E}{2} \frac{\mathrm{j}\omega\mu_0}{\kappa_i} \tag{5.19}$$

where E is a constant. This approach produces a small improvement in the convergence rate that, in our opinion, is not worthwhile compared to the added complexity of the new expressions.

Finally, equivalent expressions for (5.15) can be found for magnetic sources [37] by exciting the circuit of Fig. 5.2(b) with the voltage generator ($u = 1$ V, $j = 0$ A) and collecting the current wave at the same point.

5.3.3 Quasi-static Series

The quasi-static series in a reaction taking place at $z = z'$ with an *electric* source is obtained by substituting the asymptotic sequences (5.15) into (5.11):

$$\widehat{R}_{\mathrm{E}}(k,l) = \mathrm{j}\omega\mu_{\mathrm{e}} A^{\mathrm{TE}}(k,l) + \frac{1}{\mathrm{j}\omega\varepsilon_{\mathrm{e}}} B^{\mathrm{TM}}(k,l) \tag{5.20a}$$

and analogously, with a *magnetic* source as

$$\widehat{R}_{\mathrm{H}}(k,l) = \frac{1}{\mathrm{j}\omega\mu_{\mathrm{e}}} B^{\mathrm{TE}}(k,l) + \mathrm{j}\omega\varepsilon_{\mathrm{e}} A^{\mathrm{TM}}(k,l) \tag{5.20b}$$

where the series

$$A(k,l) = \sum_i \frac{1}{\kappa_i} C(i,k) C^*(i,l) \tag{5.21a}$$

$$B(k,l) = \sum_i \kappa_i \, C(i,k) C^*(i,l) \tag{5.21b}$$

are *frequency independent.*

The analysis of the series arising in a real problem, including hundreds of BFs, would be cumbersome and the results difficult to interpret. Instead, the scenario has been simplified to a canonic test structure that contains a few BFs placed as illustrated in Fig. 5.5.

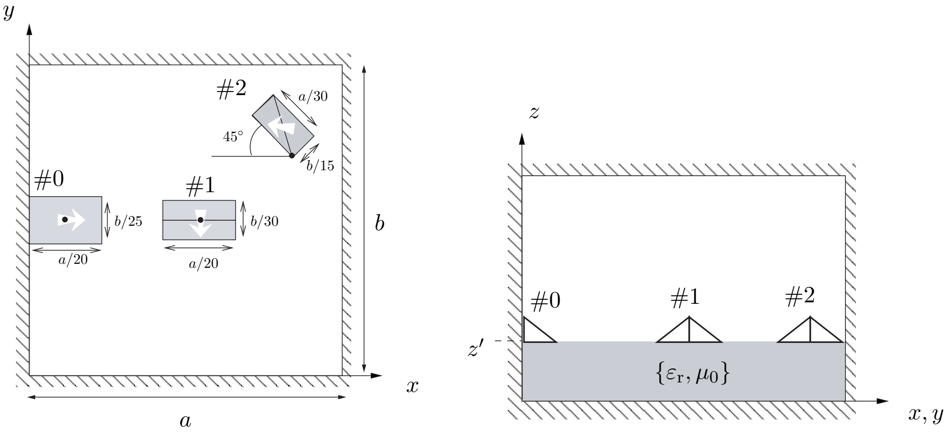

(a) Transverse view.

(b) Longitudinal view.

Figure 5.5: Test structure for series convergence studies. Rectangular PEC cavity $92 \times 92 \times 11.4$ mm^3 filled with a dielectric with permittivity $\varepsilon_{\mathrm{r}} = 2.33(1 - \mathrm{j}0.0012)$ and height $h = 1.57$ mm.

The transverse view of the structure, given in Fig. 5.5(a), shows three rectangular domains with sides $A \propto a, B \propto b$ subdivided into rectangular or triangular cells. Three linear subsectional BF (§3.4.1), symbolically represented with arrows, are defined over this simple mesh, namely a half-rooftop on the domain no. 0, a rooftop on no. 1 and a RWG BF on domain no. 2.

	$\mathrm{j}\omega\mu_\mathrm{e}A_M^{\mathrm{TE}}$	$B_M^{\mathrm{TM}}\,10^{-2}/(\mathrm{j}\omega\varepsilon_\mathrm{e})$
0–0	5.6653j	0.0014 − 1.6103j
1–1	1.4212j	0.0030 − 3.5577j
2–2	3.3407j	0.0027 − 3.1760j

Table 5.3: TE (TM) quasi-static series sums @2.5GHz up to M=1′001′129 (998′872) terms.

The MoM matrix resulting from this test problem consists of a three-by-three *symmetric* matrix, the latter being due to reciprocity. Hence, the study can be reduced to only six out of nine series filling the matrix. In this problem, the interaction between BFs take place on the same interface, therefore the series are subject to the decomposition in quasi-static and dynamic part as defined in (5.13). Let us study the quasi-static part of the TE and TM modal series at $\omega/(2\pi) = 2.5$ GHz.

The magnitude of the partial sums[†] of the quasi-static series, calculated with (5.20a), are represented in Fig. 5.6 for the TE and TM contributions, respectively. The representation of the six reactions is divided into two groups, namely the "self" and "cross" interactions depending whether the reaction takes place with itself or a different BF. The results show the series sums tend to a constant value as the number of modal terms added increases, which is a sign of convergence. The values achieved and the type of convergence differs for the self and cross interactions. In the first case, the reaction takes place within the same cell, resulting in larger values than those occurring between distant cells. The series arising in the self-interactions converge uniformly (absolute convergence) while in the cross-interactions exhibit an oscillatory behavior (Fourier convergence) that, in fact, converges faster than the previous case. Comparing the results obtained in these two groups reveal that the self-interaction series are the most critical. They have the slowest convergence and a non-converged sum, provided that they reach larger values, would cause an error in the MoM matrix with a significant impact in the linear system solution.

Within the self-interactions group, a first glance at Fig. 5.6(a) and Fig. 5.6(c) shows that the TM series converge slower compared to the equivalent TE case. This is corroborated by the comparison presented in Fig. 5.7. The figure of merit used there is a relative error with respect to a large sum, more specifically:

$$\epsilon_M(S_m) = \left\| \frac{S_m - S_M}{S_M} \right\|, \tag{5.22}$$

where S_M denotes the series sum up to $M \gg m$ terms. These reference sums are summarized in Table 5.3.

In conclusion, the most critical quasi-static series, considering the classification suggested throughout this section, corresponds to the TM series arising in the self-interactions in the MoM.

[†] Meaning $|S_m| = |\sum_{i=0}^{m} a_i|$.

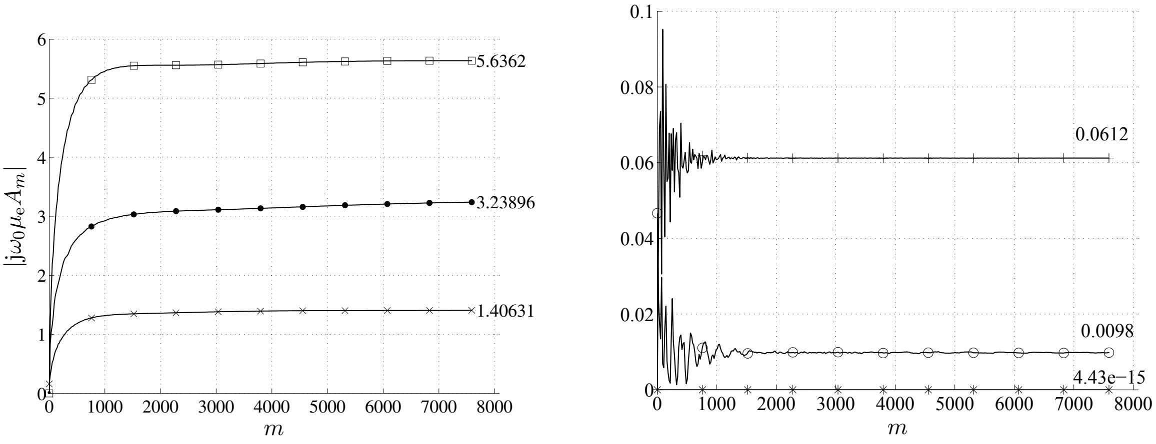

(a) Self-interactions with TE series.

(b) Cross-interactions with TE series.

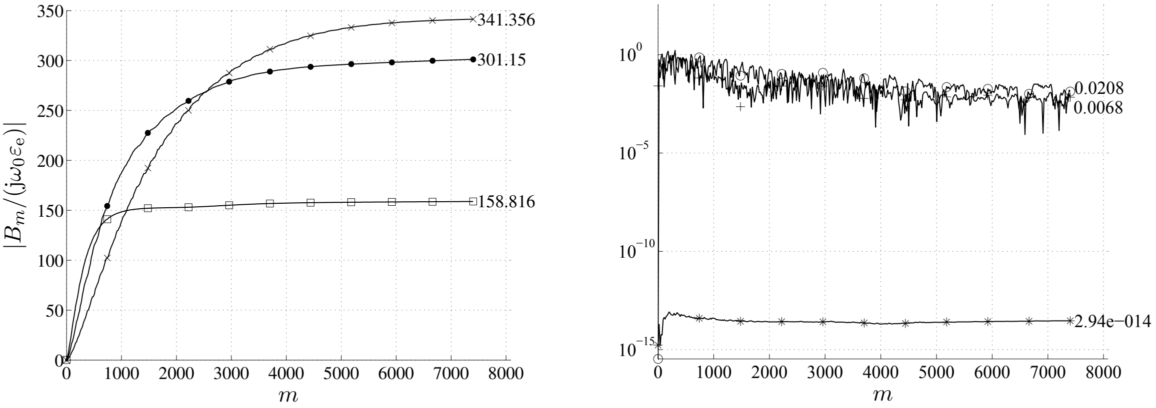

(c) Self-interactions with TM series.

(d) Cross-interactions with TM series.

Figure 5.6: Evolution of the partial sums in the quasi-static series. Self-interactions: 0–0 (□), 1–1 (×) and 2–2 (•); Cross-interactions: 0–1 (∗), 0–2(+) and 1–2(○).

5.3.4 Dynamic Series

The dynamic series are obtained by subtracting the quasi-static series (5.20a) from the original modal series, as demonstrated in (5.13).

Consider the dynamic series in the aforementioned test structure in Fig. 5.5. The partial sums of the TE and TM dynamic series are represented in Fig. 5.8. As expected from Kummer's transformation (§5.3.1), these series exhibit a fast convergence compared to the quasi-static ones. The plots display series having about three to five times improvement in the convergence rate between them. The type of convergence is analogous to the quasi-static case. The self-interactions have absolute convergence and a Fourier convergence is observed in the cross-interactions. Studying the results from the TE and TM contributions, again we find that the TM series are delayed with respect to the TE series requiring, in this case, about the double

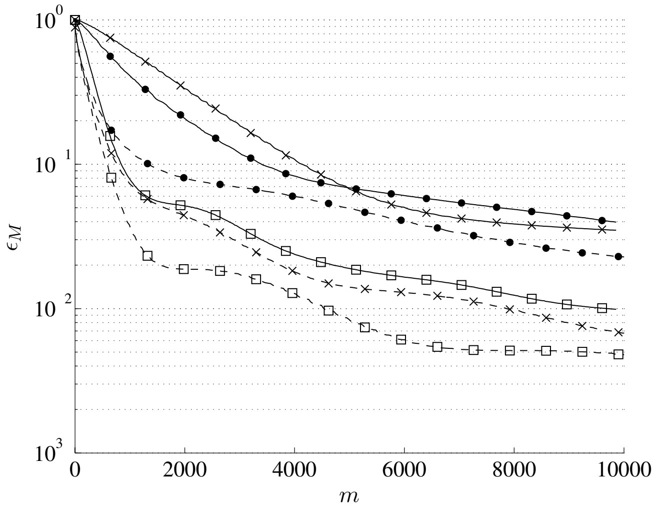

Figure 5.7: Rate of convergence for the TM/TE quasi-static series. The curves represent ϵ_M with respect to the values presented in Table 5.3 for each case. Only self-interactions are represented for the TE (dash lines) and TM (solid lines) series: 0–0 (□), 1–1 (×) and 2–2 (•).

of terms to converge.

Next example follows from the discussion in §5.3.2, where the convergence of the dynamic series was associated to the definition of the asymptotic sequence (i.e. the sequence in the quasi-static series). Consider the TM series of the dynamic part for the rooftop #1 defined at the center of our test structure (Fig. 5.5). This series will be calculated using two different types of asymptotic sequences, namely $\widehat{V}_i^{\mathrm{TM}}$ (5.15) and $\widehat{V}_i^{\mathrm{TM}*}$ (5.19), already studied in §5.3.2. The evolution of the dynamic series sum is represented in Fig. 5.9(a) and the convergence is monitored in Fig. 5.9(b) using a differential relative error defined as

$$\delta_\Delta(S_m) = \left\| \frac{S_m - S_{m-\Delta}}{S_{m-\Delta}} \right\|, \tag{5.23}$$

where Δ is a fixed integer step.

The series is calculated in problems using two different dielectric thicknesses, h and $2h$, in order to move away the reaction from the ground planes. The results confirm that the convergence rate is improved in the second case, as predicted during the discussion in §5.3.2. We can also observe a small improvement with the second order asymptotic sequence $\widehat{V}_i^{\mathrm{TM}*}$, although it is not so significant to justify its use in the quasi-static series. We have rather preferred $\widehat{V}_i^{\mathrm{TM}}$ that can be calculated easily.

To conclude this example we can state that the convergence rate of the dynamic series is related to the rate of convergence of the asymptotic sequences ($\widehat{V}_i$ and $\widehat{V}_i^{\mathrm{TM}*}$). This speed is specially dependent on the proximity of the BFs (z') to the ground plane and, in a minor degree, the

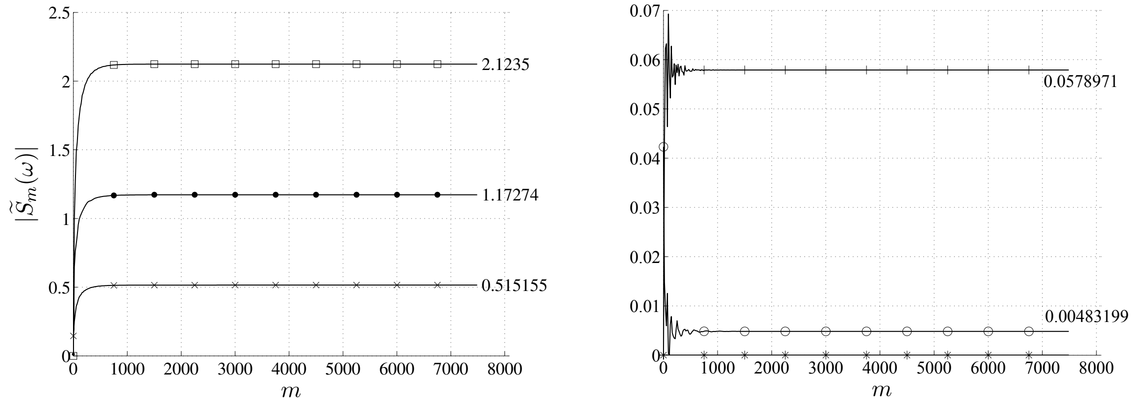

(a) Self-interactions with TE series (b) Cross-interactions with TE series

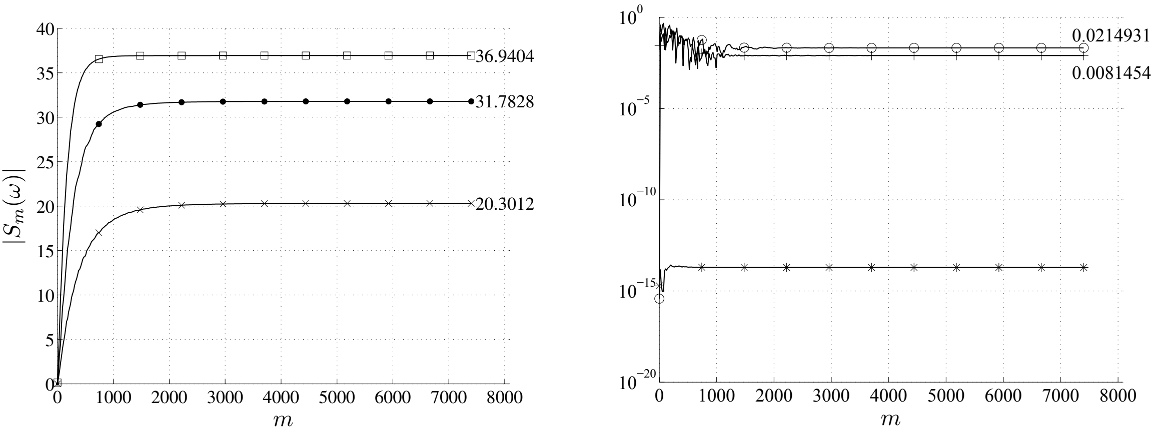

(c) Self-interactions with TM series (d) Cross-interactions with TM series

Figure 5.8: Sequence of partial sums for the TE/TM dynamic series. Self-interactions: 0–0 (□), 1–1 (×) and 2–2 (•); Cross-interactions: 0–1 (∗), 0–2 (+) and 1–2 (○).

dielectric material joining them (Fig. 5.4). Therefore, problems with high-permittivity and thin substrates over ground planes will deteriorate the convergence of these series.

5.3.5 Convergence

Up to this point, we have studied the series on a specific problem defined in Fig. 5.5 and we have performed some observations about its convergence. But the question now is, can we generalize this behavior to any scenario? For example, is there an impact of the position or size of the BF's domain on the convergence? and is it a dominant factor?

A partial answer is found straightforward in the series formulation (5.7) which shows that the size and position of the BFs are, in fact, implicit in the OIs. Therefore, there *is* an influence on the convergence of the series but its importance remains for the moment unknown.

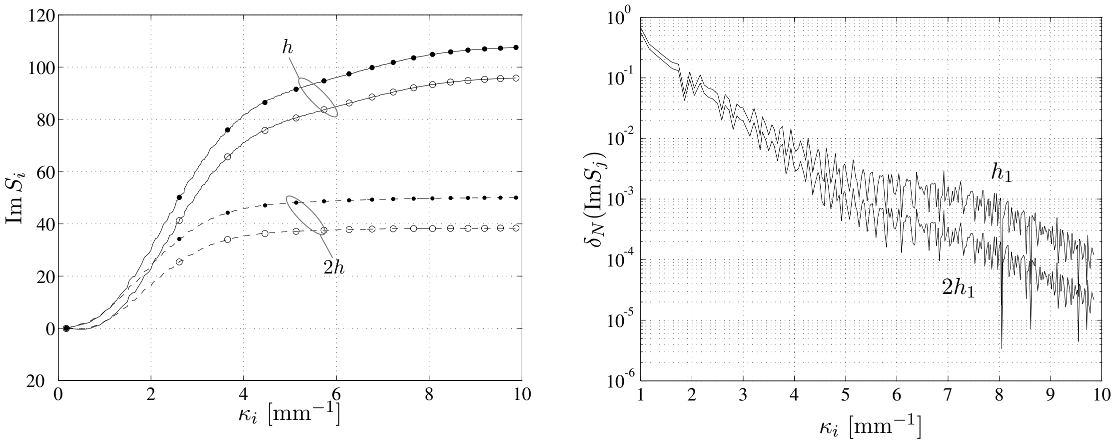

(a) TM series.

(b) Differential error $N = 20$.

Figure 5.9: (a) Partial sums of dynamic series for two substrate thickness: h (solid) and $2h$ (dash). Dynamic series constructed with the asymptotic form: $\widehat{V}_i^{\mathrm{TM}}$ (•) or $\widehat{V}_i^{\mathrm{TM}*}$ (∘). (b) Differential error δ_{20} measured on the imaginary part the dynamic series sum for two substrates with different thicknesses (only $\widehat{V}_i^{\mathrm{TM}}$ case is plotted here).

In order to find some answers to the second question we will perform some numerical experiments on our test structure. For the sake of clarity, we will only consider the worst converging series which corresponds, according to the previous sections, to the *self-interaction TM quasi-static* contribution. Therefore, the results could be extrapolated to the rest of the series since this represents the most limiting case.

Position:

Initially, we will analyze the series convergence of BFs defined at different positions, within the same plane, of the cavity. In Fig. 5.10 the position of the domains #1 and #2, with different orientation, are shifted in diagonal from the center to the cavity's corner. The series arising in the three different configurations are calculated up to $M = 998'872$ terms. These sums are complex numbers, due to the dielectric losses, and are displayed in Table 5.4. The first and second experiments with the domains # 1 and 2, respectively, correspond to the initial configuration of the test structure (Fig. 5.5), so the values here agree asymptotically with the final sums obtained in Fig. 5.6(c).

In Fig. 5.10, we plot the relative error (5.22) with respect to the reference sums given in Table 5.4. Aside from slight oscillations in the last experiment, the position of the cell does not show an important influence on the convergence of the series.

Experiment	No. 1 (center)	$B_M^{\mathrm{TM}} \times 10^{-2}/(\mathrm{j}\omega\varepsilon_\mathrm{e})$	No. 2 (lower node)	$B_M^{\mathrm{TM}} \times 10^{-2}/(\mathrm{j}\omega\varepsilon_\mathrm{e})$
1 (●)	$[0.5a, 0.5b]$	$0.0030 - 3.5577\mathrm{j}$	$[0.52a, 0.52b]$	$0.0027 - 3.1760\mathrm{j}$
2 (○)	$[0.75a, 0.25b]$	$0.0030 - 3.5575\mathrm{j}$	$[0.8a, 0.8b]$	$0.0027 - 3.1772\mathrm{j}$
3 (×)	$[0.97a, 0.03b]$	$0.0028 - 3.3903\mathrm{j}$	$[0.92a, 0.92b]$	$0.0026 - 3.1323\mathrm{j}$

Table 5.4: Sum of TM quasi-static series up to $M = 998'872$ terms @2.5 GHz for different cell's positions.

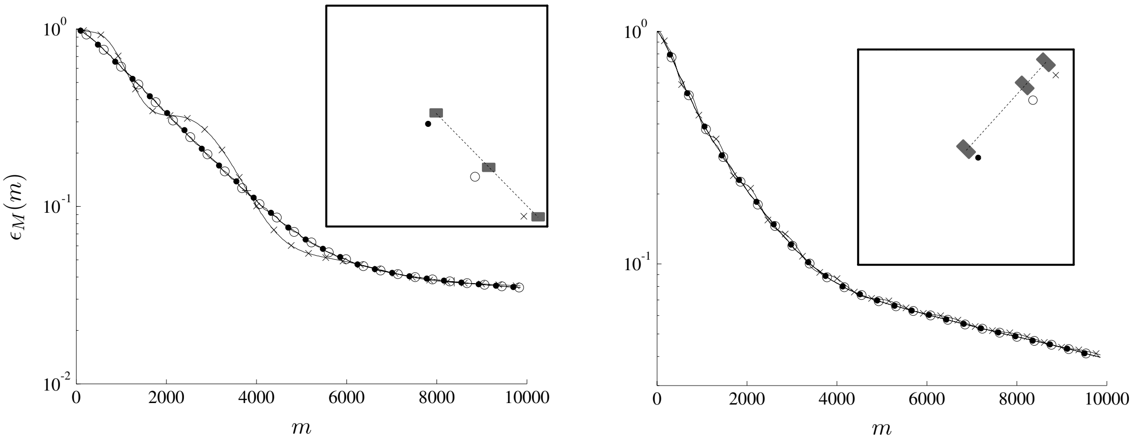

(a) Domain #1. (b) Domain #2.

Figure 5.10: Relative error in the convergence of the quasi-static TM series for different cell's positions. The position and orientation of the cells are indicated with different markers.

Size:

In a new configuration, depicted Fig. 5.11(a), we analyze the impact of the size of the BFs on the convergence. To proceed, we first define the relative surface of a domain as

$$r_\mathrm{S} = \frac{AB}{ab}, \tag{5.24}$$

where A, B and a, b are the lengths of the sides in the rectangular domains and the box cross-section, respectively.

In addition to the original scenario in Fig. 5.5, two more are considered by doubling ($k = 2$) and halving ($k = 1/2$) the dimensions A and B, simultaneously. According to the reference dimensions, the relative surface of each domain in function of the scale factor is

Domain	No. 1	No.2	No.3
$r_\mathrm{S} =$	$\frac{k^2}{500}$	$\frac{k^2}{600}$	$\frac{k^2}{450}$.

with values $k^2 = \{1, 2^2, \frac{1}{2^2}\}$ for each experiment. A study of the convergence for the quasi-static TM series is represented in Fig. 5.11. The relative error (5.22) is referred to the values

	$B_M^{\mathrm{TM}} \times 10^{-2}/(\mathrm{j}\omega_0\varepsilon_\mathrm{e})$		
No.	$k = 1/2$	$k = 1$	$k = 2$
0	$0.0027 - 3.2198\mathrm{j}$	$0.0014 - 1.6103\mathrm{j}$	$0.0007 - 0.8049\mathrm{j}$
1	$0.0060 - 7.1070\mathrm{j}$	$0.0030 - 3.5577\mathrm{j}$	$0.0015 - 1.7793\mathrm{j}$
2	$0.0053 - 6.3472\mathrm{j}$	$0.0027 - 3.1772\mathrm{j}$	$0.0013 - 1.5812\mathrm{j}$

Table 5.5: Sum of TM quasi-static series up to $M = 998'872$ terms @2.5 GHz for different cell's sizes.

in Table 5.5, and the differential error (5.23) is evaluated with a step $\Delta = 24$.

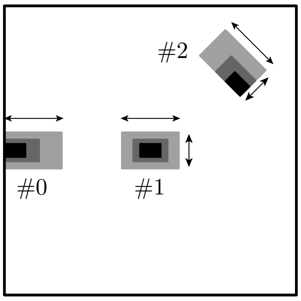

(a) Domains scaled.

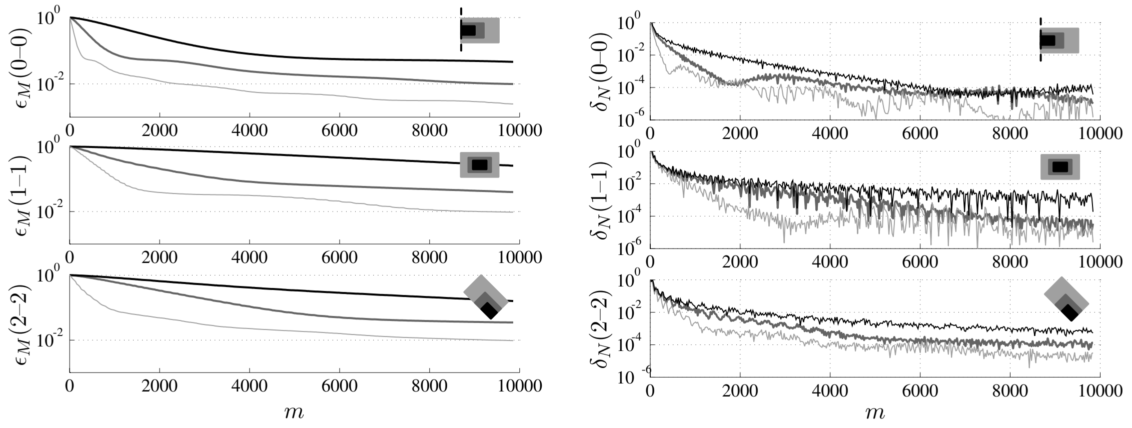

(b) Relative Error (M=998'872). (c) Differential Error (N=24).

Figure 5.11: Convergence ϵ_M, δ_N of the quasi-static TM series arising in the self-term interactions when the domains are scaled as with $k = 0.5, 1, 2$ @2.5 GHz. The different sizes considered of every domain are indicated with gray colors, from the smallest in black until the bigger in lighter gray.

The analysis of these plots reveals that an increase (decrease) on the relative surfaces rises (drops) the relative error in the first $2'000$ modes keeping afterwards a constant slope. The differential error also shows faster convergence in the cases with bigger r_S. Consequently, we can state that the convergence rate is highly influenced by the relative surface r_S of the cells.

5.3.6 Reaction Between Two Interfaces

Having a circuit structure printed on different layers represents an excellent example to study the convergence of the reaction series resulting in the interaction between BFs on different interfaces (i.e. with $z \neq z'$).

The goal of this section is to monitor the series convergence and to analyze the factors that determine this behavior in order to end up justifying the direct summation method adopted in this case.

Let us consider the test structure used so far but arranged in two different layers, as illustrated in Fig. 5.12. Our analysis will take into account the interactions between one source (labeled #1′), defined on the first interface (at z'), and two observers (#1 and #2) defined on the second interface (at z).

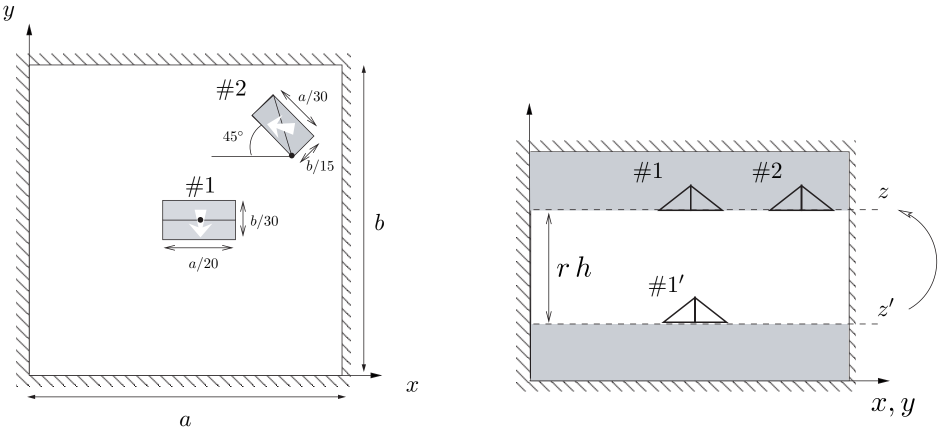

(a) Transverse view. (b) Longitudinal view.

Figure 5.12: Test structure. Rectangular cavity $32 \times 16 \times 4.08$ mm^3 filled with two dielectric slabs ($h_\mathrm{d} = 0.51$ mm, $\varepsilon_\mathrm{r} = 2.33(1 - \mathrm{j}0.0012)$) separated by an air gap ($h = 3.06$ mm).

In order to understand the convergence of these interactions, we must recall the formulation of the modal series (5.7) and rewrite them in a simplified form.

In this sense, the MoM reaction between BFs $o = \{1, 2\}$ and $1'$ is given by:

$$R_\mathrm{EE}(o, 1') = \sum_i V_i(z, z', \omega) C_i(o) C_i(1'). \tag{5.25}$$

In this equation, the OIs C_i are real values depending on the BF's footprint (x, y dependence) and the mode, while the term V_i incorporates the z and frequency dependence (ω) of the series. This function represents the voltage amplitude of the ith mode induced in z (upper layer) when it is excited in z' (lower layer). Notice then that according to the discussion in §5.3.2, its variation on different modes (i-dependence) will determine the convergence of the series.

Fig. 5.13 represents the variation of this function against different TM and TE modes. The plots in the figure correspond to the variation of the air gap distance h that separates the two interfaces in Fig. 5.12(b). We can observe that in general the strength of the function is reducing exponentially with the cutoff wavenumber. Moreover, an increment (reduction) of the gap distance h increases (decreases) this attenuation. This is caused by the natural attenuation expected in the evanescent modes (considered in large i series indices) which increases with the distance. It can be verified visually that the voltage function tends asymptotically to a single forward evanescent wave (represented in dashed lines) which is formulated as

$$V_i(z,z') \approx \mathrm{e}^{-\kappa_i |z-z'|} = \mathrm{e}^{-\kappa_i r h}, \tag{5.26}$$

where $r = \frac{1}{10}, \frac{1}{8}, \cdots, 8, 10$ is a real constant considered in this example to change the height of the gap.

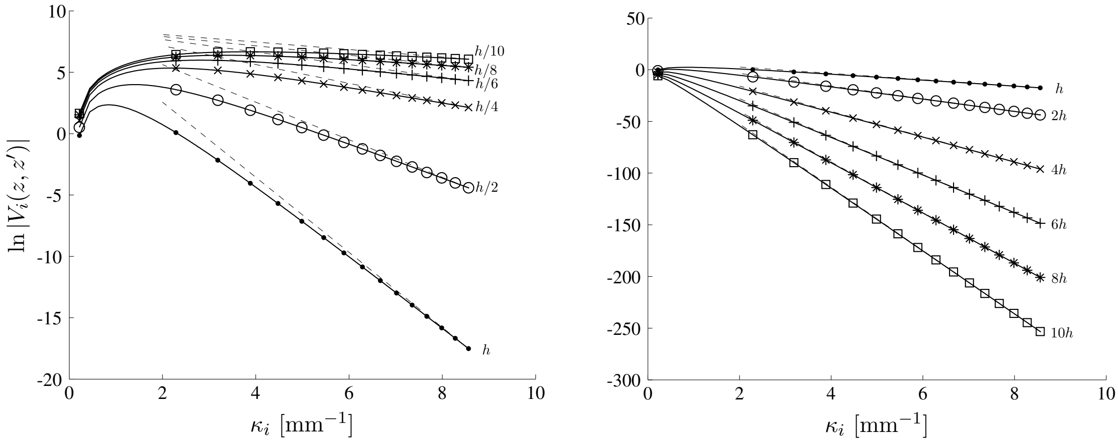

(a) TM, height $\leq h$.

(b) TM, height $\geq h$.

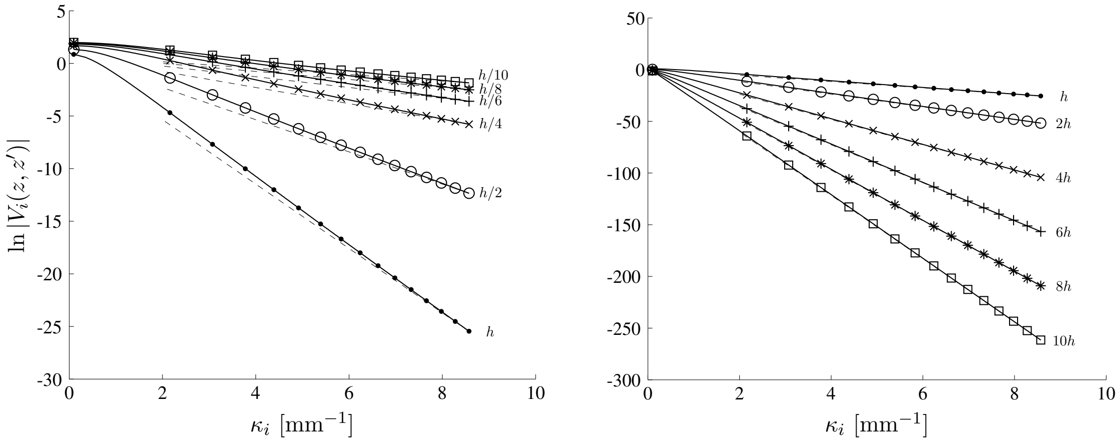

(c) TE, height $\leq h$.

(d) TE, height $\geq h$.

Figure 5.13: Voltage induced in the observer BFs (at z) by TE/TM-waves generated at source BF (at z') and for different gap thickness ($r\,h$).

Consequently, the attenuation of this factor guarantees the fast convergence of the reaction series (5.25), as can be verified in Fig. 5.14. These plots show the partial sums resulting from the direct evaluation of the TE and TM series, when small gap distances are considered. The accompanying figures show the incremental error caused with 20 terms in the sum. The series are converging and the speed is deteriorating with smaller gaps due to the factors discussed previously. Again, a substantial difference in the convergence is found between the TE and TM series.

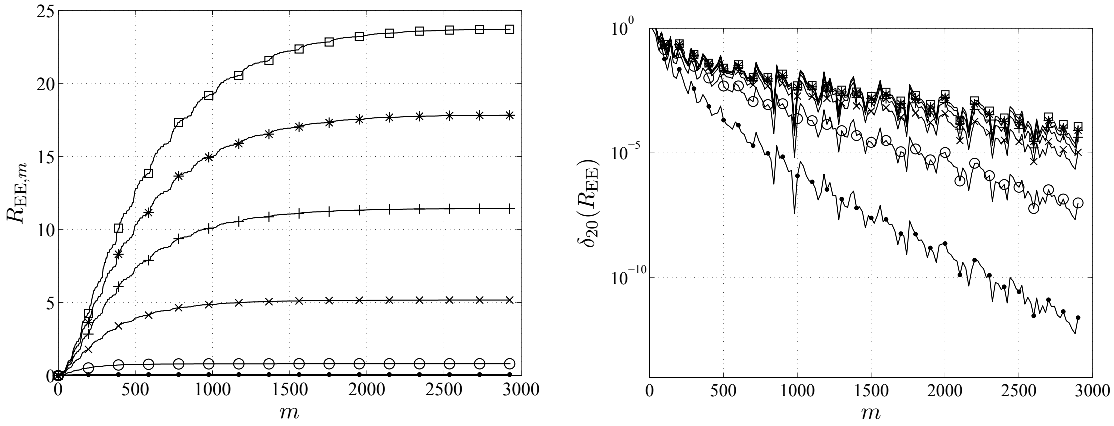

(a) TM: Partial Sums.

(b) TM: Differential Error.

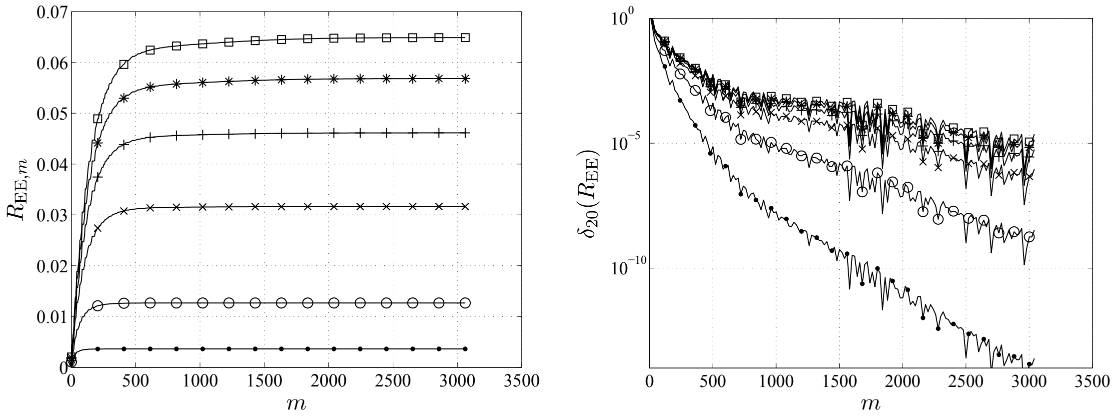

(c) TE: Partial Sums.

(d) TE: Differential Error.

Figure 5.14: Convergence of TM/TE series (reaction #1′–#1) for small gap thickness: $h(\bullet)$, $h/2(\circ)$, $h/4$ ($\times$), $h/6$ ($+$), $h/8$ ($*$) and $h/10$ ($\Box$). In the figures, the variable m is the number of TE (resp. TM) modes.

This difference is registered in Fig. 5.15, where ratio between the partial errors for the TE and TM series are represented under two different scenarios with a gap thickness of h and $h/2$. The TE series shows about one and two orders of magnitude faster convergence rate. We believe that these plots represent actually the tendencies in the convergence behavior of these inter-layer reactions so we will avoid representing the remaining possible combinations. For the moment, we have only considered the interaction between #1′ and its dual #1. Is there a big impact if we modify the position and orientation of the observer BFs? Just to ensure that this is not the case we have represented in Fig. 5.16 the interaction #1′–#2 for the different gap thickness: $h/2, h$ and $2h$.

5.3.7 General Assessment Modal Series

About the reactions at the same level ($z = z'$): A Kummer's transformation is applied to accelerate the series arising in these reactions. This technique transforms the original series in the sum of four new series, namely the quasi-static and dynamic part extended separately to every TE and TM mode. The convergence mechanisms of the modal series obtained with this study we could underline the following points:

- Among the four series involved in the evaluation of a MoM matrix element, the TM quasi-static part has the slowest convergence.
- The convergence of the series corresponding to the self-interaction terms (diagonal of the MoM matrix) have an uniform convergence.The precision of this calculation critically determines the accuracy of the system solution.
- The dynamic series converges several times faster compared to the quasi-static terms. Among them, the TE case has faster convergence.
- The relative surface of the rooftop's domains have an important influence in the series convergence. Small values of r_S in a mesh deteriorates the convergence rate of the MoM entries and therefore the computational time.

About the reactions at the different level ($z \neq z'$): The convergence of the series arising in $z \neq z'$ interactions:

- is guaranteed by the evanescent modes attenuation,
- is fast and justifies the direct evaluation of the series,
- deteriorates with small separation $|z - z'|$ between source and observer;
- TE series converge faster than TM series.
- The shape of the source and observer cells is not determinant for theses series convergence.

The only risk at this type could be the simulation of highly attenuated waves. Nevertheless, the algorithm presented in §4.2 but not present any numerical instabilities [§4.4] in this case, contrary to other formulations.

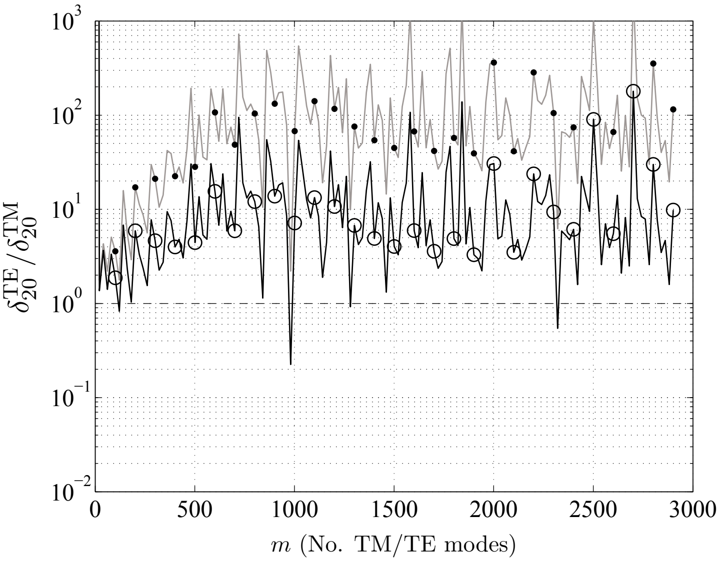

Figure 5.15: Comparison between the convergence achieved in the TM and the TE series against the number of modal terms considered in the sum: h(gray-•) and $h/10$(black-○).

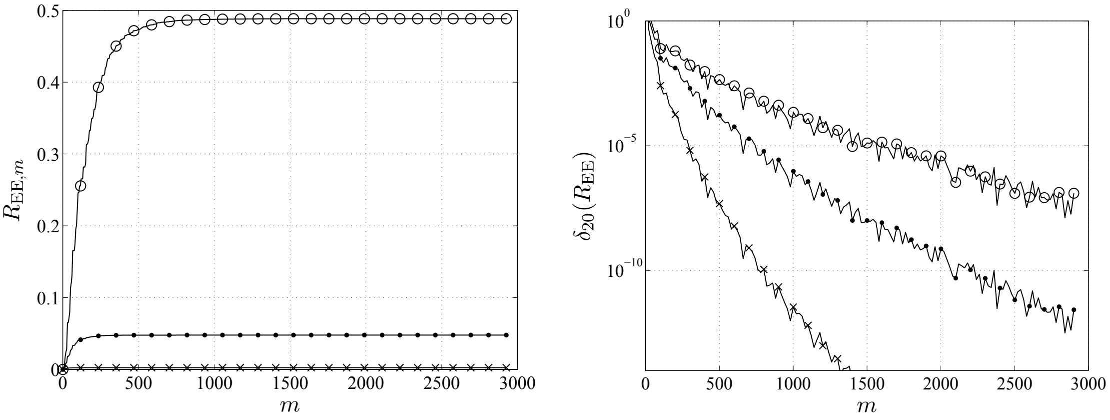

(a) TM: Partial Sums.

(b) TM: Differential Error.

Figure 5.16: Convergence of TM series (reaction #1'–#2) with the following gap thickness: h(•), $h/2$(○), $2h$ (×). The variable m is the number of TM modes.

5.4 Losses

This section is a succinct presentation of the approaches used in our simulation tool to model losses in multilayered boxed printed circuits. The losses in dielectrics are treated rigourously (from a macroscopic point of view) while in the metals, except for the upper/lower cavity covers, an approximate perturbation method has been adopted instead. Nevertheless, the latter method is accurate enough for the type of devices targeted for simulation. A summary of the origin of losses and the approaches followed to model each case is presented in Table 5.4.

5.4.1 Metallic Enclosure

A multilayered cavity, illustrated in Fig. 5.1, can be seen as a rectangular waveguide filled with dielectrics pilled up along the z-axis and short-circuited at both ends by metallic plates, corresponding to the cavity covers at $z = 0$ and $z = \sum_{i=1}^{N} h_i$. The formulation of losses follows the same strategy. The lateral walls are modeled as a rectangular waveguide losses and those produced on the top and bottom covers are taken into account as resistive loads to the propagation of this waveguide modes.

Lateral Walls

Due to the finite conductivity of the metal, a volume current density flows within the cavity wall producing a tangential component of the electric field. Consequently a PEC BC can not be applied anymore, that is, $\mathbf{E}_{\text{tan}} \neq 0$. This introduces substantial differences with respect to the lossless case [38]:

- The new boundary value problem solution (even with lossless dielectric) allows complex eigenvalues. That is, the κ_i associated to each mode becomes in general complex-valued.
- The cutoff frequency does not separate transmission from attenuation (as with lossy dielectrics)
- A good approximation for thick conductors (when the field does not traverse the conductor) can be achieved by a boundary problem involving different media [39]. The field solution, in this case, requires *hybrid modes* (to accomplish simultaneously the electric and magnetic field z-components) and therefore, the TE, TM and TEM decomposition is not valid anymore.
- The new characteristic modal set is not orthonormal as in the lossless case since this property was a mathematical consequence of the PEC BC on the waveguide's wall.

Consequently, a rigorous solution to the lossy problem [39][40, p. 324] can not be extrapolated from the lossless problem and would need a completely different and cumbersome approach even for the simplest geometry. An approximate method, based on a perturbation of the lossless case [41, p. 24], is therefore preferable since our interest is focused on devices fabricated with low-loss conductors. This theory is commonly named after the Russian physicist

Type	Location		Model	Short Description
Substrate losses	Dielectrics		Equivalent complex permittivity / permeability.	Attenuation/delay $\alpha_{\mathrm{d}} + \mathrm{j}\beta$ for each mode of the waveguide.
Ohmic Losses	Cavity	Lateral walls	Leontovich BCs on the waveguide cross-section for each mode.	Attenuation coefficient α_{c} associated to each mode of the waveguide.
		Top/bottom cover	BCs at $z = \text{const.}$	Loads the transmission line model, for each mode, with its wave impedance: $Z_{\mathrm{w}}(\sigma, \omega)$.
	Printed Circuits		IE formulation with Leontovich (Impedance) boundary conditions on printed circuit surfaces.	Separable MoM matrix: fully-populated lossless matrix + sparse lossy matrix.

Table 5.6: Quantitative description of loss models.

Leontovich and is adequate for the evaluation of losses in waveguides that satisfy the following conditions:

- **good conductive walls**: which permits the approximation of deriving the tangential *electric* field from the tangential *magnetic* field resulting in the *lossless* problem.
- **when the frequency is not too close or below the cutoff value** : the estimation of α is based on the power loss law, that is, $2\alpha_{\mathrm{c}}P = P_{\mathrm{L}}$ which associates the diminution of the power flow along the waveguide P (left side expression) to the power loss in the walls P_{L}. If a mode is under cutoff (in the lossless case), the power flow becomes zero and therefore the above formulation is not applicable anymore since $\alpha \to \infty$. Nevertheless in this case, the attenuation of the evanescent wave is usually dominant.
- **if the skin depth is considerably smaller than the wall thickness and greater than the average surface irregularities**: the field can not "see" through the waveguide walls or the surface roughness [42].

Let us assume a rectangular waveguide, with dimensions $a \times b$ and wall conductivity σ, that satisfies the above conditions. The Leontovich approximation adds an attenuating term α_{c} $\left[\mathrm{nep}\cdot\mathrm{m}^{-1}\right]$ to the propagation constant γ of each mode. Given a mode with indices (m, n) and cutoff wavenumber $\kappa^2 = k_m^2 + k_n^2$, these attenuation constants are deduced in [41, pp. 57-60] and presented here in a simplified form:

$$\alpha_{\mathrm{c}}^{\mathrm{TM}}(\omega_{\mathrm{n}}) = \frac{2\mathcal{R}}{\eta_0}\left[\frac{k_m^2/a + k_n^2/b}{\kappa^2\mathcal{D}(\omega_{\mathrm{n}})}\right] \tag{5.27a}$$

$$\alpha_{\mathrm{c}}^{\mathrm{TE}}(\omega_{\mathrm{n}}) = \frac{\mathcal{R}}{ab\,\eta_0}\left[\frac{\epsilon_n k_m^2 a + \epsilon_m k_n^2 b}{\kappa^2}\mathcal{D}(\omega_{\mathrm{n}}) + \frac{\epsilon_n a + \epsilon_m b}{\omega_{\mathrm{n}}^2\,\mathcal{D}(\omega_{\mathrm{n}})}\right] \tag{5.27b}$$

where

$$\epsilon_n = \begin{cases} 1 & n = 0 \\ 2 & n \neq 0 \end{cases} .$$

The equations (5.27) are frequency dependent due to two terms. The first one is the characteristic resistance that is expressed as

$$\mathcal{R} = \frac{k_0\eta_0}{2}\delta_{\mathrm{s}} \propto \sqrt{\omega} \quad [\Omega] \tag{5.28}$$

and is proportional to the penetration depth

$$\delta_{\mathrm{s}} = \sqrt{\frac{2}{\omega\mu_0\sigma}} \quad [\mathrm{m}], \tag{5.29}$$

the wavenumber $k_0 = \omega\sqrt{\mu_0\varepsilon_0}$ $[\mathrm{m}^{-1}]$ and the intrinsic impedance in the vacuum $\eta_0 = \sqrt{\varepsilon_0/\mu_0} \approx 120\pi$ $[\Omega]$. The second term corresponds to the following factor:

$$\mathcal{D}(\omega_{\mathrm{n}}) = \sqrt{1 - \omega_{\mathrm{n}}^{-2}} \tag{5.30}$$

that we have denoted as “dispersion factor” since it is responsible for the dispersion in the waveguide. It has been defined with respect to $\omega_{\mathrm{n}} = \omega/\omega_c$, the frequency normalized to the cutoff frequency of the current mode. Equations (5.27) are only valid over cutoff frequencies $\omega_{\mathrm{n}} > 1$.

Top/Bottom Covers

The existence of the top and bottom cavity covers in the lossy case is modeled as two semi-infinite layers of lossy dielectrics to attenuate the modes propagating along the z-axis. Therefore, the equivalent transmission line model for the GF loads the circuit’s ends with resistive impedances [$\{Z_{\mathrm{R}}, Z_{\mathrm{L}}\} \in \mathbb{C}$ in Fig. 4.1]. Their values correspond to the modal impedance of a conductive dielectric with relative permittivity [40, §2.2]

$$\varepsilon_{\mathrm{r}} = 1 - \mathrm{j}\frac{\sigma}{\omega\varepsilon_0} \tag{5.31a}$$

and consequently, a loss tangent

$$\tan\delta_{\mathrm{r}} = \frac{\sigma}{\omega\varepsilon_0}. \tag{5.31b}$$

Therefore, the propagation constant and the characteristic impedance for each mode in these “fictitious infinite” layers are affected.

5.4.2 Printed Circuits

The approach used to model the losses in the printed circuit metallizations, as for the lateral walls of the cavity, is based on the Leontovich approximation and therefore, the constraints described in §5.4.1 apply here too.

Nevertheless, in this case the method is directly used in the formulation of the IEs by imposing the so-called Leontovich or Impedance BCs (§5.2), which states that the *total* tangential E-field on the circuit’s surface Ω (i.e. the sum of the impressed and the scattered fields) must be equal to the induced surface currents modified by an impedance factor[‡]. Formally, this can be written as

$$\hat{\mathbf{z}} \times \left(\mathbf{E}_{\mathrm{t}}^{\mathrm{i}} + \mathbf{E}^{\mathrm{s}}\right) = Z_{\mathrm{s}}\mathbf{J}_{\mathrm{s}}, \tag{5.32}$$

where

$$Z_{\mathrm{s}} = \frac{1+\mathrm{j}}{\sigma\delta_{\mathrm{s}}}$$

with the penetration depth defined in (5.29).

Rewriting here, the MoM system matrix (5.4)

$$\mathbf{v} = (\mathbf{Z} - \mathbf{\Lambda}) \cdot \mathbf{i}, \tag{5.33}$$

outlines that the losses are incorporated into the problem as a correction term to the lossless MoM matrix. Due to the nature of the matrices involved, this could be also interpreted in a

---

[‡] In fact, this term represents an approximation of the actual transverse E-field on the conductive surface.

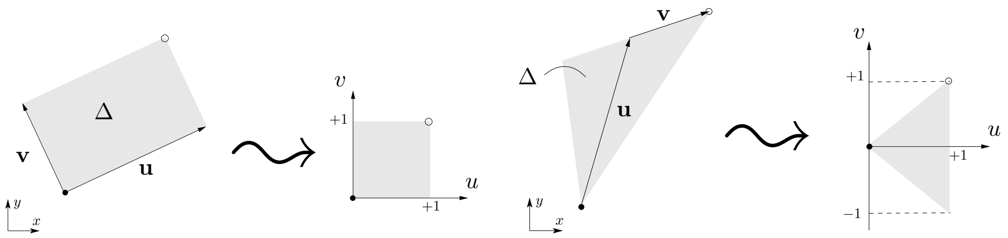

Figure 5.17: Mapping of a rectangular/triangular cells into a $u-v$ normalized domain.

circuit language as: “the losses are incorporated as complex impedances and added *in series* to the lossless circuit”.

Using linear subsectional BFs (§3.4.1) makes the losses matrix $\mathbf{\Lambda}$ sparse, since the integral in each term (5.6) will be zero if the BFs do not overlap. The non-vanishing terms can be calculated from the integral between two half-BFs as follows

$$\int\limits_{D\cap D'} \mathbf{b}\cdot\mathbf{b}'\,\mathrm{d}S = \pm\int\limits_{\Delta} \mathbf{g}^{\pm}\cdot\mathbf{g}'^{\pm}\,\mathrm{d}S, \tag{5.34}$$

provided that $\mathbf{b} = \mathbf{g}^{+} - \mathbf{g}^{-}$ is decomposed in half-BFs and they overstrike in the region $\Delta = D\bigcap D'$. Analytic solution to (5.34) can be found using a transformation of the surface of integration D into a normalized surface. This mapping is represented, for rectangular and triangular domains, in Fig. 5.17. The solution to these integrals follow.

Integration Over Rectangular Cells

There are four orthogonal orientations of a half-rooftop $\mathbf{g}$ in a rectangular subdomain D [cf. Fig. 3.3]. Considering two half-rooftop randomly oriented in the same domain, then (5.34) can be reduced to four types of integrals. Any combination of half-rooftops oriented perpendicularly gives zero. Symbolically representing the half-rooftop orientation with arrows, this could be written as follows

$$\int\limits_{\Delta} \mathbf{g}(\upuparrows)\cdot\mathbf{g}'(\rightrightarrows)\,\mathrm{d}S = \int\limits_{\Delta} \mathbf{g}(\rightrightarrows)\cdot\mathbf{g}'(\upuparrows)\,\mathrm{d}S = \cdots = 0. \tag{5.35}$$

Nonetheless, if they are parallel we can distinguish two cases. First, when they have the same orientation, the integral is given by

$$\int\limits_{\Delta} \mathbf{g}\cdot\mathbf{g}'\,\mathrm{d}S = \Delta\int\limits_{0}^{1}\int\limits_{0}^{1} |g|^2\,\mathrm{d}u\mathrm{d}v = \frac{L^2}{3\Delta}, \tag{5.36}$$

where Δ is the area of the rectangle and $L = \{|\mathbf{u}|, |\mathbf{v}|\}$ is the length corresponding to the rectangle’s common side (§3.4.1). The second case arises when the half-rooftops are defined on opposite common sides:

$$\int_{\Delta} \mathbf{g}(\angle) \cdot \mathbf{g}'(\diagdown) \, \mathrm{d}S = \Delta \int_0^1 \!\! \int_0^1 g(\angle) g'(\diagdown) \, \mathrm{d}u \mathrm{d}v = \frac{L^2}{6\Delta}, \tag{5.37}$$

where the $\angle$, $\diagdown$ symbols represent the linear variation of the half-rooftop within the cell.

Integration Over Triangular Cells

Using the local coordinate system (u, v) of the normalized triangular surface, shown in Fig. 5.17, any half-RWG can be defined as [cf. (3.18)]

$$\mathbf{g}_i = \frac{1}{2\Delta} \left[(u - \alpha_i)\mathbf{u} + (v - \beta_i)\mathbf{v} \right] \tag{5.38}$$

where Δ is the triangle's surface and the constants $\alpha_i, \beta_i = \{0, 1\}$ define the local origin, or in other words, the relative orientation of the half-RWG within the triangle. After some algebraic manipulations, the analytic solution of the overlapping integral between two generic rooftops i, j on a triangular cell is given by

$$\int_{\Delta} \mathbf{g}_i \cdot \mathbf{g}_j \, \mathrm{d}S = \frac{1}{4\Delta} \left[|\mathbf{u}|^2 \left(\alpha_i \alpha_j - 2/3(\alpha_i + \alpha_j) + 1/2 \right) + \right.$$
$$\left. |\mathbf{v}|^2 \left(\beta_i \beta_j + 1/6 \right) + \mathbf{u} \cdot \mathbf{v} \left(\alpha_i \beta_j + \alpha_j \beta_i - 2/3(\beta_i + \beta_j) \right) \right]. \tag{5.39}$$

5.4.3 Losses in Dielectrics

The electric (magnetic) type of dissipation in homogeneous isotropic substrates is introduced in the formulation by means of a complex permittivity (permeability) [39, 40, 43, 44]. These values will be considered constant in our band of interest (DC to microwave frequencies) and can be expressed, relative to the vacuum permittivity ε_0 (permeability μ_0), as follows

$$\varepsilon_{\mathrm{r}} = \frac{\varepsilon}{\varepsilon_0} = \varepsilon'_{\mathrm{r}} - \mathrm{j}\varepsilon''_{\mathrm{r}} = \varepsilon'_{\mathrm{r}}(1 - \mathrm{j}\tan\delta_{\mathrm{e}}), \tag{5.40a}$$

$$\mu_{\mathrm{r}} = \frac{\mu}{\mu_0} = \mu'_{\mathrm{r}} - \mathrm{j}\mu''_{\mathrm{r}} = \mu'_{\mathrm{r}}(1 - \mathrm{j}\tan\delta_{\mathrm{m}}), \tag{5.40b}$$

where $\tan\delta_{\mathrm{e}}$ and $\tan\delta_{\mathrm{m}}$ are the electric and magnetic loss tangents, respectively. Having done this characterization of the dielectrics, we can procede with the resolution of the transmission line model as described in §4.5.

5.5 Network Characterization.

From the engineering point of view, one of the most useful results corresponds to the network characterization of the circuit under investigation. This characterization should also consider special cases where certain ports are loaded or interconnected by means of lumped elements or in general any other type of multiport network. In particular, short-circuiting some parts of the structure is commonly employed in printed circuits. In this type of technology, this is typically achieved by means of two techniques, namely, a direct ohmic contact of the circuit to the lateral cavity walls or by means of via holes.

This section explores different approaches to model these scenarios starting with the solution of the IE-MoM problem, as described §5.2. We will also present how these techniques, in conjunction with an equivalent circuit of the vertical wire connection, can be used to approximate the via-hole effect.

5.5.1 Ports Loads and Interconnections

The design of printed circuits may require using lumped elements in the circuit or the interconnection of different ports. For example, a resistor interconnecting two ports balances a Wilkinson power divider [45, §7.3] or lumped capacitors loading a combline filter [see §5.6.4] are used to reduce the resonators length. The characterization of these problems can be treated at a network level and, therefore, reduced to the connection of different multiport networks, as represented in Fig. 5.18.

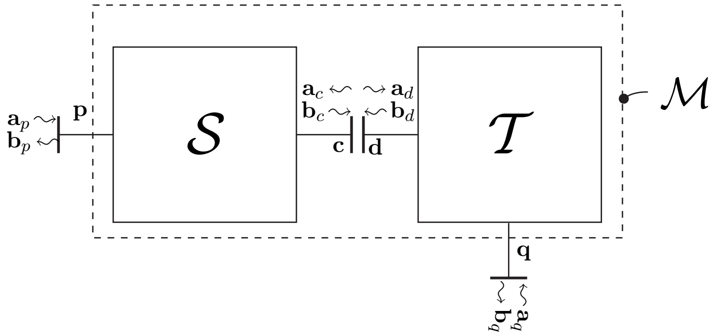

Figure 5.18: Connection of two multiport networks. The multiport network defined with $\mathcal{S}$ is associated to the EM problem and $\mathcal{T}$ incorporates external circuits or interconnections.

Once the ports are identified in the printed circuit, the scattering parameters can be derived from the solution of the EFIE-MoM problem by following the procedure described in §2.6. The resulting matrix is denoted here with $\mathcal{S}$.

At this point, the ports could be loaded or interconnected by means of lumped elements or in general any other multiport network, as soon as their scattering parameters are available. The procedure to follow is represented in Fig. 5.18. Let us denote with $\mathcal{T}$ the scattering matrix of an external circuit to be connected to the printed circuit network $\mathcal{S}$. Without loss of generality, the connection is carried out between each pair of ports $\mathbf{c} = [c_1, c_2, \cdots, c_N]$ and

$\mathbf{d} = [d_1, d_2, \cdots, d_N]$ belonging to both circuits, respectively, and reducing the network to a new $(P+Q)$-ports scattering matrix $\mathcal{M}$. The latter refers to the scattering parameters for the remaining ports $\mathbf{p} = [p_1, p_2, \cdots, p_P]$ and $\mathbf{q} = [q_1, q_2, \cdots, q_Q]$.

The connection of these two networks may be performed using the technique explained in [46, §2.10]. First the matrices are rearranged such that

$$\left[\begin{array}{c}\mathbf{b}_p\\\hline\mathbf{b}_c\end{array}\right] = \left[\begin{array}{c|c}\mathcal{S}_{pp} & \mathcal{S}_{pc}\\\hline \mathcal{S}_{pc}^{\mathrm{t}} & \mathcal{S}_{cc}\end{array}\right]\cdot\left[\begin{array}{c}\mathbf{a}_p\\\hline\mathbf{a}_c\end{array}\right] \tag{5.41a}$$

$$\left[\begin{array}{c}\mathbf{b}_q\\\hline\mathbf{b}_d\end{array}\right] = \left[\begin{array}{c|c}\mathcal{T}_{qq} & \mathcal{T}_{qd}\\\hline \mathcal{T}_{qd}^{\mathrm{t}} & \mathcal{T}_{dd}\end{array}\right]\cdot\left[\begin{array}{c}\mathbf{a}_q\\\hline\mathbf{a}_d\end{array}\right] \tag{5.41b}$$

where "t" denotes transpose matrix and $\mathbf{a}_i, \mathbf{b}_i$ are vectors containing the incident an reflected wave amplitudes for every set of ports. Then, the resulting $\mathcal{M}$ scattering matrix is calculated as

$$\mathcal{M} = \left[\begin{array}{c|c}\mathcal{S}_{pp} & \mathbf{0}\\\hline \mathbf{0} & \mathcal{T}_{qq}\end{array}\right] + \left[\begin{array}{c|c}\mathcal{S}_{pc} & \mathbf{0}\\\hline \mathbf{0} & \mathcal{T}_{qd}\end{array}\right]\cdot\left[\begin{array}{c|c}-\mathcal{S}_{cc} & \mathbf{I}\\\hline \mathbf{I} & -\mathcal{T}_{dd}\end{array}\right]^{-1}\cdot\left[\begin{array}{c|c}\mathcal{S}_{pc}^{\mathrm{t}} & \mathbf{0}\\\hline \mathbf{0} & \mathcal{T}_{qd}^{\mathrm{t}}\end{array}\right] \tag{5.42}$$

where $\mathbf{I}, \mathbf{0}$ are the identity and a null matrices, respectively. This procedure can be repeated successively for every additional $\mathcal{T}$ network to be connected. Nonetheless, if the number of networks is not large, this operation can be performed in a single iteration by generating a super-matrix gathering all the terms, as illustrated in Fig. 5.19(b).

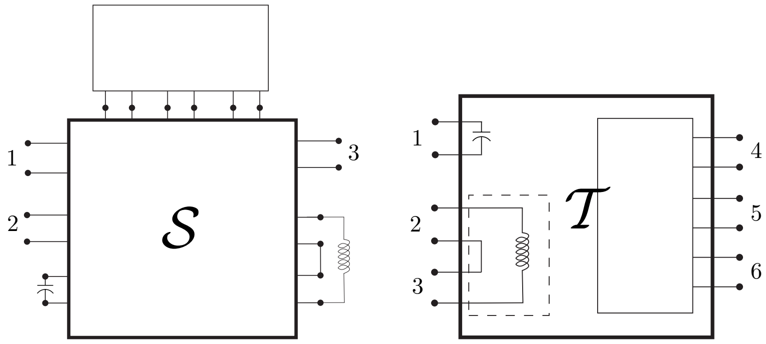

(a) Matrix $\mathcal{S}$ connected with three networks.

(b) Example of a super-matrix $\mathcal{T}$

Figure 5.19: Example of connection of multiple network using a single matrix $\mathcal{T}$.

This example starts assuming the connection of an inductance, a capacitor and a three-port network to the original $\mathcal{S}$ matrix circuit, as illustrated in Fig. 5.19(a). One possibility is to proceed successively connecting each new component by (5.42). Alternatively, this can be done in a single step. It suffices to gather all the external elements in a single scattering matrix, as represented in Fig. 5.19(b), having the following shape

$$\mathcal{T} = \left[\begin{array}{c|c|c} \Gamma_C & \mathbf{0}_{1\times 2} & \mathbf{0}_{1\times 3} \\ \hline 0 & \mathbf{S}_L & \mathbf{0}_{2\times 3} \\ \hline 0 & \mathbf{0}_{3\times 2} & \mathbf{S}_3 \end{array}\right], \tag{5.43}$$

where Γ_C is the reflection coefficient presented by the parallel capacitor and $\mathbf{S}_L, \mathbf{S}_3$ are the scattering parameters for the series inductance and the three-ports circuit, respectively.

On the other hand, if the circuit only requires loading ports, e.g. as the capacitance loading $\mathcal{S}$ in Fig. 5.19(a), it would be more advantageous to use the following formula [47]:

$$\mathcal{M}_{ij} = \mathcal{S}_{ij} + \sum_{k=1}^{N} \frac{\mathcal{S}_{ik}\Gamma_k\mathcal{S}_{kj}}{1 - \mathcal{S}_{kk}\Gamma_k} \tag{5.44}$$

where Γ_k is the reflection coefficient of the kth load.

Finally, special care must be taken in the definition of internal ports (i.e. inside the cavity) since it has been demonstrated that numerical parasitic elements arise due to the application of a localized excitation (§2.6) far from the ground/reference plane (i.e. the cavity walls) [48, 49]. Here we take advantage of the contour formulation of integrals in §3.3.2 to vanish the potential at the edge of the port cell, producing a artificial ground that avoids parasitics.

5.5.2 Connections to Ground.

The connections to ground are frequent in the printed circuit structures. These are normally achieved in at least two different ways a) direct ohmic contact with the lateral cavity wall, or b) via-hole to ground. The first case can be achieved with this formulation by adding a half-basis function at the contact region in order to allow the current flow from the printed circuit to the cavity walls. Using image theory we can see how the currents component parallel to the wall vanishes while those perpendicular are reinforced. On the other hand, the formulation of this chapter represent a constraint to accurately model via holes since only planar currents are considered. Nevertheless, an approximation can be applied by creating instead a port and loading it with an equivalent circuit of the vertical wire, as discussed in the previous section.

In order to show both techniques we will ground the microstrip stub of the structure in Fig. 4.15 from §4.6. In addition, the height b of the box cross-section has been halved in order to avoid spurious resonances from the cavity. A grounded stub of a quarter wavelength will produce the complementary response in this structure, i.e. a full transmission between ports.

In Fig. 5.20 we illustrate four different scenarios where the microstrip stubs are connected to ground and the circuit layout has different offsets $k\Delta$ for $k = 0.2, 0.5, 0.9, 1$. In the three first scenarios, the stub is loaded with an equivalent inductance that emulates the effect of four microstrip via holes [50]. The layout is shifted towards the upper wall and, in the last scenario, the short is produced directly by ohmic contact on the lateral cavity wall. The responses of these circuits are very similar and produce a transmission zero around 2.7 GHz, as shown in Fig. 5.21. The cavity resonance, caused by the TM_{10} mode, is still present at 3.5 GHz. The differences between the responses of these circuits are presumably due to the capacitive load of the cavity walls on the printed circuit, specially at the stub end.

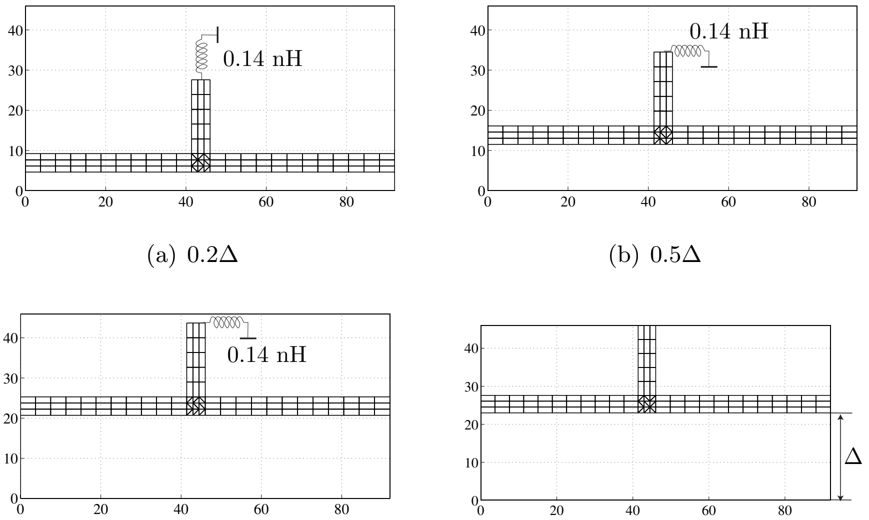

(a) 0.2Δ (b) 0.5Δ

(c) 0.9Δ (d) Δ = 23 mm

Figure 5.20: Different scenarios with grounded stubs.

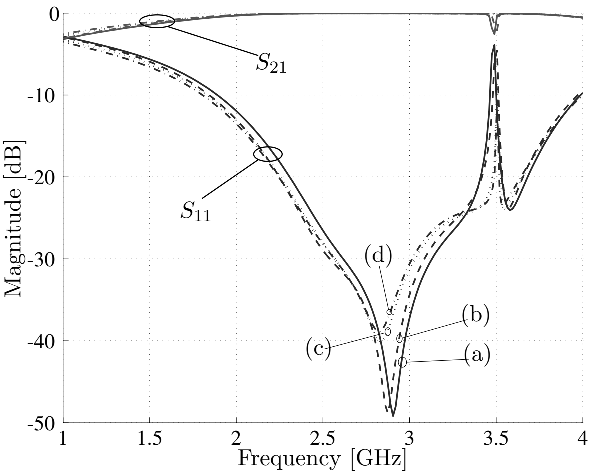

Figure 5.21: Comparison between the responses of the structures in Fig. 5.20.

5.6 Applications

Extensive numerical experiments have been carried out to assess the performance and validity of the theory presented hitherto. In this section, the results of the numerical simulations using our approach are compared to simulations obtained with other numerical solvers and with measurements for a set of carefully chosen benchmark structures. Studies of convergence, in terms of modal series and mesh density, accuracy and performance, by comparing simulation times with other solvers, have been performed for every test-structure. However, in order to keep a reasonable document size, only some of them are presented here.

5.6.1 Coupled-lines Filter

The first structure consists of a coupled-line bandpass filter in microstrip technology. This circuit, described in Fig. 5.22, is an excellent test case and being extensively used as benchmark to validate other IE-based methods [8, 22, 51] is a proof of it. This device presents three main points of interest: a) lossy dielectrics and finite conductivity in metals, b) thin dielectrics and c) strong coupling between adjacent resonators through a small gaps.

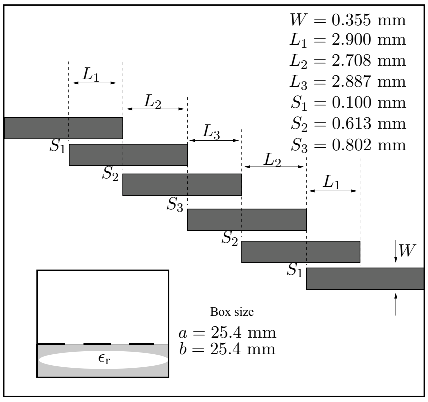

Dielectric i	Height [mm] h_i	R. Permitt. ε_{ri}	Losses $\tan\delta_{e_i}$
2. Air	3.6	1.0006	0
1. -	0.4	9.8	0.003

- Cavity: $a = 25.4$, $b = 25.4$ mm; $\rho_{\text{Cu}} = 1.82$ $\mu\Omega$·cm
- Microstrips: Copper $\rho_{\text{Cu}} = 1.82$ $\mu\Omega$·cm

(*) Figure not scaled.

Figure 5.22: Description of Coupled Lines Filter [8, 22, 51].

This device is specially lossy and therefore a good candidate to validate the approach discussed in §5.4. Based on the description of loss models in Table 5.4, we have distinguished three types of loss sources: losses in dielectrics, printed circuits and finally cavity. In order to see the relative effect of each one in the filter response we have performed several simulations with different scenarios. Starting from a lossless simulation, each scenario incorporates a new type of losses with respect to the previous one. Hence, in Fig. 5.23 the first simulation do not consider losses (thin solid line), then the dielectric losses are taken into account (dotted line). Its effect is better observed in the insertion losses. Nonetheless, the biggest variation on the frequency response is detected when the ohmic losses in the printed circuit are included (gray solid line). Finally, the last curve (tick solid line) corresponds to the simulation of all the losses in the circuit, including metallic enclosure (thick). The difference with respect to the previous response (gray solid line) is not significant meaning that losses in the cavity are not important compared to the other types of losses. This can be justified by the fact that the resonant field is mainly concentrated in the strips resonators and not in the cavity.

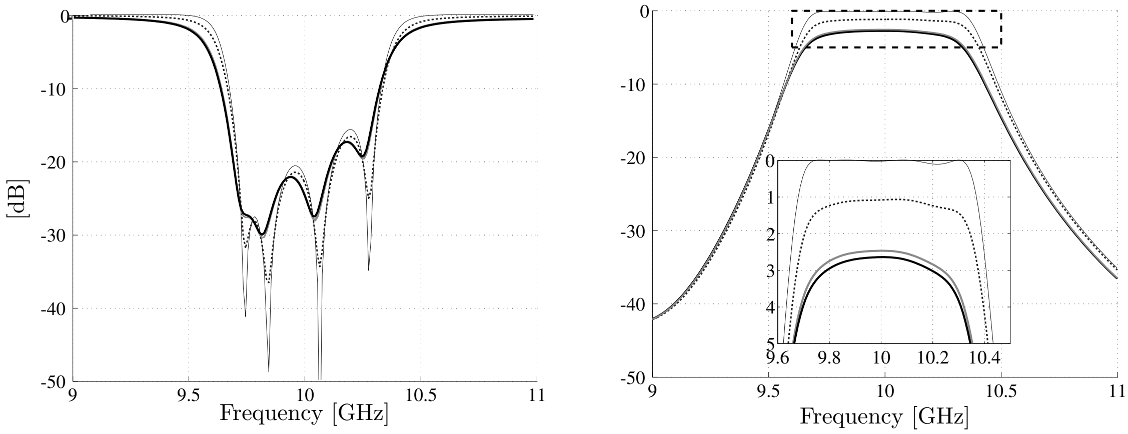

(a) Return Losses.

(b) Insertion Losses.

Figure 5.23: Influence of Losses. Lossless (thin solid line), + dielectric (dotted line), + Cu strips (gray solid line), + Cu cavity (thick solid line).

The coupling between strip resonator in the filter has an important effect in the electric circuit response [45, §8.7]. The accuracy in the simulation of couplings will depend on the *mesh* of the printed lines and the *convergence* achieved in the modal series (i.e. in the reaction terms of the MoM). This second aspect, is also compromised in this case due to the small thickness of the dielectric [cf.§5.3.4].

Let us consider three different schemes, as represented in Fig. 5.33, with different mesh densities. In all three cases, a rectangular cells mesh extends over the strip resonators with a density of ≈ 20 div/λ along the lines. A rectangular mesh will describe more ”naturally the surface current flow along straight lines and it is dense enough to shape its variation [52]. The lines' widths, on the contrary, are divided differently in each case increasing its density from one up to three cells per width.

Before comparing the responses of each mesh scheme, the modal convergence in each problem must be guaranteed. The number of modes for the quasi-static and dynamic series has to be determined. Due to the large amount of BFs, a convergence study of every entry of the MoM matrix would be cumbersome. Therefore, we will base the convergence study on the relative variation of the scattering parameters. The procedure consists of performing successive simulations where, starting from an initial guess, the number of modes in the series are risen until any significance variation is detected in the resulting scattering parameters. With this method we search the minimum number of modes necessary for stable results, first for the quasi-static part and then, keeping this results, we proceed with the dynamic part. The figure of merit for the convergence is defined with an error function that measures the relative square error in the S parameters between two consecutive simulations averaged over

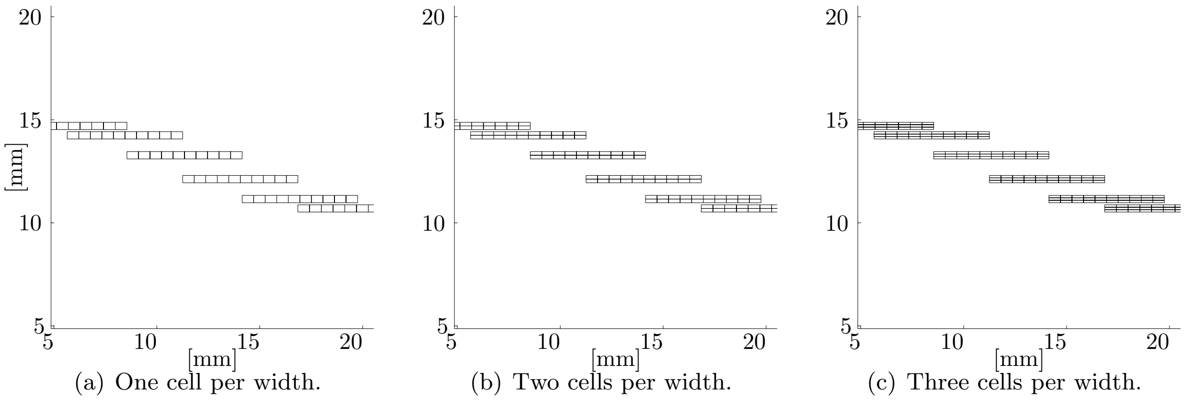

(a) One cell per width. (b) Two cells per width. (c) Three cells per width.

Figure 5.24: Three mesh schemes with rectangular mesh with lines of ≈ 20 div/λ

N frequency samples. This error function is expressed as

$$\mathcal{E} = \frac{1}{N}\sum_{i=1}^{N}\sum_{k=1}^{P}\left|\frac{S_i(k) - S_{0i}(k)}{S_{0i}(k)}\right|^2 \tag{5.45}$$

where i and k extends to the N frequency samples and the P elements of the S matrix, respectively. The subscript 0 denotes the previous iteration which is taken as a reference.

The parameters used in this process are the following:

Δ^{Qs}	Δ^{Dy}	N	$\mathcal{E}_{\mathrm{th}}$
$\times\,1.2$	$\times\,1.05$	14	0.005

where $\mathcal{E}_{\mathrm{th}}$ is the threshold error that determines when the algorithm stops, and $\Delta^{\mathrm{Qs}}, \Delta^{\mathrm{Dy}}$ represents the increment in the number of modes of the quasi-static and the dynamic series, respectively. Here, the bandwidth was split into two intervals covering [9,10.2] GHz and [10.4,11] GHz and samples were taken uniformly with steps of 0.2 and 0.1 GHz, respectively.

The error function (5.45) resulting on each iteration is represented in Fig. 5.25 for every mesh scheme. The size of cells are reduced from one scheme to the next and therefore, according to previous studies (§5.3.5), the number of modes needed for convergence is bigger. Consequently, the number of modes for the quasi-static series obtained in one scheme is used as initial guess for the next one. We can observe how the error is decreasing as the number of modes in the simulation is increased.

The previous study provided us with the number of modes that guarantees a stable response in all three scenarios considered. With these parameters, the simulated responses are shown in Fig. 5.26. The simulations show how the filter bandwidth increases as the number of cells in the lines width augments, which is normally due to a stronger coupling between resonators.

In Fig. 5.27, the response simulated with our method using the mesh of Fig. 5.33(c) is plotted over a the measurements of a prototype presented in [51]. The comparison shows excellent agreement between both responses, which validates our approach for the simulation of this

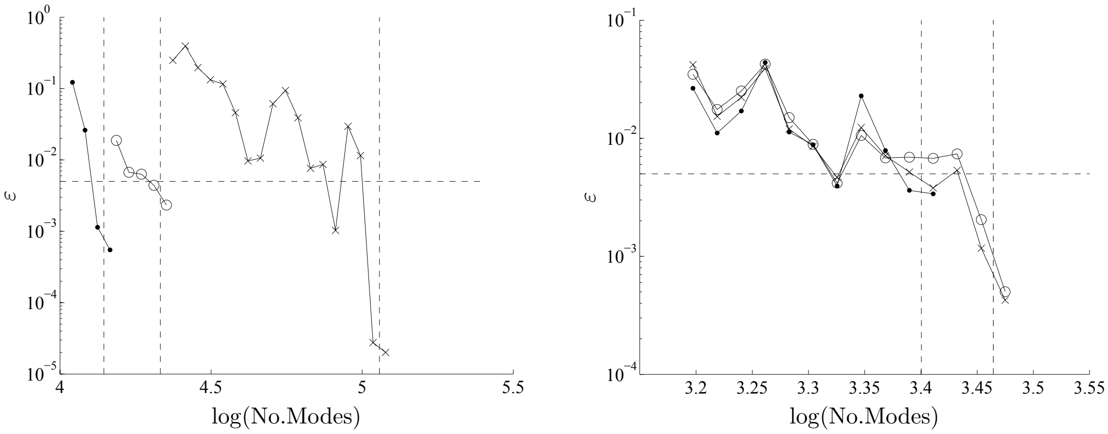

(a) Increasing No. modes in Quasi-Static Series. (b) Increasing No. modes in Dynamic series.

Figure 5.25: Representation of the error in the scattering parameters as a function of the number of modes in mesh (a)(•), (b) (○) and (c) (×) from Fig. 5.33.

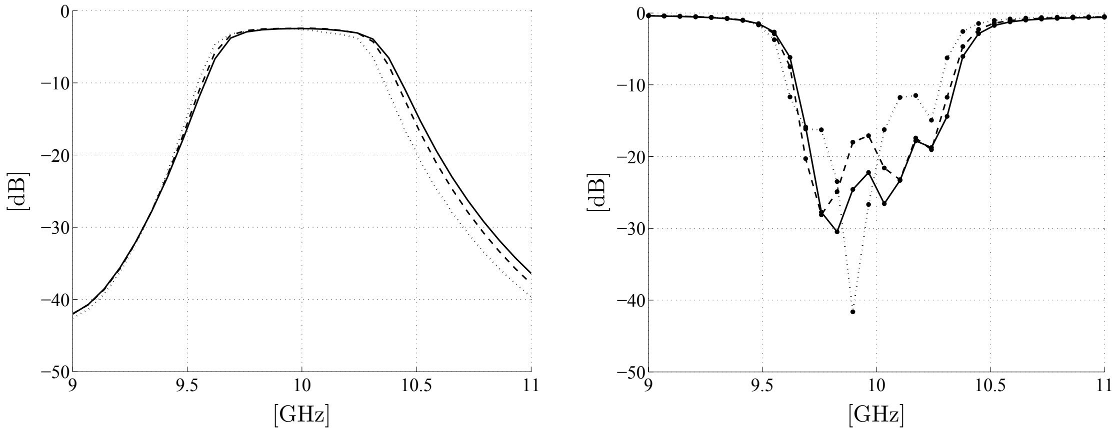

(a) Insertion Losses vs Frequency (b) Return Losses vs Frequency

Figure 5.26: Simulations with different mesh densities: Single cell (dotted line), two cells (dashed line), three cells (solid line) per width.

filter.

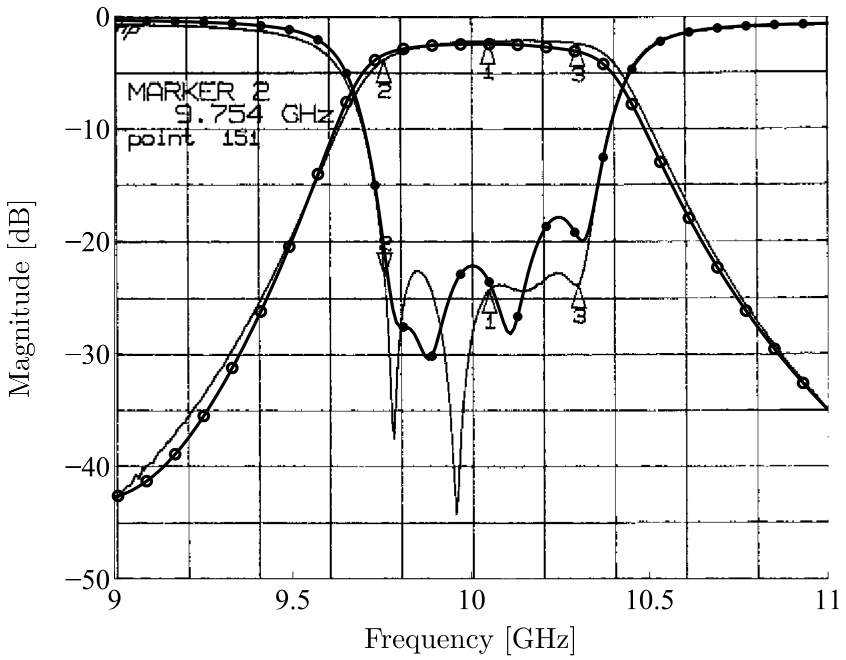

Figure 5.27: Comparison between measurements (solid lines without symbols) and simulations of the return losses (solid line with •) and insertion losses (solid line with ∘).

5.6.2 Multilayered Bandpass Filter

The next design, described in Fig. 5.28, corresponds of a coupled-line bandpass filter in a multilayered configuration and it is based on a design proposed in [22]. The filter is composed of two thin dielectrics disposed at both ends of the cavity and separated by an air gap. These dielectrics are used as support for the planar circuits that are printed at the side in contact with the air. The layouts are also illustrated in Fig. 5.28. The labels C_1 and C_2 denote the layout corresponding to the top and bottom circuits, respectively.

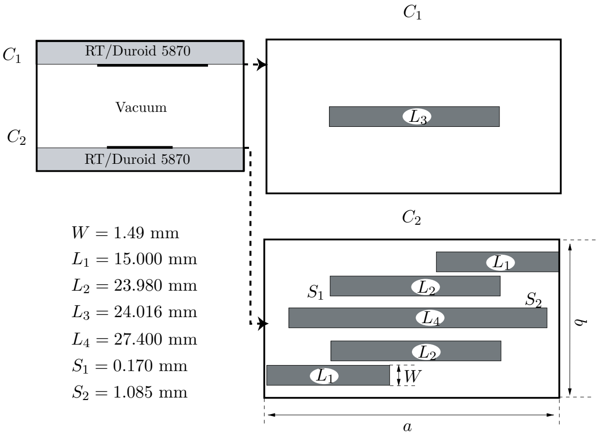

Dielectric i	Height [mm] h_i	R. Permitt. ε_{ri}	Losses $\tan\delta_{e_i}$
3. RT/Duroid 5870	0.51	2.33	0.0012
2. Air	3.06	1.0	0
1. RT/Duroid 5870	0.51	2.33	0.0012

- Cavity: $a = 32$, $b = 14.82$ mm in BeCu alloy ($\rho_{\mathrm{BeCu}} \approx 8.21\mu$·cm).
- Microstrips: $\rho_{\mathrm{Cu}} = 1.82\ \mu\Omega$·cm

Figure 5.28: Description of Three-layers Bandpass Filter.

This structure provides a suitable test case to validate the transmission line model (§4.5) that accounts for the layered media, as well as the interaction between sources at different height levels (§5.3.6). A prototype of this design has also been built and measured. The materials used in the fabrication, specially the metallic components, are quite lossy and therefore a preliminary study of the losses will also be carried out. The influence of losses in the filter response is represented in Fig. 5.29. This study follows the same criteria considered in the previous test-structure, that is, to successively introduce the losses effect.

It can be observed that the impact of ohmic losses on the printed circuit increases considerably the insertion losses. Here, the influence of the cavity losses is more significant than in the previous structure. This is not only due to the lower conductivity of the metal (lossy ground plane) but also to the cross-coupling between C_1 and C_2. The latter takes place in vertical direction and therefore the field is guided through the rectangular cross-section of the cavity. This justifies the difference between the two last responses (gray and thick black solid lines).

A prototype of this design has been built in the laboratory and Fig. 5.31 provides an overview of the fabrication process. Measured responses of the prototype is compared with our simulations in Fig. 5.30. A narrow frequency span is to monitor the filter bandwidth is plotted for magnitude in Fig. 5.30(a). The phase for the reflection coefficients $S_{ii} = S_{11}, S_{22}$ is plotted in Fig. 5.30(c) while Fig. 5.30(c) shows the phase for the transmission coefficients $S_{ij} = S_{12}, S_{21}$. Finally, the filter response is also compared in a wider frequency span in Fig. 5.30(b).

The comparison in the bandpass shows a frequency shift in-band smaller than 2% with respect

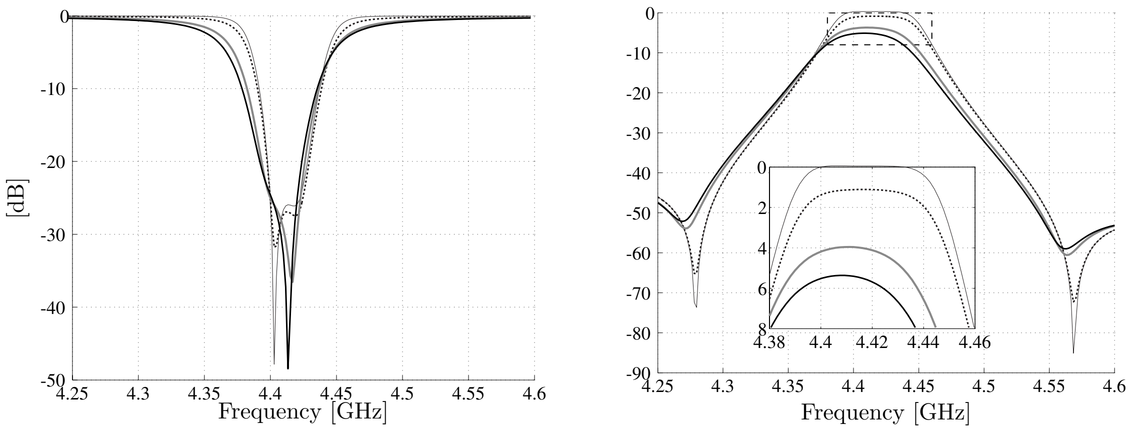

(a) Return Losses

(b) Insertion Losses

Figure 5.29: Influence of Losses. Lossless (thin solid line), + dielectric (dotted line), + Cu strips (gray solid line), + BeCu cavity (thick solid line).

to the center frequency and the error in the insertion losses is at most 5 dB for values below -40 dB. The responses in wide-band also show a good matching between simulation (black) and measurements (gray). The difference in the transmission zero around 5.1 GHz can be justified by the tolerances in the air gap height [see fabrication process in Fig. 5.31] since a variation there can change the cross-coupling path that produces such a zero.

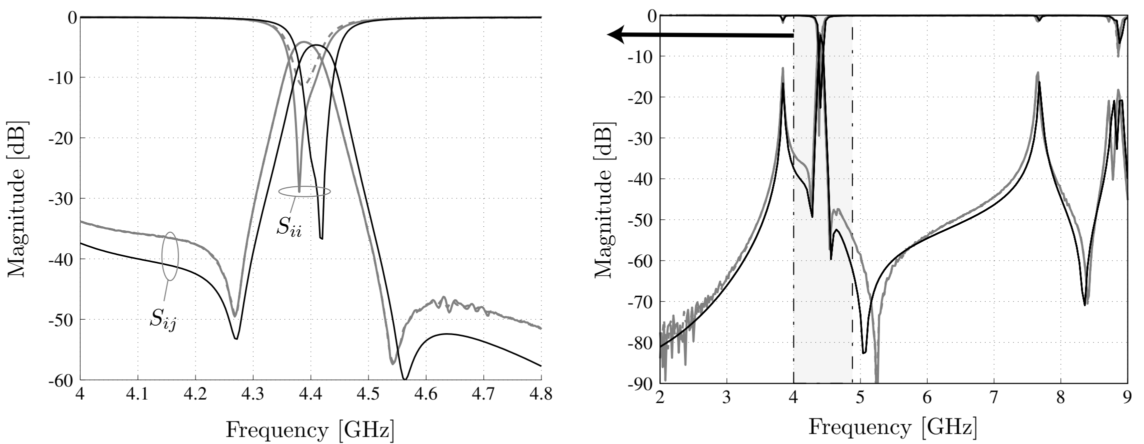

(a) Narrow span. (b) Wide span.

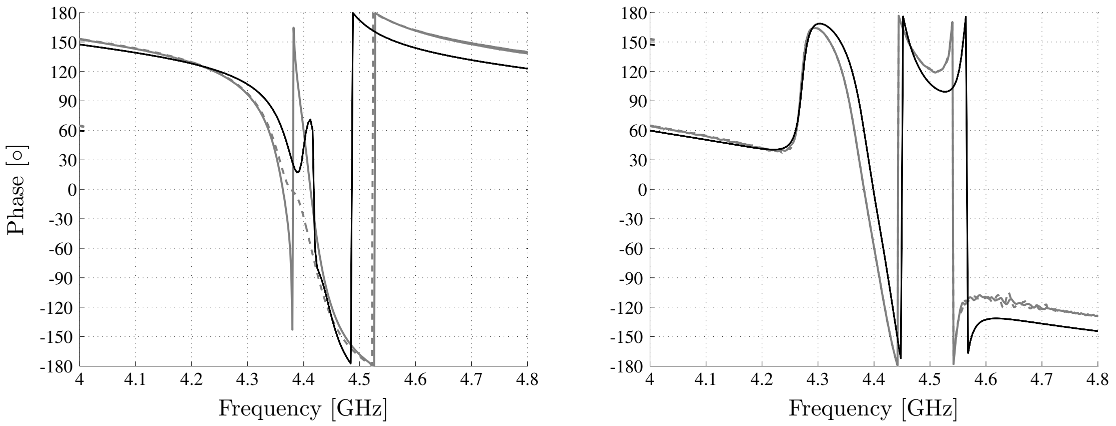

(c) Phase S_{ii}. (d) Phase S_{ij}.

Figure 5.30: Frequency response obtained with simulation (black line) and measurements (gray line). Scattering parameters S_{11}, S_{12} (solid line) and S_{22}, S_{21} (dashed line).

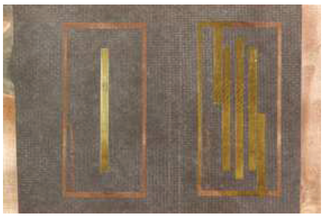

Layout printed on substrate after photolithography and wet-etching process. The backside of the dielectric is metallized.

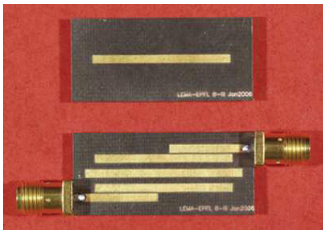

The substrate is cut according to the box dimensions into two dielectric layers: C_1 (bottom) and C_2 (top). The coaxial connectors (Huber+Suhner 82 SMA-50-0-41) are aligned to the edge of C_1 and weld to the feeding microstrip lines.

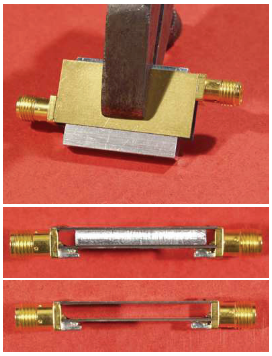

Using an auxiliary piece as support, the second layer C_2 is now weld to the connector at the proper height h_2. The auxiliary piece is then removed and the air gap expected between substrates is accurately achieved.

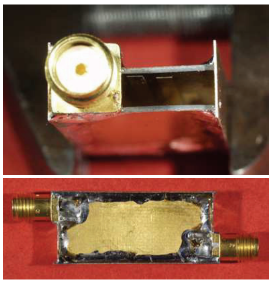

In order to complete the enclosure, lateral walls are now joined to the structure. The electric connection between the different walls of the cavity is done by welding from the outer side to keep straight the inner folds. This completes the assembling of the prototype.

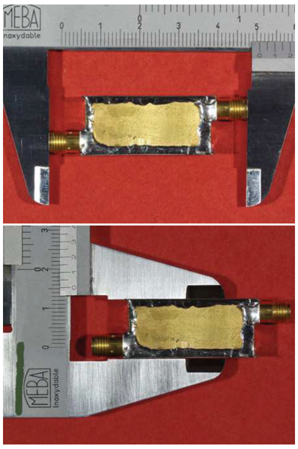

Final view and dimensions of the prototype.

Figure 5.31: Assembling of the prototype

5.6.3 Ring Resonator

The following benchmark, illustrated in Fig. 5.32, is a slow-wave bandpass filter using a single ring resonator coupled through a gap. This design was proposed in [53] but in an open microstrip structure. Other authors [24, 25] have used the same circuit enclosed inside a perfect magnetic walls box, to simulate the finite thickness of a dielectric. Here, we use the dimensions of the latter box but imposing perfect electric boundaries instead.

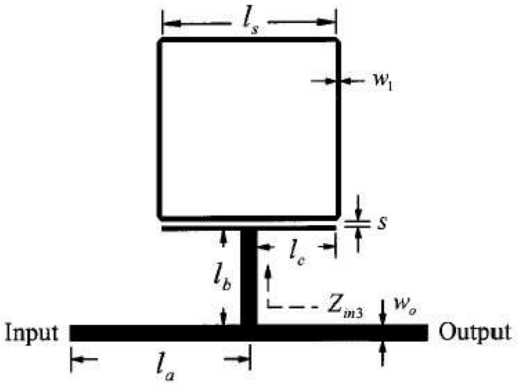

Figure extracted from [53].

l_s	s	l_a	l_b	l_c	w_0	w_1
12.070	0.200	12.376	6.500	5.456	1.158	0.300

Dielectric	Height [mm]	R. Permitt.	Losses
i	h_i	ε_{ri}	$\tan\delta_{e_i}$
2. Air	5.0	1.0006	0
1. RT/Duroid 6010	1.27	10.5	0.0024

- Cavity: $a = 24.752$, $b = 40.828$ mm; PEC.
- Microstrips: $\rho_{\mathrm{Cu}} = 1.82\ \mu\Omega\cdot\mathrm{cm}$

Figure 5.32: Description of Ring Resonator.

The novelty of this filter with respect to the other test cases lies on the shape of the printed circuit. An accurate modeling of the currents on the microstrip circuit requires a hybrid mesh combining triangular and rectangular cells. The triangles are used to model the flow in junctions and bends while the straight microstrip lines are meshed using rectangles.

Let us consider three mesh schemes represented in Fig. 5.33. Each configuration is generated with a different density. The first mesh, in Fig. 5.33(a), segments the lines into approx. 10 Div./λ using two cells in the main line's width. In the second configuration, in Fig. 5.33(b), the the lines are more densely segmented into approx. 25 Div./λ. Finally, Fig. 5.33(c) is like the previous but with a refined mesh in the coupling lines and along the ring resonator.

The response simulated for each mesh configuration is presented in Fig. 5.34, provided that the convergence of the modal series is achieved. The comparison shows very small differences between the different mesh schemes. Only a very small variation can be observed between the low-density mesh case corresponding to the scheme (a) and the rest.

The accuracy of our approach has been checked using as reference the response obtained by simulation with a commercial software [54]. The comparison of Fig. 5.35 shows an excellent agreement between both simulations.

Finally, Fig. 5.36 illustrates the induced currents on the printed circuits at two frequencies when the circuit is excited with one watt of available power (14.4 V on 50 Ω). The first plot, in Fig. 5.36(a), represents the currents at 2 GHz, corresponding to the first transmission zero in the filter response. In Fig. 5.36(b), the complementary effect is observed at the center frequency 2.48 GHz where a full transmission is produced.

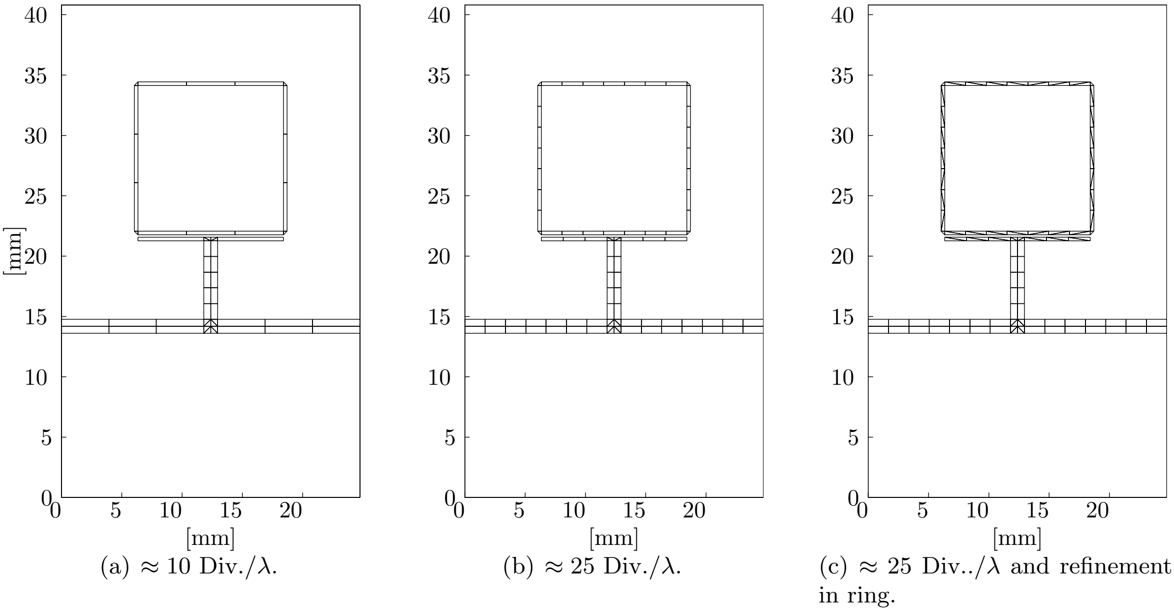

(a) ≈ 10 Div./λ.

(b) ≈ 25 Div./λ.

(c) ≈ 25 Div../λ and refinement in ring.

Figure 5.33: Three mesh schemes generated with triangular and rectangular cells.

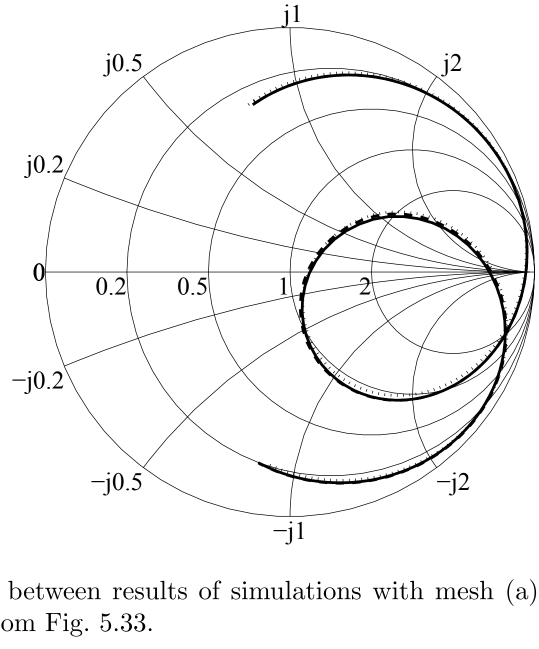

Figure 5.34: Comparison between results of simulations with mesh (a) (dotted), (b) (dashed) and (c) (solid) from Fig. 5.33.

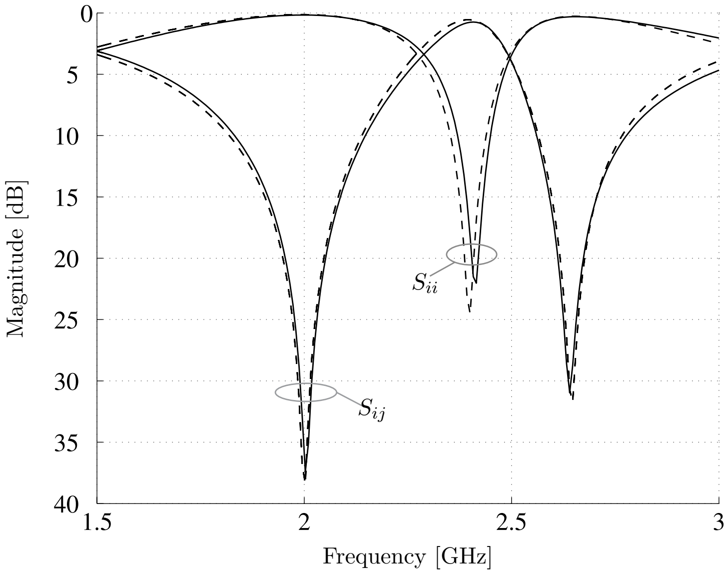

Figure 5.35: Return and insertion loss obtained with a simulation using our approach (solid line) and a commercial software [54] (dashed line).

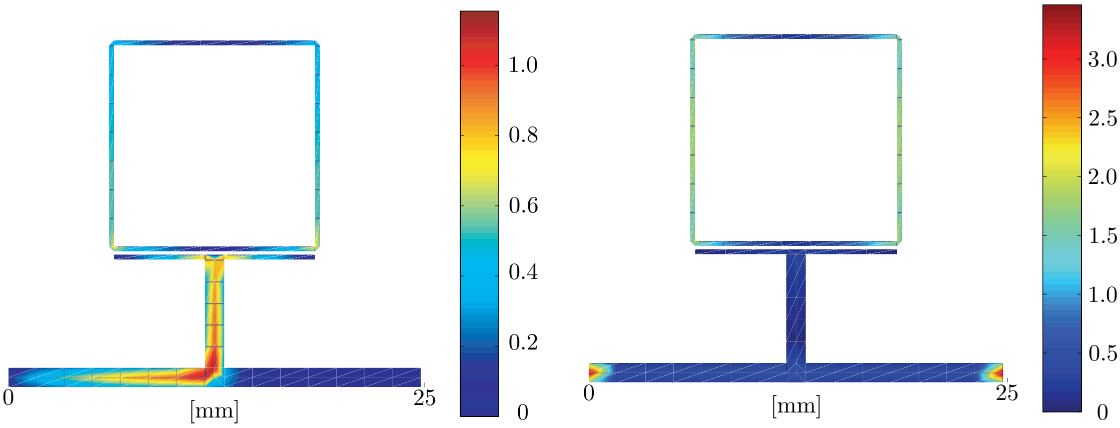

(a) Surface currents @2GHz

(b) @2.48GHz

Figure 5.36: Magnitude of the surface currents $\mathbf{J}(\mathbf{r}) \cdot \mathbf{J}^*(\mathbf{r})$ A/mm induced in the circuit by exciting first port (left-hand side) with one watt of available power ($V_g = 14.4$V and $Z_g = 50\ \Omega$).

5.6.4 Tapped-combline Bandpass Filter

Next benchmark, represented in Fig. 5.37, consists of a fifth-order tapped combline bandpass filter in microstrip technology [55]. The capacitors connected between the resonators and the cavity wall are considered lumped elements, and therefore of zero length. In the reference [55], the description of the design was not accurate and some important parameters, like the taper offset Δ or the details about the enclosure (if any), where missing.

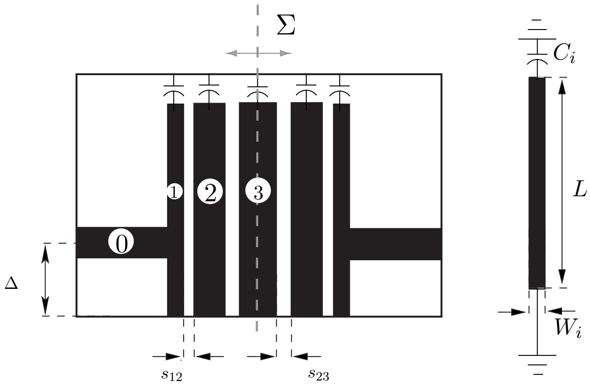

L	s_{12}	s_{23}
2.73	0.076	0.102

i	W_i[mm]	C_i[pF]
1	0.2032	0.2002
2	0.4064	0.2366
3	0.4572	0.2531

Dielectric i	Height [mm] h_i	R. Permitt. ε_{ri}	Losses $\tan\delta_{e_i}$
2. Air	3.3	1.0006	0
1.Duroid 5880	0.25	2.20	0.0009

- Cavity: $a = 6.032$, $b = 2.73$ mm; Cu $\rho_{\text{Cu}} = 1.82\ \mu\Omega\cdot$cm
- Microtrips: Cu

Figure 5.37: Description of Tapped-Combline filter [55].

This is a valuable test case that combines a coupled microstrip lines with lumped elements. Among other, it will serve to validate the connection of lumped elements to the high frequency device (§5.5).

The layout was discretized using rectangular cells in the lines and triangles in the junctions. The mesh is generated with a density of ≈ 28 div/λ along the lines and 3 cells in width. The convergence of the modal series is also verified. The simulation time, in a PC equipped with an Intel®Pentium D, 3.0GHz and 1GB RAM, is of 20 sec + (1.4 sec/freq).

Due to the incertitude in the value of some of the design variables we will perform some experiments in order to determine the behavior of the filter response.

Position of the Tapped-line: The filter is simulated with different values of offsets Δ/b relative to the first/last resonators length. The responses are plotted in Fig. 5.38 and show, as expected, how this parameter affects the matching of the filter response [56, §2]. In principle, the best matching is produced for an offset of $\Delta/b = 0.3833$.

Cavity dimensions: The reference publication describes that the filter has an upper cover and a ground plane for the microstrip circuit but it does not specifies anything about the presence of lateral walls. Nonetheless, this method requires the circuit to be enclosed inside a cavity. Hence, in Fig. 5.39, several simulations have been carried out in order to monitor the filter response for different cavity geometries. Two parameters of the cavity are changed: the width and the height. The fist case is shown in Fig. 5.39(a). The distance between the loaded end and the cavity wall is changed successively in the three simulations. The response

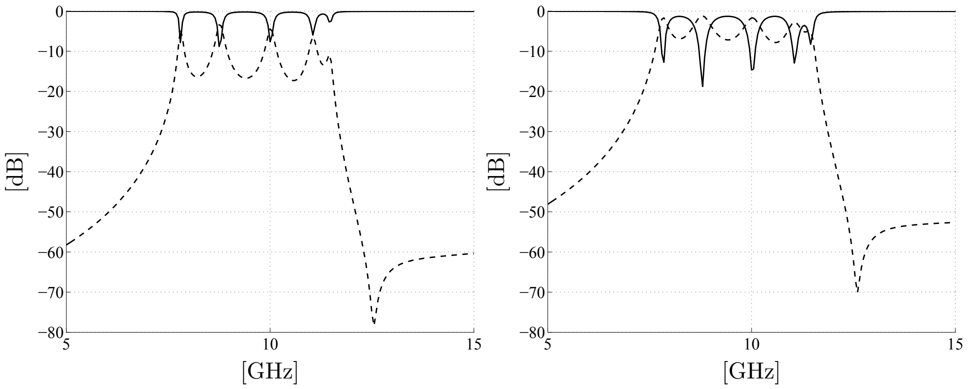

(a) $\Delta/b = 0.15$. (b) $\Delta/b = 0.2278$.

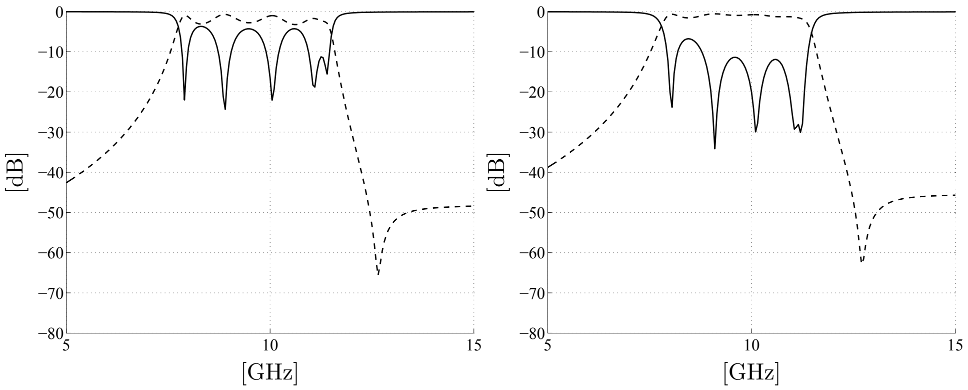

(c) $\Delta/b = 0.3056$. (d) $\Delta/b = 0.3833$.

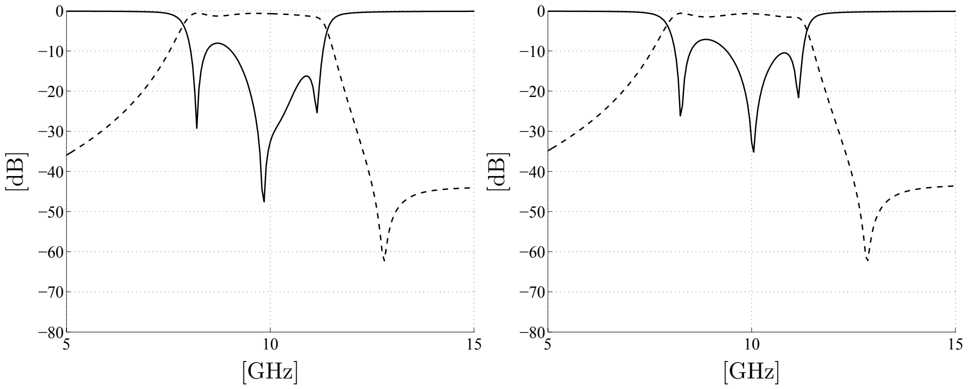

(e) $\Delta/b = 0.4611$. (f) $\Delta/b = 0.5$.

Figure 5.38: Insertion (dashed line) and return (solid line) losses (dB) versus frequency (GHz) for different positions of tapped line.

reduces its bandwidth and, in the last case, it produces a drastic shift of the transmission zero. Keeping the first configuration, the height of the cavity is modified in Fig. 5.39(b) producing an improvement in the isolation and again a reduction of the filter bandwidth.

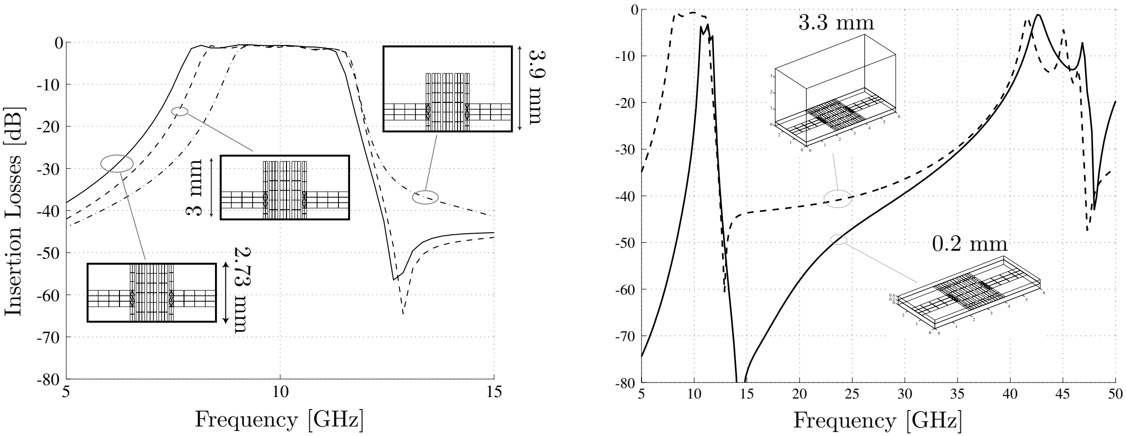

(a) Variation of the cavity width.

(b) Variation of the cavity height.

Figure 5.39: Influence of the cavity dimensions in the filter response considering a tapper offset of $\Delta/b = 0.3833$. Note: the symbols of the capacitors are not printed but the y are taken into account in the simulations.

One of the main topics to verify with this benchmark is the simulation of lumped elements within the full-wave EM analysis. The capacitors in this design determine the electric length of the filter resonators. In order to demonstrate the validity of the implementation, we have simulated the same structure by multiplying all capacitors by a factor 1.5 and 0.5. All the frequency responses are compared in the same plot in Fig. 5.40. The new electric length of the resonators shifts the filter response towards higher (resp. lower) frequencies for lower (resp. higher) capacitive loads.

Finally, using the setup of Fig. 5.37 with $\Delta/b = 0.5$ the filter response has been compared with the simulation and measurements available in [55]. The comparison is plotted in Fig. 5.41. In the bandpass, represented in Fig. 5.41(a), the response simulated with our method (①) reproduces well the position of the transmission zero and the bandpass shape although the prediction of the bandwidth is smaller than the reference (② and ③). Nonetheless, the slope in the lower band is very well predicted with our method (①) compared to the reference measurements (②). In Fig. 5.41(b) the same response is presented in a wider span, from 15 to 50GHz. In this case measurements are not available. The agreement in the filter bands and the position of transmission zeros is good but a *higher* isolation is predicted in our method's simulation along the stopband. Considering the *poor description* of the filter layout given in the reference [55], we believe that the agreement achieved is good. Observing the differences in Fig. 5.41(b) seems to show that the original design actually is not enclosed in a cavity but only has upper and lower shields. This could explain the higher isolation in the stopband due to the evanescent modes attenuating along the dielectric-filled rectangular waveguide in contrast with a laterally opened parallel plate waveguide.

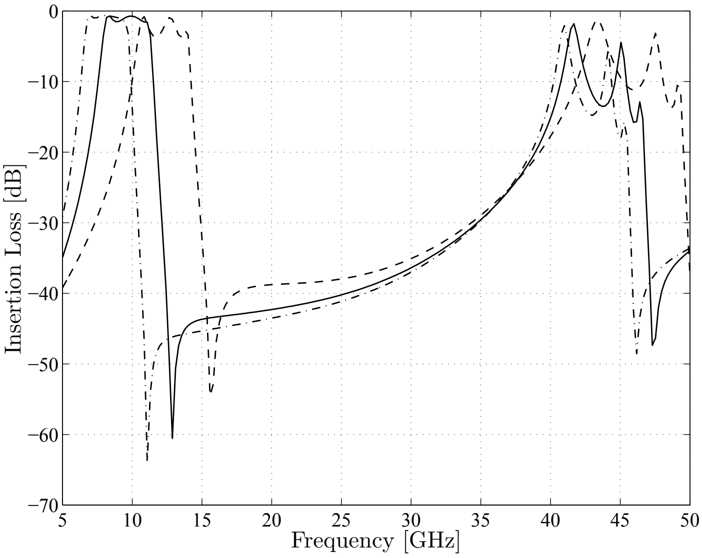

Figure 5.40: Filter responses in function of the capacitor values loading the resonators. Filter loaded with C_i from description (—); $1.5C_i$ (· −) and $0.5C_i$(− −).

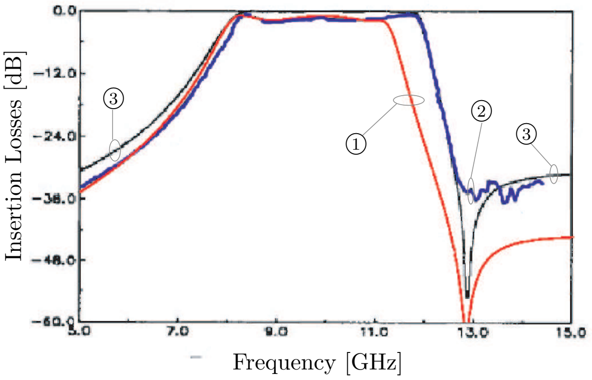

(a) Passband response.

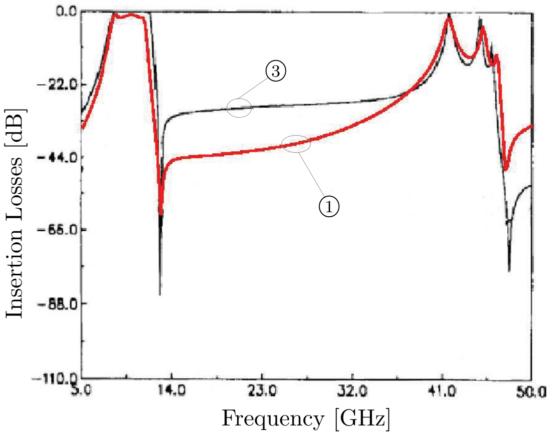

(b) Wideband response.

Figure 5.41: Insertion Losses (dB) versus frequency (GHz) of a tapped combline filter with $\Delta/b = 0.5$. Comparison between our method (① and solid red line) and published measurements (② and solid blue) and simulations (③ solid black) from [55].

5.6.5 Notch Filter

In the following example, we propose a notch filter in shielded microstrip technology. This device has been designed for the front-end of a real tracking system developed in the laboratory [57]. The specifications for the filter requires a high isolation at 4.87 GHz and very low insertion losses at 2.42 GHz. Using a shielded environment in the design aimed two things, first to avoid interferences from other EM sources and second to produce a higher rejection at the notch frequency.

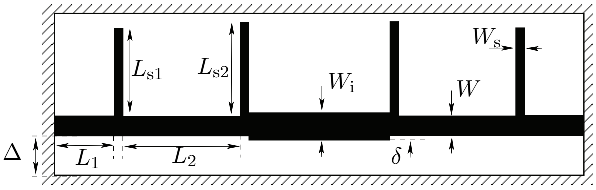

Δ	δ	W	W_s	W_i	L_1	L_2	L_{s1}	L_{s2}
3.0	0.1	0.6	0.2	0.9	3.0	8.0	6.00	6.20

Dielectric i	Height [mm] h_i	R. Permitt. ε_{ri}	Losses $\tan\delta_{e_i}$
2. Air	3.8	1.0006	0
1. TMM10i	0.635	9.8	0.0017

- Cavity: $a = 30.8$ mm, $b = 10$ mm in BeCu alloy $\rho_{BeCu} = 8.21\ \mu\Omega\cdot$cm
- Microstrips: $\rho_{Cu} = 1.82\ \mu\Omega\cdot$cm

Figure 5.42: Description of Notch Filter.

A prototype, illustrated in Fig. 5.43, is fabricated following a technique similar to that for the prototype in §5.6.2.

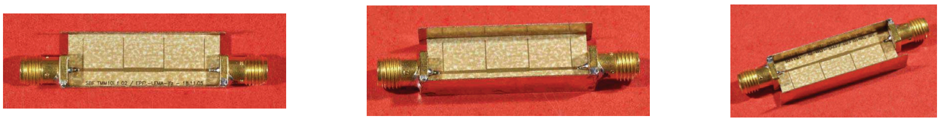

Figure 5.43: Different views of the prototype.

The results obtained in simulation and measurements are plotted in Fig. 5.44. The agreement between both curves is in general excellent. Small differences can be observed in the level of the first lobe, between 2 and 2.5 GHz, and in the prediction of the reflection zero around 3.5 GHz. The following analysis of sensitivity will reveal that these deviations can be justified by the fabrication and material tolerances.

We will explore the sensitivity of the filter response to the tolerances inherent to the materials or introduced during the fabrication process [see Fig. 5.45]. To account for theses inaccuracies, the following parameters are considered into a Monte-Carlo method:

- Materials:
  - Rogers TMM10i substrate with dielectric constant of $\varepsilon_r = 9.8 \pm 0.2$ and thickness $h_1 = 0.635 \pm 0.038$ mm.
  - Circuit layout printed in copper with resistivity $\rho_{Cu} = 1.68 \pm 0.1\ \mu\Omega\cdot$cm.
  - Shield fabricated in a beryllium-copper with estimated resistivity of $\rho_{BeCu} = 8.21 \pm 0.2\ \mu\Omega\cdot$cm.

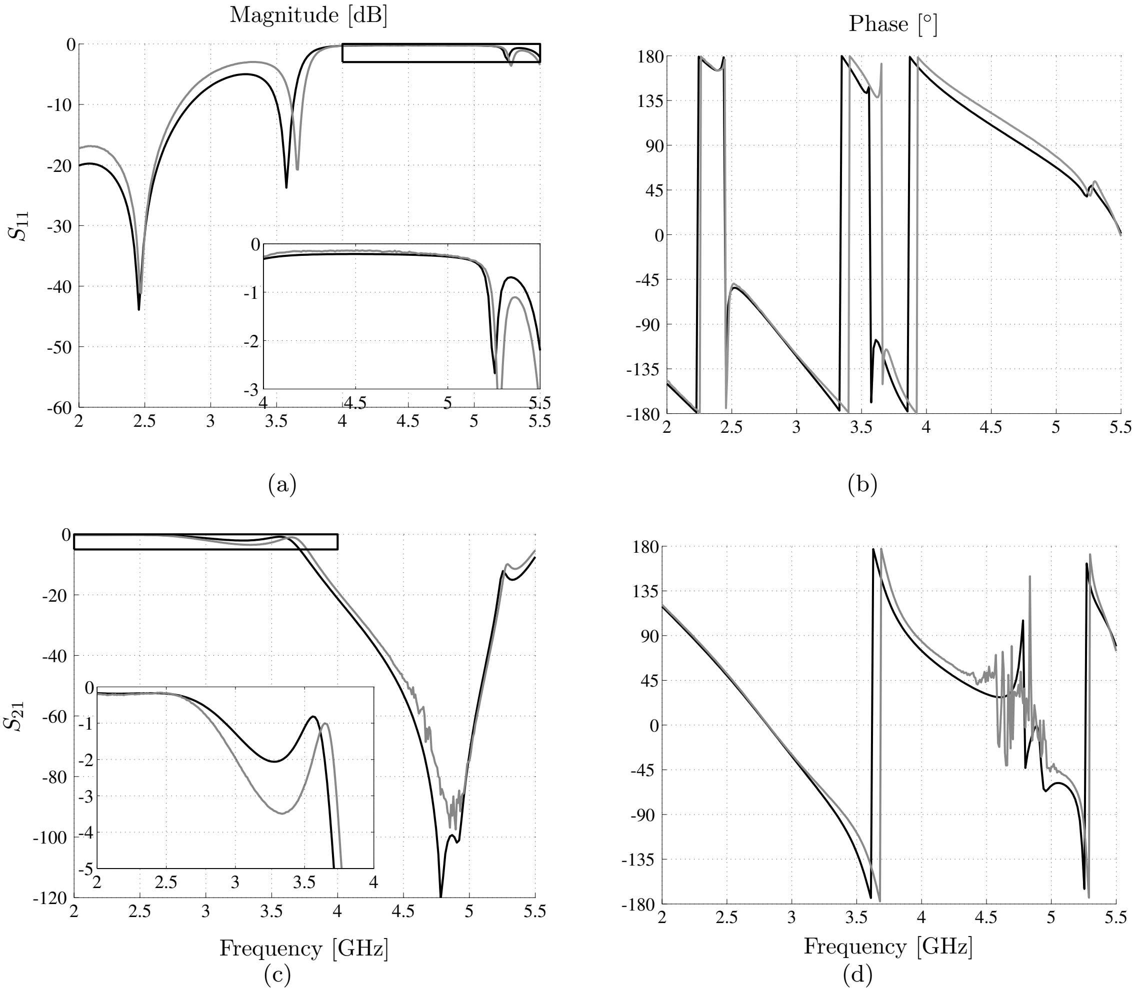

(a)

(b)

(c)

(d)

Figure 5.44: Comparison between measurements (gray lines) and simulations (black lines).

- Fabrication:
  - The circuit layout is printed with a precision (photolithography and wet-etching) of approximately ±10μm.
  - The assembling the shield-box and substrates (same technique as in Fig. 5.31) introduces inaccuracies in the air gap height of about $h_2 = 3.8 \pm 0.2$ mm and in the cavity dimensions of ±0.5 mm.
  - The alignment of the layout with respect to the box is critical due to the proximity of the end-edge of the stub lines to the cavity wall. This can be taken into account as an error in the offset $\Delta = 3 \pm 0.05$ mm.

Using a uniform variation of the 7 selected variables, a combination of 150 different structures, as illustrated in Fig. 5.45 is simulated with 50 samples on the target bandwidth. The simulations, plotted versus the prototype's measurements in Fig. 5.46, exhibit high sensitivity

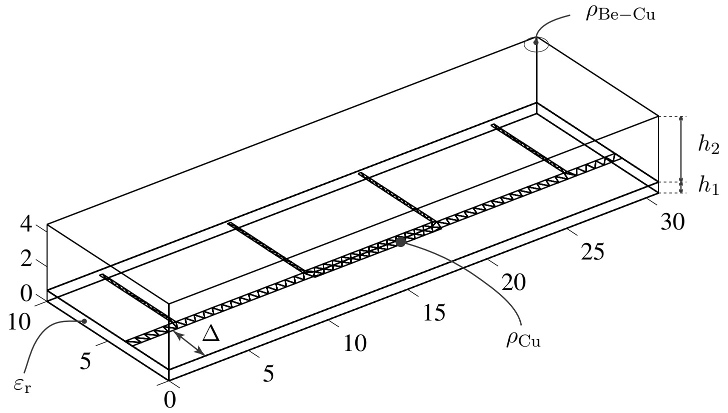

	Material			Mechanical		
	ε_{r}	$\rho_{\text{Cu}}^{\text{layout}}$	$\rho_{\text{Be-Cu}}^{\text{box}}$	h_1	h_2	Δ
Nominal value	9.8	1.68	8.21	0.635	3.8	3.0
tolerance ±	0.4	0.1	0.2	0.038	0.1	0.05

Figure 5.45: Sensitivity analysis. Monte-Carlo method parameters. Dimensions are given in mm and resistivity in $\mu\Omega$·cm.

in the regions around the resonant frequencies (zeros of transmission and reflection) which justifies the small differences appearing in Fig. 5.44.

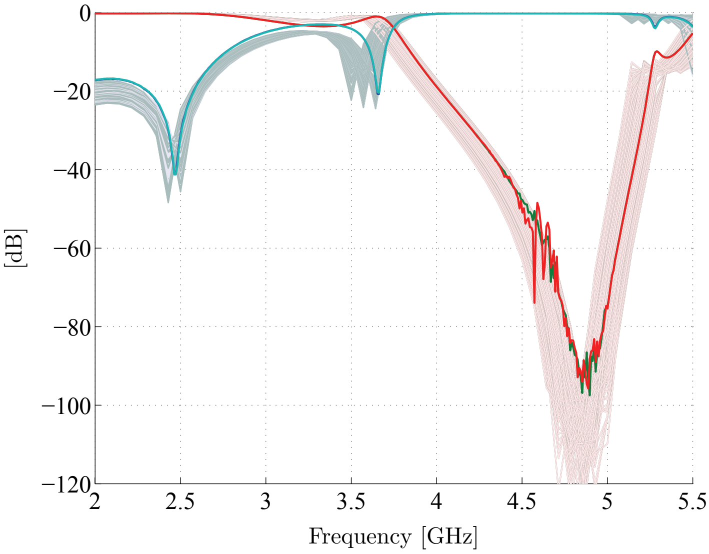

(a) Magnitude.

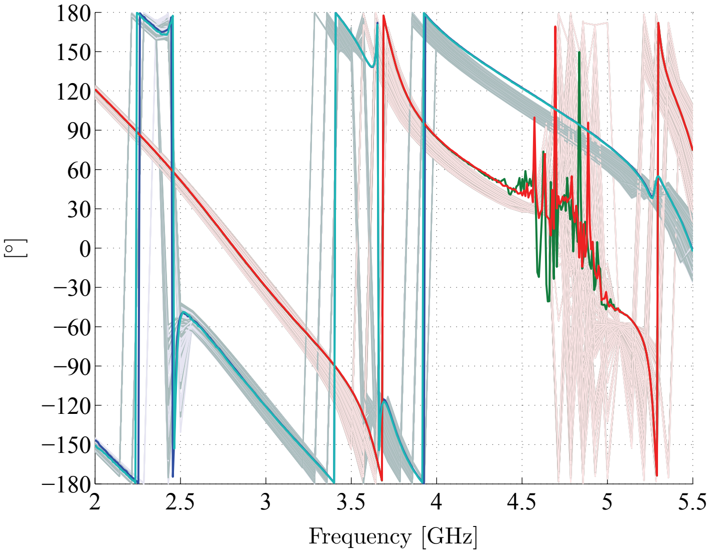

(b) Phase.

Figure 5.46: Measurements of scattering parameters (solid) compared to simulations from sensitivity analysis (watermark).

5.7 Conclusion

In this chapter we have specialized the previous methods for the analysis of multilayered boxed printed circuits.

A key concept in the method are the modal series which corresponds to the reaction terms filling the MoM matrix. When the reaction corresponds to bases situated at the same interface ($z = z'$), the slowly convergent and an acceleration technique is essential for an efficient resolution of the EM problem. An acceleration technique based on the Kummer's transformation provides us with a suitable solution. This technique is thoroughly discussed, starting with a formal mathematical definition and following with a physical interpretation based on modal propagation that provides us a valuable insight on what affects the speed of convergence in the series. This method naturally decomposes the series into quasi-static and dynamic parts. The latter has an improved convergence and the former is frequency independent. Therefore, the evaluation of this type of reactions was split in two parts. The quasi-static contribution are calculated outside the frequency loop and only the fast convergent dynamic part was calculated per frequency sample. Numerical experiments on convergence confirmed most of the theoretical advanced statements. Within the new series decomposition, the quasi-static TM series has the worst convergence, specially when it belongs to a self-reaction term. The convergence rate deteriorates in reactions taking place in small cells and when it occurs over a thin dielectric with high dielectric constant, specially in the proximity of a ground plane.

The modeling of losses in dielectric layers, printed metallizations and metallic boxes were also addressed. A Leontovich approximation was used for all the metallizations save for the upper and lower covers of the box that were modeled as metallic substrates in the multilayered media. It was interesting to find that the formulation of losses on the printed metallizations adds a sparse matrix $\mathbf{\Lambda}$ to the lossless MoM matrix. Analytic solution of the integrals arising in $\mathbf{\Lambda}$ were also presented.

In the context of an EFIE formulation, we revisited the procedure to obtain a network characterization of the device from the solution of the MoM. At the same circuit level, we presented a strategy to simulate lumped elements installed in the printed circuit. The same technique can be extended to the connection of any multiport network with the ports of the printed circuit.

Finally, extensive numerical experiments have been carried out to assess the validity and the performance of the aforementioned theory. The test-structures were specially selected to test different aspects of this type of devices. The convergence with the modal of terms in the modal series and with the mesh density were systematically verified in every case. The accuracy of the simulated responses was demonstrated by comparison with measurements and/or with other numerical solvers. When literature data were not available, sometimes a prototype was fabricated and measured. A sensitivity analysis, shown for one of the prototype designs, demonstrated the reliability and efficiency of the method to deal with a large amount of simulations. Other features presented throughout this validation process are the influence of losses in the response or the prediction of surface currents on the printed circuit for a given excitation.

References

[1] N. Ishitobi, E. Ajioka, T. Abe, and H. Ninomiya, "The improvement of miniaturized multilayer ceramic band-pass filter," in *Proc. IEEE MTT-S Digest*, 1999, pp. 1343–1346.

[2] P. Crespo-Valero, M. Mattes, and J. R. Mosig, "MAMBO: An implementation of an efficient method for the simulation of multilayered packaged printed circuits," in *Microwave Technology and Techniques Workshop*, ESA-ESTEC, Noordwijk, The Netherlands, May 15–16, 2006.

[3] J. C. Rautio and R. F. Harrington, "An electromagnetic time-harmonic analysis of shielded microstrip circuits," *IEEE Trans. Microwave Theory Tech.*, vol. 35, pp. 726–430, Aug. 1987.

[4] Harrington, *Time-Harmonic Electromagnetic Field.* New York: McGraw-Hill, 1961, p. 103.

[5] R. E. Collin, *Field Theory of Guided Waves*, 2nd ed. Piscataway, NJ: IEEE Press, 1990.

[6] R. W. Jackson, "The use of side wall images to compute package effects in mom analysis of mmic circuits," *IEEE Trans. Microwave Theory Tech.*, vol. 41, pp. 406–414, Mar. 1993.

[7] K. Knopp, *Theory and Application of Infinite Series.* New York: Dover, 1990.

[8] G. V. Eleftheriades, J. R. Mosig, and M. Guglielmi, "A fast integral equation technique for shielded planar circuits defined on nonuniform meshes," *IEEE Trans. Microwave Theory Tech.*, vol. 44, pp. 2293–2296, Dec. 1996.

[9] G. G. Gentili *et al.*, "Green's function analysis of single and stacked rectangular microstrip patch antenna enclosed in cavity," *IEEE Trans. Antennas Propagat.*, vol. 45, pp. 573–579, Apr. 1997.

[10] A. Álvarez-Melcón and J. R. Mosig, "Two techniques for the efficient numerical calculation of the green's functions for planar shielded circuits and antennas," *IEEE Trans. Microwave Theory Tech.*, vol. 48, pp. 1492–1504, Sept. 2000.

[11] I. Stevanović, P. Crespo-Valero, K. Blagović, F. Bongard, and J. R. Mosig, "Integral-equation analysis of 3-D metallic objects arranged in 2-D lattices using the Ewald transformation," *IEEE Trans. Microwave Theory Tech.*, vol. 54, no. 10, pp. 3688 – 3697, Oct. 2006.

[12] M.-J. Park, J. Park, and S. Nam, "Efficient calculation of the Green's function for rectangular cavity," *IEEE Microwave Wireless Compon. Lett.*, vol. 8, pp. 124–126, Mar. 1998.

[13] M.-J. Park and S. Nam, "Rapid calculation of the Green's function in the shielded planar structures," *IEEE Microwave Wireless Compon. Lett.*, vol. 7, pp. 326–328, Oct. 1997.

[14] Y. Hua and T. K. Sarkar, "Generalized pencil-of-function method for extracting poles on an EM system from its transient response," *IEEE Microwave Wireless Compon. Lett.*, vol. 37, pp. 229–234, Feb. 1989.

[15] C. J. Railton and S. A. Meade, "Fast rigorous analysis of shielded planar circuits," *IEEE Trans. Microwave Theory Tech.*, vol. 40, pp. 978–985, May 1992.

[16] A. Hill and V. K. Tripathi, "An efficient algorithm for the three-dimensional analysis of passive microstrip components and discontinuities for microwave and millimeter-wave integrated circuits," *IEEE Trans. Microwave Theory Tech.*, vol. 39, pp. 83–91, Jan. 1991.

[17] R. Faraji-Dana and Y. L. Chow, "Accurate and efficient CAD tool for the design of optimum packaging for (M)MICs," *IEE Proc. Microwaves, Antennas and Propagation*, vol. 142, pp. 81–88, Apr. 1995.

[18] I. Stevanović and J. R. Mosig, "A specially truncated set of images used for solving Green's functions for boxed planar structures," in *International Symposium on Antennas (JINA'02)*, vol. 1, Nice, France, Nov. 12-14, 2002, pp. 35–38.

[19] G. Conciauro, P. Arcioni, and M. Bressan, "State-space integral-equation method for the s-domain modeling of planar circuits on semiconducting substrates," *IEEE Trans. Microwave Theory Tech.*, vol. 51, pp. 2315–2326, Dec. 2003.

[20] L. Knockaert, J. Sercu, and D. D. Zutter, "Generalized Poisson-Neumann polygonal basis functions for the electromagnetic simulation of complex planar structures," *IEEE Trans. Microwave Theory Tech.*, vol. 52, pp. 954–960, Mar. 2004.

[21] B. M. Kolundzija and A. R. Djordjević, *Electromagnetic Modeling of Composite metallic and dielectric structures.* Boston: Artech House, 2002.

[22] A. Álvarez-Melcón, J. R. Mosig, and M. Guglielmi, "Efficient CAD of boxed microwave circuits based on arbitrary rectangular elements," *IEEE Trans. Microwave Theory Tech.*, vol. 47, pp. 1045–1058, July 1999.

[23] M. Bozzi *et al.*, "MoM/BI-RME Analysis of Boxed MMICs with Arbitrarily Shaped Metallizations," *IEEE Trans. Microwave Theory Tech.*, vol. 12, pp. 2227–2233, Dec. 2001.

[24] Repossi *et al.*, "Determination by the BI-RME method of entire-domain basis functions for the analysis of microstrip circuits," in *Proc. IEEE MTT-S Digest 2003*, 2003, pp. 1199–1202.

[25] ——, "Efficient analysis of printed circuits by the MoM/BI-RME method," in *Proc. 33rd European Microwave Conference 2003*, Munich, Germany, 2003, pp. 311–314.

[26] A. I. Khalil, A. B. Yakovlev, and M. B. Steer, "Efficient method-of-moments formulation for the modeling of planar conductive layeres in a shielded guided-wave structure," *IEEE Trans. Microwave Theory Tech.*, vol. 47, pp. 1730–1736, Sept. 1999.

[27] R. Boix, M. Freire, and F. Medina, "New method for the efficient summantion of double infinite series arising from the spectral domain analysis of frequecy selective surfaces," *IEEE Trans. Antennas Propagat.*, vol. 52, pp. 1080–1094, Apr. 2004.

[28] J. R. Mosig and A. Álvarez-Melcón, "The summation-by-parts algorithm - a new efficient technique for the rapid calculation of certain series arising in shielded planar structures," *IEEE Trans. Microwave Theory Tech.*, vol. 48, pp. 1492–1504, Sept. 2000.

[29] S. Hashemi-Yeganeh, "On the summation of double infinite series field computations inside rectangular cavities," *IEEE Trans. Microwave Theory Tech.*, vol. 43, pp. 641–646, Mar. 1995.

[30] N. Kinayman and M. I. Aksun, "Comparative study of acceleration thechniques for integrals and series in electromagnetic problems," *Radio Sci.*, vol. 30, pp. 1713–1722, Nov. 1995.

[31] K. A. Michalski and J. R. Mosig, "Multilayered media Green's functions in integral equation formulations," *IEEE Trans. Antennas Propagat.*, vol. 45, pp. 508–519, Mar. 1997.

[32] J. R. Mosig, "Integral-equation technique," in *Numerical Techniques for Microwave and Millimeter-Wave Passive Structures*, T. Itoh, Ed. New York: Wiley, 1989, ch. 3, pp. 133–213.

[33] A. Álvarez-Melcón, "Application of the integral equation technique to the analysis and synthesis of multilayered printed shielded microwave circuits and cavity backed antennas," Ph.D. dissertation, École Polytechnique Fédérale de Lausanne, Switzerland, 1998, thèse No. 1901.

[34] P. Sebah and X. Gourdon, "Convergence acceleration of series." [Online]. Available: http://numbers.computation.free.fr/Constants/constants.html

[35] M. Abramowitz and I. Stegun, Eds., *Handbook of Mathematical Functions.* Mineola, NY: Dover, 1964.

[36] M. Mattes, "Contribution to the electromagnetic modelling and simulation of waveguide networks using integral equations and adaptive sampling," Ph.D. dissertation, École Polytechnique Fédérale de Lausanne, Switzerland, 2003, thèse No. 2693.

[37] I. Stevanović, P. Crespo-Valero, and J. R. Mosig, “An integral-equation technique for solving thick irises in rectangular waveguides,” *IEEE Trans. Microwave Theory Tech.*, vol. 54, no. 1, pp. 189–197, 2006.

[38] J. E. Page, *Propagación de Ondas Guiadas.* Madrid: E.T.S. Ingenieros Telecomunicación (UPM), 1987.

[39] J. A. Stratton, *Electromagnetic Theory.* New York: McGraw-Hill, 1941.

[40] R. E. Collin, *Foundations for Microwave Engineering*, 2nd ed. New York: McGraw-Hill, 1992.

[41] N.Marcuvitz, *Waveguide Handbook*, ser. Radiation Laboratory. New York: McGraw Hill, 1941.

[42] J. Allison and F. Benson, “Surface roughness and attenuation of precision drawn, chemically polished, electropolished, electroplated and electroformed waveguides,” *Proceedings IEE (London)*, vol. 103(part B), pp. 251–259, 1955.

[43] Ramo, Whinnery, and V. Duzer, *Fields and Waves in communication electronics.* New York: John Wiley and Sons, Inc., 1967.

[44] K.Polivanov, *The Theory of Electromagnetic Field.* Moscow: Mir, 1983.

[45] D. M. Pozar, *Microwave Engineering*, 2nd ed. New York: Wiley, 1998.

[46] J.-S. G. Hong and M. J. Lancaster, *Microstrip Filter for RF/Microwave Applications*, ser. Microwave and Optical Engineering, K. Chang, Ed. New York: John Wiley & Sons, 2001.

[47] R. Compton, “Perspectives in microwave circuit analysis,” in *Circuits and Systems, 1989., Proceedings of the 32nd Midwest Symposium on*, vol. 2, 14-16 Aug. 1989, pp. 716–718.

[48] R. Gillard, S. Dauguet, and J. Citerne, “Correction procedures for the numerical parasitic elements associated with lumped elements in global electromagnetic simulators,” *IEEE Trans. Microwave Theory Tech.*, vol. 46, no. 9, pp. 1298–1306, Sept. 1998.

[49] V. Okhmatovski, J. Morsey, and A. Cangellaris, “On deembedding of port discontinuities in full-wave cad models of multiport circuits,” *IEEE Trans. Microwave Theory Tech.*, vol. 51, no. 12, pp. 2355–2365, Dec. 2003.

[50] M. Goldfarb and R. Pucel, “Modeling via hole grounds in microstrip,” *IEEE Microwave Guided Wave Lett.*, vol. 1, no. 6, pp. 135–137, 1991.

[51] M. Guglielmi and A. Álvarez-Melcón, “Multimode network analysis of planar transmission lines,” *IEEE Trans. Microwave Theory Tech.*, vol. 43, pp. 2621–2626, Nov. 1995.

[52] J. R. Mosig, “Integral-equation techniques for three-dimensional microstrip structures,” in *Review of Radio Science*, R. Stone, Ed. Oxford: URSI-Oxford Science Publications, 1992, ch. 6, pp. 127–152.

[53] L.-H. Hsieh and K. Chang, “Slow wave bandpass filters using ring of stepped-impedance hairpin resonators,” *IEEE Trans. Microwave Theory Tech.*, vol. 50, pp. 1795–1800, July 2002.

[54] “Ansoft Corporation.” [Online]. Available: http://www.ansoft.com/

[55] T. C. Ching-Kuang and L. Wen-Teng, “Printed-circuit realization of a tapped combline bandpass filter,” in *Proc. IEEE MTT-S Digest 1990*, 1990, pp. 131–134.

[56] J. Wong, “Microstrip tapped-line filter design,” *IEEE Trans. Microwave Theory Tech.*, vol. 27, no. 1, pp. 44–50, Jan 1979.

[57] E. de Moura Presa, J.-F. Zuercher, and A. K. Skrivervik, “A new microwave harmonic direction finding system for localization of small mobile targets using passive tags,” *Microwave and Optical Tech. Lett.*, vol. 47, pp. 134–137, Oct. 2005.

6 Conclusions

6.1 General Assessment

The work undertaken in the frame of this thesis has allowed us to enlighten some aspects concerning the EM modeling of printed circuits in bounded layered media.

The IE in conjunction with the method of moment is known to be an efficient technique for the simulation of printed circuits in open layered media. Introducing a transversally bound structure destroys the translational symmetry in the xy-plane and makes Green's functions expressions much more involved. Here the challenge was to extend this formulation to a generic bounded problem. The resulting formulation is rather complicated but we have overcome this drawback with an structured solution for a generic problem. All the results obtained are therefore applicable to a wide variety of problems considered as bounded layered media. Some examples, among others, are multilayered boxed printed circuits, waveguide discontinuities or infinitely thin irises, planar scatterers arranged in an infinite skewed lattice or planar circuits enclosed in magnetic boundaries to emulate finite dielectric.

An overall description of the strategy, that applies the equivalence principle and a surface integral formulation, is given in Chapter 2. The cornerstone of the method consists of reducing the three-dimensional EM problem into two different problems. The first is associated to the boundary cross-section and it consists of solving a two-dimensional transverse boundary problem. On the other hand, the remaining dimension, i.e. the longitudinal direction, is modeled using an equivalent circuit built up from cascaded transmission lines.

The results obtained from both problems are combined in infinite series extended to all the modes resulting from the transverse boundary problem. These modal series corresponds to the reaction terms filling the MoM matrix. The analytic expressions found for them avoids an explicit evaluation of the GF and the numerical integration of the reaction terms, both usually needed in the currently used formulations.

In Chapter 3 we have addressed the transverse boundary problem. The resolution followed a unified approach based in a general solution for the OIs arising in any formulation using integral equations and the MoM techniques. The overlapping between zero-curl & constant-change BFs and modal functions, associated to the transverse eigenvalue problem, was reduced to integrals evaluated along the contour of the basis functions domain. The new integral forms are applied with linear subsectional BFs defined over rectangular or triangular domains, resulting in expressions with a seamless transition between the two cases. The result of this specialization simplifies the procedure to two line integrals on the scalar potential of the mode considered. Hence, any transverse boundary medium could be considered if the solution to these two line integrals is available. We have demonstrated this in rectangular and circular PEC boundaries as well as for periodic lattices, always obtaining analytic solutions.

The structures considered at the end of the same chapter showed an example of a printed circuit structure enclosed by three different transverse BCs. The response in each problem was obtained using the same software tool, based on this method, and compared with other ad hoc numerical techniques. These experiments confirmed that this technique avoids having a specific formulation for each type of problem. It also offers a unified and versatile approach that, on one hand eliminates redundancy in the formulation and on the other hand simplifies each particular problem.

In Chapter 4, the longitudinal problem arising in this method has been presented. It demonstrates how a stable and efficient algorithm can be derived in order to solve a transmission line model arising for every modal solution to the transverse boundary problem. The algorithm is based on a traveling wave approach but other alternate formulations were also presented to tackle other approaches. In particular, expressing the model in terms of a bilinear form shows clearly all the degrees of freedom allowed in the equations and the separability in the source and observer variables.

One of the main goals in this chapter was to achieve an stable algorithm. Some numerical experiments revealed critical scenarios that could not be solved by traditional transmission line models. We demonstrated how these cases could be avoided and used these criteria to build the final algorithm.

In addition, the formulation of the transmission line model established the basis to understand the resonances in dielectric filled cavities. We have explored the nature of these resonances in order to get an insight about the physical mechanisms. An example showed the potential use of simultaneous printed-circuits and the multilayered-cavity resonances in the design of filter response.

It is a fact that the EM simulation of multilayered printed circuits involves an important computational burden in nowadays methods. In addition to the stability, the efficiency of the algorithm was also demonstrated for this type of structures. The simulation of an eleven layers filter was performed significantly faster than a widely used commercial solver, for a comparable accuracy.

Finally, Chapter 5 presents a specialization of the overall method for the analysis of multilayered boxed printed circuits. This type of structure is of special interest for RF / microwave applications since it provides a miniaturized and low-cost solution, in addition to a solid mechanical support and an adequate EM compatibility behavior.

In this particular frame, we have explored the behavior of the modal series and applied a Kummer's transformation to accelerate its convergence. The method decomposed, for the reaction taking place in the same plane, each series into a quasi-static and dynamic parts. Now, the simulation time is reduced since the quasi-static series are calculated outside the frequency loop and only the fast convergent dynamic part are calculated at each frequency sample. Within the new series decomposition, the quasi-static TM series has the worst convergence, specially when it belongs to a self-reaction term. In addition, the convergence rate deteriorates in reactions taking place in small cells and when if occurs over a thin and high dielectric, specially in the proximity of a ground plane.

Another topic considered in this chapter corresponds to the modeling of losses in the complete structure. Losses in dielectric layers, printed metallizations and metallic box were all considered. Using the Leontovich approximation on most of the metallic surface in the structure simplified the formulation of the problem, giving accurate results for good conducting surfaces. The influence of losses in the circuit response has been presented for different filter structures and the loss model has been considered in all the simulations presented throughout the chapter.

The current flow over an arbitrary shaped printed circuit has been discretized into rooftops, with rectangular support, and Rao-Wilton-Glisson BFs over triangular domains. The difference in the implementation of both BFs is unified and only differs in some constant values, as was anticipated in Chapter 5.

The simulation of lumped elements in the printed circuit were considered at the circuit level. These elements were connected to the multiport scattering parameters derived from the solution of the method of moments.

Finally, extensive numerical experiments have been carried out to assess the validity and the performance of the aforementioned theory. The accuracy of the simulated responses was demonstrated by comparison with measurements and/or other numerical solvers. Two prototype were fabricated and measured. A sensitivity analysis, shown for one of the prototype designs, demonstrated the reliability and efficiency of the method to deal with a large amount of simulations. Other features presented there are the prediction of surface currents on the printed circuit for a given excitation.

6.2 Original Contributions

The original contributions of this thesis are the following:

Chapter 2 a) Systematic and complete treatment of the full mathematical chain from the fundamental Maxwell-Hertz-Heaviside equations to the method of moments implementation. b) Innovative approach for translating the raw MoM results into a network representation.

Chapter 3 A unified and systematic approach that provides a formulation of the OIs (combining a basis and a modal functions) for locally curl-free & constant charge basis functions and any transverse boundary problem.

Chapter 4 a) Provides a complete exploration of all the possible formulations for the transmission line model b) Efficient algorithm which remains stable even in the most harsh conditions.

Chapter 5 Summarizes the work carried out in the development of `MAMBO`, a complete software tool specially design for the efficient EM modeling of multilayered boxed printed circuits.

For a complete list of publications, the reader is referred to the page 167 of this thesis.

6.3 Perspectives

There are several possible improvements that can be carried out as a continuation to the presented developments. These ideas are presented in the following paragraphs.

We have shown that the current acceleration technique provides very good simulation times. Nonetheless, we believe that there is still room for improvements in this direction. The basic idea consist of exploring the decomposition into multiple reflections of §4.3 to develop asymptotic expressions for the reaction terms while keeping a general transverse boundary problem.

The thickness of the printed circuits plays an important role, not only in the modeling of losses but the complete IE method itself. The latest improvements in the manufacture process are producing printed circuits with metallization below the penetration depth $\delta_{\mathrm{s}} \gg t$ at microwave frequencies. On the other hand, many applications are working in higher frequencies, where a printed circuit, fabricated with a standard technology, becomes electrically thick $t \gg \lambda$. Hence, an interesting research line would be: a) exploring a rigorous IE formulation considering both electric and magnetic equivalent currents; b) explore different approaches (perhaps approximate) to tackle the above cases; c) gain an insight into physical meaning and consequences of having very lossy circuit, $\delta_{\mathrm{s}} \gg t$ and $t \gg \lambda$.

The formulation presented considers only planar circuits. Most of the surface of the printed circuit devices is planar. Nevertheless, novel techniques, like Low Temperature co-fired Ceramics (LTCC) filters or the so called surface integrated waveguides (SIW), are extensively using vertical metallizations. Since most of the applications used long metallic cylinders, this problem could be addressed using at least two complementary approaches. One possibility would be dealing with the cylindrical surfaces as equivalent currents which will increase the size of the linear system in the MoM. On the other hand, the scattering from vertical cylinders could be formulated in the Green's functions (at least this is true in free space) which will reduce the number of unknown but increase the complexity of the formulation.

Other improvements could also be considered. However the author believes that the current software tool, eventually enlarged with the above mentioned developments, is the target that should be aimed at in a very near future.

List of Abbreviations

BC Boundary Condition

BF Basis Function

CAD Computer Aided Design

EFIE Electric Field Integral Equation

EM Electromagnetic

EMC Electromagnetic Compatibility

ESA-ESTEC European Space and Technology Center of the European Space Agency

FFT Fast Fourier Transform

FSS Frequency Selective Surface

GF Green's function

GTR Generalized Transverse Resonance

IE Integral Equation

IM Images

MAMBO siMulation of Arbitrary Multilayer Boxed printed circuits

ME Modal Expansion

MEMS Micro-Electro-Mechanical Systems

MFIE Magnetic Field Integral Equation

MHH Maxwell–Hertz–Heaviside

MM Mode Matching

MMIC (Monolithic) Microwave Integrated Circuit

MoM Method of Moments

OI Overlapping Integral

PEC Perfect Electric Conductor

PMC Perfect Magnetic Conductor

RF Radio Frequency

RWG Rao–Wilton–Glisson

TE Transverse Electric

TEM Transverse Electromagnetic

TL Transmission Line

TLMo Transmission Line Model

TM Transverse Magnetic

List of Figures

1.1 An example of printed circuits in a bounded layered media. (a) transverse boundary conditions, (b) layered media, (c) three-dimensional view. 2

2.1 Discontinuity in fields produced by surface currents over S. 8
2.2 Transverse view of a general problem: a planar circuit (Ω_1) embedded in a medium bounded by $\partial\Omega$. 8
2.3 Equivalence principle for flat conducting screen. 9
2.4 Equivalence principle for an aperture in a conducting plane. 11
2.5 General representation of the GF problem and an associated model. 12
2.6 Dual electric and magnetic problems on a region D 17
2.7 Representation of the reaction taking place when electric and magnetic sources are considered. The circuit terminals in the electric and magnetic case are short- and open- circuited respectively since the excitation coefficients are zero (in the lossless case). The electric terminals are represented as external accesses to the circuit 18

3.1 The cross-section (left) and longitudinal view (right) of planar electric (**J**) and magnetic (**M**) sources embedded in a medium with BCs imposed on an arbitrary cylindrical surface $\partial\Omega$ 24
3.2 Discretization of planar surface with $\mathrm{Q} = \{\mathrm{E}, \mathrm{H}\}$-type sources into D domains. 30
3.3 A half-BF $\mathbf{g}$ defined on a triangular (half-RWG function) and rectangular (half-rooftop) subdomain $D^{\pm}$. The arrows represent the vector function $\mathbf{g}_p$, the lines the contour plot of the auxiliary function f_p and the nodes and sides are enumerated counterclockwise. 31
3.4 Triangular path. 32
3.5 Waveguide boundaries. 36
3.6 General two-dimensional (2-D) skewed lattice of planar objects. 40
3.7 A rectangular strip conductor of $w \times l = 2.38 \times 13.3$ mm^2 of zero thickness with three different transverse boundary conditions. 46
3.8 Scattering of the TE$_{01}$ mode from a strip inside a rectangular waveguide in Fig. 3.7(a). The presented method using only rooftops (solid line) or RWG BFs (dashed line), IE method of [25] (dotted line) and MM/GTR technique of [26] (dashed-dotted line). 47
3.9 Scattering of the TE$^y_{11}$ mode (y-polarized) from a strip inside a circular waveguide as in Fig. 3.7(b). $\mathrm{S}_{11} = S_{22}$ (solid line) and $S_{21} = S_{12}$ (dashed line). . . . 47

3.10 Reflection coefficient for a TE_{00} Floquet mode (y-polarized) impinging the periodic lattice Fig. 3.7(c) with angles $\theta = 1^\circ, \phi = 1^\circ$. This method using only rooftops (solid line) or RWG basis functions (dashed line) and simulations from [27] (dotted line). 48

3.11 Geometry and frequency response for the TE_{10} mode in the WR-90 waveguide (22.86 × 10.16 mm): this method (solid lines) and method of [25] (dashed lines). 49

A.1 Evaluation $I(m) = \int\limits_0^1 \sin(\pi/2+mt)\,\mathrm{d}t$ for small values of m, using the expression given in (A-3a) (denoted with f and plotted with $\bullet$ symbol) and the formula (A-3b) (denoted with $\hat{f}$ and represented with $\circ$). The difference between them is also plotted below. 52

4.1 Source radiating in a bounded layered medium and the equivalent circuit for each mode. 56

4.2 Voltage and current along a transmission line. 57

4.3 Interaction between source (vertical arrow) and observer (circle) points in a loaded TL. 57

4.4 Representation of P'-type excitations: (a) parallel current ($P' = I$); (b) series voltage generator ($P' = V$) and (c) symbolic representation of a source in a TL. These relations are demonstrated in Appendix. 59

4.5 Source and observer within the same layer. 59

4.6 TL section with source and observer interaction in the same layer $z, z' \in [\varsigma_0\, \varsigma_1]$. 61

4.7 Source and observer in different sections of a layered media. 61

4.8 Paths followed by each ray component in the multiple rays decomposition. . . . 65

4.9 Computation of a decreasing exponential using hyperbolic functions $\tilde{f} = \cosh(x) - \sinh(x)$ (dashed line with dot markers) and the exact formula $f = \mathrm{e}^{-x}$ (solid line). Note: Results equal to zero are plotted as 10^{-11}. 67

4.10 Comparison between a method based on a standing-wave formulation (solid $\bullet$ line) and this method (dashed line) when the wave is highly attenuated. Voltage/Current distribution for $\kappa \approx 0.59\pi$ and $k_0 \approx \frac{\pi}{5}$ mm^{-1} ($\mathrm{TE}_{50,21}$-mode in a 92×92 mm^2 waveguide at 30 GHz) generated by a current source injected at the interface between ① and ②. The multilayered configuration is: $\varepsilon_{\mathrm{r}1} = 30$, $h_1 = 1.54$ mm (high permittivity dielectric); $\varepsilon_{\mathrm{r}2} = 1$, $h_2 = 12.83$ mm (TL section *under cutoff*). This structure is short-circuited at both ends and $\mu_{\mathrm{r}} = 1$ in all dielectric layers. 68

4.11 TL at cutoff condition. 70

4.12 Adapting TL section to a new reference impedance ζ. 71

4.13 Voltage/Current amplitude (solid/dashed lines) for $\kappa \approx 0.25\pi$ and $k_0 \approx \frac{\pi}{30}$ mm^{-1} ($\mathrm{TM}_{1,2}$-mode in a 21×8 mm^2 waveguide at 5 GHz) generated by a voltage source injected at the interface between ① and ②. The multilayered medium is: $\varepsilon_{\mathrm{r}1} = 131 - \mathrm{j}0.3, \mu_{\mathrm{r}1} = 1, h_1 = 2.81$ mm (lossy $0.4\lambda_g$ section); $\varepsilon_{\mathrm{r}2} = 19.4, \mu_{\mathrm{r}2} = 3, h_2 = 2$ mm (*line at cutoff*); $\varepsilon_{\mathrm{r}3} = 124 - \mathrm{j}, \mu_{\mathrm{r}3} = 1.2, h_3 = 3.77$ mm (lossy $0.6\lambda_g$ TL). The structure is short-circuited at both ends. 73

4.14 Voltage/Current distribution for for $\kappa \approx \frac{\pi}{21}$ and $k_0 \approx \frac{\pi}{30}$ mm^{-1} (TE$_{10}$-mode in a 21×8 mm^2 waveguide at 5 GHz) generated by a current source injected at the interface between media ⑤ and ⑥. The multilayered configuration is: $\varepsilon_{\mathrm{r}1} = 4.59 - \mathrm{j}0.3$, $h_1 = 15.026$ mm; $\varepsilon_{\mathrm{r}2} = 4.59 - \mathrm{j}3 \cdot 10^4$, $h_2 = 1$ mm (0.012Ωcm low resistivity silicon); $\varepsilon_{\mathrm{r}3} = 9.88$, $h_3 = 25.72$ mm; $\varepsilon_{\mathrm{r}4} = 1 - \mathrm{j}2.14 \cdot 10^8$, $h_8 = 1$ mm (copper sheet); $\varepsilon_{\mathrm{r}5} = 4.59$, $h_5 = 33.809$ mm; $\varepsilon_{\mathrm{r}6} = 2.04$, $h_6 = 2$ mm; $\varepsilon_{\mathrm{r}7} = 5.22 - \mathrm{j}$, $h_7 = 20.176$ mm; in ⑧ copper sheet again; $\varepsilon_{\mathrm{r}9} = 3.45 - \mathrm{j}0.002$, $h_9 = 12.641$ mm and $\varepsilon_{\mathrm{r}10} = 1.65$, $h_{10} = 5$ mm. The structure is short-circuited at both ends and $\mu_{\mathrm{r}} = 1$ in all cases. 75
4.15 Description of Parallel Stub [12]. 76
4.16 Frequency response simulated with this method (solid line), with commercial software (dashed line) and measurements from [12] (in gray and only available in magnitude). 76
4.17 Magnitude and phase of the characteristic function at 3.5 GHz in the ℂ-plane (contour plot) and mode wavenumbers (positive real eigenvalues $\bar{\kappa}_{mn}^2 k_0^2 = (m\pi/a)^2 + (n\pi/b)^2$) of the rectangular waveguide (dots). 78
4.18 Variation of the normalized reactance in function of real values of κ_ρ/k_0. 79
4.19 Prediction of resonances in the frequency response [below: insertion (○) and return (●) losses] from the TM-resonance chart (above). The cavity dimensions are $a = 92$ mm, $b = 1.1a$. 81
4.20 Layout of Broadside Filter [15]. From left to right: Vertical distribution of dielectric layers, printed circuits and ports; Top view of three types of resonators; Dielectrics and metallizations. 82
4.21 Broadside bandpass filter simulated with this method (solid line) and a commercial software (dashed line). 82
4.22 Time profile for simulations with this method and a commercial software. Legend in table. 83
A.1 Lumped current and voltage generators. 85
A.2 Wave and reflection coefficient propagation (a) through an interface between adjacent TLs and (b) along a TL. 87
A.3 Transition between adjacent TLs. 88
A.4 Determination of impedance regions giving $|\Gamma| \lesseqgtr 1$ in function of the reference impedance. 90

5.1 Transverse (a) and longitudinal (b) cross section views of a multilayer boxed printed circuit. 94
5.2 Simplified scheme for the resolution of a quasi-static problem. (a) Evanescent field at the interface between two layers; (b) Equivalent circuit consisting of two semi-infinite TLs. 100
5.3 TM-voltage response generated by a current excitation with two different substrate thickness: h and $2h$. Dielectric filled cavity ($h = 0.4$ mm, $\varepsilon_{\mathrm{r}} = 9.9$) with a 25.4×25.4 mm^2 cross-section and height 4 mm. 101
5.4 Relative error by the limit (5.12) definition, with respect to $\widehat{V}_i$ when the substrate permittivity is $\varepsilon_{\mathrm{r}} = 9.9$ (solid line) or $\varepsilon_1/4$ (dashed line). 102

5.5 Test structure for series convergence studies. Rectangular PEC cavity $92 \times 92 \times 11.4$ mm^3 filled with a dielectric with permittivity $\varepsilon_\mathrm{r} = 2.33(1 - \mathrm{j}0.0012)$ and height $h = 1.57$ mm. 103
5.6 Evolution of the partial sums in the quasi-static series. Self-interactions: 0–0 (□), 1–1 (×) and 2–2 (●); Cross-interactions: 0–1 ($*$), 0–2(+) and 1–2(○). . . . 105
5.7 Rate of convergence for the TM/TE quasi-static series. The curves represent ϵ_M with respect to the values presented in Table 5.3 for each case. Only self-interactions are represented for the TE (dash lines) and TM (solid lines) series: 0–0 (□), 1–1 (×) and 2–2 (●). 106
5.8 Sequence of partial sums for the TE/TM dynamic series. Self-interactions: 0–0 (□), 1–1 (×) and 2–2 (●); Cross-interactions: 0–1 ($*$), 0–2 (+) and 1–2 (○). 107
5.9 (a) Partial sums of dynamic series for two substrate thickness: h (solid) and $2h$ (dash). Dynamic series constructed with the asymptotic form: $\widehat{V}_i^{\mathrm{TM}}$ (●) or $\widehat{V}_i^{\mathrm{TM}*}$ (○). (b) Differential error δ_{20} measured on the imaginary part the dynamic series sum for two substrates with different thicknesses (only $\widehat{V}_i^{\mathrm{TM}}$ case is plotted here). 108
5.10 Relative error in the convergence of the quasi-static TM series for different cell's positions. The position and orientation of the cells are indicated with different markers. 109
5.11 Convergence ϵ_M, δ_N of the quasi-static TM series arising in the self-term interactions when the domains are scaled as with $k = 0.5, 1, 2$ @2.5 GHz. The different sizes considered of every domain are indicated with gray colors, from the smallest in black until the bigger in lighter gray. 110
5.12 Test structure. Rectangular cavity $32 \times 16 \times 4.08$ mm^3 filled with two dielectric slabs ($h_\mathrm{d} = 0.51$ mm, $\varepsilon_\mathrm{r} = 2.33(1 - \mathrm{j}0.0012)$) separated by an air gap ($h = 3.06$ mm). 111
5.13 Voltage induced in the observer BFs (at z) by TE/TM-waves generated at source BF (at z') and for different gap thickness ($r\,h$). 112
5.14 Convergence of TM/TE series (reaction #1′–#1) for small gap thickness: h(●), $h/2$(○), $h/4$ (×), $h/6$ (+), $h/8$ ($*$) and $h/10$ (□). In the figures, the variable m is the number of TE (resp. TM) modes. 113
5.15 Comparison between the convergence achieved in the TM and the TE series against the number of modal terms considered in the sum: h(gray-●) and $h/10$(black-○). 115
5.16 Convergence of TM series (reaction #1'–#2) with the following gap thickness: h(●), $h/2$(○), $2h$ (×). The variable m is the number of TM modes. 115
5.17 Mapping of a rectangular/triangular cells into a $u - v$ normalized domain. . . . 120
5.18 Connection of two multiport networks. The multiport network defined with $\mathcal{S}$ is associated to the EM problem and $\mathcal{T}$ incorporates external circuits or interconnections. 122
5.19 Example of connection of multiple network using a single matrix $\mathcal{T}$. 123
5.20 Different scenarios with grounded stubs. 125
5.21 Comparison between the responses of the structures in Fig. 5.20. 125

5.22 Description of Coupled Lines Filter [8, 22, 51]. 126
5.23 Influence of Losses. Lossless (thin solid line), + dielectric (dotted line), + Cu strips (gray solid line), + Cu cavity (thick solid line). 127
5.24 Three mesh schemes with rectangular mesh with lines of ≈ 20 div/λ 128
5.25 Representation of the error in the scattering parameters as a function of the number of modes in mesh (a)($\bullet$), (b) ($\circ$) and (c) ($\times$) from Fig. 5.33. 129
5.26 Simulations with different mesh densities: Single cell (dotted line), two cells (dashed line), three cells (solid line) per width. 129
5.27 Comparison between measurements (solid lines without symbols) and simulations of the return losses (solid line with $\bullet$) and insertion losses (solid line with $\circ$). 130
5.28 Description of Three-layers Bandpass Filter. 131
5.29 Influence of Losses. Lossless (thin solid line), + dielectric (dotted line), + Cu strips (gray solid line), + BeCu cavity (thick solid line). 132
5.30 Frequency response obtained with simulation (black line) and measurements (gray line). Scattering parameters S_{11}, S_{12} (solid line) and S_{22}, S_{21} (dashed line).133
5.31 Assembling of the prototype 134
5.32 Description of Ring Resonator. 135
5.33 Three mesh schemes generated with triangular and rectangular cells. 136
5.34 Comparison between results of simulations with mesh (a) (dotted), (b) (dashed) and (c) (solid) from Fig. 5.33. 136
5.35 Return and insertion loss obtained with a simulation using our approach (solid line) and a commercial software [54] (dashed line). 137
5.36 Magnitude of the surface currents $\mathbf{J}(\mathbf{r}) \cdot \mathbf{J}^*(\mathbf{r})$ A/mm induced in the circuit by exciting first port (left-hand side) with one watt of available power ($V_{\mathrm{g}} = 14.4$V and $Z_{\mathrm{g}} = 50\ \Omega$). 137
5.37 Description of Tapped-Combline filter [55]. 138
5.38 Insertion (dashed line) and return (solid line) losses (dB) versus frequency (GHz) for different positions of tapped line. 139
5.39 Influence of the cavity dimensions in the filter response considering a tapper offset of $\Delta/b = 0.3833$. Note: the symbols of the capacitors are not printed but the y are taken into account in the simulations. 140
5.40 Filter responses in function of the capacitor values loading the resonators. Filter loaded with C_i from description (—); $1.5C_i$ $(\cdot -)$ and $0.5C_i(- -)$. 141
5.41 Insertion Losses (dB) versus frequency (GHz) of a tapped combline filter with $\Delta/b = 0.5$. Comparison between our method (① and solid red line) and published measurements (② and solid blue) and simulations (③ solid black) from [55]. 142
5.42 Description of Notch Filter. 143
5.43 Different views of the prototype. 143
5.44 Comparison between measurements (gray lines) and simulations (black lines). . 144
5.45 Sensitivity analysis. Monte-Carlo method parameters. Dimensions are given in mm and resistivity in $\mu\Omega$·cm. 145

5.46 Measurements of scattering parameters (solid) compared to simulations from sensitivity analysis (watermark). 146

List of Tables

3.1 Transverse field components of a mode expressed in terms of scalar potentials. . 26
3.2 Different representation of OIs. 29
3.3 Variation of **g**-components on a triangular (2nd row) and rectangular (3rd row) subdomain. 34
3.4 Perfect electric conductor (PEC) boundary conditions on $\partial\Omega$. 36
3.5 Scalar potentials for rectangular PEC boundaries [21]. 37
3.6 Scalar potentials for PEC circular boundaries [21]. 38
3.7 Scalar potentials for skewed periodic boundaries. 42
3.8 Relations and expressions for modal functions. 43

4.1 Expressions for the propagation constant, characteristic impedance and general impedance for different intervals of κ_ρ/k, assuming $\kappa_\rho \in \mathbb{R}$ (see Fig. 4.18). . . . 79

5.1 Quantitative comparison between modal and image-based formulations. 95
5.2 List of methods and some relevant publications for the formulation of multilayered rectangular cavity GF. 96
5.3 TE (TM) quasi-static series sums @2.5GHz up to M=$1'001'129$ ($998'872$) terms. 104
5.4 Sum of TM quasi-static series up to $M = 998'872$ terms @2.5 GHz for different cell's positions. 109
5.5 Sum of TM quasi-static series up to $M = 998'872$ terms @2.5 GHz for different cell's sizes. 110
5.6 Quantitative description of loss models. 117

CV

Pedro Crespo Valero was born on April 23, 1976 in Antas (Almería), Spain. He received the Ingeniero de Telecomunicación degree from the Escuela Superior de Ingenieros de Telecomunicación (ETSI), Universidad Politécnica de Madrid (UPM), in 2001. In February 2003, he started PhD studies at the Laboratoire d'Electromagnétisme et d'Acoustique (LEMA), Ecole Polytechique Fédérale de Lausanne (EPFL).

In June 2001, he obtained in UPM his final diploma project with honors for a work entitled "Equivalent Circuit of a Radial Stub in Circular Waveguide" where he developed a Computer Aided Design (CAD) tool based on the MM technique to assist in the creation of new equivalent circuits for discontinuities and the design of waveguide filters. In February 2002, he joined LEMA where he is currently Research and Teaching Assistant. He has been active Research member in the following projects:

- "Integrated planar and waveguide simulation tool". Responsible for the design of a CAD tool (`MAMBO`) for the analysis of multilayered boxed media printed circuits. ESA/ESTEC Contract No. 16332/02/NL/LvH. European Space Agency Project (2004-Present).
- "Innovative MEMs Devices for Wideband Reconfigurable RF Microsystems (WIDERF)". Interdisciplinary research project for the development of Micro-Electro-Mechanical Systems (MEMS) devices and functions. Responsible for the characterization of MEMS and design of innovative True-Time Delay Lines.European Project Reference IST-2001-33286 (2003-2005).
- "Millimetre-wave and microwave components design framework for ground and space multimedia network (MMCODEF)". Research training network with partners from university , research institutes and industry. Responsible for the characterization of high frequency planar antennas.European Project Reference HPRN-CT-2000-00043 (2002-2004).

Among his teaching activities he has assisted in the exercises for the courses of Electromagnetics I and II and Antennas and Propagation, graded exams, and proposed and supervised student semester and final diploma projects.

Pedro Crespo Valero has completed the Elementary degree in Music for piano and classical guitar. He is also a former member of Colegio Mayor Diego de Covarrubias, Universidad Complutense de Madrid (UCM), Spain.

List of Publications

REFEREED JOURNAL PAPERS

1. P. Crespo-Valero, I. Stevanović, D. Llorens del Río, and J. R. Mosig, "A Formulation of the Overlapping Integrals Arising in Transversally Bounded Problems," *IEEE Transactions on Microwave Theory and Techniques*, in preparation.

2. I. Stevanović, P. Crespo-Valero, K. Blagović, F. Bongard, and J. R. Mosig, "Integral-equation analysis of 3-D metallic objects arranged in 2-D lattices using the Ewald transformation," *IEEE Transactions on Microwave Theory and Techniques*, vol. 54, no. 10, pp. 3688 – 3697, Oct. 2006.

3. I. Stevanović, P. Crespo-Valero, and J. R. Mosig, "An integral-equation technique for solving thick irises in rectangular waveguides," *IEEE Transactions on Microwave Theory and Techniques*, vol. 54, no. 1, pp. 189–197, Jan. 2006.

4. J. Perruisseau-Carrier, R. Fritschi, P. Crespo-Valero, and A. K. Skrivervik, "Modeling of periodic distributed MEMS application to the design of variable true-time delay lines," *IEEE Transactions on Microwave Theory and Techniques*, vol. 54, no. 1, pp. 383–393, Jan. 2006.

REFEREED CONFERENCE PAPERS

1. P. Crespo-Valero, I. Stevanović, and J. R. Mosig, "A Unified Approach to Model Planar Multilayered Structures with Lateral Perfect Electric/Magnetic and Periodic BCs," in *Proc. European Conference on Antennas and Propagation (EuCAP 2006)*, Nice, France, Nov. 6–10, 2006.

2. M. Navarro-Tapia, M. Mattes, P. Crespo-Valero, P. Otero, and J. R. Mosig, "Filtros en tecnología SIW," in *XXI Simpósium Nacional de la Unión Científica Internacional de Radio (URSI 2006)*, no. 2023, Oviedo, Asturias, Spain, Sept. 12–15, 2006.

3. I. Stevanović, P. Crespo-Valero, and J. R. Mosig, "Electromagnetic scattering from a 2-D array of 3-D metallic objects," in *Proc. IEEE Antennas and Propagation Society Symposium (AP-S)*, Albuquerque, New Mexico, USA, July 9-14, 2006, pp. 4535–4538.

4. P. Crespo-Valero, M. Mattes, I. Stevanović, and J. R. Mosig, "Analysis of multilayer boxed printed circuits," in *13th IEEE Mediterranean Electrotechnical Conference (MELECON 2006)*, Torremolinos, Málaga, Spain, May 16–19, 2005, pp. 206–209.

5. ——, “A numerically stable transmission line model for multilayered Green’s functions,” in *Proc. IEEE Antennas and Propagation Society Symposium (AP-S)*, vol. 3A, Washington DC, USA, July 3–8, 2005, pp. 200–203.
6. I. Stevanović, P. Crespo-Valero, and J. R. Mosig, “Nearfield computation in planar multilayered structures,” in *Proc. International Symposium on Antennas (JINA’04)*, Nice, France, Nov. 8–11, 2004, pp. 58–59.
7. P. Crespo-Valero and J. E. Page, “Circuito equivalente del iris circular centrado en guía circular. aplicación al diseño de dispositivos de microondas,” in *XVI Simpósium Nacional de la Unión Científica Internacional de Radio (URSI 2001)*, Madrid, Spain, Sept. 2001.

WORKSHOP PRESENTATIONS

1. P. Crespo-Valero, M. Mattes, and J. R. Mosig, “Full-wave simulation of multi-layered boxed printed circuits,” in *Proc. International Workshop on Microwave Filters (IWMF 2006)*, CNES, Toulouse, France, Oct. 16–18, 2006.
2. P. Crespo-Valero, M. Mattes, and J. R. Mosig, “MAMBO: An implementation of an efficient method for the simulation of multilayered packaged printed circuits,” in *Microwave Technology and Techniques Workshop*, ESA-ESTEC, Noordwijk, The Netherlands, May 15–16, 2006.
3. A. Skrivervik and P. Crespo-Valero, “MEMS in antennas,” in *Workshop on MEMS for Millimeter-Wave Communications (MEMSWAVE’05)*, Montreux, Switzerland, June 23–24, 2005.
4. J. Perruisseau-Carrier, R. Fritschi, P. Crespo-Valero, C. Hibert, J.-F. Zurcher, P. Fluckiger, A. K. Skrivervik, and A. M. Ionescu, “Fabrication process and model for a MEMS parallel plate capacitor above a CPW line,” in *Workshop on MEMS for Millimeter Wave Communications (MEMSWAVE’04)*, Uppsala, Sweden, June 30–2, 2004.

TECHNICAL REPORTS

1. P. Crespo-Valero and M. Mattes, and J. R. Mosig, “Validation and verification of the electromagnetic kernel,” Technical Notes TN504-0,1,2,3,4,5 and 6, ESA-ESTEC Activity 16332/02/NL/LvH : Planar and waveguide simulation tools, Feb. 2006.
2. P. Crespo-Valero and M. Mattes, and J. R. Mosig, “Losses in metallic enclosures, printed circuits and dielectrics,” Technical Note TN501, ESA-ESTEC Activity 16332/02/NL/LvH : Planar and waveguide simulation tools, Feb. 2006.
3. P. Crespo-Valero and M. Mattes, and J. R. Mosig, “Electromagnetic code development: Implementation of MAMBO,” Technical Note TN502, ESA-ESTEC Activity 16332/02/NL/LvH: Planar and waveguide simulation tools, Apr. 2005.

4. P. Crespo-Valero and M. Mattes, and J. R. Mosig, “Analysis of multilayer boxed printed circuits: Review of numerical techniques and mathematical formulation,” Technical Note TN501, ESA-ESTEC Activity 16332/02/NL/LvH: Planar and waveguide simulation tools, Feb. 2005.

5. P. Crespo-Valero, J. Perruisseau-Carrier, J.-F. Zürcher, A. Skrivervik, R. Fritschi, F. Cannehan, G.-A. Racine, P. Langlet, and P. Flückiger,, “Fabrication of a test kit for the characterization of CPW microwave circuits on R-plane sapphire,” Center of Micro and Nano Technology annual report, Dec. 2003.

6. R. Fritschi, C. Hibert, P. Flckiger, A. Ionescu, P. Crespo-Valero, J. Perruisseau, J.-F. Zürcher and A. Skrivervik, “Complanar waveguide RF-MEMS shunt capacitive switches,” Center of Micro and Nano Technology annual report, Dec. 2003.

7. R. Koss and P. Crespo-Valero, “An efficient algorithm for calculating any number of coaxial waveguide eigenvalues with any desired precision,” LEMA-EPFL Internal report, Nov. 2002.